Development of a wide-spectrum thermochemical code with application to planar reacting and non-reacting shocks

Alberto Cuadra Lara

$$G = \sum_{j \in \mathbf{S}} \mu_j(T, p, \mathbf{n})\, n_j,$$

$$\min G(T, p, \mathbf{n}) \;\Leftrightarrow\; \mathrm{d}G(T, p, \mathbf{n}) = 0,$$

$$q_i = \sum_{j \in \mathbf{S}} a_{ij} n_j - b_i^{\circ} = 0, \quad \forall i \in \mathbf{E}$$

$$\mathcal{L}(T, p, \mathbf{n}, \boldsymbol{\lambda}) = G(T, p, \mathbf{n}) + \boldsymbol{\lambda}\, \mathbf{q}(\mathbf{n}),$$

$$\mathrm{d}\mathcal{L} = 0.$$

PhD thesis

Doctoral Thesis

Development of a wide-spectrum thermochemical code with application to planar reacting and non-reacting shocks

Alberto Cuadra Lara

A dissertation submitted in partial fulfillment of the requirements for the degree of Doctor of Philosophy in Fluid Mechanics

Universidad Carlos III de Madrid

Advisors:
Marcos Vera Coello
César Huete Ruiz de Lira

Leganés, June 2023

To my family.

"Science, my lad, is made up of mistakes,
but they are mistakes which it is useful to make,
because they lead little by little to the truth."

– Jules Verne

Agradecimientos

Después de varios meses de ausencia, ha llegado el momento de cerrar un capítulo en mi vida en el que no puedo evitar sentir una profunda gratitud. Quiero expresar mi sincero agradecimiento a todas las personas que me han acompañado y brindado su apoyo incondicional durante esta travesía. Sin vuestra presencia, esto no habría sido lo mismo.

En primer lugar, quiero expresar mi profundo agradecimiento a mis directores, Marcos y César, por su inquebrantable apoyo a lo largo de este camino, tanto en lo personal como en lo profesional. En particular, quiero agradecer a Marcos por haber sacado lo mejor de mí durante esta tesis, gracias por tu juicio impecable y búsqueda constante de la perfección. Tu guía ha sido fundamental en el desarrollo de este trabajo. César, gracias por contagiarme esa pasión por la investigación y poder contar siempre contigo. Tu mente inquieta y tus ideas constantes han sido un impulso incalculable para mi aprendizaje y crecimiento en este campo. Sencillamente por todo, por tu orientación, por confiar en mí y por tu paciencia a lo largo de este proceso.

I would like to express my sincere gratitude to Mario Di Renzo for his guidance, warm hospitality, and the privilege of working together. During my research stay in Lecce, Italy, I truly felt at home, and I am honored to have had this incredible opportunity. I also would like to extend my thanks to Danilo for his companionship during my time there. We shared many enjoyable moments. It was a pleasure spending time with you. Additionally, I want to recognize the exceptional people with whom I have had the privilege of collaborating. Javier (Urzay), your contributions and perfectionism have been instrumental in shaping my scientific career, you are a constant source of inspiration. Chris (Williams), I am continually learning from you in every meeting we have. Your unwavering dedication and profound knowledge are truly remarkable. Thank you both for your invaluable contributions.

Agradezco de manera especial a mis profesores de la UMA, Carlos del Pino y Luis Parras, por despertar en mí el interés por la investigación y transformar mis metas profesionales. Su invaluable orientación y labor docente han sido fundamentales en mi desarrollo académico. Carlos, ha sido un privilegio poder aprender de ti y espero que nuestros caminos se cruzen en un futuro. Luis, en particular, quiero agradecerte

por ser el impulsor de mi decisión de cursar el máster de Matemática Industrial en la Universidad Carlos III de Madrid (UC3M). Sin tu consejo, mi camino habría tomado un rumbo distinto y no habría tenido la oportunidad de conocer a las personas que forman parte de mi vida.

A mis compañeros de la UC3M, con los que he tenido la suerte de compartir grandes momentos juntos. Por supuesto, a mi compañera de despacho Vanesa. Ha sido realmente gratificante y enriquecedor poder aprender de ti. Fer y Ale (Millán), espero que tengamos muchas más aventuras juntos. El congreso en Tenerife fue inolvidable. Gracias por todos vuestros consejos y apoyo. Mi compañero de gym Dani (Moreno), ha sido todo un placer poder aprender de ti. Volveré "fuerte". Gracias Marta, Patri y Rafa por alegrarme mis días. Andrés, sacamos todo lo que se podía de Phoenix. Fue un viaje memorable. Quique y Dani (Galisteo), gracias por todos vuestros consejos. Por todos vosotros, Alex (Martinez), Javi (Redolat), María, Pablo (Prieto), Miguel, Jesús, Esperanza, Alen, Desiree, Mariano, Mario (Sánchez), Javi (Rodríguez), Wil, Sergio, Lorenne, Pablo (García), Antonio, Alejando (Sevilla), Domingo y todo el resto del departamento. Imma, gracias por confiar en mi.

A mis amigas de la infancia María (Ansino), Ana, Andrea (Trueba), Rosa, Andrea (Díaz), Ele, Selma y Paula, a las que admiro y no puedo estar más orgulloso. María, gracias por ser auténtica y poder contar siempre contigo. Por supuesto, Luis, espero que me sigas maravillando con tus anécdotas y aventuras. Habéis sido un apoyo fundamental. A mis compañeros del M2i, Javi, Rafa y Víctor, gracias por motivarme con vuestro talento y espíritu. Por más *Pequeña Graná* juntos. Mi grupo Erasmus en Rumanía, Robert, Vicky, Marina, Lili, Quino y Jaime, sois más que compañeros de viaje. Gracias por crear recuerdos inolvidables. A todo el grupo Netsales, Juan, José Alberto, Raquel, Irene, Giu, Ramón, Claudia (Mata), Sandra, Eloy y Francesco. Gracias por sacarme siempre una sonrisa y contagiarme con vuestra positividad y actitud, sois grandes.

Special thanks to my backpacking group, René, Markus, and Sebastian. The unforgettable adventures we experienced while exploring Mexico, Croatia, Bosnia and Herzegovina, Montenegro, and many other places will be with me forever.

Por último, quiero dirigirme a toda mi familia. Gracias por vuestro apoyo incondicional y confiar siempre en mí. A ti, Claudia, mi compañera de vida, espero seguir aprendiendo de ti. Eres una persona maravillosa y un pilar fundamental en mi vida. Sin tu apoyo constante esto no habría sido posible. Gracias por inspirarme cada día. Por seguir evolucionando a tu lado. A mi madre, Eva, quien me ha enseñado que las barreras las creamos nosotros mismos. Eres fuente de inspiración. A mi padre, Javi,

y a Ana, gracias por todo lo que me habéis enseñado y demostrarme que no hay que rendirse nunca. A mis abuelos, Juan (Lara) y Mariló, Juan (Cuadra) y Charo, y Juan (Gutierrez) y Mari, por vuestra valiosa ayuda a lo largo de mi vida. A mis hermanos, Javi, María, David y Laura, de quienes continúo aprendiendo constantemente. Sois luz, gracias por enseñarme tanto. A Sandra, Rubén, Sensi y, por supuesto, Aroa, por llegar a nuestras vidas. A Carmen, por darme tan buenos consejos y hacerme sentir como en casa. A mis tíos, especialmente a Juan (Lara), Caroli, Mari Carmen, Estrella, Jessi, Fran, Elena, José Manuel y Flas, gracias por vuestro apoyo y hacerme crecer como persona. Estéis donde estéis, Juan (Cuadra) y Diego, me habría encantado hablar de ciencia con vosotros. A mis primos, en especial a Mari Carmen (Cuadra), Juan y Gonzalo. Sois todos magníficos y no hay palabras suficientes para describir lo que significáis para mí. Habéis contribuido a mi crecimiento personal, y espero seguir mejorando a vuestro lado. Este trabajo va dedicado a todos vosotros.

A. Cuadra
Madrid, 2023

Published and submitted content

The following publications have contributed directly or indirectly to this thesis.

Journal articles

1. **A. Cuadra**, C. Huete, M. Vera (2020). Effect of equivalence ratio fluctuations on planar detonation discontinuities. Journal of Fluid Mechanics, 903, A30. doi: 10.1017/jfm.2020.651. This publication is totally included in **Chapter 3** of this PhD thesis, but it is not indicated as a reference in the main text.

2. C. Huete, **A. Cuadra**, M. Vera, J. Urzay (2021). Thermochemical effects on hypersonic shock waves interacting with weak turbulence. Physics of Fluids 33, 0861111 (featured article). doi: 10.1063/5.0059948. This publication is totally included in **Chapter 4** of this PhD thesis, but it is not indicated as a reference in the main text.

3. **A. Cuadra**, C. Huete, M. Vera. Combustion Toolbox: An open-source thermochemical code for gas and condensed-phase problems involving chemical equilibrium. Submitted for publication in Computer Physics Communications. This publication is totally included in **Chapter 2** of this PhD thesis, but it is not indicated as a reference in the main text.

4. **A. Cuadra**, C. T. Williams, M. Di Renzo, M. Vera, C. Huete. Direct numerical simulations and linear analysis for hypersonic shock-turbulence interaction in air. In preparation for submission to Journal of Fluid Mechanics. This publication is partially included in **Chapter 5** and **Appendix D** of this PhD thesis, but it is not indicated as a reference in the main text.

Published and submitted content

Conference proceedings

1. **A. Cuadra**, M. Vera, M. Di Renzo, C. Huete (2023). Linear Theory of Hypersonic Shocks Interacting with Turbulence in Air. In 2023 AIAA SciTech Forum, National Harbor, USA. doi: 10.2514/6.2023-0075. Conference presentation. This publication is totally included in **Chapter 5** of this PhD thesis, but it is not indicated as a reference in the main text.

2. **A. Cuadra**, C. Huete, M. Vera (2022). Desarrollo de un código termoquímico para la evaluación de las propiedades teóricas de explosivos (CT-EXPLO) y la estimación del rendimiento de motores cohete (CT-ROCKET). In 9th Congreso Nacional de I+D en Defensa y Seguridad, Pontevedra, Spain. Conference presentation. This publication is partially included in **Chapter 2** of this PhD thesis, but it is not indicated as a reference in the main text.

3. **A. Cuadra**, C. Huete, M. Vera (2022). Amplificación de la turbulencia a través de una onda de choque en régimen hipersónico. In 9th Congreso Nacional de I+D en Defensa y Seguridad, Pontevedra, Spain. Conference presentation. This publication is partially included in **Chapter 4** of this PhD thesis, but it is not indicated as a reference in the main text.

4. **A. Cuadra**, C. Huete, M. Vera (2022). Combustion Toolbox: A MATLAB-GUI based open-source tool for solving combustion problems. In 12th National and 3rd International Conference on Engineering Thermodynamics (CNIT), Madrid, Spain. Conference presentation. This publication is totally included in **Chapter 2** of this PhD thesis, but it is not indicated as a reference in the main text.

5. **A. Cuadra**, C. Huete, M. Vera (2022). Theory of turbulence augmentation across hypersonic shock waves in air. In 1st Spanish Fluid Mechanics Conference (SFMC), Cádiz, Spain. Conference and poster presentation. This publication is totally included in **Chapter 5** of this PhD thesis, but it is not indicated as a reference in the main text.

6. **A. Cuadra**, C. Huete, M. Vera, J. Urzay (2021). Theory of turbulence augmentation across hypersonic shock waves. In 74th Annual Meeting of the Division of Fluid Dynamics (APS DFD), Phoenix, USA. Conference presentation. This publication is totally included in **Chapter 4** of this PhD thesis, but it is not indicated as a reference in the main text.

7. **A. Cuadra**, C. Huete, M. Vera (2021). Effect of fuel mass fraction heterogeneity on the detonation propagation speed. In 25th International Congress of Theoretical and Applied Mechanics (ICTAM), Milano, Italy. Poster presentation. This publication is totally included in **Chapter 3** of this PhD thesis, but it is not indicated as a reference in the main text.

8. **A. Cuadra**, M. Vera (2019). Development and validation of a new MATLAB/GUI based thermochemical code. In 11th International Mediterranean Combustion Symposium (MSC), Tenerife, Spain. Poster presentation. This publication is partially included in **Chapter 2** of this PhD thesis, but it is not indicated as a reference in the main text.

9. **A. Cuadra**, M. Vera (2019). Development of a GUI-based thermochemical code with teaching and research applications. In 1st Colloquium of the Spanish Theoretical and Applied Mechanics Society (STAMS), Madrid, Spain. Poster presentation. This publication is partially included in **Chapter 2** of this PhD thesis, but it is not indicated as a reference in the main text.

Other research merits

During the research period, one paper was published, but it is not included in this thesis since its content is out of the scope of the present work. Additionally, there is another paper that has yet to be published, which is also not related to the main focus of this thesis.

1. J. Sánchez, **A. Cuadra**, C. Huete, M. Vera (2022). SimEx: A tool for rapid evaluation of the effects of explosions. Applied Sciences 2022, 12(18), 9101. doi: 10.3390/app12189101.

2. G. A. Patiño-Jaramillo, **A. Cuadra**, M. Vera, I. Iglesias. Implementation of Hydraulic Network Models for networks representing transformer winding cooling systems (work in progress).

3. **A. Cuadra**, C. Huete, M. Vera (2022). Finalist *"6ª edición Premio Isdefe I+D+i Antonio Torres"* and second place *"1ª edición Premio Estudiante Universitario Isdefe"* at the 9th Congreso Nacional de I+D en Defensa y Seguridad held in Pontevedra, Spain. Our article *Amplificación de la turbulencia a través de una onda de choque en régimen hipersónico* was selected as one of the top 10 finalists out of 207 submitted and accepted articles by the judging panel.

Abstract

The recent scientific and technological advancements have underscored the critical necessity for reliable, robust, and efficient numerical codes capable of predicting the chemical composition and properties of complex mixtures at chemical equilibrium. In response to this demand, this thesis presents the development and validation of a novel open-source thermochemical code called Combustion Toolbox (CT). This tool is designed to determine the equilibrium state of multi-species mixtures in gaseous or pure condensed phases, including ions. The code incorporates a comprehensive suite of algorithms, ranging from fundamental chemical equilibrium problems to complex computations of steady shock and detonation waves in various flow configurations, as well as predictions of rocket engine performance. Implemented in MATLAB, CT is accompanied by a user-friendly graphical user interface, ensuring flexibility and accessibility for all users. Extensive validation demonstrates excellent agreement with established codes such as NASA's CEA, Cantera within Caltech's Shock and Detonation Toolbox, and the recent Thermochemical Equilibrium Abundances code. CT has been utilized in all of the studies presented in this thesis, demonstrating its reliability and versatility.

The second part of the thesis delves into the theoretical analysis of reactive and non-reactive shocks propagating through non-homogeneous conditions. Conducting experiments and high-fidelity simulations in this field can be challenging and computationally expensive. In this context, linear interaction analysis has emerged as a valuable tool to evaluate the hydrodynamical aspects contributing to the amplification of disturbances across the shock. Two prominent cases are investigated. Firstly, the study focuses on detonations with inhomogeneities in the upstream fuel mass fraction. The findings reveal that, in most cases, the detonation propagation speed is higher than in equivalent homogeneous scenarios. Subsequently, the investigation shifts towards the interaction of hypersonic shocks with turbulent flows, incorporating the associated thermochemical effects in single-species diatomic gases. The analysis is further extended to multi-species mixtures using CT, with a particular emphasis on air. These studies demonstrate that thermochemical effects arising at hypersonic velocities significantly enhance turbulent fluctuations in the post-shock gas compared to the simplified thermochemical frozen gas assumption.

Resumen

Los avances científicos y tecnológicos recientes han destacado la necesidad crítica de contar con códigos numéricos fiables, robustos y eficientes capaces de predecir la composición química y las propiedades de mezclas complejas en equilibrio químico. En respuesta a esta demanda, esta tesis presenta el desarrollo y la validación de un novedoso código termoquímico de código abierto llamado *Combustion Toolbox* (CT). Esta herramienta permite determinar el estado de equilibrio de mezclas multiespecie en fases gaseosas o condensadas puras, incluyendo iones. El código incorpora una amplia gama de algoritmos, desde problemas fundamentales de equilibrio químico hasta complejos cálculos de ondas de choque y detonación estacionarias en varias configuraciones de flujo, así como predicciones del rendimiento de motores cohete. Implementado en MATLAB, CT cuenta con una interfaz gráfica de usuario fácil de usar, que garantiza flexibilidad y accesibilidad para todos los usuarios. Se ha realizado una extensa validación que demuestra una excelente concordancia con códigos establecidos como el CEA de la NASA, Cantera y *Shock and Detonation Toolbox* del Caltech, así como el reciente código *Thermochemical Equilibrium Abundances*. CT se ha utilizado en todos los estudios presentados en esta tesis, demonstrando su fiabilidad y versatilidad.

En la segunda parte de la tesis, se analizan los choques reactivos y no reactivos que se propagan en condiciones no homogéneas. Realizar experimentos y simulaciones de alta fidelidad en este campo puede ser desafiante y costoso computacionalmente. En este contexto, el análisis de interacción lineal ha surgido como una herramienta valiosa para evaluar los aspectos hidrodinámicos que contribuyen a la amplificación de las perturbaciones a través del choque. Se investigan dos casos destacados. En primer lugar, el estudio se centra en las detonaciones con inhomogeneidades aguas arriba de la fracción másica del combustible. Los resultados indican que, en la mayoría de los casos, la velocidad de propagación de la detonación es mayor que en escenarios homogéneos equivalentes. Posteriormente, la investigación se centra en la interacción de choques hipersónicos con flujos turbulentos, incorporando los efectos termoquímicos asociados en gases diatómicos de una sola especie. El análisis se extiende además a mezclas multiespecie utilizando CT, con un énfasis particular en el aire. Estos estudios demuestran que los efectos termoquímicos que surgen a velocidades hipersónicas aumentan significativamente las fluctuaciones turbulentas en el gas posterior al choque en comparación con la aproximación de gas termoquímicamente congelado.

Contents

List of Figures

List of Tables

Nomenclature

Each symbol is conveniently defined in every chapter, and symbols with multiple definitions should be clear from the context.

Constants

$\hbar$	reduced Planck's constant
κ_b	Boltzmann constant
N_A	Avogadro number
R	universal gas constant, $R = \kappa_b N_A$

Roman Symbols

$\bar{e}_{\mathrm{vib}}$	dimensionless vibrational component of the specific internal energy
$\delta\mathcal{U}$	correction streamwise velocity ratio
$\delta\mathcal{V}$	correction specific volume ratio
ℓ	integral length size of the upstream turbulence
ℓ_i	detonation induction length
ℓ_T	thermochemical nonequilibrium region behind the shock
$\langle l_{\mathrm{f}} \rangle$	dimensionless second-order turbulent correction to the mass
$\langle m_{\mathrm{f}} \rangle$	dimensionless second-order turbulent correction to the streamwise momentum
$\langle n_{\mathrm{f}} \rangle$	dimensionless second-order turbulent correction to the energy fluxes
$\mathbf{E}$	list of elements
$\mathbf{f}$	objective function vector
$\mathbf{J}$	Jacobian matrix
$\mathbf{k}$	wavenumber vector
$\mathbf{M}_0$	property matrix
$\mathbf{n}$	molar vector
$\mathbf{q}$	atom balance vector
$\mathbf{S}^{\mathbf{C}}$	list of condensed-phase species
$\mathbf{S}^{\mathbf{G}}$	list of gaseous-phase species

$\mathbf{S}$	list of species
$\mathbf{x}$	unknowns vector
$\mathcal{G}$	ratio electronic partition functions
$\mathcal{I}$	turbulent intensity
$\mathcal{K}$	Donzis similarity argument
$\mathcal{L}$	Lagrangian objective function
$\mathcal{M}$	Mach number
$\mathcal{M}_t$	turbulent Mach number
$\mathcal{P}$	pressure ratio
$\mathcal{R}$	density ratio
$\mathcal{S}$	detonation propagation speed correction
$\mathcal{T}$	temperature ratio
$\mathcal{U}$	streamwise velocity post-shock perturbation amplitude
$\mathcal{V}$	spanwise velocity post-shock perturbation amplitude
$\mathbb{D}$	density post-detonation perturbation amplitude
$\mathbb{O}$	vorticity post-detonation perturbation amplitude
$\mathbb{P}$	pressure post-detonation perturbation amplitude
$\mathbb{U}$	streamwise velocity post-detonation perturbation amplitude
$\mathbb{V}$	spanwise velocity post-detonation perturbation amplitude
$\mathbb{X}$	corrugated post-detonation perturbation amplitude
A	area
a	speed of sound
A^e	entropic post-shock degree of dissociation pre-factor
a_{ij}	stoichiometric coefficient
a_i	NASA's polynomials coefficients
B	dimensionless parameter
b_i°	initial number of atoms of the i-th element
C_p°	species molar specific heat at constant pressure
c_t	arbitrary constant defined with the temporal reference frame
c_p	specific heat at constant pressure
c_v	specific heat at constant volume
d	degrees of freedom

E	energy spectrum
e	internal energy
E_e	initial number of electrons
e_f	internal energy of formation
f	state function
G	Gibbs free energy of the system
g	Gibbs free energy
G°	species molar specific Gibbs free energy
G^a	acoustic density-variance pre-factor
G^e	entropic density-variance pre-factor
H	Helmholtz free energy of the system
H	local slope of the heat release
h	enthalpy
H°	species molar specific enthalpy
h_f	enthalpy of formation
I_{sp}	ambient pressure specific impulse
I_{vac}	vacuum specific impulse
J_{ij}	components of the Jacobian matrix
K	turbulent kinetic energy amplification factor
k	wavenumber amplitude
k_o	characteristic wavenumber
m	mass
N	normalization parameter
n	mixture number of moles in gaseous-phase
n_j	number of moles of the j-species
p	pressure
p°	reference pressure, $p^\circ = 1$ bar
Q	dimensionless heat release, $Q = \frac{(\gamma^2-1)}{2a_1^2} q_1$
q_1	heat release
q_d	net change of specific chemical enthalpy caused by the gas dissociation reaction
q_i	net change of specific chemical enthalpy caused by the gas ionization reaction

Q_{el}	electronic partition function
R_{g}	specific gas constant
R_{ii}	diagonal Reynolds stresses
Re_{ℓ}	turbulent Reynolds number
Re_{λ}	Taylor-scale Reynolds number
s	entropy
S°	species molar specific entropy
T	temperature
t	time
u	streamwise/longitudinal velocity
V	specific volume
v	spanwise/transverse velocity
v	volume
W	enstrophy amplification factor
W	local slope of the upstream density
W	mixture molar mass
$W_{\perp}$	enstrophy amplification factor in the transverse direction
W_i	species molar mass
W_z	amplification factor of the rms of the z-component of the vorticity
X	mole fraction
x	spatial coordinate
Y	mass fraction
NC	number of condensed-phase species
NE	number of elements
NG	number of gaseous-phase species
NS	number of species
P	probability-density distribution

Greek Symbols

α	degree of dissociation
β	wave/incidence angle
β_i	dimensionless characteristic temperature, $\beta_i = \Theta_i/T_1$

Δ	variation of the post-detonation state due to the upstream changes in density and heat release
ϵ	scaled upstream mass fraction perturbation, $\varepsilon(k)\sqrt{W^2+H^2}$
ϵ_0	tolerance
η	degree of overdrive
η_i	degree of ionization of species i
Γ	normalized slope of the Hugoniot curve
γ	adiabatic index
κ_i	dimensionless wavenumber in the i-direction
κ_j	phase value of the j-th species, $0 \equiv$ gas, $1 \equiv$ condensed
Λ	reduced wavenumber amplitude, $\Lambda = k/k_o$
λ_i	Lagrange multiplier of the i-th element
λ	Lagrange multiplier vector
μ	effective amplitude of the upstream excitation
μ_j°	chemical potential of the j-th species at the reference pressure
μ_j	chemical potential of the j-th species
ν	kinematic viscosity
Ω	dimensionless vorticity
ω	frequency
Φ	one-dimensional power spectra
ϕ	equivalence ratio
ϕ_i	acoustic, entropic, rotational, or displacement phase angle, denoted with subscripts a, e, r or ξ, respectively
Π	pressure post-shock perturbation amplitude
π_i	dimensionless Lagrange multiplier of the i-th element, $\pi_i = \lambda_i/RT$
Ψ	anisotropy factor
ρ	density
σ	spatial decay rate
σ_i	auxiliary factors
τ	dimensionless time
Θ	characteristic temperature
θ	deflection angle

θ	incidence angle
ε	upstream mass fraction perturbation amplitude
ε_u	upstream streamwise velocity perturbation amplitude
ϖ	vorticity
ϑ	local shock incidence angle
ξ_s	shock displacement
ζ	frequency parameter

Subscripts

(L)	liquid phase
0	initial condition/estimate
1	upstream flow; pre-shock state
2	downstream flow; post-shock state
3	reflected post-shock state
A	monatomic species
A_2	diatomic species
g	gas phase
cj	Chapman-Jouguet
M	species from Third Millennium database (Burcat)
A	air
a	acoustic
aa	acoustic-acoustic
c	critical
d	dissociation
e	entropic
er	entropical-rotational
F	final state
F	fuel
h	high frequency contribution
I	initial state
i	i-th element
i	ionization
j	j-th species

k	k-th iteration
l	reference frame moving with the shock/detonation front
l, i	low frequency contribution
n	normal to the shock
p	piston
r	rotational
s	normal to the shock
st	stoichiometric
v	vibrational
c	combustor end
e	exit
el	electronic
f	flux
inf	infinite area chamber
inj	injector
n	normal
over	over-driven
t	tangential
t	throat

Superscripts

$+$	cation
$-$	anion
$\bar{f}$	small perturbation of the variable f
$\mathrm{non-van}$	non-vanishing contribution
van	vanishing contribution
a	atom
aa	molecule
total	total contribution, vanishing and non-vanishing contributions

Chemical formulae

A	monatomic species
$\mathrm{A_2}$	diatomic species
Ar	argon

C_2H_2	acetylene
C_3H_8	propane
C_6H_5OH	phenol
C_{gr}	solid carbon (graphite)
CH_4	methane
CO	carbon monoxide
CO_2	carbon dioxide
DME	dymethylether
e^-	electron
H_2	molecular hydrogen
H_2O	water
HCN	hydrogen cyanide
LCH_4	liquid methane
LH_2	liquid molecular hydrogen
LOX	liquid molecular oxygen
M	third body species
MMH	monomethyl-hydrazine
N	atomic nitrogen
N_2	molecular nitrogen
N_2H_4	nitrogen tetroxide
O	atomic oxygen
O_2	molecular oxygen
RP1	kerosene rocket propellant-1
Si	silica
UDMH	unsymmetrical dimethylhydrazine

Acronyms

1D, 2D, 3D	one-, two-, three-dimensional
ANL	Argonne National Laboratory
ATcT	Active Thermochemical Tables
BKW	Becker-Kistiakowsky-Wilson equation of state
C	Constants
CEA	Chemical Equilibrium with Applications

CFD	Computational Fluid Dynamics
CFL	Courant-Friedrichs-Lewy
CFRP	Carbon-Fiber-Reinforced-Polymers
CJ	Chapman-Jouguet
CT	Combustion Toolbox
DB	Database
DNS	Direct Numerical Simulations
E	Elements
ECP	Equality Constraint Problem
EN	European Standard
EoS	Equation of State
EV	Internal Energy-Volume
FAC	Finite Area Chamber
fBm	Fractional Brownian Motion
GPL	General Public License
GUI	Graphic User Interface
H9	Heuzé equation of state
HIT	Homogeneous Isotropic Turbulence
HP	Enthalpy-Pressure
HTR	Hypersonic Task-based Research
IAC	Infinite Area Chamber
ISA	International Standard Atmosphere
JANAF	Joint Army Navy Air Force
JCZ	Jacobs–Cowperthwaite–Zwisler equation of state
KHT	Kihara–Hikita–Tanaka equation of state
LAPACK	Linear Algebra Package
LES	Large Eddy Simulations
LIA	Linear Interaction Analysis
MATLAB	Matrix Laboratory
MEX	MATLAB Executable
Misc	Miscellaneous
NASA	National Aeronautics and Space Administration

NIST	National Institute for Standards and Technology
NR	Newton-Raphson
ODWE	Oblique Detonation Wave Engine
OOP	Object-Oriented Programming
PCHIP	Piecewise Cubic Hermite Interpolating Polynomials
PD	Problem Description
PDF	Probability Density Function
PS	Problem Solution
RAM	Random Access Memory
RANS	Reynolds-Averaged Navier-Stokes Simulations
RDE	Rotating Detonation Engine
RH	Rankine-Hugoniot
S	Species
SD	Shock-Detonation
SDT	Spatially Developed Turbulence
SimEx	Simulador de Explosiones
SP	Entropy-Pressure
STANJAN	Stanford-JANAF
STI	Shock Turbulence Interaction
SV	Entropy-Volume
TEA	Thermochemical Equilibrium Abundances
TKE	Turbulent Kinetic Energy
TN	Thermochemical Network
TN	Tuning Properties
TP	Temperature-Pressure
TPS	Thermal Protection System
TV	Temperature-Volume
UC3M	Universidad Carlos III de Madrid
VCS	Version Control System

1 Introduction

Each chapter in this thesis has its own extended introduction, which builds upon the motivation provided below. The subsequent chapters delve deeper into specific applications, theories, and methodologies related to thermochemical codes, and reactive and non-reactive shocks with inhomogeneities in the upstream flow, offering comprehensive justifications for their individual contributions to the field.

1.1 Motivation

The drive to be the first to reach the Moon (21 July 1969), combined with advancements prompted by wartime needs, motivated the development of rocket engines and the modeling of high-energy materials such as explosives, propellants, and pyrotechnics, as well as combustion processes [1]. A fundamental requirement for comprehending and modeling these intricate systems is the accurate characterization of their chemical composition and properties, whether in the gaseous or condensed phase. Over the years, extensive theoretical, numerical, and experimental research has been conducted, giving rise to methodologies that form the foundation of present-day investigations.

In 1946, Brinkley outlined the first generalized analytical method for solving systems with numerous species using chemical equilibrium constants [2]. The author extended this approach to a numerical method in 1947 [3]. Subsequently, Huff et al. [4] at NASA presented a new numerical code capable of obtaining the chemical composition given two state functions, e.g., enthalpy and pressure for isobaric combustion processes. White's pioneering work in 1958 [5] revolutionized the field by introducing a novel numerical approach that shifted the focus to chemical potentials, laying the basis of virtually all state-of-the-art thermochemical codes to date [6–23]. In the early 1960s, Zeleznik and Gordon [6, 24] at NASA further advanced the work of Huff et al. while incorporating the insights from White's work. Their efforts culminated in the development of the widely recognized and extensively used Chemical Equilibrium with Applications (CEA) code, created by Gordon & Mcbride [10, 25]. The NASA CEA code enables the solution of problems involving multi-species single-phase gas mixtures with pure-condensed species. It has numerous capabilities, which will be discussed in the subsequent chapter. More

recently, Reynolds made another important contribution to the field with the STANJAN code [8] in the 1980s. This code extended the mathematical framework to encompass multi-phase systems and exhibited superior suitability for constrained equilibrium calculations [26, 27] due to its robust initialization scheme. However, this code is now part of the commercial program Chemkin [28] and is no longer freely available.

Thermochemical codes also found application in the determination of the theoretical properties of high-energy materials, such as high explosives, propellants, and pyrotechnics [29]. However, accurately modeling these processes presents an increased challenge due to the compressibility effects and phase transitions that cannot be adequately captured by the ideal gas equation of state (EoS). To address this, complex empirical non-ideal EoS are required [30], such as Becker–Kistiakosky–Wilson (BKW) [31], Jacobs–Cowperthwaite–Zwisler (JCZ) [32], or Kihara–Hikita–Tanaka (KHT) [33]. Prominent examples of computer programs that incorporate these non-ideal EoS are CHEETAH [34, 35], EXPLO5 [36, 37], and CARTE [38, 39].

The thermochemical codes discussed above have certain limitations and inconveniences that need to be addressed. Specifically, there are concerns related to the utilization of older software, limited availability due to their critical importance to the defense industry, proprietary concerns, lack of support, and challenges associated with integrating them into modern software environments [40]. Additionally, the scientific and technological advancements achieved during the last decades in fields such as combustion, aerospace engineering, and astrophysics (discussed below) have underscored the critical necessity for reliable, robust, and efficient numerical codes capable of predicting the chemical composition and properties of complex mixtures at chemical equilibrium. In response to this, many open-source computer programs have been developed, e.g., Cantera [41] and TEA [18], written in C++ and Python, respectively. Despite these advancements, there is still room for further improvement, and a significant part of this thesis is devoted to it.

In addition to the progress made in thermochemical codes, the study of reactive and non-reactive shocks has attracted considerable attention. Reactive shocks, also known as detonations, can propagate solely through self-sustaining chemical reactions without requiring any external contribution to maintain their propagation. On the other hand, non-reactive shocks rely on external contributions to sustain their propagation. Despite this difference, both types of shocks share the common characteristic of rapid gas compression, leading to substantial changes in the thermodynamic properties across the shock.

Strong shock waves play a crucial role in various physics-related problems. These include the dynamics of high-energy interstellar medium [42–45], the explosions of giant stars [46–49], the fusion of matter in inertial-confinement devices [50–52], and the ignition of combustible mixtures by lasers [53, 54]. In addition to those, an important contemporary problem of relevance for aeronautical and astronautical engineering is the aerothermochemistry of hypersonic flight [55, 56]. When it comes to detonation waves, they have emerged as a promising alternative to deflagrative premixed combustion, especially in propulsion applications. Rotating detonation engines (RDE) have gained considerable attention in recent years due to their ability to extract additional work from the thermodynamic cycle and reduce the size of the combustor [57].

These problems present a significant challenge due to the non-uniform conditions prevailing ahead of the shock. For instance, hypersonic flights have to deal with atmospheric turbulence, which introduces a random vorticity field behind the shock. Understanding how the energy is distributed and quantifying turbulence amplification in these extreme conditions is crucial for accurately predicting vehicle aerodynamics, heat transfer, and structural integrity [58, 59]. This fascinating research area involves a multidisciplinary approach encompassing experimental, computational, and theoretical investigations. The limitations of current hypersonic test facilities pose a challenge in studying shock/turbulence interactions (STI) [60]. Hypersonic flows involve high speeds and extreme conditions, making it difficult to replicate them accurately in experimental setups. To overcome this, numerical simulations play a crucial role in STI research. However, high-fidelity simulations of STI can be computationally demanding. These simulations require advanced computational models and algorithms to capture complex flow physics accurately. Researchers employ numerical techniques such as direct numerical simulations (DNS) [61–76] and large eddy simulations (LES) [77–79] to capture the intricate details of the flow field and provide valuable insights into the underlying physics of STI problems.

In this context, theoretical analysis, specifically the linear interaction analysis (LIA) introduced by Ribner [80–82] that relies on Kovásznay's mode decomposition [83], provides valuable insights into the fundamental mechanisms underlying shock wave and turbulence interaction. However, it is important to note that the complexities of STI pose challenges in developing comprehensive theoretical models. The intricate nature of the interaction between shock waves and turbulence, combined with the nonlinearity of the governing equations, makes challenging to capture all aspects of the phenomenon in a single theoretical framework. Hence, further advancements in this area are necessary to develop more accurate models.

1.2 Direct application of thermochemical codes

In line with the motivation described above, thermochemical codes have arisen as an essential tool for a wide range of applications in many fields of science and engineering. In this section, we will explore some of the prominent applications of thermochemical codes in combustion, atmospheric entry problems, exoplanetary atmospheres, and the study of shock and detonation waves.

1.2.1 Combustion

As a consequence of the urgent need to address global warming, it is imperative to explore alternative sources of energy. While the transition to greener energy is vital, it is important to acknowledge that fossil fuels continue to play a significant role in meeting our current energy demands [84]. To mitigate their environmental impact, biodiesel has emerged as a promising transitional opportunity [85].

To fully harness the potential of biodiesel engines, it is crucial to thoroughly evaluate their performance, pollution emissions, and combustion characteristics [86]. Various factors, such as altitude above sea level and the chemical and physical properties of the fuel, significantly influence engine performance and combustion behavior [87]. Therefore, conducting combustion diagnostics becomes essential in determining the optimal operating range for biodiesel engines. In this pursuit, thermochemical codes prove invaluable as they enable comprehensive initial analysis, providing insights into performance metrics, emission levels, and combustion characteristics.

The search for improved performance and reduced emissions extends beyond terrestrial applications and encompasses the realm of rockets. With the exponential rise in the number of rocket launches, driven by reduced costs [88], it becomes imperative to explore innovative approaches to enhance both performance and environmental sustainability in space exploration [89]. Analogous to other combustion systems, rockets require a thorough evaluation of performance and emissions characteristics, considering factors such as propellant composition, combustion efficiency, and engine design [90]. Careful analysis and optimization of these factors are essential to achieve optimal performance while minimizing pollution emissions [91, 92]. In parallel to biodiesel engines, thermochemical codes can assess the preliminary diagnosis of rocket performance metrics, emission levels, and combustion efficiency [93–97].

1.2.2 Atmospheric entry problems

The study of atmospheric entry of vehicles involves complex interactions between the vehicle and the surrounding atmosphere. During entry, the high-speed at which de vehicle goes, leads to the formation of a bow shock ahead of the vehicle that can reach extreme temperatures of the order of ten of thousand of kelvin. Hence, estimating the intense aerothermodynamic loads at which the vehicle will be is vital for the mission's success. In this context, besides 90% of the energy is dissipated into the atmosphere by convection and radiation, the remainder requires additional technologies [98].

To address this need, vehicles and aircraft usually incorporate thermal protection systems (TPS), albeit at the cost of increased weight. Consequently, accurate models are essential to optimize the shield thickness based on mission requirements [99]. Depending on the entry velocity and expected heat load, two types of TPS are distinguished: reusable and ablative. Reusable TPS are designed to endure multiple entry cycles while maintaining their integrity, as exemplified by space shuttles and reusable launch systems. In contrast, ablative TPS are specifically engineered to intentionally erode or ablate during entry, effectively dissipating the heat load [98]. Regarding ablative TPS, Helber et al. [100] used a chemical equilibrium code to investigate the ablation of carbon-based materials under the conditions experienced during Earth's atmospheric entry. Milos & Rasky [99] and Milos & Chen [101, 102] developed a numerical procedure for modeling the surface ablation based on the chemical equilibrium assumption. Their studies have contributed to the design of efficient thermal protection systems.

1.2.3 Exoplanetary atmospheres

In recent years, the study of exoplanets, planets that orbit stars beyond our solar system, has gained significant momentum. With the discovery of the first confirmed exoplanet in the 1990s [103], approximately 5300 exoplanets have been confirmed to date (see http://exoplanet.eu/catalog), a new frontier in astronomy and planetary science was opened.

Researchers have since been intrigued by the possibility of finding Earth-like exoplanets that may harbor life or provide insights into the formation and evolution of planetary systems [104]. In response to this demand, there has been a concerted effort to develop new instruments, such as the recent *James Webb Space Telescope* (launched in 2021) [105] and the enduring *Hubble Space Telescope* (launched in 1990) [106], empowering scientists to collect vast amounts of data about exoplanetary atmospheres.

Determining the chemical composition of exoplanets is a crucial aspect of understanding their physical and atmospheric properties, as well as their potential habitability [107]. However, this pursuit necessitates the utilization of powerful tools capable of modeling complex atmospheric processes and simulating phenomena like vertical mixing [108–110], clouds/hazes [109, 111–113], and photochemistry [114–117], where thermochemical codes have proven to be indispensable in these endeavors.

1.2.4 Shocks and detonations

Thermochemical codes can also be used to model shock and detonation waves. This is exemplified by Caltech's Shock and Detonation toolbox (SD-Toolbox) developed by Shepherd et al. at Caltech in 2008 [40, 118]. Since its initial release, SD-Toolbox has become the go-to software library for academic research in this field. It leverages the capabilities of Cantera [41], a widely-used chemical kinetics software package, to evaluate the thermodynamics and transport properties of gases, obtain chemical reaction rates, and solve chemical equilibrium problems.

Certainly, conducting experiments and high-fidelity simulations in this high-Mach domain can be challenging and computationally expensive. However, as an initial analysis, it is possible to simplify real problems by applying the chemical equilibrium approximation. For instance, by combining the Chapman-Jouguet regime and the Taylor-Zeldovich similarity solution, we can study the flow field behind a steadily-propagating detonation wave in a tube. The solution of oblique detonation for a given degree of overdrive is also of particular interest in RDE. Oblique shock waves also play a crucial role in scramjet engines, where they aid in adapting atmospheric air to conditions optimal for combustion in high-speed propulsion systems. When operating at extremely high speeds within the hypersonic regime, the gas can no longer be accurately treated as non-reacting or calorically perfect. In such cases, thermochemical codes are employed to predict the comprehensive flow-field characteristics. Thermochemical codes prove valuable in addressing more complex problems involving non-homogeneous conditions. These situations arise when the characteristic chemical time is significantly faster than the residence time, which is associated with extremely large Damköhler numbers. In such cases, it is reasonable to assume that post-shock conditions reach chemical equilibrium, allowing for the decoupling of the chemical and hydrodynamic aspects of the problem. Notable examples addressed in this thesis include detonations propagating through non-uniform gaseous mixtures or shocks interacting with turbulent flows.

1.3 Objectives and outline of the thesis

In this research, the primary objective is to develop an open-source thermochemical code capable to effectively address a wide range of problems associated with gas- and condensed-phase species. The second part focuses on the the theoretical investigation of reactive and non-reactive shocks propagating through non-homogeneous conditions. This investigation aims to gain deeper insights into these complex problems and expand our understanding of the underlying mechanisms governing reactive and non-reactive shocks. Additionally, the development of an open-source thermochemical code will be an important contribution for academic research and educational purposes [119], providing an accessible and reliable tool for researchers and practitioners.

The present thesis dissertation is structured into six chapters (including this introduction) composed of previously published and submitted articles. Each chapter begins with a summary and a table of contents.

Chapter 2 details the development and validation of Combustion Toolbox (CT), a new thermochemical code designed to solve a wide range of gas- and condensed species-related equilibrium problems. The tool features a comprehensive suite of algorithms, ranging from fundamental chemical equilibrium problems to complex computations of steady shock and detonation waves for a variety of flow configurations, as well as rocket engine performance predictions. Written in MATLAB, the code is also encapsulated in a user-friendly graphical user interface (GUI), making it flexible and accessible to every user. CT has been utilized in all of the studies presented in this thesis, demonstrating its reliability and versatility. Additionally, this chapter is complemented with Appendices A and B for the thermodynamic data and code examples of CT, respectively. Additional information about its use can be found in https://combustion-toolbox-website.readthedocs.io.

Chapter 3 proposes a linear asymptotic theory for detonation fronts propagating through heterogeneous gaseous mixtures. First, the chapter derives the transfer functions that establish a connection between upstream fuel-mass-fraction inhomogeneities and burnt-gas perturbations through a normal mode analysis, which is described in detail in Appendix C. Subsequently, we apply a Fourier analysis to investigate the interaction between a detonation wave and isotropic, two- and three-dimensional heterogeneous fields. This provides the integral formulae for various properties of the detonation wave, including their second-order corrections, demonstrating that upstream fuel-mass-fraction inhomogeneities tend to accelerate the detonation front in most scenarios studied.

Chapter 4 presents the interaction between a weakly turbulent free stream and a hypersonic shock wave using linear theory. The formulation is developed under the assumption that the thermochemical nonequilibrium region downstream of the shock is much smaller than the characteristic size of turbulence-induced shock wrinkles. By employing modified Rankine-Hugoniot jump conditions that account for vibrational excitation and dissociation, we analyze the modal structure of the post-shock gas and provide integral formulas for the amplification of enstrophy, concentration variance, turbulent kinetic energy, and turbulence intensity. The results highlight the consequences of these thermochemical effects, revealing amplified fluctuations and turbulent Reynolds numbers at hypersonic conditions. These findings are evaluated by comparing them with the results obtained using the Combustion Toolbox (presented in Chapter 2), emphasizing the accuracy, robustness, and limits of the approach. To this end, an extension of the mathematical framework, including electronic excitation and ionization for monatomic and diatomic gases, is described in Appendix D.

Chapter 5 extends the theoretical framework presented in the preceding chapter to account for recombination into multi-species mixture, electronic excitation and ionization effects. This is achieved by integrating the unperturbed jump conditions from the Combustion Toolbox (described in Chapter 2), with the theoretical foundation established in Chapter 4. This integration enables the study of more complex and realistic scenarios. Specifically, an analysis for air has been included, accounting for variations in flight altitude and different upstream conditions. Additionally, we have included a one-to-one comparison with DNS data collected from other works, demonstrating that LIA accurately describes and predicts the TKE amplification factor.

Chapter 6 summarizes the main contributions of the thesis and suggestions for future work.

2 Development of Combustion Toolbox

> *Debugging is like being a detective in a crime movie where you are also the murderer.*
>
> — **Filipe Fortes**

Contents

Summary

This chapter introduces a new open-source thermochemical code—hereafter referred to as Combustion Toolbox (CT)—that solves problems involving chemical equilibrium of gas- and condensed-phase species. The kernel of the code is based on the theoretical framework set forth by NASA's computer program CEA (Chemical Equilibrium with Applications) while incorporating new algorithms that significantly speed up the convergence rate. The thermochemical properties are computed under the ideal gas approximation using an up-to-date version of NASA's 9-coefficient polynomial fits. These fits use the Third Millennium database, which includes the available values from Active Thermochemical Tables. Combustion Toolbox is programmed in MATLAB with a modular architecture composed of three main modules: CT-EQUIL, CT-SD, and CT-ROCKET. The core module, CT-EQUIL, minimizes the Gibbs/Helmholtz free energy of the system using the technique of Lagrange multipliers combined with a multidimensional Newton-Raphson method, upon the condition that two state functions are used to define the mixture properties (e.g., enthalpy and pressure). CT-SD solves processes involving strong changes in dynamic pressure, such as steady shock and detonation waves under normal and oblique incidence angles. Finally, CT-ROCKET estimates rocket engine performance under highly idealized conditions. The new tool is equipped with a versatile Graphical User Interface and has been successfully used for teaching and research activities over the last four years. Results are in excellent agreement with CEA, Cantera within Caltech's Shock and Detonation Toolbox (SD-Toolbox), and the recent Thermochemical Equilibrium Abundances (TEA) code. CT is available under an open-source GPLv3 license via GitHub https://github.com/AlbertoCuadra/combustion_toolbox, and its documentation can be found in https://combustion-toolbox-website.readthedocs.io.

2.1 Introduction

The computation of chemical equilibrium has been widely used during the last century to determine the composition of multi-component mixtures subject to complex thermochemical transformations. The resulting mathematical problem is simple in systems involving only a few species, such as the complete combustion of rich hydrocarbon-air mixtures, or dissociation of diatomic gas mixtures, e.g., air at moderate temperatures. However, the incomplete combustion of a typical hydrocarbon, for instance, methane, with air, involves hundreds of reactions and more than fifty species [120]. This makes finding the final equilibrium state of the products a challenging task.

Two equivalent methods can be employed to determine the composition of the products at equilibrium: using equilibrium constants or minimizing the Gibbs/Helmholtz free energy of the system [24]. The first method requires specifying a sufficiently large set of elementary reactions at equilibrium (see, e.g., Refs. [2, 3, 121–124]). This favors the second, where each species is treated independently, and the focus is shifted to the chemical potentials of the different species involved [1, 125]. The second method was first introduced by the pioneering work of White in 1958 [5] and has become the cornerstone in the development of virtually all state-of-the-art thermochemical codes [6–23].

The solution to the resulting minimization problem requires the evaluation of the thermodynamic properties of all species involved at a given temperature. For this purpose, extensive thermodynamic databases have been compiled, such as the NIST-JANAF tables [126, 127], NASA's polynomials [128] and, more recently, the Third Millennium (Burcat) Database [129] with updates from the Active Thermochemical Tables (ATcT) [130] to evaluate the enthalpies of formation. The ATcT rely on the use of a complete thermochemical network (TN) instead of the more traditional datasets based on individual reactions. The use of the full TN yields more accurate results that are, in addition, fully documented (uncertainties included). But more important is the fact that databases are easily updated with new knowledge, and readily provide new values for the thermochemical properties of all species [131]. A recent work by Scoggins et al. [132] reported an exhaustive review of over 1200 unique chemical species from several databases that fully (Goldsmith [133] and Blanquart [134–137]), partially (Burcat), or did not (NASA) rely on the ATcT. They identified significant differences between Burcat's and NASA's databases due to the inconsistency of the species enthalpy of formation in the latter. Although this type of analysis is out of the scope of this work, all chemical species from Burcat's database are also available in Combustion Toolbox (CT) and can be identified by the suffix "_M". Thus, when both databases contain a given species, the final choice is left to the user.

Thermochemistry is firmly rooted in the study of combustion problems, high-speed flows, reactive and non-reactive shocks, rocket engine performance, and high explosives [138, 139]. For instance, strong hypersonic shocks involve changes in the molecular structure of the gas, including vibrational excitation leading to dissociation (see Chapter 4 and Ref. [140]), and later electronic excitation leading to ionization (see Chapter 5, Appendix D, and Ref. [141]), which eventually transform the gas into a plasma. Turbulent combustion and gaseous detonations have also been the topic of intense research due to their high thermodynamic efficiency in propulsion applications [142, 143]. But they often exhibit strong deviations from equilibrium due to the wide range of length

and time scales involved, making it necessary to rely on complex fluid dynamical analyses and numerical simulations with a high computational cost [144, 145]. Despite the deep understanding provided by the latter approach, there are still cases in which a proper physical explanation can not be found based only on numerical results. In these cases, separation of scales may allow to split the problem into simpler ones, where the assumption of chemical equilibrium could be justified in some representative scenarios, as detailed in Chapters 3 to 5.

Chemical equilibrium can be formulated either for single-phase gas mixtures [5, 12, 14, 15, 18, 19, 122, 124], single-phase gas mixtures with pure-condensed species—as in NASA's CEA code [10], Refs. [3, 7, 123], and this work [23]—or for multi-phase systems [8, 9, 11, 13, 16, 17, 20–22, 121, 146, 147]. The latter case requires special treatments to ensure that the global minima are reached, due to the non-convexity of the Gibbs free energy [13, 16, 148]. These include global optimization methods like the tunneling method [149] or differential evolution [150, 151].

The above review has identified many thermochemical codes currently available to the community. Nevertheless, to the best of our knowledge, there is not yet an open-source code based on up-to-date databases, written in a high-level programming language, fully documented, with high-performance computing capabilities, able to model a wide variety of applications, and equipped with a user-friendly Graphic User Interface (GUI). Combustion Toolbox was conceived with these long-term goals in mind, and is now presented and validated in this work. This MATLAB-GUI thermochemical code represents the core of an ongoing research work the has been used to investigate a series of problems during the last few years (see Chapters 3 to 5 and Ref. [152]). Results are in excellent agreement with NASA's CEA code [10], Cantera [41] within Caltech's Shock and Detonation Toolbox (SD-Toolbox) [40, 118], and the recent Thermochemical Equilibrium Abundances (TEA) code [18].

The chapter is structured as follows. Section 2.2 starts with an initial overview of CT. The equilibrium kernel (CT-EQUIL) is presented in Sec. 2.3. The shock and detonation module (CT-SD) is discussed in Sec. 2.4, followed by the rocket performance module (CT-ROCKET) in Sec. 2.5. The results of all modules are validated against other codes in Sections 2.3 to 2.5. A detailed description of the GUI is given in Sec. 2.6. And, finally, the conclusions are presented in Sec. 2.7.

2.2 Overview of Combustion Toolbox

Combustion Toolbox is a GUI-based thermochemical code written in MATLAB with an equilibrium kernel based on the mathematical formulation set forth by NASA in its CEA code [10]. The thermodynamic properties of the gaseous species are modeled with the ideal gas equation of state (EoS), and an up-to-date version of NASA's 9-coefficient polynomial fits from [128–130]. CT is a new thermochemical code written from scratch in a modular architectural format composed of three main modules: CT-EQUIL, CT-SD, and CT-ROCKET.

The first module, CT-EQUIL, computes the composition at the equilibrium of multi-component gas mixtures that undergo canonical thermochemical transformations from an initial state (reactants), defined by its initial composition, temperature, and pressure, to a final state (products), defined by a set of chemical species (in gaseous—included ions—or pure condensed phase) and two thermodynamic state functions, such as enthalpy and pressure, e.g., for isobaric combustion processes. CT-SD solves steady-state shock and detonation waves in either normal or oblique incidence. Finally, CT-ROCKET computes the theoretical performance of rocket engines under highly idealized conditions. Even though all modules are enclosed in a user-friendly GUI, they can also be accessed from MATLAB's command line (in plain code mode).

There is a fourth closed-source (i.e., proprietary) module, CT-EXPLO, that estimates the theoretical properties of high explosive mixtures and multi-component propellants with non-ideal EoS. Although still under development, CT-EXPLO is distributed in its current form as the thermochemical module of SimEx [152] subject to a proprietary license. Further details on this module will be provided elsewhere.

2.2.1 Software architecture

As previously mentioned, the program was developed from scratch using MATLAB and a modular architectural design. All the modules rely on CT-EQUIL (core module) to compute the thermodynamic properties of the species involved and the chemical composition of the mixtures at equilibrium. The full package can be accessed from the GUI (see Sec. 2.6) or from MATLAB's command line (see Appendix B). Additionally, the main computations performed using the GUI are callbacks to the plain code. Consequently, any change made to the code is immediately reflected in the GUI, leading to a more flexible and adaptable tool. Overall, there are more than 10^4 lines of genuine code (built-in functions), all encapsulated in the GUI.

MATLAB was selected as programming language due to its excellent linear algebra, visualizing and debugging capabilities, extensive documentation, active community, and dedicated app development framework (App Designer). The code has been written using procedural techniques for their better performance compared to MATLAB Object-Oriented-Programming (OOP). Even though MATLAB is an interpreted language, which introduces a significant performance cost compared to other (compiled) languages [153], CT computational times are still competitive compared to similar codes. For instance, as shown in Sec. 2.4, CT is about one order of magnitude faster than the MATLAB version of Caltech's SD-Toolbox used with Cantera (written in C++). However, there is room for further improvement by isolating specific demanding tasks into C++ subroutines and accessing them from MATLAB using MEX files, an optimization technique that will be explored in future code releases.

Most CT routines have as first argument a variable called *self* that contains all the shared data required for the calculations. Thus, this variable has been organized in a hierarchical tree structure as shown in Figure 2.1, namely:

- *self*: parent node; contains all the data of the code, e.g., databases, input values, and results.
- *Constants (C)*: contains constant values.
- *Elements (E)*: contains data of the chemical elements in the problem (names and indices for fast data access).
- *Species (S)*: contains data of the chemical species in the problem (names and indices for fast data access), as well as lists (cells) with the species for complete combustion.
- *Problem Description (PD)*: contains data of the problem to solve, e.g., initial mixture (composition, temperature, pressure), problem type, and its configuration.
- *Problem Solution (PS)*: contains results (mixtures).
- *Tuning Properties (TN)*: contains parameters that control the numerical error of the algorithms implemented in the different modules.
- *Miscellaneous (Misc)*: contains values that configure the auto-generated plots and export setup, as well as flags, e.g., setting `FLAG_RESULTS = true` (by default) the results are shown in the command window (only in the desktop environment).

- *Database master (DB_master)*: a structured thermochemical database including data from [128, 129].
- *Database (DB)*: a structured thermochemical database with *griddedInterpolant* objects (see MATLAB built-in function `griddedInterpolant.m`) that contain piecewise cubic Hermite interpolating polynomials (PCHIP) [154] for faster data access.

The use of *griddedInterpolant* objects in DB speeds up the data access by a factor of 200% with respect to the evaluation of NASA's polynomials. Furthermore, for temperatures outside the bounds, we avoid the higher order terms of the polynomials by linear extrapolation, similar to Ref. [122], extending the range of validity of the thermodynamic data available (e.g., see Fig. D.1). It should be emphasized that this extension is limited to a narrow temperature range and may not apply to temperatures significantly outside of this range.

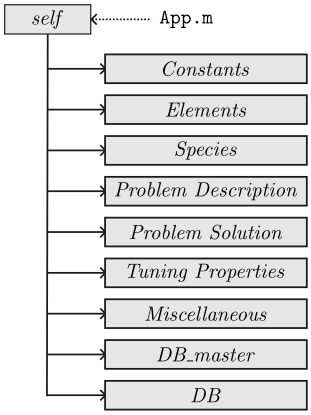

Figure 2.1: Combustion Toolbox hierarchical data tree structure, where `App.m` is the initialization function.

Data for nodes in the *self* parent node must be initialized before use. This can be easily done with one of the following sample statements:

```
self = App()
self = App('Soot formation extended')
self = App({'N2', 'O2', 'NO', 'N', 'O'})
self = App('Complete')
```

The first option, used by default, directs the code to select all possible species that can appear based on the elements present in the reactants (see routine `find_products.m`). The second option directs the code to use an expanded list of

94 species that typically appear in CHON mixtures, solid carbon $C_{(gr)}$ included. The third option demonstrates how to limit the computations to a specific set of species. Finally, by specifying either *complete* or *complete_reaction*, the code carries out calculations under the assumption of complete combustion, which considers only the seven major species involved in $C_xH_yO_zN_w$ systems: CO_2, CO, H_2O, H_2, O_2, N_2, and $C_{(gr)}$. This option is particularly relevant for the solution of combustion problems in academic contexts. Solid carbon $C_{(gr)}$ is known to appear in the products at equilibrium whenever the equivalence ratio ϕ is sufficiently large, $\phi \geq \phi_c$. The code estimates the critical equivalence ratio as $\phi_c \approx 2/(x-z)(x+y/4-z/2)$ and, if the above inequality is satisfied, modifies the species list used for the calculations automatically (see functions `Species.m` and `define_F.m`).

The source code of the Combustion Toolbox is organized into several top-layer folders: *databases*, *examples*, *gui*, *installer*, *modules*, *utils*, and *validations*. The *database* folder mainly consists of raw data and `.mat` files that contain the thermochemical properties of the individual chemical species [128–130]. The *examples* folder includes various examples that demonstrate the wide variety of problems that can be solved with CT. The *gui* folder contains the routines that are specifically designed for the GUI. The *installer* folder contains all the installation files of the GUI: the MATLAB toolbox and the royalty-free stand-alone version. This step is straightforward (see `INSTALL.m`), and for additional information we refer to the CT website (https://combustion-toolbox-website.readthedocs.io/en/latest/install.html). The *modules* folder contains the functions of the different modules, CT-EQUIL, CT-SD, and CT-ROCKET, as well as the routines for initializing CT. The *utils* folder houses utility functions with different purposes. Finally, the *validation* folder includes the routines used to validate CT with the results obtained with other codes, the unit testing files to ensure the correct functionality of the code, and all the graphs generated from these verifications.

Figure 2.2 summarizes the main steps required to solve a problem with CT. First, the system must be initialized using one of the statements indicated above, which defines the list of chemical species involved. Second, one must detail the initial state of the mixture (temperature, pressure, and molar composition) and the type of problem. Depending on the constraints of the selected problem, additional parameters may be required, e.g., for planar shocks, it is necessary to specify the pre-shock velocity in m/s or, equivalently, the pre-shock Mach number. When the setup is finished, CT calls the routine `solve_problem.m` to compute the results of the posed problem. Lastly, CT shows predefined plots using the function `post_results.m`, and it can save the results into a spreadsheet or as a `.mat` file (see routine `Miscellaneous.m`).

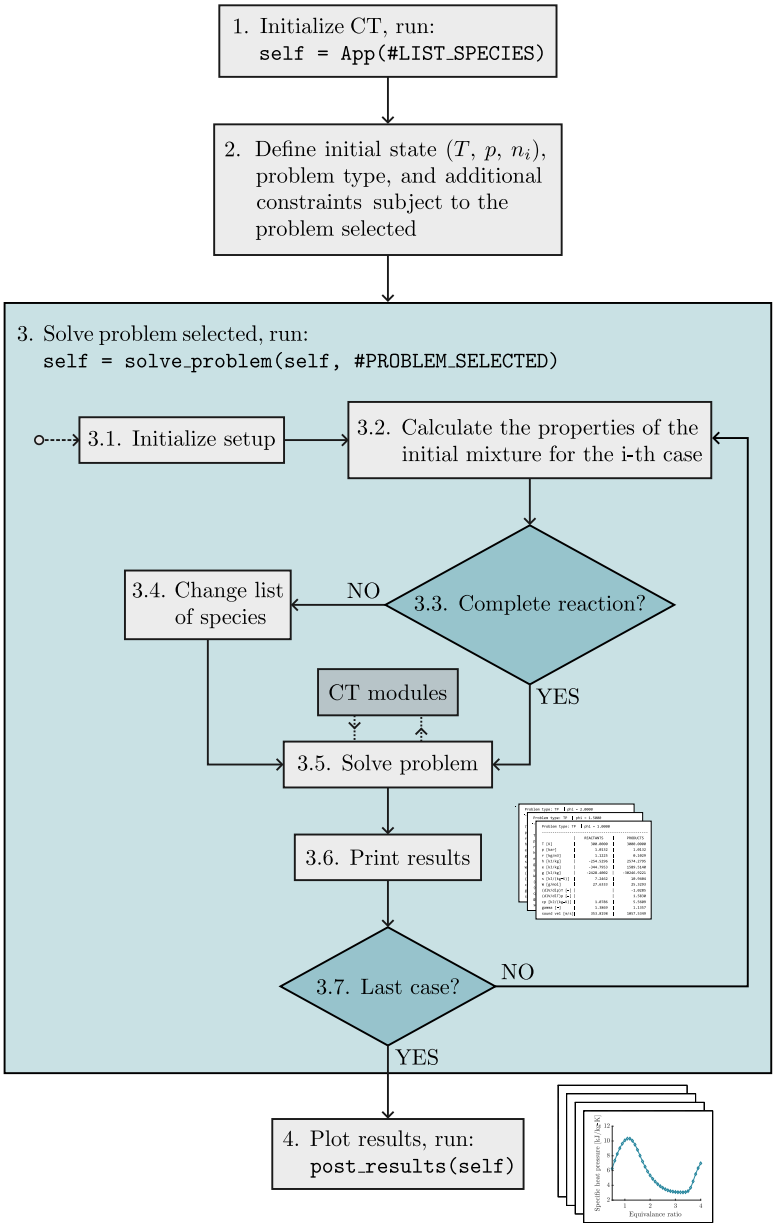

Figure 2.2: Combustion Toolbox simplified workflow.

2.2.2 Collaborative framework and version control system

The collaborative process of open-source code can greatly benefit from the contributions of other authors. However, in the absence of adequate tools, this process may become disorderly. To mitigate this risk, we employ Git as version control system (VCS) and GitHub as online hosting service. These technologies enable comprehensive tracking of all changes made to the code while maintaining complete transparency throughout the development process [155–158]. To further ensure the integrity of the package, all contributions are subject to rigorous testing prior to being merged into the two primary branches (`master` and `develop`) by using GitHub Actions, giving a powerful tool to retrace errors in the code.

2.2.3 Documentation

A notable fraction of open-source codes lack sufficient documentation, which impedes the code's usability and accessibility. To amend this issue, we use Sphinx [159], a documentation generator written and used by the Python community, along with its MATLAB-domain extension [160]. All function headers are written following Google's Python-style docstrings. The online documentation is hosted on Read the Docs and is regularly updated from the GitHub repository. The new routines are automatically included in the online documentation using GitHub Actions. The framework allows having specific documentation for each distributed version. Additionally, the package includes several examples and all the validations carried out with other codes.

2.2.4 Benchmarks

The calculations presented in this work were performed on a laptop computer with the following specifications: Intel(R) Core(TM) i7-11800H CPU @ 2.30GHz with 8 physical cores and 64GB of RAM, running on a 64-bit Windows 11 Pro system and using MATLAB R2022b. The computation time represents the elapsed time from CT's initialization until the end of the calculations. For reference, only loading the databases (~ 3600 species with their *griddedInterpolant* objects) takes an average of 0.9685 seconds and is included in the times presented in this study.

2.3 Thermochemical equilibrium module

This section presents the kernel module of the code, CT-EQUIL, namely the thermochemical equilibrium module. This module is composed of four main routines:

- `equilibrium_gibbs.m`
- `equilibrium_helmholtz.m`
- `equilibrate_T.m`
- `equilibrate.m`

The first two are described in Secs. 2.3.1 and 2.3.2 and are used to compute the chemical equilibrium composition for given temperature-pressure (TP), or temperature-volume (TV) states, respectively. The third is employed to compute the thermodynamic properties of the mixture and is an upper layer of the previous routines, as shown in Algorithm 1. The latter, described in Sec. 2.3.3, represents the top layer of CT-EQUIL and is implemented to compute the chemical equilibrium composition and thermodynamic properties for any of the following pairs of specified state functions: TP, HP, SP, TV, EV, and SV, where T stands for temperature, P for pressure, H for enthalpy, S for entropy, E for internal energy, and V for volume.

Combustion Toolbox enables the computation of chemical equilibrium under various assumptions regarding the final gas mixture, including calorically perfect gas, calorically imperfect gas with frozen chemistry, or calorically imperfect gas with equilibrium chemistry, including dissociation and ionization. An example of these calculations is presented in Sec. 2.4. It is also possible to freeze the composition of a subset of the species considered as possible products at equilibrium by defining them as inert species.

2.3.1 Equilibrium composition at specified temperature and pressure

The `equilibrium_gibbs.m` routine computes the molar equilibrium composition $\mathbf{n} = \{n_1, n_2, \ldots, n_{\mathrm{NS}}\}$ of a mixture $\mathbf{S} = \{S_1, S_2, \ldots, S_{\mathrm{NS}}\}$ of NS species at a given temperature T and pressure p for a closed system by minimizing the Gibbs free energy of the system $G(T, p, \mathbf{n})$. This is an equality-constrained problem (ECP) subject to mass

conservation, namely

$$\min\, G(T,p,\mathbf{n}) \;\Leftrightarrow\; \mathrm{d}G(T,p,\mathbf{n}) = \sum_{j\in\mathbf{S}} \mu_j(T,p,\mathbf{n})\,\mathrm{d}n_j = 0, \tag{2.1a}$$

$$q_i = \sum_{j\in\mathbf{S}} a_{ij} n_j - b_i^\circ = 0, \quad \forall i \in \mathbf{E} \tag{2.1b}$$

where n_j and μ_j are the number of moles and chemical potential of species j, respectively, a_{ij} are the stoichiometric coefficients, i.e., the number of atoms of element i per molecule of species j, and b_i° is the number of atoms of the i-th element in the initial mixture. There are as many linear constraints q_i as NE elements $\mathbf{E} = \{E_1, E_2, \ldots, E_{\mathrm{NE}}\}$ involved. The NS species can be either gaseous or condensed, assuming pure components. Thus, there are NG gaseous species $\mathbf{S^G} = \{S_1, S_2, \ldots, S_{\mathrm{NG}}\}$ and $\mathrm{NS} - \mathrm{NG}$ condensed species $\mathbf{S^C} = \{S_{\mathrm{NG}+1}, S_{\mathrm{NG}+2}, \ldots, S_{\mathrm{NS}}\}$, where $\mathbf{S^G}$ and $\mathbf{S^C}$ are the respective subsets of $\mathbf{S}$. In addition, the problem must satisfy $\mathrm{NE} \leq \mathrm{NS}$. Equation (2.1a) must be supplemented with an EoS to define the thermodynamic functions. Our code implements the ideal gas EoS for the chemical potential

$$\mu_j\,(T,p,\mathbf{n}) \quad = \quad \mu_j^\circ\,(T) \;+\; \kappa_j RT \left(\ln \frac{n_j}{\sum\limits_{j\in\mathbf{S^G}} n_j} + \ln \frac{p}{p^\circ} \right), \quad \forall j \quad \in \quad \mathbf{S} \tag{2.2}$$

where $\mu_j^\circ(T)$ is the chemical potential of species j at the reference pressure ($p^\circ = 1$ bar) and the specified temperature, κ_j is either one or zero depending on whether the species is in gaseous or condensed phase, and R is the universal gas constant. As stated above, the CT-EQUIL module computes all thermochemical properties within the ideal gas approximation using an up-to-date version of NASA's 9-coefficient polynomial fits [128] that incorporates the Third Millennium database [129], including the available values from Active Thermochemical Tables. For more details on the calculation of the thermochemical properties from the values contained in these databases the reader is referred to Appendix A.

The ECP formulated in (2.1) and (2.2) is solved using the method of Lagrange multipliers (an extended description thereof can be found in Ref. [161]), which introduces the Lagrangian function

$$\mathcal{L}(T,p,\mathbf{n},\boldsymbol{\lambda}) = G(T,p,\mathbf{n}) + \boldsymbol{\lambda}\,\mathbf{q}(\mathbf{n}), \tag{2.3}$$

where $\boldsymbol{\lambda}$ represents the multiplier vector, of length NE. If there is an infinitesimal change,

$\mathrm{d}\mathbf{n}$ and $\mathrm{d}\boldsymbol{\lambda}$, the differential of $\mathcal{L}$ can be obtained from Eq. (2.3) with use made of (2.1) to yield $\mathrm{d}\mathcal{L} = 0$, namely

$$\sum_{j\in\mathbf{S}}\left[\mu_j(T,p,\mathbf{n}) + \sum_{i\in\mathbf{E}} a_{ij}\lambda_i\right]\mathrm{d}n_j + \sum_{i\in\mathbf{E}}\left[\sum_{j\in\mathbf{S}} a_{ij}n_j - b_i^\circ\right]\mathrm{d}\lambda_i = 0. \tag{2.4}$$

Additionally, the sum of the molar compositions must equal the total number of moles of gaseous species in the system, thus

$$\sum_{j\in\mathbf{S^G}} n_j = n. \tag{2.5}$$

Considering that $\mathrm{d}n_j$, $\mathrm{d}\lambda_i$, and n are independent, (2.4) and (2.5) constitute a system of NS non-linear equations subject to a set of NE + 1 linear constraints. Furthermore, to ensure that the molar composition n_j is strictly positive, it is convenient to work with the functions $\ln n_j$ and $\ln n$ in the gaseous species. There is no need to apply these definitions to the condensed-phase species because the algorithm solves the ECP problem for the gas phase first, and then considers the condensed species without specifying an initial estimate of their composition.

Using these definitions, Eqs. (2.4) and (2.5) can be rearranged in the form $\mathbf{f}(\mathbf{x}) = 0$, where $\mathbf{x}$ is the vector of unknowns composed of $\ln n_j$ (for $j \in \mathbf{S^G}$), n_j (for $j \in \mathbf{S^C}$), $\ln n$, and $\pi_i = -\lambda_i/RT$ (for $i \in \mathbf{E}$). To solve this system of equations, Combustion Toolbox uses a multidimensional Newton-Raphson (NR) method

$$\mathbf{J}\cdot\delta\mathbf{x} = -\mathbf{f}(\mathbf{x}), \tag{2.6}$$

where $\mathbf{J}$ is the Jacobian matrix with components $J_{ij} \equiv \partial f_i/\partial x_j$, $\delta\mathbf{x}$ is the correction vector composed of $\Delta\ln n_j$ (for $j \in \mathbf{S^G}$), Δn_j (for $j \in \mathbf{S^C}$), $\Delta\ln n$ and $\Delta\pi_i$, and $\mathbf{f}$ is the vector function. Equation (2.6) can be expanded as the following system of NS + NE + 1 linear equations

$$\Delta\ln n_j - \Delta\ln n - \sum_{i\in\mathbf{E}} a_{ij}\Delta\pi_i = -\frac{\mu_j}{RT}, \quad \forall j \in \mathbf{S^G} \tag{2.7a}$$

$$\sum_{i\in\mathbf{E}} a_{ij}\Delta\pi_i = \frac{\mu_j}{RT}, \quad \forall j \in \mathbf{S^C} \tag{2.7b}$$

$$\sum_{j\in\mathbf{S^G}} a_{ij}n_j\Delta\ln n_j + \sum_{j\in\mathbf{S^C}} a_{ij}\Delta n_j = b_i^\circ - a_{ij}n_j, \quad \forall i \in \mathbf{E} \tag{2.7c}$$

$$\sum_{j\in\mathbf{S^G}} n_j\Delta\ln n_j - n\Delta\ln n = n - \sum_{j\in\mathbf{S^G}} n_j, \tag{2.7d}$$

where the dimensionless Lagrange multiplier π_i has been taken equal to zero in the right hand side of Eqs. (2.7a) and (2.7b). This is a suitable simplification as long as λ_i appears linearly in the first square bracket of (2.4), as discussed in Ref. [6]. Algebraic manipulation of (2.7) allows to reduce the system's dimensions due to the spareness of the upper left corner of the Jacobian matrix $\mathbf{J}$. Thus, substituting $\Delta \ln n_j$ from (2.7a) in (2.7c) and (2.7d), NG equations are drop out from (2.7), providing a reduced system of $\mathrm{NE} + \mathrm{NS} - \mathrm{NG} + 1$ equations, namely

$$\sum_{i\in\mathbf{E}}\sum_{j\in\mathbf{S}} a_{lj}a_{ij}n_j\Delta\pi_i + \left(\sum_{j\in\mathbf{S^G}} a_{lj}n_j\right)\Delta\ln n + \sum_{j\in\mathbf{S^C}} a_{lj}\Delta n_j = b_l^\circ - \sum_{j\in\mathbf{S}} a_{lj}n_j + \sum_{j\in\mathbf{S^G}} \frac{a_{lj}n_j\mu_j}{RT}, \quad \forall l \in \mathbf{E} \tag{2.8a}$$

$$\sum_{i\in\mathbf{E}} a_{ij}\Delta\pi_i = \frac{\mu_j}{RT}, \quad \forall j \in \mathbf{S^C} \tag{2.8b}$$

$$\sum_{i\in\mathbf{E}}\sum_{j\in\mathbf{S}} a_{ij}n_j\Delta\pi_i + \left(\sum_{j\in\mathbf{S^G}} n_j - n\right)\Delta\ln n = n - \sum_{j\in\mathbf{S^G}} n_j + \sum_{j\in\mathbf{S^G}} \frac{n_j\mu_j}{RT}, \tag{2.8c}$$

which is solved using MATLAB's linear programming routines built on LAPACK [162]. The updated solution vector $\mathbf{x}$ at the $(k+1)$-th iteration is given by $\mathbf{x}_{k+1} = \mathbf{x}_k + \tau_k\,\delta\mathbf{x}_k$, where τ_k is the step size, or relaxation, parameter for the k-th iteration, defined in Ref. [10]. As previously indicated, the solution vector $\mathbf{x}_k$ has $\pi_i = 0$ (for $i \in \mathbf{E}$); consequently, it is not necessary to relax the new value obtained, i.e., $\pi_{i,k+1} = \Delta\pi_{i,k}$. Note that in Eq. (2.8), $\mathbf{x}$ is composed of n_j (for $j \in \mathbf{S^C}$), $\ln n$, and $\pi_i = 0$ (for $i \in \mathbf{E}$). Consequently, to update the terms of the gaseous species $\ln n_j$, the correction $\Delta \ln n_j$ must be obtained from (2.7a) after each solution of (2.8), which requires defining a set of initial estimates $\mathbf{x}_0$ for the molar number n_j of all the possible products. We proceed by setting the number of condensed species to zero, and assuming that initially the gaseous species appear with a uniform molar distribution $n_j = 0.1/\mathrm{NG}$, obtained by considering 1 g of mixture with an average molecular mass of 10 g/mol [10]. However, when performing parametric sweeps, CT starts with the moles of the gaseous species n_j obtained from the previous calculation, provided that their magnitudes exceed a predefined threshold value of 10^{-6}. This approach facilitates the convergence of the iterative procedure and accelerates the overall computational efficiency.

Camberos and Moubry [163] evaluated other initial guesses for the molar composition using, e.g., a probability density function (PDF) based on the thermal enthalpy. Nevertheless, they concluded that the uniform distribution was, in fact, the best estimate

of the tested distributions due to its combined simplicity and effectiveness. Mathematically, the uniform distribution PDF represents the maximum uncertainty in the molar composition.

Once convergence is achieved (by default, the tolerance for the molar composition is set to 10^{-14} and for the NR is 10^{-5}), if there are condensed species in the set of products, a second iteration process is conducted. The procedure is similar, but now we include in the set of unknowns the condensed species that satisfy the vapor pressure test, namely

$$\frac{1}{RT}\frac{\partial \mathcal{L}}{\partial n_j} = \frac{\mu_j^\circ}{RT} - \sum_{i\in\mathbf{E}} \Delta\pi_i a_{ij} < 0, \quad \forall j \in \mathbf{S^C} \tag{2.9}$$

whose addition to the system will reduce the Gibbs free energy of the system even further, corresponding with the first term of (2.4) in dimensionless form. Note that if Eq. (2.9) yields negative values, the Lagrange function may not be at equilibrium ($\mathrm{d}\mathcal{L} = 0$), which means that the added species can appear at the final state of equilibrium. When several condensed species satisfy this condition, CT only includes the species with the minimum value of $(\partial\mathcal{L}/\partial n_j)/W_j$, as suggested Mcbride [25], where W_j represents the molecular mass of the species. If in the new equilibrium state that considers condensed species the molar composition n_j of the added species is negative, or the Jacobian $\mathbf{J}$ is a singular matrix, these species are omitted from the set $\mathbf{S^C}$. The process is repeated until all the condensed species in $\mathbf{S^C}$ that satisfy $T \in [T_{\min}, T_{\max}]$, i.e., whose temperature range is compatible with the system's temperature, have been tested.

In the presence of ionized gases, the algorithm neglects the Coulombic interactions associated with ideal plasmas. In this case, there is only an additional restriction that is given by the electroneutrality of the mixture [164]

$$\sum_{j\in\mathbf{S^G}} a_{ej} n_j = 0, \tag{2.10}$$

where the stoichiometric coefficient a_{ej} represents the number of electrons in ion j relative to the neutral species. Thus, for $\{\mathrm{e}^-, \mathrm{N}_2^+\}$ we have $a_{ej} = \{1, -1\}$. This means that the electron E_e, with index e, is treated as an element. This assumption is valid only when the ion density is sufficiently small, i.e., for weakly ionized gases. The code directly detects if there are ions in the set of possible products $\mathbf{S}$ and calls another subroutine that ensures that condition (2.10) is met.

Algorithm 1 Pseudocode to compute the final equilibrium composition of an initial mixture mix_1, for given temperature-pressure (TP), or given temperature-volume (TV). For problems at constant volume, p is not used.

function `equilibrate_T`($self$, mix_1, p, T)
  Step 1. Check settings ▷ `ProblemDescription.m`
    if FLAG_TCHEM_FROZEN **then** ▷ calorically perfect gas
      $mix_2 \leftarrow$ `equilibrate_T_tchem`($self$, mix_1, p, T)
      `return`
    end if
    if FLAG_FROZEN **then** ▷ calorically imperfect frozen gas
      $mix_2 \leftarrow$ `equilibrate_T_frozen`($self$, mix_1, p, T)
      `return`
    end if
  Step 2. Set list of species LS for calculations
    $LS \leftarrow$ `set_LS_original`($self$)
  Step 3. Solve ECP at constant TP or TV
    if TP **then** ▷ calorically imperfect gas with dissociation/ionization
      $n_j \leftarrow$ `equilibrium_gibbs`($self, p, T, mix_1$)
    else
      $n_j \leftarrow$ `equilibrium_helmholtz`($self, v, T, mix_1$)
    end if
  Step 4. Add inert species to n_j
    $n_j \leftarrow n_{j,\text{inert}}$
  Step 5. Compute property matrix $\boldsymbol{M_0}$
    $\boldsymbol{M_0} \leftarrow$ `set_species`($self, LS, n_j, T$)
  Step 6. Compute properties of the mixture
    $mix_2 \leftarrow$ `compute_properties`($self, \boldsymbol{M_0}, p, T$)
end function

2.3.2 Equilibrium composition at specified temperature and volume

For calculating the molar equilibrium composition of the mixture at a given temperature T and volume v, we have to minimize the Helmholtz free energy of the system, defined as $F = G - pv$. Upon use of this relation into the minimization condition $\mathrm{d}F\,(T, v, \mathbf{n}) = 0$, we get

$$\sum_{j \in \mathbf{S}} \mu_j(T, v, \mathbf{n})\; n_j - pv = 0 \tag{2.11}$$

to be used in substitution of Eq. (2.1a). For convenience, the chemical potential of species j is now expressed as a function of the mixture's volume v. For an ideal gas

EoS we have

$$\mu_j\left(T,v,\mathbf{n}\right) \;=\; \mu_j^{\circ}\left(T\right) \;+\; \kappa_j RT\left(\ln\frac{n_j}{\sum\limits_{j\in\mathbf{S^G}} n_j}+\ln\frac{n_j RT}{p^{\circ}v}\right), \quad \forall j \;\in\; \mathbf{S} \tag{2.12}$$

which ultimately gives a different reduced system of equations

$$\begin{aligned}\sum_{i\in\mathbf{E}}\sum_{j\in\mathbf{S}} a_{lj}a_{ij}n_j\Delta\pi_i+\sum_{j\in\mathbf{S^C}} a_{lj}\Delta n_j&\\ = b_l^{\circ}-\sum_{j\in\mathbf{S}} a_{lj}n_j+\sum_{j\in\mathbf{S^G}}\frac{a_{lj}n_j\mu_j}{RT}, &\quad \forall l\in\mathbf{E}\end{aligned} \tag{2.13a}$$

$$\sum_{i\in\mathbf{E}} a_{ij}\Delta\pi_i=\frac{\mu_j}{RT}, \quad \forall j\in\mathbf{S^C}. \tag{2.13b}$$

to be solved instead of Eq. (2.8).

Unlike in the TP calculations, the linear system no longer includes the total number of moles, n, and its correction factor, $\Delta\ln n$, as they are drop out of the system of $\mathrm{NE}+\mathrm{NS}-\mathrm{NG}$ dimensions written above. Here, μ_j is given by Eq. (2.12) and the correction values $\Delta\ln n_j$ do not depend of $\Delta\ln n$, yielding

$$\Delta\ln n_j=\sum_{i\in\mathbf{E}} a_{ij}\Delta\pi_i-\frac{\mu_j}{RT}, \quad \forall j\in\mathbf{S^G}. \tag{2.14}$$

As indicated in Algorithm 1, the computation of the chemical composition and thermodynamic properties of a given mixture at specified temperature and volume is performed by the routine `equilibrium_helmholtz.m`.

2.3.3 Equilibrium composition for other pairs of state functions

In many practical applications, the equilibrium temperature of a system is not initially determined, thereby necessitating the provision of supplementary information to close the problem. This additional information may be obtained from an enthalpy, internal energy, or entropy conservation equation, subject to the requirement that the corresponding state function f remains unchanged, namely

$$\Delta f\left(T\right)\equiv f_{\mathrm{F}}\left(T\right)-f_{\mathrm{I}}\left(T_{\mathrm{I}}\right)=0, \tag{2.15}$$

Algorithm 2 Pseudocode to compute the final equilibrium composition of an initial mixture mix_1 at pressure p, for a given pair of state functions XY (included in $self$ variable). For problems at constant volume, p is not used. In TP/TV problems, steps 1-3 are omitted.

function `equilibrate`($self$, mix_1, p)
  Step 1. Get attribute ▷ e.g., enthalpy 'h' in case of HP
    $att \leftarrow$ `get_attr_name`($self$) ▷ depends on X
  Step 2. Get initial estimates of T
    $T \leftarrow$ `regula_guess`($self, mix_1, p, att$)
  Step 3. Solve Eq. (2.15)
    switch `@root_method` **do** ▷ `TuningProperties.m`
      case `newton` ▷ second-order method
        $T \leftarrow$ `newton`($self, mix_1, p, att, T$)
      case `nsteff` ▷ third-order method
        $T \leftarrow$ `nsteff`($self, mix_1, p, att, T$)
  Step 4. Solve ECP at constant TP or TV
    $mix_2 \leftarrow$ `equilibrate_T`($self, mix_1, p, T$)
end function

where the subscripts F and I refer here to the final and initial states of the mixture, respectively. Unlike in NASA's CEA code, we have increased the flexibility of the CT-EQUIL module by decoupling this additional equation and retrieved the new condition by using a second-order NR method

$$T_{k+1} = T_k - \frac{f\left(T_k\right)}{f'\left(T_k\right)}. \tag{2.16}$$

The derivatives of the state functions $f'\left(T\right)$ involved in the different transformations can be expressed analytically in the form: $\left(\partial h/\partial T\right)_p = c_p$, $\left(\partial e/\partial T\right)_v = c_v$, $\left(\partial s/\partial T\right)_p = c_p/T$, and $\left(\partial s/\partial T\right)_v = c_v/T$, for HP, EV, SP, and SV transformations, respectively. Following common practice, h, e, s, c_p, and c_v denote the enthalpy, internal energy, entropy, and the specific heats at constant pressure and constant volume, respectively. It is worth noting that that although they are written in lower case letters, these variables refer here to extensive magnitudes.

The initial estimate T_0 is computed using a *regula falsi* method. Nevertheless, when carrying out parametric studies, the program uses the temperature obtained in the previous calculation as an initial estimate to accelerate convergence toward the new solution. However, if T_k is significantly distant from the actual solution, this approach can lead to unsatisfactory convergence. To overcome this issue, we can select

a more robust root-finding method, as Eq. (2.15) has been purposely decoupled. In particular, the code has implemented an implicit third-order Newton-Steffensen root-finding algorithm [165], defined as follows:

$$T_{k+1} = T_k - \frac{f^2\left(T_k\right)}{f'\left(T_k\right)\left[f\left(T_k\right) - f\left(T_{k+1}^*\right)\right]}, \tag{2.17}$$

where the temperature at the $(k+1)$-th iteration, T_{k+1}, is re-estimated by using the provisional value T_{k+1}^* provided by the application of the classical method defined in Eq. (2.16). The convergence criterion $\max\{|(T_{k+1} - T_k)/T_{k+1}|, |\Delta f/f_F|\} < \epsilon_0$ is set by default to 10^{-3} in both methods and is generally reached in two to five iterations. Algorithm 2 describes the pseudocode to calculate the equilibrium composition for any given pair of state functions.

2.3.4 Validations

To illustrate the wide variety of applications of Combustion Toolbox and asses the capabilities of the CT-EQUIL module, several validation tests have been conducted. In this work, we provide three of them in which only a reduced set of species are presented for clarity. Further validation tests can be easily accessed through the CT website or by just utilizing the user-interface validation add-on, *uivalidation*, which is implemented in the GUI (see Fig. 2.18 below). Alternatively, the user can also run the scripts included in the *validations* folder.

First test: In planetary science, thermochemical equilibrium codes like TEA [18], Fastchem [122, 124], and $\mathrm{GG_{CHEM}}$ [123], are used to model the atmospheric composition of giant planets, brown dwarfs, and other celestial bodies. Further examples can be found in Refs. [166–169]. Such models can help to unveil the physicochemical processes (chemical and radiative) that drive the evolution of these atmospheres, such as the formation of clouds and the escape of atmospheric gases into space [104]. This motivates the first validation case: the composition of the hot-Jupiter exoplanet WASP-43b's atmosphere. To this end, it is necessary to provide temperature and pressure profiles, as well as the planet's metallicity, which refers to the abundance of elements heavier than hydrogen and helium present in its composition. For example, Fig. 2.3 shows the variation of the species molar fractions $X_j = n_j / \sum_{j \in \mathbf{S}} n_j$ with pressure (right panel) corresponding to the temperature-pressure profile given in [170] (left panel), and assuming an atmospheric $50\times$ solar metallicity. This value is needed to determine the mixture's initial number of moles n_j, upon knowledge of the elemental solar abun-

dances that are here estimated from [171], which considers H the reference element. A specific routine, `read_abundances.m`, reads the solar mass abundances that are then converted into molar abundances using the function `abundances2moles.m`, which considers a metallicity equal to unity by default. It is important to note that different exoplanets may necessitate the utilization of distinct solar abundances. Nevertheless, the program is compatible with additional datasets that follow the same format as the original dataset: `abundances.txt` (located in the *database* folder). The results (solid lines) show an excellent agreement with those obtained with the recently developed Thermochemical Equilibrium Abundances (TEA) code [18] (symbols) even down to the μbar level. The minor differences in HCN, C_2H_2 (acetylene), and HS_M (the subscript M denotes that is obtained from Burcat's database) come from the discrepancies of the free energies compared to the NIST-JANAF database [126, 127] that is implemented in TEA. In this test, the computation time with a tolerance of 10^{-32} for the molar composition was (TEA: 6.42 seconds) for a set of 26 species considered and a total of 90 case studies, which represents a $5.8\times$ speed-up factor for our code ($22\times$ speed-up factor loading a specific database for this case).

Second test: As previously indicated, thermochemical codes are a crucial tool for understanding and predicting the intricate chemistry that takes place during combustion processes. As a result, it is essential to validate CT with a canonical combustion test. With this purpose, the second validation test involves the investigation of the adiabatic isobaric combustion of acetylene and air, a potential mixture for advanced internal combustion engines owing to the high energy density and low carbon content of acetylene. Specifically, the investigation focuses on the isobaric reactive mixture at an initial pressure of $p_1 = 1$ atm and temperature of $T_1 = 300$ K, and considers a wide range of equivalence ratios $\phi \in [0.5, 4]$. Figure 2.4 shows the variation of the molar composition of the products with ϕ (top panel) along with other mixture properties (a-h). It should be noted that, unlike the previous test, in this case the results obtained with CT (represented by solid lines) are compared to those of NASA's CEA [10] (represented by symbols). Once again, the results are in excellent agreement with the benchmark code, which includes the generation of solid carbon $C_{(gr)}$ when the equivalence ratio reaches or exceeds $\phi \approx 2.6$. This value is near the theoretical value $\phi_c = 2.5$ predicted by the complete combustion approximation. The computation time elapsed 4.57 seconds for a set of 94 species and 351 case studies. For this test, the tolerance was set to 10^{-18} for the molar composition and 10^{-3} for the root finding method.

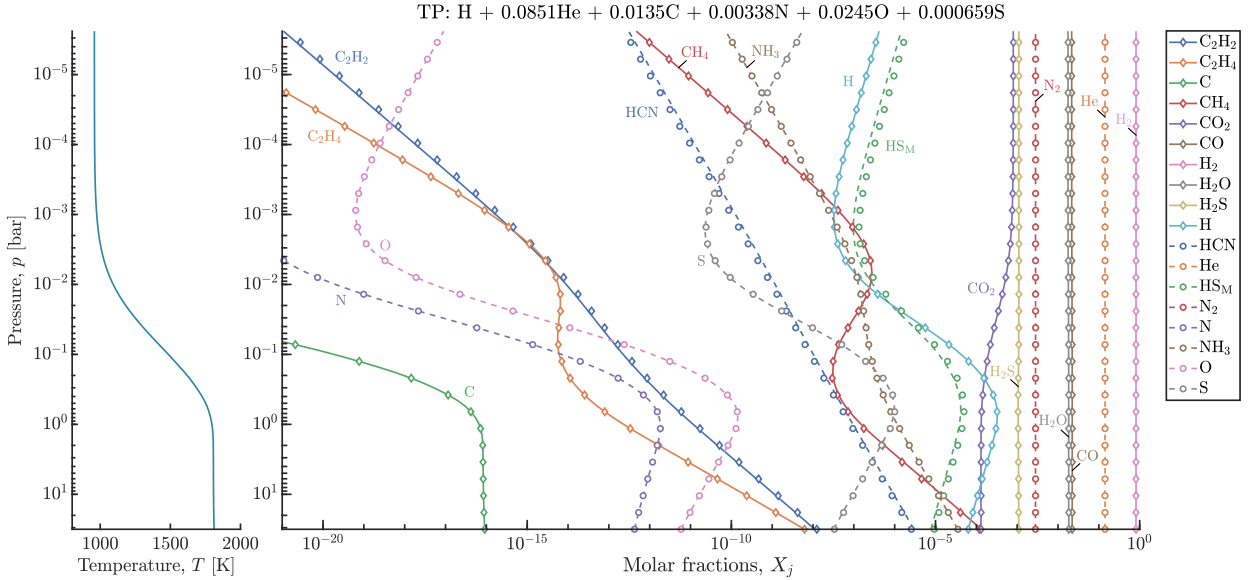

Figure 2.3: Variation of molar fraction with pressure (right panel) for the temperature-pressure profile of exoplanet WASP-43b (left panel) with an atmospheric $50\times$ solar metallicity; solid line: numerical results obtained with CT; symbols: numerical results obtained with TEA [18]. The species denoted with subscript M is obtained from Burcat's database [129].

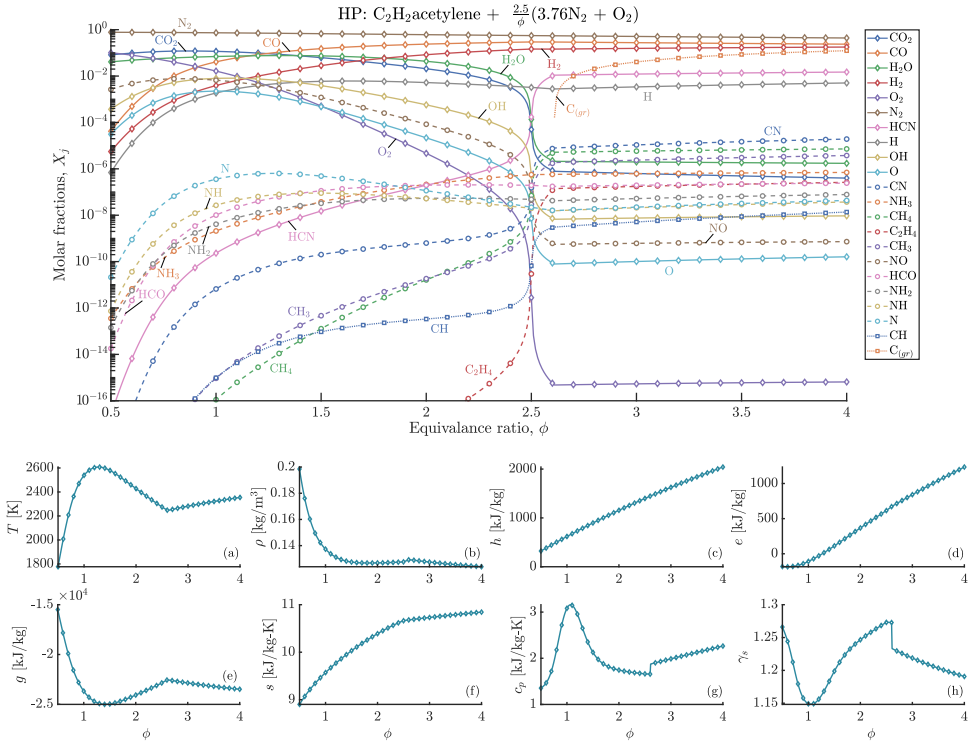

Figure 2.4: Variation of the molar fractions, X_j (top), and of different thermodynamic mixture properties: (a) temperature, T, (b) density, ρ, (c) enthalpy, h, (d) internal energy, e, (e) Gibbs energy, g, (f) entropy, s, (g) specific heat capacity at constant pressure, c_p, and (h) adiabatic index, γ_s, for an HP transformation in lean-to-rich acetylene (C_2H_2)-air mixtures at standard conditions ($T_1 = 300$ K, $p_1 = 1$ bar); solid line: numerical results obtained with CT; symbols: numerical results obtained with NASA's CEA [10]. The code snippet is shown in Appendix B Listing B.1.

Third test: Recent advancements in chemical equilibrium solvers have opened up new avenues for studying the complex phenomena that take place on the surface of ablator materials during atmospheric reentry. For instance, Helber et al. [100] used a chemical equilibrium code to investigate the ablation of carbon-based materials under the conditions experienced during Earth's atmospheric reentry. Other studies focused on carbon-fiber-reinforced-polymers (CFRP) [172] or silicon-based ablative materials [173]. Regardless of the composition of the ablator, predicting the equilibrium species during ablation is a challenging task, as it involves the evaluation of numerous condensed species at very high enthalpies. To assess the capabilities of CT under more demanding scenarios than those of the previous tests, we recall in this third test the example

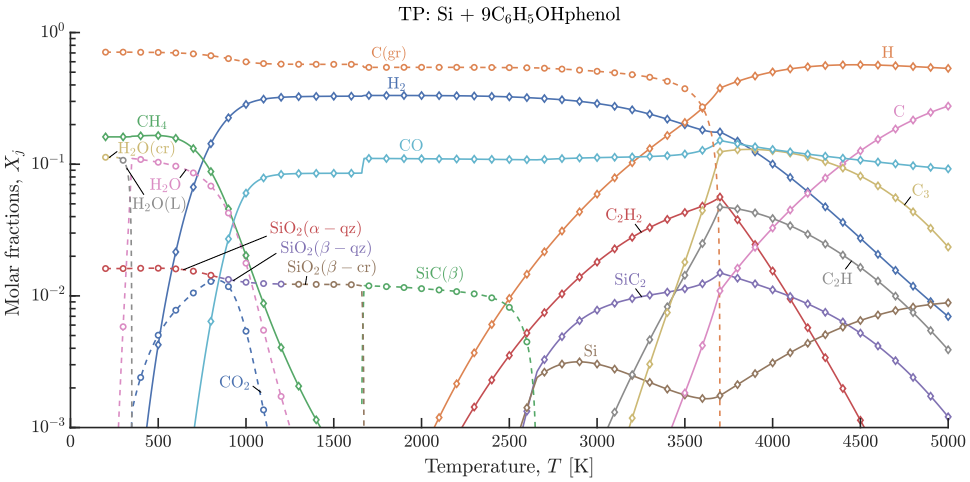

Figure 2.5: Variation of the molar fractions X_j for a Silica-Phenolic mixture at atmospheric pressure ($p = 1$ atm) with $T \in [200, 5000]$; solid line: numerical results obtained with CT; symbols: numerical results obtained with NASA's CEA [10].

presented in Ref. [17]. The problem consists of a parametric study of a Si-C_6H_5OH mixture at atmospheric pressure ($p = 1$ atm) for a wide range of temperatures $T \in [200, 5000]$. The variation with temperature of the molar fractions X_j for the Silica-Phenolic mixture is shown in Figure 2.5, which also shows the same results computed with NASA's CEA [10] code. It is readily seen that there is a total agreement of the results even for the multiple condensed species. Previous work [17] reported that NASA's CEA code was not able to converge for $T < 400$. However, this is only true when computing the parametric study, not the individual cases, whereas CT converges in both situations. In this test, the computation time was 5.08 seconds for a set of 178 species (21 in condensed phase) and 481 case studies. The molar composition's tolerance was 10^{-18}.

2.4 Shock and detonation module

This section presents the routines of the shock and detonation module, CT-SD. This module determines the post-shock equilibrium state of steady non-reactive and reactive shocks with arbitrary incidence angles, β [see inset on the right panel of Figure 2.6(b)]. The routines are based on the algorithm outlined in NASA's Reference Publication 1311 [10, Chapters 7-9] for the solution of normal shocks and detonation waves, $\beta = \pi/2$, along with the CT-EQUIL module described in the previous section.

2.4.1 Oblique shocks

Let us first consider the problem of an undisturbed, planar, normal shock wave. The pre-shock density, pressure, enthalpy, and velocity (in the reference frame attached to the shock) are denoted, respectively, as ρ_1, p_1, h_1, and u_1. The corresponding flow variables in the post-shock gases are denoted as ρ_2, p_2, h_2, and u_2. The well-known Rankine-Hugoniot (RH) relations for the variation of pressure and enthalpy are, respectively

$$\frac{p_2}{p_1} = 1 - \frac{\rho_1 u_1^2}{p_1}\left(\frac{\rho_1}{\rho_2} - 1\right), \tag{2.18a}$$

$$h_2 = h_1 + \frac{u_1^2}{2}\left[1 - \left(\frac{\rho_1}{\rho_2}\right)^2\right]. \tag{2.18b}$$

These equations must be supplemented by the equation of state, in our case, the ideal EoS $p = \rho RT/W$, where $W = \sum_{j\in\mathbf{S^G}}(n_j/\sum_{j\in\mathbf{S^G}} n_j)W_j$ stands for the average molecular mass of the gaseous mixture computed in terms of the gas-phase molar fractions, $n_j/\sum_{j\in\mathbf{S^G}} n_j$, and the molecular masses of the gaseous species, W_j. Also required is the caloric EoS, $h = \sum_{j\in\mathbf{S}} n_j H_j^\circ(T)$, that gives enthalpy in terms of the temperature and gas mixture composition. As discussed above, the molecular masses, W_j, and the molar specific enthalpies, $H_j^\circ(T)$, are evaluated from a combination of NASA's [128] and Burcat's (Third Millennium) [129] thermochemical databases.

The solver employs a NR method (see Ref. [10, Chapters 7-9] for more information) to determine the roots of the system of equations governing both reactive and non-reactive shocks (see routines `det_cj.m` and `shock_incident.m`, respectively). Consequently, the jump relationships, such as p_2/p_1 and ρ_2/ρ_1, can be calculated with ease. In this subsection, we focus on the oblique shock configuration that implicitly includes the solution of the normal shock wave. When the angle formed by the shock plane and the upstream flow is not $\pi/2$, the pre- and post-shock velocities, u_1 and u_2, must be replaced by their respective components normal to the shock, u_{1n} and u_{2n}, in the RH equations (2.18). These equations can be readily reformulated in terms of the magnitudes of the pre- and post-shock velocities upon direct substitution of the trigonometric relationships $u_{1n} = u_1 \sin\beta$ and $u_{2n} = u_2 \sin(\beta - \theta)$, where β is the shock incidence angle and θ is the flow deflection angle, both measured with respect to the upstream flow direction. For oblique shocks, the continuity of the tangential velocity across the shock, $u_{1t} = u_{2t}$, or, equivalently, $u_1 \cos\beta = u_2 \cos(\beta - \theta)$, is also required.

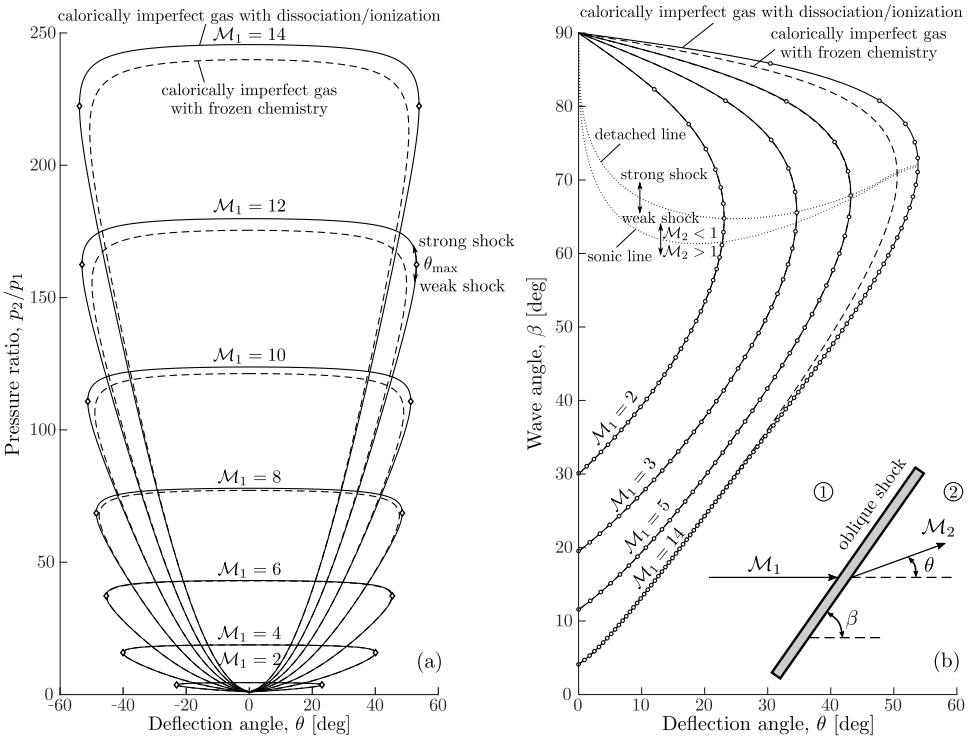

Figure 2.6: Pressure-deflection (a) and wave angle-deflection (b) shock polar diagrams for air (78% N_2, 21% O_2, and 1% Ar) at pre-shock temperature $T_1 = 300$ K and pressure $p_1 = 1$ atm, and a range of pre-shock Mach numbers $\mathcal{M}_1$ between 2 and 14; solid line: calorically imperfect gas with ionization/dissociation; dashed: calorically imperfect gas with frozen chemistry; circles: results obtained with Cantera [41] within Caltech's SD-Toolbox [40]; diamonds: maximum deflection angle θ_{max}. The code snippet is shown in Listing B.2.

In the case of a normal shock wave, the gas properties downstream of the shock are determined by two factors: the upstream thermodynamic state and a parameter that characterizes the intensity of the shock, usually either the shock speed u_1 relative to the upstream gas or the shock Mach number, $\mathcal{M}_1 = u_1/a_1$ (where a_1 represents the speed of sound upstream the shock), as given in Eq. (A.7). Other problems, such as those concerning blast waves, impose the post-shock pressure p_2 as the initial input parameter describing the shock intensity. Oblique shocks, on the other hand, require an additional geometrical restriction given by the value of the incidence angle β or the flow deflection angle θ. When the value of β is specified, there exists a unique solution for the post-shock fluid state (see routine `shock_oblique_beta.m`). However, in the case where θ is given, there are two possible solutions for β: a weak shock solution linked

to a smaller value of β, representing the weakest possible shock, and a strong solution corresponding to a larger β (see routine `shock_oblique_theta.m`). The two solutions converge for $\theta = \theta_{\max}$, which corresponds to the maximum deflection angle of the shock for a given $\mathcal{M}_1$ (see Fig. 2.6), above which the problem does not admit solution. Remarkably close to the maximum deflection angle, in the weak-shock branch, we find the sonic condition $\mathcal{M}_2 = 1$, below and above which the post-shock flow is supersonic (weak shocks) and subsonic (strong shocks, and weak shocks between the sonic line and the maximum deflection angle), respectively. Then, the supersonic branch always corresponds to the weak shock solution.

In either scenario, when the value of θ is specified, β becomes an implicit variable that must be determined numerically. To this end, CT employs an iterative procedure based on the continuity of the tangential velocity across the shock, which can be manipulated using the above trigonometric identities to give

$$f(\beta) \equiv \theta + \tan^{-1}\left(\frac{u_{2n}}{u_1 \cos\beta}\right) - \beta = 0. \tag{2.19}$$

This equation must be solved for the shock incidence angle β (see Algorithm 5) with use made of the RH relations (2.18), the ideal gas EoS, and provided that $f'(\beta)$ and $f''(\beta)$ can be written as explicit functions. This enables the use of Halley's third-order iterative method [174]

$$\beta_{k+1} = \beta_k - \frac{2f(\beta_k) f'(\beta_k)}{2f'(\beta_k) - f(\beta_k) f''(\beta_k)} \tag{2.20}$$

to find the root of Eq. (2.19). This approach exhibits rapid convergence and meets the default convergence criterion of 10^{-3} within two or three iterations. However, it is worth noting that like other root-finding methods, Halley's method only provides one of the possible roots of the nonlinear system, which generally corresponds to the root closest to the initial guess used during the iterative process. Therefore, we must supply sufficiently accurate guesses to cover the whole set of solutions that include both the weak- and strong-shock branches. One straightforward approach to acquiring such guesses is to anticipate the solution domain bounded by the acoustic weak-shock limit $\beta_{\min} = \sin^{-1}(1/\mathcal{M}_1)$ and the normal shock configuration $\beta_{\max} = \pi/2$. In particular, we choose $\beta_0 = 0.5(\beta_{\min} + \beta_{\max})$ for the weak-shock branch and $\beta_0 = 0.97\beta_{\max}$ for the strong-shock branch.

The left and right plots in Fig. 2.6 depict the pressure ratio-deflection angle and the incidence angle-deflection angle shock polar diagrams for dry air (consisting of 78% N_2,

21% O_2, and 1% Ar) initially at room conditions ($T_1 = 300$ K, $p_1 = 1$ atm). These results were obtained using the `shock_polar.m` routine. It is worth noting that CT provides users with a variety of gas models to choose from: *i)* calorically perfect gas with frozen chemistry (constant specific heat at constant pressure c_p, adiabatic index γ, and n_j), *ii)* calorically imperfect gas with frozen chemistry (constant n_j), and *iii)* calorically imperfect gas with variable composition, including dissociation, ionization, and recombination reactions at equilibrium. These effects are incorporated by specifying a sufficiently large set of species for the calculations, and using NASA's [128] and Burcat's (Third Millennium) [129] databases for evaluating the thermodynamic properties.

Figure 2.6 displays the results obtained with models *ii)* and *iii)* spanning a set of pre-shock Mach numbers $\mathcal{M}_1$ ranging from 2 to 14. The results are compared with Caltech's Shock and Detonation Toolbox [118], which uses Cantera [41] as kernel for the computations of chemical equilibrium. It is found that the lobes in the pressure ratio-deflection angle diagram expand due to dissociation/ionization effects, particularly in the hypersonic flow regime, $\mathcal{M}_1 > 5$. As a result, weak oblique shocks exhibit smaller pressure ratios while strong ones exhibit larger pressure ratios for the same deflection angle. Moreover, the endothermic (cooling) effect caused by dissociation/ionization in hypersonic oblique shocks leads to an increase in the post-shock density that also increases the wave deflection angle at all incidence angles. The results obtained from both codes are in complete agreement for all conditions tested. However, CT-SD exhibits superior performance compared to Caltech's SD-Toolbox with Cantera, reducing computation time by more than 95% (CT-SD: 4.12 s vs. Caltech's SD-Toolbox & Cantera: 99.72 s; for a large subset that contains 1200 points of all the cases represented in Fig. 2.6(b), with both codes running on the same platform and with the same subset of 14 chemical species), which demonstrates the excellent performance of the CT-SD module.

2.4.2 Regular reflections

Understanding the reflection of shock waves off flat surfaces is a problem of great relevance to high-speed flows. The angle subtended by the incident shock and the flat surface determines the type of shock reflection, with $\beta = 0$ representing normal reflections and $0 < \beta < \pi/2$ oblique reflections. In a reference frame with origin at the point of contact of the shock with the wall, the latter exhibit an incoming free stream parallel to the wall with $\mathcal{M}_1 > 1$. For sufficiently small incidence angles, the incident shock deflects the free stream uniformly towards the wall an angle θ. The reflected shock then deflects back the perturbed stream to its original flow direction parallel to

the wall. This type of reflection is said to be regular, and is depicted in Fig. 2.8. Regular reflections leave uniform flow patterns behind both the incident and reflected shocks that can be described with Combustion Toolbox.

By contrast, for incidence angles above a certain critical value, $\beta > \beta_{\max}(\mathcal{M}_1)$, the reflected wave, with $\mathcal{M}_2 < \mathcal{M}_1$ and thus a lower maximum deflection angle, is not able to deflect the flow back to its upstream direction parallel to the wall. This leads to the so-called irregular, or Mach, reflections, where the reflected and incident shocks merge into a single wave called the Mach stem, which connects the wall to the triple point where the three shocks meet. These reflections produce non-uniform flows that include a high-speed shear layer or slipstream emanating from the triple point [175]. The properties of these flows cannot be determined solely by the polar-plot charts or the zero-dimensional RH equations and thus, are out of the scope of this work.

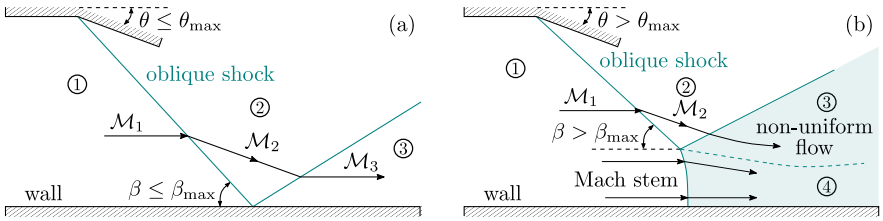

Figure 2.7: Sketch regular reflection (a) and Mach reflections (b).

To calculate regular reflections, Combustion Toolbox uses the routine `shock_oblique_reflected_theta.m` to compute the incident wave by specifying the wave angle β (or the flow deflection θ) and the pre-shock velocity u_1. This results in the calculation of the post-shock state (2), which serves as pre-shock state for the reflected wave, as illustrated in Fig. 2.7(a). If the incident shock is sufficiently strong, the transition to state (2) can result in significant thermochemical effects that may cause changes in the aerothermal properties compared to those of a calorically perfect fixed-composition gas. In this case, the values of $\mathcal{M}_2$ and θ may change accordingly. The reflected shock increases the gas pressure and temperature even further, and the properties in state (3) can be determined using the code routine employed for single oblique shocks imposing the counter deflection angle θ calculated for the incident shock. This guarantees that the streamlines in state (3) are parallel to the reflecting surface. If there is no solution for the reflected shock (which occurs for sufficiently large values of θ), irregular Mach reflections occur [see Fig. 2.7 (b)]. As discussed above, these reflections involve non-uniform flow properties and non-steady solutions, and thus their computation is beyond the capabilities of CT.

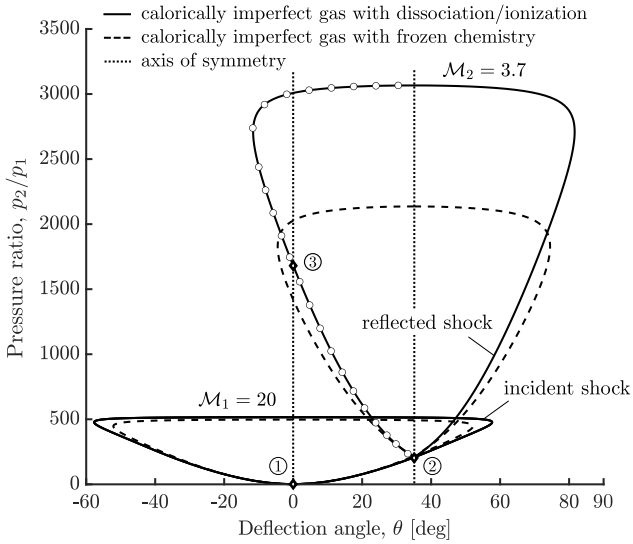

Figure 2.8: Pressure-deflection shock polar diagrams for a regular shock reflection in atmospheric air (78% N_2, 21% O_2, and 1% Ar) at 30 km above sea level (pre-shock temperature $T_1 = 226.51$ K and pressure $p_1 = 1.181 \cdot 10^{-2}$ atm; see Fig. 2.9(b) for reference), pre-shock Mach number $\mathcal{M}_1 = 20$, and deflection angle $\theta = 35°$; solid line: calorically imperfect gas with dissociation/ionization; dashed line: calorically imperfect gas with frozen chemistry; dotted line: axes of symmetry; circles: results of Zhang et al. [176]; diamonds: states 1, 2, and 3.

As an illustrative example, Fig. 2.8 represents the pressure-deflection shock polar diagrams for a regular shock reflection in atmospheric air at 30 km above sea level (see Fig. 2.9(b) for reference) with an incident Mach number of $\mathcal{M}_1 = 20$ and a deflection angle of $\theta = 35°$ under the same gas models *ii)* and *iii)* used in the oblique shock charts presented above. The polar plot starting from state (2), obtained by increasing the incident wave angle from 0 to $\pi/2$, determines the solution of state (3) for the deflection angle $\theta = 35°$. This, in turn, determines the reflected shock at the intersection of the second polar with the vertical axis ($\theta = 0$). As can be seen, the dissociation and ionization effects are more pronounced in the reflected shock, as the accumulated temperature jump in both shocks amplifies the endothermicity of the chemical reactions, resulting in substantially higher overall pressure ratios. Finally, the outcomes are compared with those acquired by Zhang et al. [176] under the same flow conditions, revealing excellent agreement in all instances. In our calculations, the computation time was 2.58 s (1.07 s) for a group of 28 species (3 species) and 200 case studies. These values depend on the tolerance, which was set to 10^{-14} for the molar composition and 10^{-5} for the root-finding method.

Algorithm 3 Pseudocode to obtain pre-shock and post-shock states at the limit of regular reflections for a given mixture mix_1 and pre-shock velocity u_1.

function `shock_polar_limitRR`($self$, mix_1, u_1)
  Step 1. Get polar diagrams at state (1).
    $mix_{2,\text{polar}} \leftarrow$ `shock_polar`$(self, mix_1, u_1)$
  Step 2. Set initial estimates
    $\theta \leftarrow \theta_{\max}/2$
    $f'(\theta) \leftarrow 2$ ▷ derivative of $f(\theta) \equiv \theta_{3,\max} - \theta$
    STOP, $k \leftarrow 1, 0$
  Step 3. Get θ_2 using Broyden's method
    while STOP $> \epsilon_{\text{limitRR}}$ & $k < k_{\max,\text{limitRR}}$ **do**
      $k \leftarrow k + 1$
      Step 3.1 Solve oblique shock (weak branch) for θ
        $mix_2 \leftarrow$ `shock_oblique_theta`$(self, mix_1, u_1, \theta)$
      Step 3.2 Get polar diagrams at state (2)
        $mix_{3,\text{polar}} \leftarrow$ `shock_polar`$(self, mix_2, u_2)$
      Step.3.3 Compute $f(\theta)$ and $f'(\theta)$
      Step.3.4 Update estimate θ
        $\theta \leftarrow \theta - f(\theta)/f'(\theta)$
      Step.3.5 Calculate STOP criteria
        STOP $\leftarrow \max\left(\left|\frac{\theta_{k+1} - \theta_k}{\theta_k}\right|, \left|\frac{f(\theta_{k+1})}{\theta_{k+1}}\right|\right)$
    end while
end function

If the incident angle becomes larger, the polar diagram of the reflected shock moves farther away from the $\theta = 0$ axis, making it harder for the second shock to redirect the flow to its initial upstream direction parallel to the reflecting wall. For each $\mathcal{M}_1$, there exists a maximum value of β (and, consequently, of θ) beyond which regular reflection is impossible. This maximum value is determined by the condition at which the polar diagram of the reflected shock is tangent to the $\theta = 0$ axis. Our code is able to compute $\beta_{\max}$ and $\theta_{\max}$ in cases involving high-temperature thermochemical effects. To determine this limit, we impose the condition $\theta_{3,\max} - \theta = 0$, and employ an iterative algorithm based on Broyden's method [177], which makes use of the set of routines described above (see Algorithm 3 for further details).

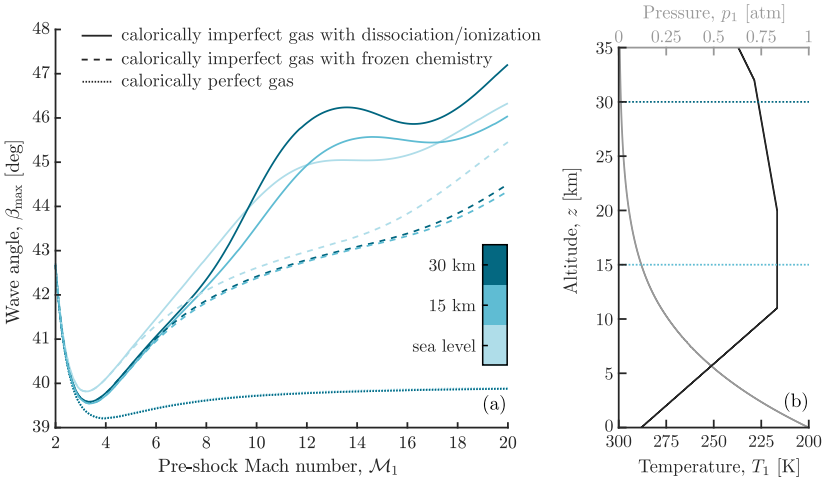

Figure 2.9: Maximum wave angle $\beta_{\max}$ in the limit of regular reflection as a function of pre-shock Mach number $\mathcal{M}_1$ for an air mixture (78% N_2, 21% O_2, and 1% Ar) in the atmosphere at different flight altitudes (0, 15, and 30 km) above sea level in the ISA model (see panel b); solid line: calorically imperfect gas with dissociation/ionization; dashed: calorically imperfect gas with frozen chemistry; dotted: calorically perfect gas.

Figure 2.9 represents the maximum incidence angle $\beta_{3,\max}$ for regular shock reflections as a function of the pre-shock Mach number $\mathcal{M}_1$ for three atmospheric conditions corresponding to increasing flight altitudes in the ISA model [178] [see panel (b)]. Results are presented for the three gas models defined above *i)*, *ii)*, and *iii)*. As expected, the upstream pressure and temperature do not have any effect on the calorically perfect gas solution, which can be written analytically for $\gamma = 1.4$. Nevertheless, the results including high-temperature thermochemical effects show large deviations from the calorically perfect gas solution. Thus, the endothermic effects associated with the dissociation of O_2 and N_2 are seen to increase the value of $\beta_{\max}$ and widen the domain

of regular reflections. These effects occur primarily across the reflected shock, which by increasing its flow deflection angle also increases its ability to deflect the disturbed current back to its initial direction parallel to the surface. In conditions where endothermic effects occur mainly across the incident shock (for very high pre-shock temperatures or very high Mach numbers), the situation is reversed, and the maximum incidence angle for regular shock reflection exhibits a slight decrease.

2.4.3 Planar gaseous detonations

The thermochemical framework employed to describe shock waves involving endothermic molecular transformations can be easily extended to account for exothermic reactions, as occurs in planar detonations. As with shock waves, the computation of detonations requires knowledge of the pre-shock state and the degree of overdrive that measures the contribution of the external supporting mechanism. However, unlike shock waves, detonations can be self-sustained, i.e., propagate without any external contribution exerting additional pressure from behind. This propagation mode, named after Chapman-Jouguet (CJ), involves the maximum possible expansion of the hot products. Therefore, the burnt-gas state is obtained by imposing the sonic condition in the post-wave flow $\mathcal{M}_2 = 1$. If the pressure behind the detonation wave is larger than what is anticipated by the CJ condition, which can only be achieved using an external forcing mechanism, the detonation is considered *over-driven* and results in subsonic downstream conditions, with $\mathcal{M}_2 < 1$. Conversely, *under-driven* detonations occur when the burnt gas is in a supersonic state with $\mathcal{M}_2 > 1$, but this is not compatible with the internal structure of the detonation wave.

The over-driven/under-driven solutions can be determined numerically for a defined upstream mixture and a given degree of overdrive $\eta = u_1/u_{\mathrm{cj}}$ (see functions `det_overdriven.m` and `det_underdriven.m`) by using the routines designed for CJ detonations (see `det_cj.m`) and normal shocks (see `shock_incident.m`). The former is necessary to determine the minimum velocity $u_1 = u_{\mathrm{cj}}$ (or $\eta = 1$) required for a planar detonation to propagate, while the latter is employed to obtain the post-detonation state for a given degree of overdrive η.

Careful selection of the initial guesses is required to obtain the solutions for over-driven and under-driven detonations. For instance, $T_{2,\mathrm{guess}}$ and $p_{2,\mathrm{guess}}$ denote the estimated temperature and pressure after the detonation, and should be anticipated considering the significant variations arising from the degree of overdrive and the type of propagation mode. To obtain the initial guesses for over-driven detonations, $p_{2,\mathrm{guess}}$ is computed using Eq. (2.18a), assuming a constant $\gamma = \gamma_1 = \gamma_{2,\mathrm{guess}}$. This gives

$p_{2,\text{guess}} = p_1(2\gamma\mathcal{M}1^2 - \gamma + 1)/(\gamma + 1)$. The temperature guess is based on the fact that, for sufficiently strong shocks, the kinetic energy downstream is much lower than upstream of the shock, $u_2^2/u_1^2 \sim (\rho_1/\rho_2)^2 \ll 1$. This simplifies Eq. (2.18b) to $h_{2,\text{guess}} = h_1 + u_1^2/2$, thus enabling the computation of $T_{2,\text{guess}}$ by solving the thermo-chemical equilibrium problem at specified enthalpy and pressure, $h_{2,\text{guess}}$ and $p_{2,\text{guess}}$. This approximation becomes more accurate with increasing degrees of overdrive, as the differences between u_1 and u_2 become more significant. This estimation method is the same as the one utilized in the incident normal shocks routine.

For under-driven detonations, a reasonable initial guess can be obtained by considering the range of acceptable values for the mean post-shock density. By defining the dimensionless parameter $\zeta \in (0, 1)$ to measure how close $\rho_{2,\text{guess}}$ is to the CJ state compared to the initial state, we can construct an initial guess for the density as follows: $\rho_{2,\text{guess}} = [\zeta/\rho_{2,\text{cj}} + (1-\zeta)/\rho_1]^{-1}$. The pressure and temperature values can then be determined using Eq. (2.18a) and the ideal gas EoS, respectively. It has been found that a value of $\zeta = 0.1$ is suitable for the set of Mach numbers tested. The pseudocode for under-driven/over-driven detonations is shown in Algorithm 4.

Algorithm 4 Pseudocode to solve under-driven detonations for a given mixture mix_1 and degree of overdrive η. For over-driven detonations step 3 is omitted.

function `det_underdriven`($self$, mix_1, η)
  Step 1. Solve CJ pre-shock and post-shock states
    $mix_{1,\text{cj}}, mix_{2,\text{cj}} \leftarrow$ `det_cj`$(self, mix_1)$
  Step 2. Compute pre-shock velocity
    $u_1 \leftarrow u_{\text{cj}}\eta$
  Step 3. Calculate initial estimates of post-shock state
    $\rho_2 \leftarrow [\zeta/\rho_{2,\text{cj}} + (1-\zeta)/\rho_1]^{-1}$ ▷ $\zeta = 0.1$
    $p_2 \leftarrow$ Eq. (2.18a)
    $W_2 \leftarrow W_{2,\text{cj}}$ ▷ same as CJ post-shock state
    $T_2 \leftarrow p_2 W_2/(\rho_2 R)$ ▷ ideal EoS
  Step 4. Compute pre-shock and post-shock states for u_1
    $mix_1, mix_2 \leftarrow$ `shock_incident`$(self, mix_1, u_1, mix_2)$
end function

Table 2.1 lists the CJ velocities of planar gaseous detonations computed by CT for various near-stoichiometric fuel-air/O_2 mixtures. The results are compared with the experimental data reported in the literature, showing good agreement in all cases. The validation with other codes is performed in the following subsection in the context of oblique detonations. However, for detonation velocities related to condensed-phase explosives, we refer to SimEx [152]. SimEx includes an extensive database of pure CHNO

Mixture	ϕ	CT [m/s]	Exp. [m/s]	Source
CH_4-air	0.989	1797.21	1798.17	[179]
H_2-air	1	1965.45	1825.64	[180]
H_2-O_2	1	2838.12	2898.39	[181]
DME-O_2	1	2318.12	2299.71	[182]

Table 2.1: Chapman-Jouguet detonation propagation velocities for different near-stoichiometric fuel-air/O_2 mixtures at $p_1 = 1$ atm and $T_1 \sim 293.15$ K computed by Combustion Toolbox and measured experimentally by various authors.

propellants and explosives, and its kernel from CT was adapted to solve the products' composition with the ideal gas EoS following the norm UNE 31-002-94 [183]. SimEx also employs more complex computations based on the European Standard EN 13631-15 [184], which use the semi-empirical Becker–Kistiakowsky–Wilson (BKW) [31, 185] or the Heuzé (H9) EoS [186].

2.4.4 Oblique gaseous detonations

Detonation waves can take on oblique configurations, which are less common compared to oblique shocks. However, such detonations are crucial in Oblique Detonation Wave Engines (ODWE) [187, 188], where the combustion process occurs along an oblique detonation that revolves around a cylindrical combustion chamber.

To compute oblique detonations, knowledge of the pre-shock state and the degree of overdrive caused by the supporting mechanism, typically a wedge deflecting a reactive supersonic stream and generating the oblique detonation, is required, just like in the oblique shocks. Thus, given the temperature, pressure, composition, and pre-shock velocity, one can calculate the detonation polar diagrams with the particularity that now the exothermicity of the reaction increases the number of possible solutions, as occurs for planar detonations [189, 190]. Then, for a given detonation angle β (or deflection angle θ), two solutions for the burnt-gas state can be found, associated with under-driven ($\mathcal{M}_{2n} > 1$) and over-driven ($\mathcal{M}_{2n} < 1$) conditions (see routines `det_oblique_beta.m` and `det_oblique_theta.m`).

At the Chapman-Jouguet regime the two solutions merge into a single solution. This state is characterized by a sonic normal component of the downstream velocity vector ($\mathcal{M}_{2n} = 1$). The corresponding values for the upstream Mach number and shock angle are $\mathcal{M}_1 = \mathcal{M}_{1,\mathrm{cj}}$ and $\beta = \beta_{\mathrm{cj}}$. Both in the under-driven and over-driven cases, the RH-equations only produce real solutions if the values for the upstream Mach number and

Algorithm 5 Pseudocode to solve weak and strong branches of over-driven oblique detonations for a given mixture mix_1, degree of overdrive η, and deflection angle θ. For non-reactive shocks step 1 and 2 are omitted, u_{1n} is calculated rather than η_n, and `det_overdriven` is changed to `shock_incident`$(self,\ mix_1,\ u_{1n},\ mix_2)$. Calculations for a given wave angle β only require steps 1-3, 4.1, 4.2, and 5.

function `det_oblique_theta`$(self,\ mix_1,\ \eta,\ \theta)$

Step 1. Obtain CJ pre-shock state

$mix_{1,\text{cj}} \leftarrow$ `det_cj`$(self, mix_1)$

Step 2. Get pre-shock velocity and sound velocity

$u_1, a_1 \leftarrow u_{1,\text{cj}}\eta,\ a_{1,\text{cj}}$

Step 3. Obtain wave angle limits and their initial guesses

$\beta_{\min}, \beta_{\max} \leftarrow \sin^{-1}(a_1/u_1),\ \pi/2$

$\beta_{\text{weak}}, \beta_{\text{strong}} \leftarrow (\beta_{\min} + \beta_{\max})/2,\ 0.97\beta_{\max}$

Step 4. Solve weak/strong branch using Halley's method

while STOP $> \epsilon_{\text{oblique}}$ & $k < k_{\max,\text{oblique}}$ **do**

$k \leftarrow k + 1$

Step 4.1 Get normal component degree-overdrive η_n

$\eta_n \leftarrow \eta \sin(\beta)$

Step 4.2 Obtain post-shock state and there fore u_{2n}

$mix_2 \leftarrow$ `det_overdriven`$(self, mix_1, \eta_n)$

Step.4.3 Compute $f(\beta)$, $f'(\beta)$, and $f''(\beta)$

Step.4.4 Update estimate β

$$\beta \leftarrow \beta - \frac{2f(\beta)f'(\beta)}{2f'(\beta)^2 - f(\beta)f''(\beta)}$$ ▷ Eq. (2.20)

Step.4.5 Calculate STOP criteria

$$\text{STOP} \leftarrow \max\left(\left|\frac{\beta_{k+1} - \beta_k}{\beta_k}\right|, \left|\frac{f(\beta_{k+1})}{\beta_{k+1}}\right|\right)$$

end while

Step 5. Calculate post-shock velocity u_2

$u_2 \leftarrow u_{2,n} \sin^{-1}(\beta - \theta)$

end function

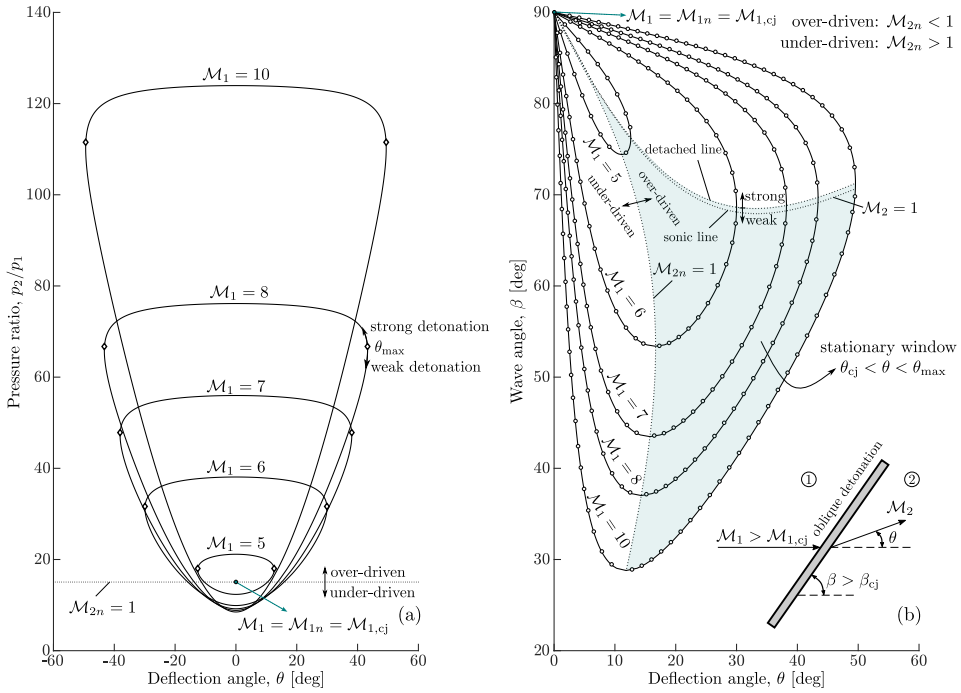

Figure 2.10: Pressure-deflection (a) and wave angle-deflection (b) detonation polar diagrams for a stoichiometric hydrogen (H_2) air (79% N_2, 21% O_2) mixture at pre-shock temperature $T_1 = 300$ K and pressure $p_1 = 1$ atm, and a range of pre-shock Mach numbers $\mathcal{M}_1$ between 5 and 10; solid line: results with CT considering a calorically imperfect gas with dissociation; circles: results from Zhang et al. [176].

shock angle are greater than the corresponding values for the CJ condition, $\mathcal{M}_1 \geq \mathcal{M}_{1,\text{cj}}$ and $\beta \geq \beta_{\text{cj}}$. For oblique detonations with angles in the range $\beta_{\text{cj}} < \beta < \pi/2$, a given shock angle corresponds to two different deflection angles, namely θ_{over} and θ_{under}.

In the over-driven branch, the solution resembles that of an oblique shock (see Algorithm 5). The point where $\mathcal{M}_2 = 1$ is reached below the maximum deflection angle separating the strong and weak solutions. Since the solution is multi-valued, the computation of the different branches requires an accurate initial estimate regardless of the input parameter, be it the shock or the flow deflection angle (see Sec. 2.4.3). Figure 2.10 shows the pressure-deflection (a) and wave angle-deflection (b) polar diagrams for detonations in stoichiometric hydrogen (H_2)-air (79% N_2, 21% O_2) mixtures at pre-shock temperature $T_1 = 300$ K and pressure $p_1 = 1$ atm, for a range of pre-shock Mach numbers $\mathcal{M}_1$ between 5 and 10.

CT provides embedded functionalities for obtaining polar diagrams that characterize incident oblique detonations (see function `det_polar.m`). These functionalities perform a direct computation of a set of cases (100 by default) by sweeping the range of possible solutions for both the under-driven and over-driven branches, as depicted in Fig. 2.10. These results have been compared with the values from Zhang et al. [176], which are found to be in remarkable agreement. The computation time was 9.74 seconds for a set of 26 species and 1500 case studies, for a tolerance of 10^{-14} for the molar composition and 10^{-5} for the root-finding method. For comparative purposes, the computation time required by Caltech's SD-Toolbox [40] with Cantera [41], which only provides the over-driven branch, was 101.77 seconds, which represents a $10\times$ speed-up factor for our code.

The blue-shaded area shown in Fig. 2.10 corresponds to weak over-driven conditions, which are the most likely to occur in oblique detonations. This region, bounded by $\theta_{\mathrm{cj}} < \theta < \theta_{\max}$, is of significant interest due to its applicability to the study of ODWE systems [191, 192]. For instance, recent research by Guo et al. [192] investigated the impact of pre-shock conditions on the stationary window for CH_4-air oblique detonations. The authors discovered that the limits θ_{cj} and $\theta_{\max}$ depend strongly on the pre-shock velocity and heat release associated with the mixture, while variations with the upstream temperature and pressure are not as prominent. Combustion Toolbox allows to perform these calculations easily, highlighting its relevance in carrying out preliminary studies before tackling more complex flow configurations.

2.5 Rocket module

The calculation of the theoretical performance of rocket engines has drawn renewed attention in recent times, primarily driven by the emergence of private space companies such as Virgin Galactic, SpaceX, Blue Origin, Rocket Lab, and the Spanish PLD Space, which are focused on developing low-cost and reusable launch vehicles [193]. Despite the inherent complexities of these systems associated with the variety of physicochemical phenomena involved, a reasonably accurate estimation of engine performance can be achieved. Thus, since rocket engines typically operate at moderate pressures, the ideal gas assumption can be applied without the need for more complex equations of state. Additionally, the long residence times of the reacting gases in the combustion chamber compared to the chemical reaction times allow further simplification of the calculations. This simplification allows for the utilization of thermochemical equilibrium tools such as CT.

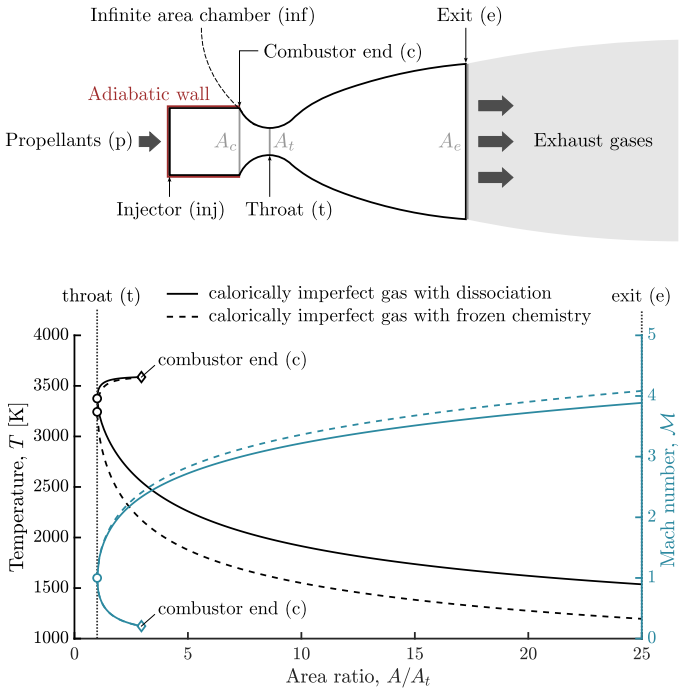

Figure 2.11: Sketch of the cross section of a finite area chamber (FAC) rocket engine. The dashed line represents the difference with an infinite area chamber (IAC), which is only included for the top region for clarity. Chemical transformations: (p-inj) and (p-inf) instant adiabatic combustion at constant pressure (HP); (inj-c) entropic process; (inf-t), (c-t), and (t-e) isentropic process at defined pressure (SP). Bottom: variation of the temperature (——) and Mach number (——) from the combustor end (c) to the exit (e) for a LOX/RP1 mixture with equivalence ratio $\phi = 1.5$ in a high-pressure combustion chamber $p_1 = 100$ atm considering calorically imperfect gas with dissociation (line) and calorically imperfect gas with frozen chemistry (dashed).

The initial release of CT-ROCKET incorporates the mathematical description proposed in [10]. The approach is based on a number of simplifying assumptions, such as one-dimensional flow, uniform cross-sectional area, negligible flow velocity at the inlet of the combustion chamber, adiabatic combustion, isentropic expansion at the nozzle, homogeneous flow, ideal equation of state, and continuity of temperatures and velocities between gaseous and condensed species. Further details on the numerical implementation can be found in Ref. [10, Chapter 6].

CT-ROCKET utilizes the CT-EQUIL module to determine the gas composition within the rocket engine at various points of interest, such as the injector (inj), the

combustion chamber outlet (c), the nozzle throat (t), and different points between (t) and (c/inf) where the hot gases are compressed (subsonic region) or between (t) and the nozzle outlet (e) where the hot gases expand (supersonic region), as illustrated in Fig. 2.11 (top). The bottom panel shows the temperature and the Mach number of the fluid particles from the combustion chamber outlet (c) to the exit (e), passing through the throat (t) with $A_t = A_c/3$, for a LOX/RP1 mixture with equivalence ratio $\phi = 1.5$ (representing a 2.27 oxidizer/fuel weight ratio) in a high-pressure combustion chamber at $p_1 = 100$ atm. The area ratio is taken as the control variable, upon condition that thermochemical equilibrium is achieved at each position.

Additionally, the module calculates the thrust generated by the rocket engine. CT-ROCKET allows for calculations using either frozen chemistry or chemical equilibrium, accounting for combustion chambers with both finite (entropic process) and infinite (isentropic process) dimensions. The frozen chemistry and chemical equilibrium approaches provide an estimate of the performance limits of rocket engine nozzles, as demonstrated by Grossi et al. [194] through two-dimensional numerical simulations based on finite-rate kinetics. This feature enables the performance of parametric analyses to determine the optimal theoretical configuration for a given launch condition or to evaluate the environmental impact at various stages of the rocket vehicle. For instance, with the increasing number of space launches [88, 89], there has been a shift away from highly toxic fuels such as unsymmetrical dimethylhydrazine (UDMH) during the early phases of launch, towards so-called "green" propellants like kerosene (RP1) [94]. It is expected that the use of toxic fuels will be further restricted or even prohibited in the near future, thus driving the need to gain more experience with alternative "green" propellants [92]. The CT-ROCKET module can prove to be a valuable tool in this endeavor.

As previously discussed, this module also includes various routines to compute the state of the mixture at different points of the rocket engine. These states can be modeled using either an infinite area chamber (IAC) or a finite area chamber (FAC). The main steps to calculate the mixture properties using the finite area chamber (FAC) model are defined in the top-layer routine `rocket_performance.m`, as described in Algorithm 6. In brief, an iterative procedure is used to determine the mixture states at the chamber outlet (c) and at the throat (t) by using the infinite area chamber (IAC) model upon defining the initial fresh mixture (composition, temperature, and pressure), A_c/A_t, and A_e/A_t.

Numerous validations were conducted using NASA's CEA code to ensure the reliability and robustness of CT-ROCKET. As an example, Fig. 2.12 displays a range

Algorithm 6 Pseudocode to obtain the theoretical performance of a rocket engine at the points displayed in Fig. 2.11, for the FAC model, a given mixture mix_1, and aspect ratios A_e/A_t and A_c/A_t. The value of A_c/A_t is included in the *self* variable.

function `rocket_performance`($self$, mix_1, A_e/A_t)
  Step 1. Calculate mixture state at the injector, chamber outlet, and throat
  ▷ includes callbacks to the IAC model
  $mix_{2,\mathrm{inj}}, mix_{2,\mathrm{c}}, mix_3 \leftarrow$ `compute_FAC`($self, mix_1$)
  Step 2. Calculate mixture state at the exit points
  $mix_4 \leftarrow$ `compute_exit`($self, mix_{2,\mathrm{c}}, mix_3, mix_4, A_e/A_t, mix_{2,\mathrm{inj}}$)
  Step 3. Calculate performance parameters
  $mix_3, mix_{2,\mathrm{c}}, mix_4 \leftarrow$ `rocket_parameters`($mix_{2,\mathrm{inj}}, mix_3, self.C.gravity, ... mix_{2,\mathrm{c}}, mix_4$)
end function

of thermodynamic properties computed at the nozzle exit (e). The geometrical aspect ratios defining the combustion chamber and the nozzle are $A_\mathrm{c}/A_\mathrm{t} = 2$ and $A_\mathrm{s}/A_\mathrm{t} = 3$. Several reacting mixtures were utilized in the computations, including LOX/LH_2, LOX/RP1, LOX/LCH_4, and N_2O_4/MMH, the latter consisting of nitrogen tetroxide and monomethyl-hydrazine, both of which are highly toxic. The reactants were introduced in a combustion chamber where they reacted isobarically under high-pressure conditions, $p_1 = 100$ atm. The inlet temperature of the propellants was set to their respective boiling points, except for N_2O_4, which was evaluated at 300 K. The computations were performed over a wide range of equivalence ratios, $\phi \in [0.5, 4]$, to investigate the impact of the fuel-to-oxidizer ratio on the combustion process and the resulting reaction products.

As illustrated in Fig. 2.12, CT-ROCKET accurately predicts the properties of primary interest at the nozzle exit, including temperature (T) in (a), pressure (p) in (b), enthalpy (h) in (c), specific heat capacity at constant pressure (c_p) in (d), adiabatic index (γ_s) in (e), gas velocity (u) in (f), specific impulse at specific pressure (I_sp) in (g), and specific impulse in a vacuum (I_vac) in (h). The results demonstrate excellent agreement with the CEA code, with uniform convergence. However, the NASA code showed numerical instabilities for certain cases, such as LOX/RP1 at $\phi = 3$ and LOX/LCH4 at $\phi = 4$. The computation time for LOX/H2 was 19.53 seconds for a set of 11 species and a total of 351 cases. The other mixtures were computed using 94 species, with an average computation time of 57.25 seconds. It is noteworthy that the computation time per species is almost three times less for the latter cases.

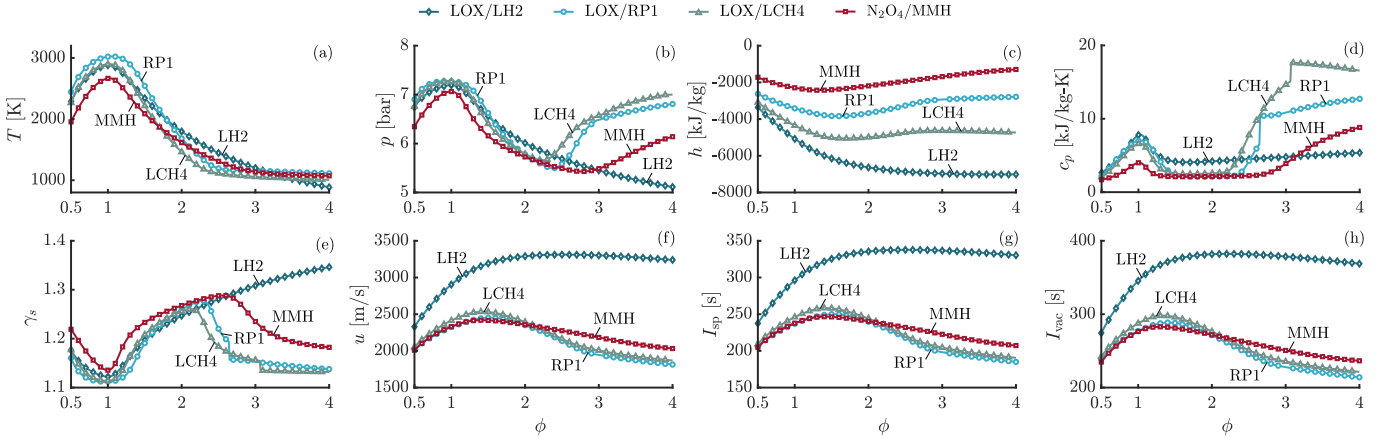

Figure 2.12: Thermodynamic properties at the nozzle exit of a rocket engine with aspect ratios $A_c/A_t = 2$ and $A_e/A_t = 3$ for different liquid bi-propellant mixtures in a high-pressure combustion chamber, $p_1 = 100$ atm, with equivalence ratios $\phi \in [0.5, 4]$: temperature, T (a), pressure, p (b), enthalpy, h (c), specific heat capacity at constant pressure, c_p (d), adiabatic index, γ_s (e), gas velocity, u (f), specific impulse at sea level, I_{sp} (g), specific impulse in a vacuum, I_{vac} (h); solid line: results obtained with CT; symbols: results obtained with the NASA's CEA [10]: LOX/LH_2 (♢), LOX/RP1 (○), LOX/LCH_4 (△), N_2O_4/MMH (□). The code snippet for the LOX/LH_2 case is shown in Listing B.4.

2.6 Graphic User Interface

This section presents a detailed overview of the Graphic User Interface (GUI) developed in this study. The GUI is intended to provide a user-friendly and intuitive interface for the visualization and analysis of data. Most of the functions presented in the manuscript's code, listed in Table 2.2 (at the end of this section), are encapsulated in the GUI. The remainder will be included in the next update of the package. Figures 2.13 to 2.15 depict the fundamental elements of the GUI: the menu bar, the tabs and sub-tabs, the control panel, the command window, the dialog box, the lamp, the tree, and the data visualization area. Each of these objects is described in detail below.

- The *menu bar* comprises predefined actions such as clear, save, snapshot, and check for updates, along with options to access online documentation, tutorials, examples, and license. It also provides access to additional tools, or add-ons, that can expand the GUI's capabilities. These add-ons include controls for numerical errors and visualization settings, species selection, as well as the ability to perform code validations and provide feedback to the development team.
- The interface is divided into two main *tabs* (setup and results) and additional *sub-tabs* designed to organize the content and prevent the user from feeling overwhelmed. The setup tab contains a control panel to configure the problem to be addressed. The results tab contains a data visualization area for post-processing all collected data.
- The *control panel* is a crucial part of the GUI that enables users to configure the problem conditions. It provides a range of controls and options to adjust parameters such as the chemical species (reactants and products), the initial state (composition, temperature, and pressure), the type of problem to be solved, and other parameters for the setup of single-case or parametric studies.
- The *command window* provides a command-line interface that allows users to interact with the GUI through a series of text commands. This feature is particularly useful for advanced users who prefer to work with code or scripts. Through this tool, users can input commands and execute scripts, while the *dialog box* prompts the user for further input or confirmation before executing a command. The dialog box displays practical information like warnings, errors, and execution time, providing valuable feedback to the user.

- The *lamp* component serves as a visual indicator of the analysis status. When the analysis is complete, the lamp emits a green light, while a yellow light indicates that the computations are still in progress. A red light indicates an error in the analysis.
- The *data visualization area* displays the computed results in a visual format, such as plots or tables. It allows users to interact with and explore the data in a way that's intuitive and easy to understand.
- The *tree* component collects all the data and exhibits the hierarchical organization of the obtained outcomes, which enables users to explore and access distinct aspects of each case.
- Additional features have been incorporated to improve the GUI's usability, including context menus and keyboard shortcuts. These functionalities enable users to perform intricate tasks with ease and speed.

For illustrative purposes, Figs. 2.13 to 2.15 exhibit Combustion Toolbox GUI screenshots captured during a parametric study of the adiabatic and isobaric combustion of acetylene-air mixtures for a wide range of equivalence ratios. This case corresponds to the data displayed in Fig. 2.4 in Sec. 2.3.4. As observed in Fig. 2.13, the first step includes setting up the problem conditions, which include *i)* the initial mixture (composition, temperature, and pressure), that can be chosen from the predefined mixtures via the *reactants* drop-down menu, or by manually adding the appropriate species name one-by-one to the same object; *ii)* the problem configuration (adiabatic at constant pressure, etc.); *iii)* the control parameter for a parametric or individual study, such as the equivalence ratio; and *iv)* additional input parameters that may be required based on the type of problem.

If a parametric study is selected with the equivalence ratio as the control parameter, the post-processing step can be initiated (as depicted in Fig. 2.14). If the problem is well-posed, the *lamp* object will turn green, meaning that the computations were obtained successfully, and a message will appears in the *dialog box* of the GUI. Subsequently, the obtained dataset is re-structured in the background to fit into the *tree* object for result post-processing. By selecting each solution of the *tree* object, the GUI automatically updates the thermodynamic properties of the mixtures in the data visualization area (see Figs. 2.13 and 2.14). Additionally, in the *results* $\hookrightarrow$ *custom figures* tab, all mixture properties can be analyzed by plotting the results, as illustrated in Fig. 2.15. The datasets collected using the GUI can also be exported to a structured spreadsheet or *.mat* file.

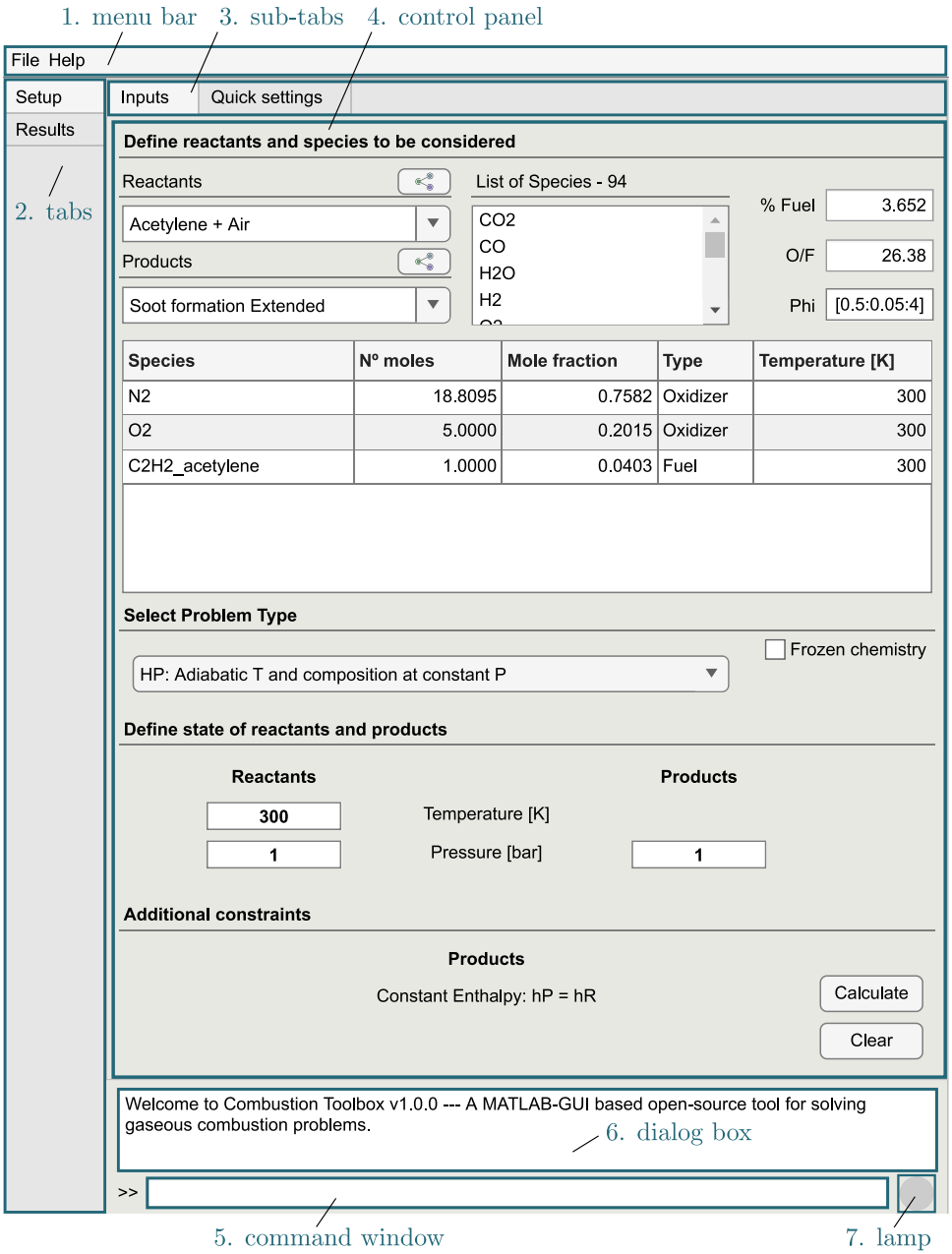

Figure 2.13: Example of how to configure the GUI to reproduce the results of Fig. 2.4.

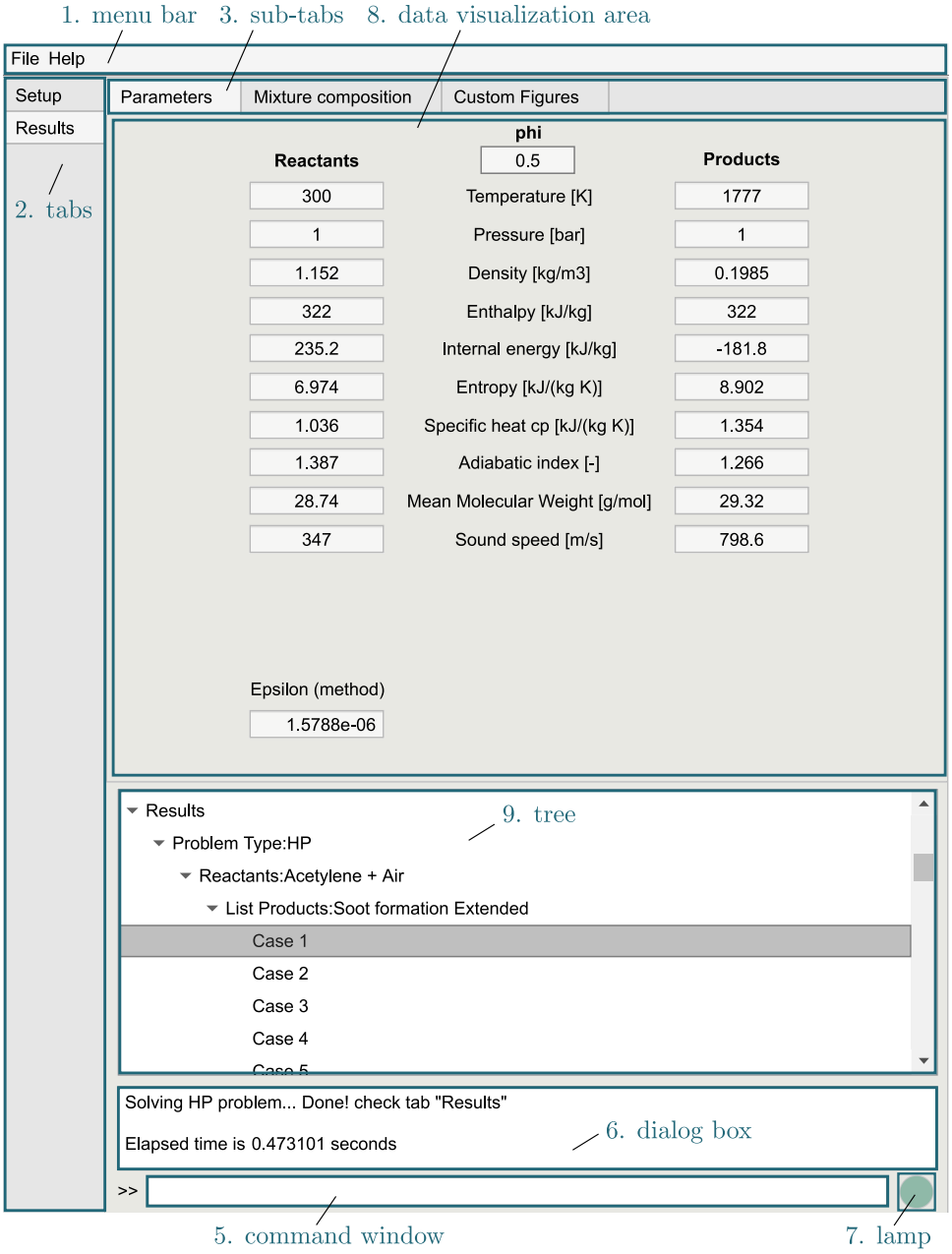

Figure 2.14: Post-processing the results of Fig. 2.4 through the GUI. In particular, the thermodynamic properties correspond to the case selected in the tree object ($\phi = 0.5$).

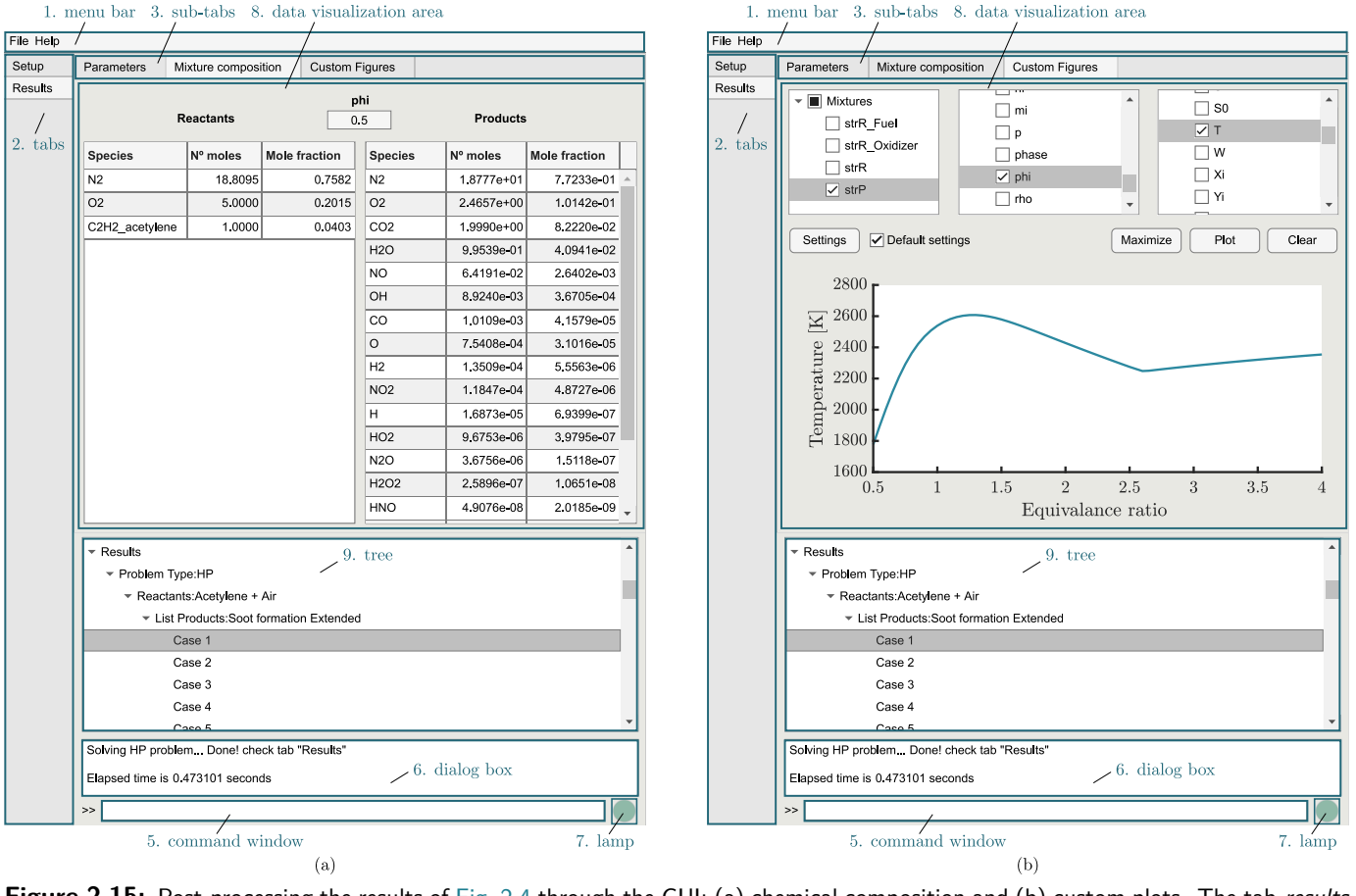

Figure 2.15: Post-processing the results of Fig. 2.4 through the GUI: (a) chemical composition and (b) custom plots. The tab *results* ↪ *mixture composition* shows the mixture composition for the case selected in the tree object ($\phi = 0.5$).

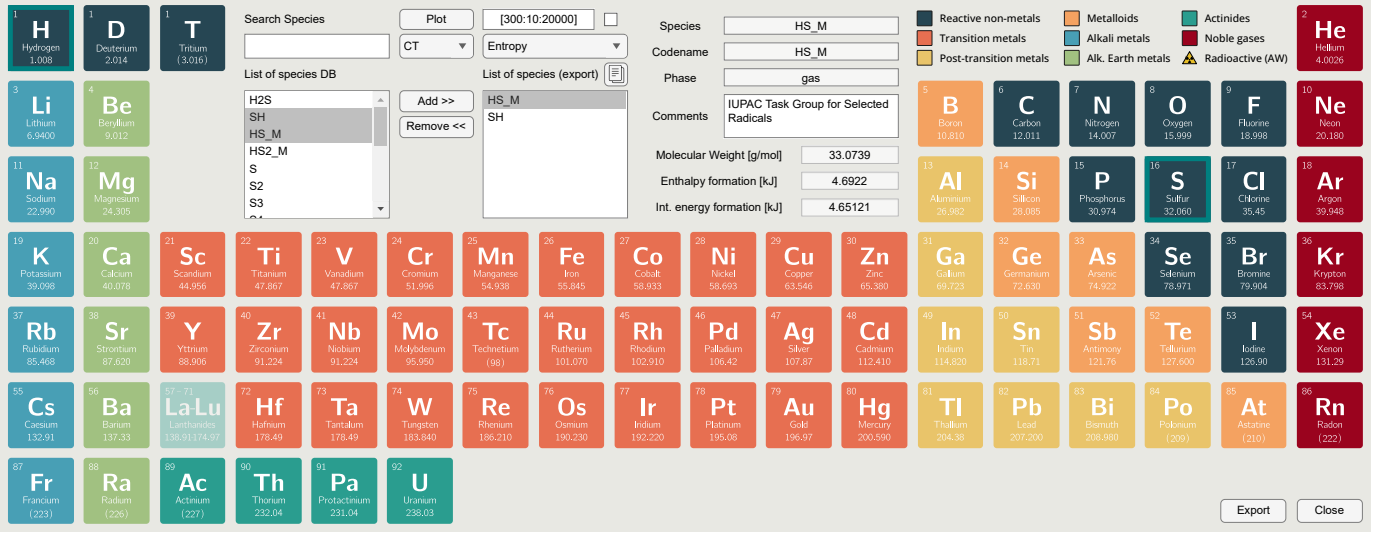

Figure 2.16: Periodic table add-on used to browse and select the species from the database that contain a particular set of elements. The suffix _M in the name of a given species from the drop-down list indicates that its thermochemical properties are obtained from the Third Millennium database [129].

As commented before, CT has implemented several add-ons to enhance the capabilities of the main GUI. For example, the add-on *uielements* (see Fig. 2.16) facilitates the selection of the chemical species allocated in the databases. It also allows to evaluate and plot the thermodynamic data of the individual species. The CT settings can be conveniently adjusted using the *uipreferences* add-on, as illustrated in Fig. 2.17. Of particular interest for potential users, the validations conducted in CT can be replicated using the *uivalidations* add-on, which reads all the tests stored in the *validations* folder. Lastly, all users can report bugs, ideas, or queries using the *uifeedback* add-on, which will include predefined templates to maintain consistent standards.

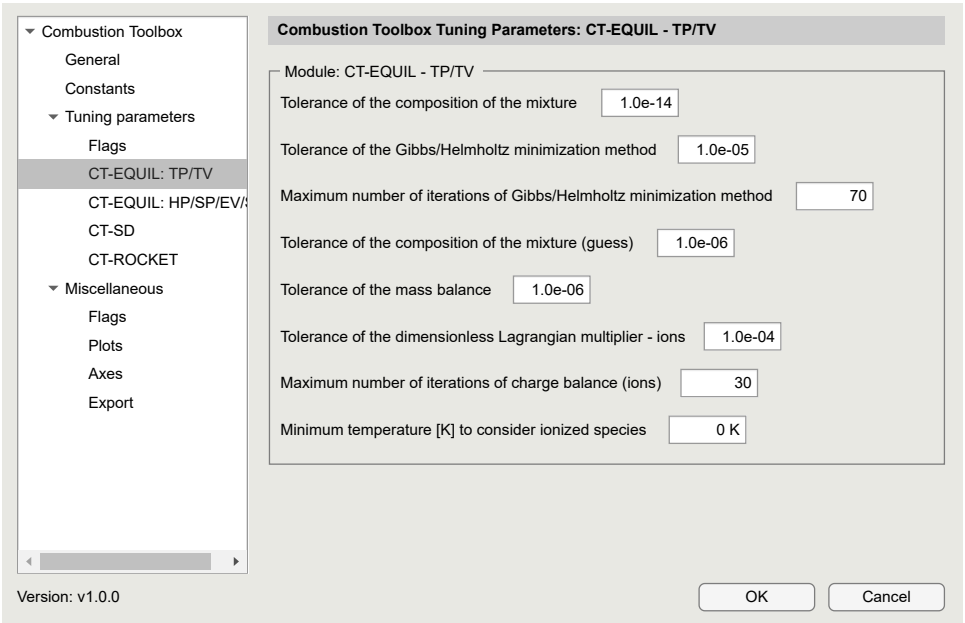

Figure 2.17: Add-on to set all the preferences of the Combustion Toolbox.

In brief, the GUI offers a broad range of tools for examining problems related to chemical equilibrium. The user-friendly design and intuitive features make it accessible to a variety of users, including those with a limited technical background. The GUI is an essential tool for researchers and practitioners who need to perform and analyse extensive parametric studies of the wide range of problems that can be addressed by the code. However, it is important to note that the GUI is intended to supplement traditional coding approaches instead of replacing them. Despite its ability to streamline tasks for non-experts, plain code actually exhibits greater versatility. The GUI itself is constructed upon an existing codebase, whose fundamental functions and calculations

are still available for access and manipulation via the command line interface. In fact, proficient users interested in intricate analytical requirements may find that direct coding and execution is a more efficient and effective method than relying exclusively on the GUI. Thus, the GUI ought to be regarded as a tool that assists users with specific tasks rather than as a replacement for the potent and flexible nature of traditional coding.

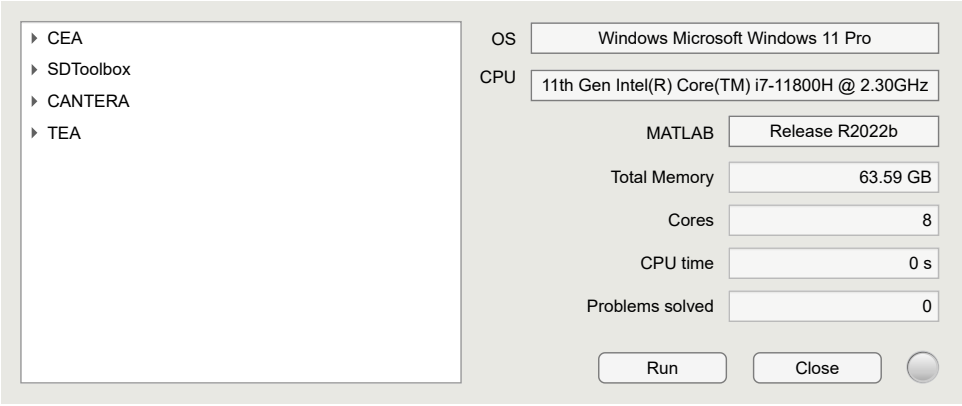

Figure 2.18: Add-on to reproduce all the validations of the Combustion Toolbox.

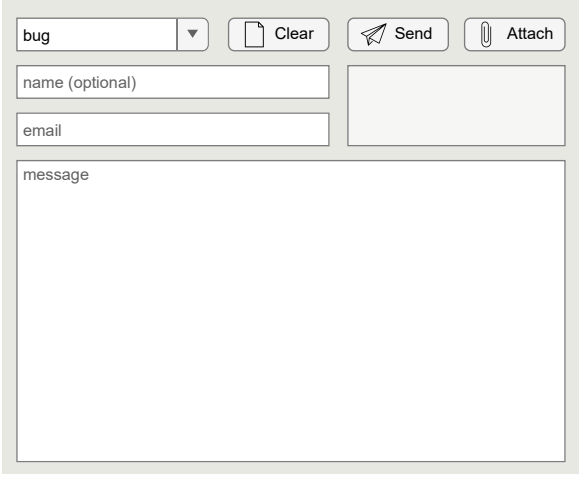

Figure 2.19: Add-on to report bug/inquiries of the Combustion Toolbox.

Description	Module	GUI	Main callbacks
CE at defined TP, TV	CT-EQUIL	✓	`equilibrate_T`
CE at defined HP, SP, EV, SV	CT-EQUIL	✓	`equilibrate`
CE for a given TP profile - Exoplanets	CT-EQUIL		`equilibrate_T`
Normal shocks	CT-SD	✓	`shock_incident`
Reflected normal shocks	CT-SD	✓	`shock_reflected`
Oblique shocks for a given β	CT-SD	✓	`shock_oblique_beta`
Oblique shocks for a given θ	CT-SD	✓	`shock_oblique_theta`
Shock polar diagrams	CT-SD	✓	`shock_polar`
Reflected oblique shocks for a given θ	CT-SD		`shock_oblique_theta`, `shock_oblique_beta`
Reflected shock polar diagrams for a given β	CT-SD	✓	`shock_polar`, `shock_oblique_beta`
Reflected shock polar diagrams for a given θ	CT-SD	✓	`shock_polar`, `shock_oblique_theta`
Shocks within the limit of regular reflections	CT-SD		`shock_polar_limitRR`
CJ detonations	CT-SD	✓	`det_cj`
Over-driven detonations	CT-SD	✓	`det_overdriven`
Under-driven detonations	CT-SD	✓	`det_underdriven`
Reflected CJ detonations	CT-SD	✓	`det_cj`, `shock_reflected`
Reflected over-driven detonations	CT-SD	✓	`det_overdriven`, `shock_reflected`
Reflected under-driven detonations	CT-SD	✓	`det_underdriven`, `shock_reflected`
Oblique detonation for a given β	CT-SD	✓	`det_oblique_beta`
Oblique detonation for a given θ	CT-SD	✓	`det_oblique_theta`
Detonation polar diagrams	CT-SD	✓	`det_polar`
Rocket engine performance assuming IAC	CT-ROCKET	✓	`rocket_performance`
Rocket engine performance assuming FAC	CT-ROCKET	✓	`rocket_performance`

Table 2.2: Summary of problems that can be solved using the Graphic User Interface.

2.7 Conclusions

This chapter presented the Combustion Toolbox (CT), an innovative open-source thermochemical code developed for the calculation of equilibrium states in gaseous reacting systems. While CT primarily focuses on combustion problems that may involve the formation of condensed-phase species, its abilities extend to other areas of interest, including the calculation of the atmospheric compositions of gaseous exoplanets, ablation processes, hypersonic shocks, and detonations. CT has been implemented in MATLAB and designed with a modular architecture, making it both user- and developer-friendly.

At present, the three modules included in CT are CT-EQUIL, CT-SD, and CT-ROCKET. The first module, CT-EQUIL, is the kernel of the Combustion Toolbox and is responsible for solving the chemical composition of the system at equilibrium. This is achieved by minimizing the Gibbs/Helmholtz free using the Lagrange multiplier approach coupled with a multidimensional Newton-Raphson method. The second module, CT-SD, solves post-shock/detonation states for normal and oblique incident flows, including the computation of reflected waves. The third module, CT-ROCKET, is designed to determine the mixture composition at various points of interest within rocket engines, along with the calculation of the theoretical rocket performance. Additionally, CT is equipped with an advanced Graphic User Interface (GUI) that encapsulates the three modules and multiple built-in functions, providing users with a convenient operating experience.

The modules have been validated against existing state-of-the-art codes, including NASA's Chemical Equilibrium with Applications (CEA) [10], Cantera [41] within Caltech's Shock and Detonation Toolbox (SD-Toolbox) [40, 118], and the newly developed Thermochemical Equilibrium Abundances (TEA) code [18]. All tests showed excellent agreement. As a matter of fact, CT exhibits superior computational performance in terms of cost and time, outperforming Caltech's SD-Toolbox and TEA by a significant margin. Additional validations can be accessed through the web at https://combustion-toolbox-website.readthedocs.io, which also provides further documentation and examples. The tool is actively maintained and can be accessed at https://github.com/AlbertoCuadra/combustion_toolbox.

While Combustion Toolbox has obtained promising results, it is still an ongoing research project that requires additional development to enhance its capabilities. We aim to introduce additional functionalities in future versions of the code, such as the incorporation of non-ideal equations of state (currently under implementation), the analysis of multi-phase systems, a more accurate model for rocket propellant performance, and

the extension of the database to include transport properties. We are also considering expanding the code to other well-known open-source programming languages, such as C++ and Python. The former is preferred due to its exceptional performance compared to MATLAB [153], while the latter is preferred due to its simplicity [195]. Additionally, a functional version of the CT-EQUIL module has been developed in Python. An intermediate step will involve using MEX functions in the kernel of the code to combine C++ and MATLAB for calculating chemical equilibrium at defined temperature and pressure/volume, which is anticipated to substantially improve the speed of the code.

3 Effect of equivalence ratio fluctuations on planar detonations

> *I was taught that the way of progress was neither swift nor easy.*
>
> — **Marie Curie**

Contents

Summary

In this chapter, a linear asymptotic theory is proposed to describe the propagation of planar detonation fronts through heterogeneous mixtures of reactive gases that exhibit random fluctuations in the fuel mass fraction. The analysis starts with the derivation of the transfer functions that relate the upstream fuel-mass-fraction inhomogeneities with the burnt-gas perturbations via normal mode analysis. These results are then used in a Fourier analysis of a detonation wave interacting with two- and three-dimensional isotropic heterogeneous fields. This yields integral formulae for the turbulent kinetic

energy, sonic energy, averaged vorticity, and entropy production rates. Second-order corrections for the turbulent Rankine-Hugoniot conditions are also obtained, along with analytical expressions for the deviation of the detonation velocity with respect to that of the equivalent homogeneous mixture. Upstream inhomogeneities are found to speed up the detonation front in the vast majority of scenarios studied, with a velocity amplification factor that depends on the properties of the fuel-air mixture, particularly on the variation of the density and the heat release with the fuel mass fraction.

3.1 Introduction

Detonation waves have been explored extensively for propulsion applications given their theoretical advantage over deflagrative premixed combustion. For instance, rotating detonation engines, which do not operate under the Brayton Cycle, benefit from the additional work extraction from the cycle and a decrease in the physical size of the combustor [57]. Premixing of fuel and air may be necessary due to finite ignition delay times compared to the residence time of the fluid particles in the combustion chamber. Consequently, it is of paramount importance to understand how standing detonation waves may be affected by the inhomogeneities of the reactive gas mixture to design efficient supersonic combustors [55, 196, 197]. However, many challenges must be surmounted before detonation-based engines can be presented as a competitive alternative. Some hurdles include the incomplete fuel-air mixing at the molecular level, the stability of the detonation, and the strong noise generated by the system even in highly idealized configurations [188, 198]. Non-idealized configurations representative of more realistic systems may include additional complexities, such as detonation-wall interaction, confinement, turbulence, multi-phase flow, and non-perfect mixing, in addition to the complexities that arise in the modeling of chemical kinetics and transport properties [199].

When the burning process in the premixed environment occurs at high Mach numbers, acoustics play a dominant role in the reactive flow dynamics, as is the case of detonations. Unlike deflagrations, the thickness of the hydrodynamic region affecting the detonation front only compares to the detonation thickness because there is no possibility for a preheat layer. Moreover, diffusive effects become subdominant given that the residence time of the reactive mixture in the induction-burning layer is considerably reduced compared with the characteristic diffusion time. Radicals formation and recombination affect the detonation thickness and dynamics, but they do not influence the propagation speed, at least in the first order. When the planar detonation exhibits

an unstable propagation pattern [200–207], the disturbances generated downstream affect the averaged Rankine-Hugoniot (RH) relationships, since the energy employed in the generation of vorticity, entropy, and sonic perturbations comes from the only source available in self-sustained detonations: the heat released by combustion. It has been found that upstream heterogeneities play a pivotal role in the detonation dynamics [208–214]. Enhancement of the propagation speed has been observed in gaseous mixtures due to the turbulence induced by the detonation front wrinkling [214–217]. When moving through fuel-air sprays with large droplets, detonations exhibit a deficit in the propagation velocity compared to the gas-phase velocity [218]. Similar effects have been observed in detonations moving through reactive gaseous media with water clouds [219–222]. However, a clear correlation between the upstream properties of the heterogeneous mixture and the detonation propagation velocity has not been presented to date.

This work aims to shed further light, from a theoretical framework, on the hydrodynamical aspects that contribute to the modification of detonation velocity when the detonation wave propagates through a non-uniform mixture of reactive gases. The linear-interaction analysis predicts a second-order propagation velocity augmentation for weakly overdriven detonations independently of the type of perturbations generated by the equivalence ratio fluctuations, i.e., positive or negative perturbations in the upstream density and/or heat of combustion fields. For strongly overdriven detonations, a weak deficit in the propagation speed is found only when upstream perturbations in the equivalence ratio are dominated by heat release perturbations.

Earlier work on the interaction of small-amplitude perturbations with detonation waves can be found in Refs. [223–232]. When the problem is addressed numerically, chemical kinetic models can be implemented [223–226], which allows the description of the detonation unstable modes. Numerical studies by Massa and Lu [223] and Massa et al. [224] demonstrate enhanced interactions between turbulence and detonations when sizes of the inhomogeneities and the unperturbed reaction zones are comparable. For certain values of the activation energy, small scales of the post-shock perturbation modes increase unbounded owing to acoustic resonance. However, turbulence may cushion the self-induced detonation oscillations in different conditions by forcing the reaction wave to adapt to the ever-changing upstream conditions. Under this stable condition, the present theory and that employed in Refs. [227–230, 232] can be applied.

Furthermore, employing the fast-reaction limit allows the detonation wave to be treated as a single discontinuity front, and the chemical process exclusively enters through the non-adiabatic Hugoniot curve. The motivation was to improve descrip-

tions of the influences of compressible turbulence on detonation propagation and, in particular, to determine how the passage of a planar detonation modifies the turbulence. This work complements these fundamental studies, particularly the work Huete et al. [229] on the interaction of detonation with density perturbations, by placing the focus on the mixture imperfections that add another type of convective perturbation [231, 233], i.e., the local heat of combustion of the mixture. Results presented below demonstrate that the combination of the two sources of entropic perturbations derived from fuel-mass-fraction heterogeneities—i.e., perturbation of density and heat-release—may lead to order-of-magnitude differences in the turbulence generation rate when scaled with the fuel mass fraction variations. In addition, the acoustic energy, which typically exhibits a low-impact role in canonical shock-turbulence interactions, is of great importance here for weakly overdriven detonations.

The analysis makes use of the same mathematical description as that employed in the pioneering works of Ribner [80–82] for shock waves and the posterior analyses in reactive shocks of Jackson et al. [227, 228], who assumed the ideal gas equation of state with constant specific heats and employed the fast-reaction limit to treat the detonation as a reactive shock. In addition to considering the effect of heat-release changes induced by the non-uniform upstream mixture, this work computes modified turbulent RH equations. It distinguishes a heterogeneous mixture from the corresponding uniform mixture with the same averaged upstream values [234]. As a result of the presence of heterogeneities in the fresh mixture, the averaged propagation speed of the detonation wave is modified, which also occurs with inert shocks [235–237]. Indeed, changes in the propagation speed have also been reported for detonations [214–216, 238–243]. The present work provides closed-form analytical expressions in terms of the detonation properties based on the burnt-gas dynamics to predict the averaged propagation speed.

The study begins in Sec. 3.2 with the problem formulation for both base and linearly perturbed flow in the thin-detonation limit. In Sec. 3.3, a Fourier analysis is employed for two-dimensional and three-dimensional isotropic turbulent fields to provide integral formulae for the amplification of the kinetic energy, vorticity, and density fluctuations. The near-field acoustic energy and the effect of the detonation passage in the turbulence scales are also analyzed. The modification of the averaged RH conditions is obtained in Sec. 3.4, along with the variation of the detonation propagation speed as a result of the upstream mixture heterogeneities. Final conclusions are presented in Sec. 3.5. Additionally, Appendix C provides the normal mode analysis employed to describe the interaction of the planar detonation with a monochromatic pattern in the fuel mass fraction.

3.2 Problem description

3.2.1 Upstream heterogeneous mixture

The presence of non-equilibrium perturbations in the upstream gas coming from fuel mass fraction fluctuations must be accompanied with velocity perturbations to satisfy the conservation equations consistently. Similarly, pressure perturbations may be present in the heterogeneous mixture ahead of the shock. When the rotational, acoustic, entropic, and composition perturbations result from the same physical mechanism, the corresponding spectra associated with the different types of perturbations are very similar. In particular, for stationary compressible isotropic turbulence [244, 245], the scalar energy spectra for the fuel mass fraction disturbances peak at the same wave number as the kinetic energy dissipation spectrum, thereby suggesting the use of a similar spectrum form for all turbulent variables.

The relative influence of the different upstream perturbations on the downstream evolution of the flow depends on the initial perturbation amplitudes and the propagation Mach number. The latter dependence can be investigated using the linearized RH jump conditions, which show that the amplification factor affecting the mass fraction perturbations as they cross the front (with the corresponding changes in density and heat release) remains finite in the limit of large propagation Mach numbers $\mathcal{M}_1 \gg 1$. In contrast, the corresponding amplification factors for the pressure and vorticity perturbations become proportional to $\mathcal{M}_1^{-2}$ and $\mathcal{M}_1^{-1}$, respectively. As a result, in the strong shock limit, the upstream perturbations of vorticity and pressure play a secondary role with regard to the downstream flow. When dealing with multi-component mixtures, the local specific-heat ratio γ is also affected by mixture proportions, but this effect can also be neglected in the first approximation. Variations in γ are expected to range between 1.1 and 1.4 between mixture compounds for light hydrocarbon fuels. Thus, order-of-unity variations in the fuel mass fraction provoke weak changes that are one order of magnitude smaller in the local value of γ. In addition, even admitting same-order variations in γ, these perturbations can be neglected for the same reason that velocity and pressure perturbations upstream are not considered, namely they become proportional to $\mathcal{M}_1^{-2}$ in the strong shock limit.

In this work, a planar detonation front is considered to propagate through a heterogeneous gaseous mixture that is static and isobaric, so that the variations of the fuel mass fraction are only associated with perturbations in density and heat release, as

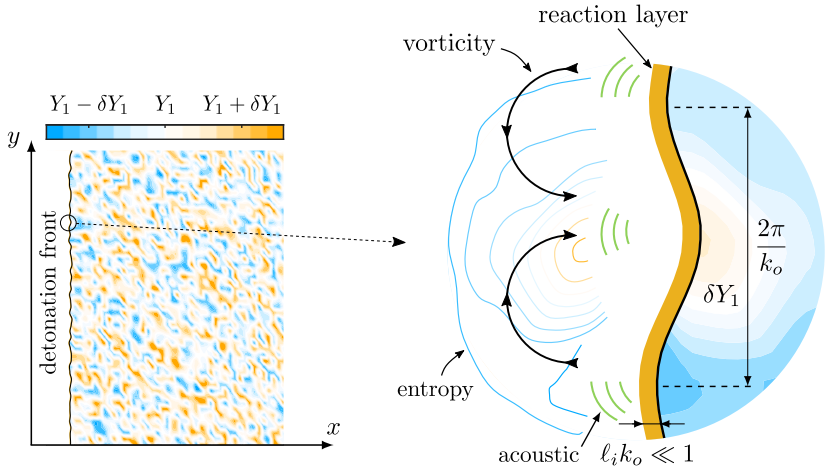

Figure 3.1: An schematic of the corrugated detonation front through a heterogeneous gaseous mixture, where the variation of the local fuel mass fraction satisfies $|\delta Y_1| = |Y_1 - \langle Y_1 \rangle| \ll 1$ in order to apply linear theory. The detonation induction length ℓ_i is assumed to be considerably reduced than the characteristic upstream length k_o^{-1}.

sketched[1] in Fig. 3.1. It is assumed that the deviation of the local fuel mass fraction Y_1 with respect to its average value $\langle Y_1 \rangle \sim 1$ is sufficiently small for the linear theory to be applicable, $|\delta Y_1| = |Y_1 - \langle Y_1 \rangle| \ll 1$. For sufficiently weak perturbations, the isotropic heterogeneous mixture can be approximated by the linear superposition of independent modes, each one being characterized by a wavenumber $\boldsymbol{k}$, so that

$$\delta Y_1(\boldsymbol{k}, \boldsymbol{x}_1) = \varepsilon(\boldsymbol{k}) \mathrm{e}^{\mathrm{i}\, \boldsymbol{k} \cdot \boldsymbol{x}_1}, \tag{3.1}$$

where $\boldsymbol{x}_1$ is the vector defining the position in a reference frame at rest with respect to the upstream flow, and $\varepsilon(\boldsymbol{k})$ is the amplitude of the fuel mass fraction perturbations corresponding to a given wavenumber vector $\boldsymbol{k}$.

[1] This thesis presents two similar schematics (see Figs. 3.1 and 5.1) produced using MATLAB, and further refined with Inkscape and LaTeX (using the TikZ package). These illustrations aim to represent the intricate nature of shock-turbulence-interaction problems when subjected to different types of upstream perturbations. Upon crossing the shock, these perturbations experience a sudden increase in magnitude, resulting in significant alterations to the turbulence generated downstream the shock. To artistically represent this fascinating phenomenon on the thesis cover, an algorithm was developed based on the Fractional Brownian Motion (fBm) method—a widely used mathematical process for generating noise. By leveraging fBm, the algorithm generates visually intricate and captivating patterns, successfully conveying the chaotic and unpredictable characteristics of turbulence. The source code for this algorithm is publicly available on GitHub at https://github.com/AlbertoCuadra/fbm.

Assuming that there is no privileged direction in the upstream flow, the spectrum of the fuel mass fraction perturbations is considered spatially homogeneous and isotropic. Thus, the wavenumber vector $\boldsymbol{k}$ is uniformly distributed over the unit sphere (or around the unit semicircle in two dimensions). Therefore, the analysis consists of a superposition of linear perturbations whose amplitudes are exclusively functions of the wavenumber amplitude $k = |\boldsymbol{k}|$. In such cases, the mean square of the fuel mass fraction perturbations in two-dimensional and three-dimensional geometries are

$$\langle \delta Y_1^2 \rangle_{2\mathrm{D}} = \pi \int_0^\infty \varepsilon(k)^2 k \, \mathrm{d}k \quad \text{and} \quad \langle \delta Y_1^2 \rangle_{3\mathrm{D}} = 4\pi \int_0^\infty \varepsilon(k)^2 k^2 \, \mathrm{d}k, \tag{3.2}$$

respectively, where $\varepsilon(k)$ represents the spectrum of the fuel mass fraction. When fuel mass fraction perturbations are related to turbulent velocity fluctuations [244, 245], a plausible but arbitrary choice for the isotropic spectrum may be $\varepsilon(k)^2 \sim (k/k_o)^2/[1 + (k/k_o)^2]^{17/6}$, where k_o is the most representative wavenumber associated to the upstream turbulent flow [77, 246–248]. Compared to the detonation front, the fast-reaction model assumes that the detonation thickness is considerable reduced than the characteristic wavelength k_o in the unimodal probability density distributions such that $k_o \ell_i \ll 1$ as displayed in Fig. 3.1. The two length scales are independent of each other. The characteristic scale of the spectrum depends on the type of mixing and turbulence upstream, whereas the detonation thickness mainly depends on the detonation properties through the reaction kinetics and temperature conditions. Although order-of-magnitude differences can be observed between different mixture properties, a rough estimate is 0.01-1 centimeters as a characteristic scale for ℓ_i, albeit upstream temperature and detonation overdrive can significantly change this value.

For a generic fuel-air mixture, if the fuel is heavier than air, positive values of δY_1 are associated with positive upstream density perturbations, $\delta\rho_1 > 0$, and vice-versa. The sign of the perturbations of heat release can also be anticipated by taking into account the fact that heat release typically peaks under slightly rich conditions. Thus, positive values of δY_1 lead to negative perturbations of heat release, $\delta q_1 < 0$, in sufficiently rich environments, while the opposite occurs for lean mixtures.

The small parameter δY_1 will be employed below to write the perturbed density and heat release fields as follows:

$$\rho_1 = \langle \rho_1 \rangle + \delta\rho_1 = \langle \rho_1 \rangle (1 + \delta Y_1 W), \tag{3.3}$$

$$q_1 = \langle q_1 \rangle + \delta q_1 = \langle q_1 \rangle (1 + \delta Y_1 H), \tag{3.4}$$

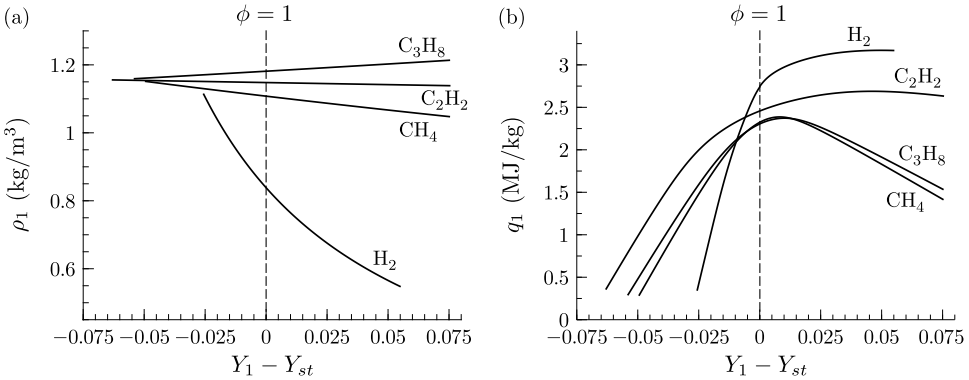

Figure 3.2: Variation of density (a) and heat release (b) with the fuel mass fraction for representative fuel-air mixtures. The dashed line represents the stoichiometric condition given by $Y_1 = Y_{st}$ ($\phi = 1$). Computations were obtained using the Combustion Toolbox and are given for hydrogen (H_2), methane (CH_4), acetylene (C_2H_2), and propane (C_3H_8) at $T_1 = 300$ K and $p_1 = 1$ bar in fresh conditions. The associated stoichiometric fuel mass fractions are $Y_{st} = 0.0285$, 0.0552, 0.0705, and 0.0603, respectively.

where the parameters $W = \rho_1^{-1}(\mathrm{d}\rho_1/\mathrm{d}Y_1)$ and $H = q_1^{-1}(\mathrm{d}q_1/\mathrm{d}Y_1)$ relate to the local slopes of the $\rho_1(Y_1)$ and $q_1(Y_1)$ curves, respectively. For a "binary" fuel-air mixture with fuel and air mass fractions being Y_1 and $1 - Y_1$, respectively, the dependence of the mixture density and the dimensionless function W with the fuel mass fraction is noted as follows:

$$\frac{\rho_1}{\rho_A} = \frac{1}{1 - \left(1 - \frac{W_A}{W_F}\right) Y_1} \quad \text{and} \quad W = \frac{1}{\rho_1}\frac{\mathrm{d}\rho_1}{\mathrm{d}Y_1} = \frac{1 - \frac{W_A}{W_F}}{1 - \left(1 - \frac{W_A}{W_F}\right) Y_1}, \tag{3.5}$$

where ρ_A is the air density, and W_A and W_F refer to the air and fuel molecular weights, respectively.

The variation of the heat release with the fuel mass fraction cannot be accurately anticipated because it depends on the final composition of the burnt mixture. Detonations induce a strong compression work—through the irreversible transformation made by the shock—and a later expansion of the fluid, which makes the final temperature differ from the adiabatic flame temperature of isobaric combustion. It is widely known, however, that heat release peaks close to stoichiometric conditions for slightly rich mixtures, a property that can be used to anticipate the sign of the slope of the heat release-fuel mass fraction curve. Accurate values of q_1 can be obtained with either numerical codes or experimental data. Figure 3.2 has been computed with the Combustion Toolbox [23], an in-house thermochemical code validated with NASA's CEA code [10], Cantera [41]

Fuel	Slopes	Equivalence ratio ϕ							
		0.25	0.5	0.75	1	1.25	1.5	1.75	2
H_2	W	-12.14	-11.17	-10.35	-9.65	-9.05	-8.53	-8.07	-7.66
	H	136.94	60.22	32.71	15.08	5.88	3.58	2.45	1.66
CH_4	W	-0.79	-0.78	-0.77	-0.77	-0.76	-0.75	-0.74	-0.74
	H	69.07	33.40	18.44	6.70	-3.02	-6.59	-7.85	-8.88
C_2H_2	W	-0.11	-0.11	-0.11	-0.11	-0.11	-0.11	-0.11	-0.11
	H	52.91	23.21	9.36	4.77	2.50	1.08	-0.03	-0.8
C_3H_8	W	0.35	0.35	0.35	0.35	0.36	0.36	0.36	0.36
	H	62.88	30.29	15.91	5.79	-1.89	-5.76	-7.08	-8.02

Table 3.1: Dimensionless slopes of the density and heat release curves, W and H, for H_2, CH_4, C_2H_2, and C_3H_8. The orange and blue background colors are applied for positive and negative values of the relation H/W, respectively.

within Caltech's Shock and Detonation Toolbox [40], and TEA [18] (see Chapter 2 for an extensive description of the Combustion Toolbox). Here, the variation of density (a) and heat release (b) with the fuel mass fraction is shown for different gases, including hydrogen (H_2), methane (CH_4), acetylene (C_2H_2) and propane (C_3H_8), with stoichiometric fuel mass fractions $Y_{st} = 0.0285$, 0.0552, 0.0705, and 0.0603, respectively. Representative values of W and H obtained from these computations are given in Table 3.1 for these fuels and different equivalence ratios ranging from very lean to moderately rich mixtures.

3.2.2 Homogeneous Rankine-Hugoniot equations

Neglecting the deviation from the mean values, the flow variables in the burnt gas are obtained by integrating the conservation equations in the streamwise direction, yielding

$$\rho_1 u_1 = \rho_2 u_2, \tag{3.6a}$$

$$p_1 + \rho_1 u_1^2 = p_2 + \rho_2 u_2^2, \tag{3.6b}$$

$$h_1 + \frac{1}{2} u_1^2 = h_2 + \frac{1}{2} u_2^2, \tag{3.6c}$$

for the mass, streamwise momentum, and energy conservation equations, respectively. Here, the subscripts 1 and 2 refer to the upstream and downstream dimensional flow

properties, respectively, including the velocity u, density ρ (or specific volume $V = \rho^{-1}$), pressure p, and enthalpy h. The upstream flow comprises a mixture of gases, each of which is modeled as a calorically perfect gas, i.e., the specific heats, and therefore the adiabatic index γ, are assumed to be constant throughout the shock compression and combustion processes. Thus, the enthalpy variation is written as a function of a single value of γ

$$h_2 - h_1 = q_1 + \frac{\gamma}{\gamma - 1}\left(\frac{p_2}{\rho_2} - \frac{p_1}{\rho_1}\right), \tag{3.7}$$

where q_1 represents the heat released in the reaction front per unit mass of mixture. In realistic conditions, the value of γ depends on both mixture composition and temperature, which experience significant changes across the detonation wave. In qualitative terms, when the effect of temperature dominates the variation of γ by the excitation of vibrational modes, the specific heat ratio is expected to decrease with temperature monotonically. However, a change in the molecules' structure exists due to the combustion process. Thus, the total variation of γ must include information of the initial and final composition of the mixture. Nevertheless, since upstream thermal energy can be neglected in the first approximation, the value used in the computations should be the value associated with the burnt gas conditions to minimize the error when γ is constant.

Algebraic manipulation of Eqs. (3.6a) to (3.7) provides the jump equations across the reaction front, namely,

$$\mathcal{R} = \frac{\rho_2}{\rho_1} = \frac{(\gamma+1)\,\mathcal{M}_1^2}{\gamma\mathcal{M}_1^2 + 1 - \left[(\mathcal{M}_1^2 - 1)^2 - 4Q\mathcal{M}_1^2\right]^{1/2}}, \tag{3.8}$$

$$\begin{aligned}\mathcal{P} = \frac{p_2}{p_1} &= \frac{\gamma\mathcal{M}_1^2 + 1 + \gamma\left[(\mathcal{M}_1^2 - 1)^2 - 4Q\mathcal{M}_1^2\right]^{1/2}}{\gamma + 1} \\ &= \frac{(\gamma+1)\,\mathcal{R} - \gamma + 1 + 4\mathcal{R}Q\gamma/(\gamma+1)}{\gamma + 1 - (\gamma-1)\,\mathcal{R}}\end{aligned} \tag{3.9}$$

for density and pressure, respectively, while the Mach number of the burnt-gas flow is

$$\mathcal{M}_2 = \frac{u_2}{a_2} = \left\{\frac{\gamma\mathcal{M}_1^2 + 1 - \left[(\mathcal{M}_1^2 - 1)^2 - 4Q\mathcal{M}_1^2\right]^{1/2}}{\gamma\mathcal{M}_1^2 + 1 + \gamma\left[(\mathcal{M}_1^2 - 1)^2 - 4Q\mathcal{M}_1^2\right]^{1/2}}\right\}^{1/2}, \tag{3.10}$$

where a_2 denotes the speed of sound and

$$Q = \frac{(\gamma^2 - 1)}{2a_1^2} q_1 \tag{3.11}$$

is the dimensionless heat release per unit mass.

The so-called Chapman-Jouguet (CJ) regime, which is given by $(\mathcal{M}_1^2 - 1)^2 - 4Q\mathcal{M}_1^2 = 0$, defines the minimum detonation strength. Thus, the maximum downstream Mach number is associated with a given energy release as follows:

$$\mathcal{M}_{\mathrm{cj}} = (1+Q)^{1/2} + Q^{1/2}. \tag{3.12}$$

This value is related to the maximum flow expansion of the hot gases in the reaction layer. Within this subsonic region behind the shock, the flow is expanded up to sonic conditions, $\mathcal{M}_2 = 1$, corresponding to the well-known Chapman-Jouguet regime for detonation waves. As a result, the detonation wave decouples from downstream influences, and its motion is self-sustained by the expansion of the products resulting from the exothermic transformation.

3.2.3 Linear interaction analysis

As illustrated in Fig. 3.2 and Table 3.1, deviations in the fuel mass fraction are often accompanied by perturbations in density and/or heat release. Depending on the particular conditions, i.e., type of fuel and average equivalence ratio of the unburnt mixture, the dimensionless slope H may reach values of order 10 or greater. It also occurs with the function W in hydrogen-air mixtures (or any other fuel much heavier than air not shown in the table). This finding suggests that δY_1 may not be a good reference scale for the upstream perturbation field given that linear (small) variations in the fuel mass fraction may be associated with non-linear (large) perturbations in ρ_1 and/or q_1. For any flow condition, to ensure that small changes δY_1 do not lead to large input perturbations into the system, the small parameter should be redefined in the form $\epsilon(k) = \varepsilon(k)\sqrt{W^2 + H^2}$, and $\epsilon(k) \ll 1$ is a requirement. Thus, even if W or H are large compared to unity, the perturbations in the fuel mass fraction will be sufficiently small for all flow perturbations to remain within the limits of linear theory. Similarly, larger fuel mass fraction perturbations will be permitted for $W \sim H \ll 1$.

When written in a reference frame moving with the detonation front, $x_l = u_1 t$, the upstream density and heat-release perturbations can be written as follows:

$$\bar{\rho}_1 = \frac{\delta\rho_1}{\langle\rho_1\rangle} = \epsilon(k)\frac{W}{\sqrt{W^2+H^2}}\mathrm{e}^{\mathrm{i}\,(k_x u_1 t + k_y y + k_z z)} \tag{3.13}$$

and

$$\bar{q}_1 = \frac{\delta q_1}{\langle q_1\rangle} = \epsilon(k)\frac{H}{\sqrt{W^2+H^2}}\mathrm{e}^{\mathrm{i}\,(k_x u_1 t + k_y y + k_z z)}, \tag{3.14}$$

where use is composed of Eqs. (3.1), (3.3) and (3.4), and the above definition of $\epsilon(k)$. The pre-exponential factors $W/\sqrt{W^2+H^2}$ and $H/\sqrt{W^2+H^2}$ represent the relative effects on density and heat-release fluctuations of a small change of the fuel mass fraction. A closer inspection of the RH jump relationships shows that positive values of $\delta\rho_1$ and δq_1 result in higher downstream pressures. In terms of fuel mass fraction perturbation δY_1, constructive effects are to be expected in lean heavy-fuel or rich light-fuel mixtures, while destructive contributions will occur in lean light-fuel or rich heavy-fuel mixtures.

Using the modulus of the wavenumber vector k and its product with the speed of sound in the burnt gas $a_2 k$ as characteristic spatial and temporal frequencies, the spatio-temporal variables can be written in non-dimensional form as $(\bar{x},\bar{y},\bar{z}) = k\boldsymbol{x}$ and $\tau = a_2 k t$, where $\boldsymbol{x}$ is measured in the burnt gas reference frame. However, it is always possible to simplify the formulation by rotating the reference frame around the direction of propagation of the detonation such that only two spatial coordinates remain in the problem: one in the axis of the detonation propagation, $\bar{x}$, and the other perpendicular to it at any arbitrary direction, $\bar{y}$.

The linear perturbations in the burnt gas are defined with functions of order unity (denoted with bar symbol) and scaled with the small parameter ϵ, namely

$$p(x,y,\tau) = \rho_2 a_2^2 \left[\gamma^{-1} + \epsilon\ \bar{p}(\bar{x},\bar{y},\tau)\right], \tag{3.15a}$$
$$\rho(x,y,\tau) = \rho_2 \left[1 + \epsilon\ \bar{\rho}(\bar{x},\bar{y},\tau)\right], \tag{3.15b}$$
$$u(x,y,\tau) = a_2 \left[\mathcal{M}_2(\mathcal{R}-1) + \epsilon\ \bar{u}(\bar{x},\bar{y},\tau)\right], \tag{3.15c}$$
$$v(x,y,\tau) = a_2 \epsilon\ \bar{v}(\bar{x},\bar{y},\tau), \tag{3.15d}$$

which are introduced in the Euler equations to give

$$\frac{\partial\bar{\rho}}{\partial\tau} = -\frac{\partial\bar{u}}{\partial\bar{x}} - \frac{\partial\bar{v}}{\partial\bar{y}}, \tag{3.16a}$$
$$\frac{\partial\bar{u}}{\partial\tau} = -\frac{\partial\bar{p}}{\partial\bar{x}}, \tag{3.16b}$$
$$\frac{\partial\bar{v}}{\partial\tau} = -\frac{\partial\bar{p}}{\partial\bar{y}}, \tag{3.16c}$$
$$\frac{\partial\bar{\rho}}{\partial\tau} = \frac{\partial\bar{p}}{\partial\tau}. \tag{3.16d}$$

The system of linear equations must be supplemented by the boundary conditions associated with isolated detonation. As the burnt-gas flow field reduces to linear gas dynamics within the domain contained between $\bar{x} = -\tau + c_t$ (first left-traveling acoustic

wave) and $\bar{x} = \mathcal{M}_2\tau + c_t$ (detonation front position) in the $\bar{x} - \tau$ plane. The arbitrary constant c_t, which is defined with the temporal reference frame, does not play any role in the long-time asymptotic analysis.

For the sake of simplicity, the isolated assumption is considered in this work, which translates into the omission of front-traveling waves reaching the detonation wave from behind. As a direct consequence, the detonation is only excited with the monochromatic perturbation of the upstream flow, thereby resulting in a single oscillation frequency $\omega = (k_x/k)(u_1/a_2) = \kappa_x\mathcal{R}\mathcal{M}_2$, where $\kappa_i = k_i/k$ for $i = \{x, y, z\}$ is the dimensionless wave number component of the upstream flow. Linearized RH relationships, which involve the perturbation of the detonation position with respect to its planar form $\xi_2 = k\,[x_{l,s}(t) - u_1 t]$,

$$\frac{\mathcal{R}-1}{\mathcal{R}}\frac{\mathrm{d}\xi_2}{\mathrm{d}\tau} = \frac{1-\Gamma}{2\mathcal{M}_2}\bar{p}_2 - \frac{\mathcal{M}_2\,(\mathcal{R}-2+\Delta)\,W - \mathcal{M}_2\,(1-\Delta)\,H}{2\sqrt{W^2+H^2}}\mathrm{e}^{-\mathrm{i}\omega\tau}\mathrm{e}^{\mathrm{i}\kappa_y\bar{y}}, \tag{3.17a}$$

$$\bar{u}_2 = \frac{1+\Gamma}{2\mathcal{M}_2}\bar{p}_2 - \frac{\mathcal{M}_2\,(\mathcal{R}-\Delta)\,W + \mathcal{M}_2\,(1-\Delta)\,H}{2\sqrt{W^2+H^2}}\mathrm{e}^{-\mathrm{i}\omega\tau}\mathrm{e}^{\mathrm{i}\kappa_y\bar{y}}, \tag{3.17b}$$

$$\bar{\rho}_2 = \frac{\Gamma}{\mathcal{M}_2^2}\bar{p}_2 + \frac{\Delta W - (1-\Delta)\,H}{\sqrt{W^2+H^2}}\mathrm{e}^{-\mathrm{i}\omega\tau}\mathrm{e}^{\mathrm{i}\kappa_y\bar{y}}, \tag{3.17c}$$

$$\bar{v}_2 = -\mathcal{M}_2\,(\mathcal{R}-1)\,\frac{\partial\xi_2}{\partial\bar{y}}, \tag{3.17d}$$

are employed to calculate the amplitudes accompanying the factor $\mathrm{e}^{-\mathrm{i}\omega\tau}\mathrm{e}^{\mathrm{i}\kappa_y\bar{y}}$ in the non-dimensional perturbations. The quantity

$$\Gamma = \frac{p_2 - p_1}{V_1 - V_2}\left.\frac{\mathrm{d}V}{\mathrm{d}p}\right|_2 = \frac{\gamma\mathcal{M}_1^2}{\mathcal{R}^2}\left(\frac{\partial\mathcal{P}}{\partial\mathcal{R}}\right)^{-1} \tag{3.18}$$

measures the slope of the Hugoniot curve relative to the Rayleigh-Mickelson line, and the term

$$\Delta = \frac{1 + Q\mathcal{R}\left(\dfrac{\gamma-1}{\gamma+1}\right)}{1+Q} < 1 \tag{3.19}$$

accounts for the variation of the post-detonation state due to the upstream changes in density and heat release. Notice that the linear perturbation variables admit the breakdown in terms of potential (acoustic) and entropic-rotational contributions [83, 249]. The former takes the form of traveling waves, while the latter remains steady in the reference frame moving with the burnt-gas particles in absence of diffusive effects. This property is exploited in the normal mode analysis performed in Appendix C, where

the transfer functions describing the amplitude of the burnt-gas perturbation modes as a function of the detonation properties are described.

3.3 Detonation-induced turbulence

This section is devoted to the interaction of a planar detonation wave with a 2D/3D isotropic 2D/3D field of fuel-mass-fraction fluctuation. In the previous section, it was shown that the pre-shock field can be characterized by the wave number vector $\boldsymbol{k} = (k_x, k_y) = k(\cos\theta, \sin\theta)$ in a reduced 2D geometry, i.e., a planar transverse wave with wavenumber $\boldsymbol{k}$ that intersects a planar detonation wave with an incidence angle θ. In two dimensions, isotropy translates into considering situations where k is uniformly distributed in the range $0 \leq \theta \leq \pi$. In three dimensions, it is assumed that k is uniformly distributed over the unit sphere. Linear theory admits the computation of the full spectrum by direct superposition of small perturbations, in which the amplitudes are an exclusive function of k with the different modes being uncorrelated.

3.3.1 Turbulent kinetic energy

An important feature that deserves particular attention is the turbulence kinetic energy (TKE) generated by the wrinkled detonation front. When scaled with the square of the sound speed in the burnt gas, it can be expressed as

$$\mathrm{TKE}_{2\mathrm{D}} = \frac{1}{2}\frac{\langle \delta v_i \delta v_i \rangle}{a_2^2} = \frac{1}{2}\langle \bar{u}^2 + \bar{v}^2 \rangle_{2\mathrm{D}} \int_0^\infty \epsilon(k)^2 k \, \mathrm{d}k = \frac{1}{2}\langle \bar{u}^2 + \bar{v}^2 \rangle_{2\mathrm{D}} \langle \delta Y_1^2 \rangle_{2\mathrm{D}} \quad (3.20)$$

with

$$\langle \bar{u}^2 + \bar{v}^2 \rangle_{2\mathrm{D}} = \frac{2}{\pi} \int_0^{\pi/2} \left(|\bar{u}|^2 + |\bar{v}|^2 \right) \mathrm{d}\theta, \quad (3.21)$$

provided $\langle \delta Y_1^2 \rangle_{2\mathrm{D}}$ is known from Eq. (3.2). Although 2D turbulence is not realistic, it serves as an interesting benchmark for complex code validations. Thanks to the isotropy condition of the perturbation field, the influence of the shape of the spectrum enters as an integral contribution that can be factored out. Equivalent three dimensional computations can be performed by defining

$$\langle \bar{u}^2 + \bar{v}^2 \rangle_{3\mathrm{D}} = \int_0^{\pi/2} \left(|\bar{u}|^2 + |\bar{v}|^2 \right) \sin\theta \, \mathrm{d}\theta, \quad (3.22)$$

where $\bar{u}$ and $\bar{v}$ are the streamwise and transverse velocity components, respectively. The normalization criterion applied is that $\langle \bar{u}^2 + \bar{v}^2 \rangle_{\mathrm{2D,3D}}$ must be equal to unity when the integrand function is spatially uniform and equal to unity.

In the far-field asymptotic regime, the kinetic energy can be conveniently computed by accounting for the separate contributions of the rotational and acoustic velocity fields $\langle \bar{u}^2 + \bar{v}^2 \rangle = \langle \bar{u}_r^2 + \bar{v}_r^2 \rangle + \langle \bar{u}_a^2 + \bar{v}_a^2 \rangle$, to give

$$\begin{aligned} \langle \bar{u}^2 + \bar{v}^2 \rangle_{\mathrm{2D}} &= \frac{2}{\pi} \int_0^{\pi/2} \left(\mathbb{U}_r^2 + \mathbb{V}_r^2 \right) \mathrm{d}\theta + \frac{2}{\pi} \int_0^{\theta_c} \left(\mathbb{U}_a^2 + \mathbb{V}_a^2 \right) \mathrm{d}\theta, \\ \langle \bar{u}^2 + \bar{v}^2 \rangle_{\mathrm{3D}} &= \int_0^{\pi/2} \left(\mathbb{U}_r^2 + \mathbb{V}_r^2 \right) \sin\theta \ \mathrm{d}\theta + \int_0^{\theta_c} \left(\mathbb{U}_a^2 + \mathbb{V}_a^2 \right) \sin\theta \ \mathrm{d}\theta, \end{aligned} \tag{3.23}$$

where the amplitudes $\mathbb{U}_r$, $\mathbb{V}_r$, $\mathbb{U}_a$, and $\mathbb{V}_a$, provided in Appendix C, are explicit functions of $\theta = \tan^{-1}(k_y/k_x)$ and the remaining governing parameters: γ, $\mathcal{M}_1$, Q, W, and H. To compute the rotational contribution one must separate the high-frequency and low-frequency amplitudes, as given in (C.29), which must be integrated over the two different domains $\int_0^{\theta_c}(\dots)\,\mathrm{d}\theta$ and $\int_{\theta_c}^{\pi/2}(\dots)\,\mathrm{d}\theta$, respectively.

Figure 3.3 shows the acoustic (a-b) and rotational (c-d) contributions to the total kinetic energy in both two-dimensional (a and c) and three-dimensional (b and d) isotropic configurations. The averages are plotted as a function of the overdrive parameter $\mathcal{M}_1/\mathcal{M}_{\mathrm{cj}} - 1$. The correlation between W and H has a strong impact on the generation of turbulent kinetic energy. For example, heat-release variations, either for $|H| \gg |W|$ or $H = -W$, produce higher levels of acoustic energy when the overdrive is small, a finding that can be anticipated with the normal mode analysis, as shown in Fig. C.2 in Appendix C. The unbounded growth of the acoustic perturbations in the CJ condition warns about the limits of validity of the linear thin-detonation model, which gains in reliability as the overdrive increases.

The cases selected for the calculations and the associated color code will be maintained in the following figures. In all the plots, the black curves correspond to the reference case where the upstream perturbation field is dominated by density changes, as in Huete et al. [229]. In this case, the average fuel mass fraction is close to the peak of heat release, which leads to a negligible contribution of heat-release variations with the fuel mass fraction. As an opposite limit, the green curves represent cases where heat-release variations dominate over density changes, which is applicable to mixtures of gases with similar density and located far-off the heat release peak. The other two distinguished cases refer to positive (orange) and negative (blue) correlations of density and heat release perturbations. The former applies to light fuel-air mixtures ($W_F < W_A$)

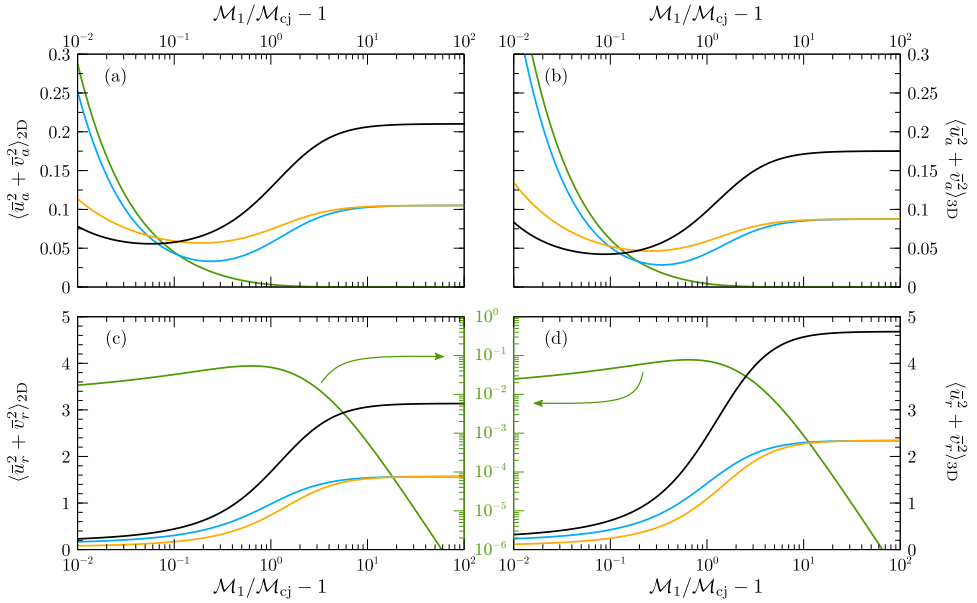

Figure 3.3: Acoustic (a-b) and rotational (c-d) contributions to the turbulent kinetic energy in 2D (a and c) and 3D (b and d) geometries. Computations are shown as a function of the overdrive parameter $\mathcal{M}_1/\mathcal{M}_{cj} - 1$ for $\gamma = 1.2$, $Q = 1$, and $|W| \gg |H|$ (——), $|H| \gg |W|$ (——), $W = H$ (——) and $W = -H$ (——).

in sufficiently rich conditions or heavy fuel-air mixtures ($W_F > W_A$) in sufficiently lean conditions. On the other hand, negative correlations apply to light fuel-air mixtures in sufficiently lean conditions or heavy fuel-air mixtures in sufficiently rich conditions. Four examples are given in Table 3.1 where the orange and blue background colors denote the mentioned positive and negative correlations, respectively.

Regarding the rotational contribution, the degree of overdrive does not modify the hierarchy of effects associated with the correlation between H and W for one single frequency, as displayed in Fig. C.3 in Appendix C. Notice that the case $|H| \gg |W|$ (green lines) uses its own log-log scale, which is shown between subplots (c) and (d), because it would have been impossible to distinguish it from the horizontal axis otherwise. With this consideration in mind, it is seen that the case with exclusively density perturbations yields the highest intensity of turbulence generation, and the effect of heat release is to cushion the kinetic energy deposited in the form of eddies behind the detonation wave. The results also show that the rotational contribution dominates the generation of turbulent kinetic energy over the acoustic field by one order of magnitude, except for weakly overdriven detonations, when both become the same order. Some features

in Fig. 3.3 are similar for the acoustic and rotational contributions. For example, the qualitative picture of two-dimensional and three-dimensional cases is very similar. In addition, density disturbances dominate for finite to high degrees of overdrives. Thus, the turbulent kinetic energy generated for $|H| \gg |W|$ is much smaller and tends to zero with the overdrive, while the cases $H = -W$ and $H = W$ render similar values for strongly overdriven detonations, an asymptotic value that corresponds to the half of that obtained for $|W| \gg |H|$. The latter is easily deduced from Eq. (3.13) since the relative amplitude of the density field squared, $W^2/(W^2+H^2)$, is unity for $|W| \gg |H|$ and $1/2$ for $H = \pm W$, while the relative amplitude of the heat release field squared, $H^2/(W^2+H^2)$, vanishes for $|W| \gg |H|$.

The breakdown of longitudinal and transverse contributions of the kinetic energy can be computed separately as

$$\begin{aligned}
\langle \bar{u}^2 \rangle_{2\mathrm{D}} &= \langle \bar{u}_r^2 \rangle_{2\mathrm{D}} + \langle \bar{u}_a^2 \rangle_{2\mathrm{D}} = \frac{2}{\pi} \int_0^{\pi/2} \mathbb{U}_r^2 \, \mathrm{d}\theta + \frac{2}{\pi} \int_0^{\theta_c} \mathbb{U}_a^2 \, \mathrm{d}\theta, \\
\langle \bar{u}^2 \rangle_{3\mathrm{D}} &= \langle \bar{u}_r^2 \rangle_{3\mathrm{D}} + \langle \bar{u}_a^2 \rangle_{3\mathrm{D}} = \int_0^{\pi/2} \mathbb{U}_r^2 \sin\theta \, \mathrm{d}\theta + \int_0^{\theta_c} \mathbb{U}_a^2 \sin\theta \, \mathrm{d}\theta,
\end{aligned} \tag{3.24}$$

and

$$\begin{aligned}
\langle \bar{v}^2 \rangle_{2\mathrm{D}} &= \langle \bar{v}_r^2 \rangle_{2\mathrm{D}} + \langle \bar{v}_a^2 \rangle_{2\mathrm{D}} = \frac{2}{\pi} \int_0^{\pi/2} \mathbb{V}_r^2 \, \mathrm{d}\theta + \frac{2}{\pi} \int_0^{\theta_c} \mathbb{V}_a^2 \, \mathrm{d}\theta, \\
\langle \bar{v}^2 \rangle_{3\mathrm{D}} &= \langle \bar{v}_r^2 \rangle_{3\mathrm{D}} + \langle \bar{v}_a^2 \rangle_{3\mathrm{D}} = \int_0^{\pi/2} \mathbb{V}_r^2 \sin\theta \, \mathrm{d}\theta + \int_0^{\theta_c} \mathbb{V}_a^2 \sin\theta \, \mathrm{d}\theta,
\end{aligned} \tag{3.25}$$

respectively, where $\langle \bar{u}^2 + \bar{v}^2 \rangle_{2\mathrm{D},3\mathrm{D}} = \langle \bar{u}^2 \rangle_{2\mathrm{D},3\mathrm{D}} + \langle \bar{v}^2 \rangle_{2\mathrm{D},3\mathrm{D}}$ for both rotational and acoustic contributions, independently.

Figure 3.4 shows the average streamwise (a-b) and transverse (c-d) contributions to the total kinetic energy in both two-dimensional (a and c) and three-dimensional (b and d) isotropic flows. The averages are plotted as a function of the overdrive parameter $\mathcal{M}_1/\mathcal{M}_{\mathrm{cj}} - 1$. In consonance with Fig. C.3, the lateral component is higher than the longitudinal part. As expected, the strong-shock limit is governed by the density-induced turbulence in both longitudinal and transverse contributions. In the case $|H| \gg |W|$, shown on its own log-log scale, the turbulence generation is very weak over most of the overdrive domain. For weakly overdriven detonations, however, the effect of heat-release variations has a non-negligible impact in the generation of turbulence, which, as observed in Fig. 3.3, is mainly derived from the acoustic contribution. In agreement with the previous plot, for three-dimensional random isotropic fields, the generation of

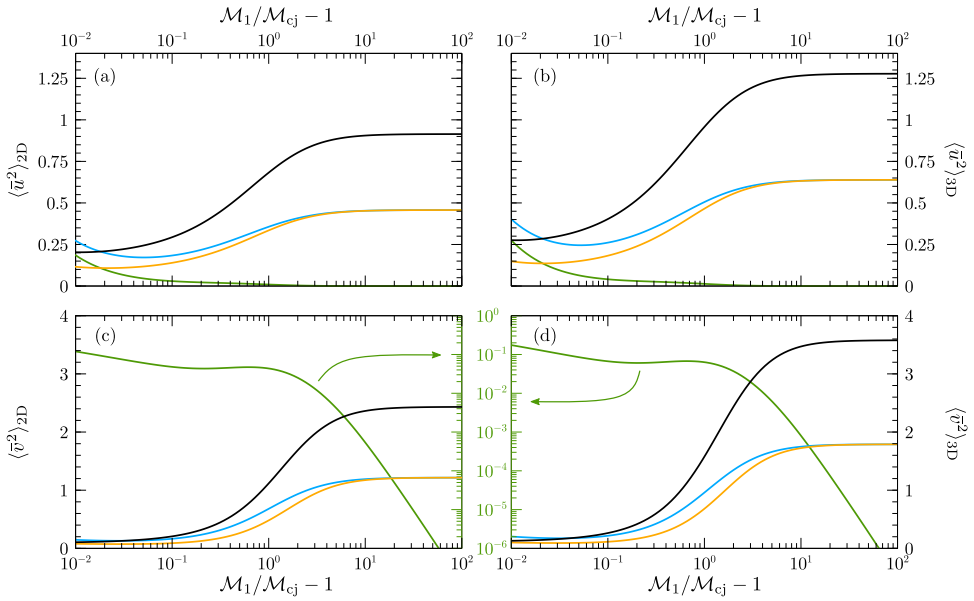

Figure 3.4: Longitudinal (a-b) and transverse (c-d) contributions to the turbulent kinetic energy in 2D (a and c) and 3D (b and d) geometries. Computations are shown as a function of the overdrive parameter $\mathcal{M}_1/\mathcal{M}_{\rm cj}-1$ for $\gamma = 1.2$, $Q = 1$, and $|W| \gg |H|$ (——), $|H| \gg |W|$ (——), $W = H$ (——) and $W = -H$ (——).

turbulence is more intense for both lateral and streamwise components, and negative correlations render higher levels of turbulence. Thus, when the fuel mass fraction is outside the heat-release peak, turbulence generation is expected to be enhanced from the hydrodynamical point of view in light fuel-air mixtures in sufficiently lean conditions or heavy fuel-air mixtures in sufficiently rich conditions.

3.3.2 Enstrophy and averaged pressure and density fields

The average rotational motion behind the detonation can be measured by the so-called enstrophy that takes the form

$$\langle\Omega^2\kappa_y^2\rangle_{2\mathrm{D}} = \frac{2}{\pi}\int_0^{\pi/2} \mathbb{O}^2\sin^2\theta\ \mathrm{d}\theta, \qquad \langle\Omega^2\kappa_y^2\rangle_{3\mathrm{D}} = \int_0^{\pi/2} \mathbb{O}^2\sin^3\theta\ \mathrm{d}\theta, \tag{3.26}$$

where $\mathbb{O}$ must be evaluated from Eq. (C.25) in Appendix C and $\kappa_y = \sin\theta$. By similar arguments, the averaged values of the squared density perturbations are

$$\begin{aligned}
\langle\bar{\rho}^2\rangle_{2\mathrm{D}} &= \langle\bar{\rho}_e^2\rangle_{2\mathrm{D}} + \langle\bar{\rho}_a^2\rangle_{2\mathrm{D}} = \frac{2}{\pi}\int_0^{\pi/2}\mathbb{D}_e^2\ \mathrm{d}\theta + \frac{2}{\pi}\int_0^{\theta_c}\mathbb{D}_a^2\ \mathrm{d}\theta,\\
\langle\bar{\rho}^2\rangle_{3\mathrm{D}} &= \langle\bar{\rho}_e^2\rangle_{3\mathrm{D}} + \langle\bar{\rho}_a^2\rangle_{3\mathrm{D}} = \int_0^{\pi/2}\mathbb{D}_e^2\sin\theta\ \mathrm{d}\theta + \int_0^{\theta_c}\mathbb{D}_a^2\sin\theta\ \mathrm{d}\theta,
\end{aligned} \tag{3.27}$$

where the far-field acoustic contribution satisfies $\mathbb{D}_a^2 = \mathbb{U}_a^2 + \mathbb{V}_a^2 = \mathbb{P}_a^2$, and therefore

$$\begin{aligned}
\langle\bar{\rho}_a^2\rangle_{2\mathrm{D}} &= \langle\bar{u}_a^2\rangle_{2\mathrm{D}} + \langle\bar{v}_a^2\rangle_{2\mathrm{D}} = \langle\bar{p}^2\rangle_{2\mathrm{D}} = \frac{2}{\pi}\int_0^{\theta_c}\mathbb{P}_h^2\ \mathrm{d}\theta,\\
\langle\bar{\rho}_a^2\rangle_{3\mathrm{D}} &= \langle\bar{u}_a^2\rangle_{3\mathrm{D}} + \langle\bar{v}_a^2\rangle_{3\mathrm{D}} = \langle\bar{p}^2\rangle_{3\mathrm{D}} = \int_0^{\theta_c}\mathbb{P}_h^2\sin\theta\ \mathrm{d}\theta.
\end{aligned} \tag{3.28}$$

The averaged vorticity generated by the detonation front is computed in Fig. 3.5 (a-b) in both two-dimensional (a) and three-dimensional (c) configurations as a function of the overdrive parameter $\mathcal{M}_1/\mathcal{M}_{\mathrm{cj}} - 1$. The amplification of the entropic density fluctuations is shown in Fig. 3.5 (c-d). As noted for the turbulent kinetic energy, the highest level of vorticity generation is given when heat release perturbations upstream are negligible, i.e., when the mixture is in the heat-release peak. This case, which is in black lines, is similar to that found in Huete et al. [229]. The opposite limit, which occurs for same-density gases in sufficiently rich or lean conditions, shows a peak in the enstrophy generation at finite degrees of overdrive $\mathcal{M}_1/\mathcal{M}_{\mathrm{cj}} - 1 \sim 1$ (see the green curve with its own log-log scale). Expectedly, when heat release variations are comparable to

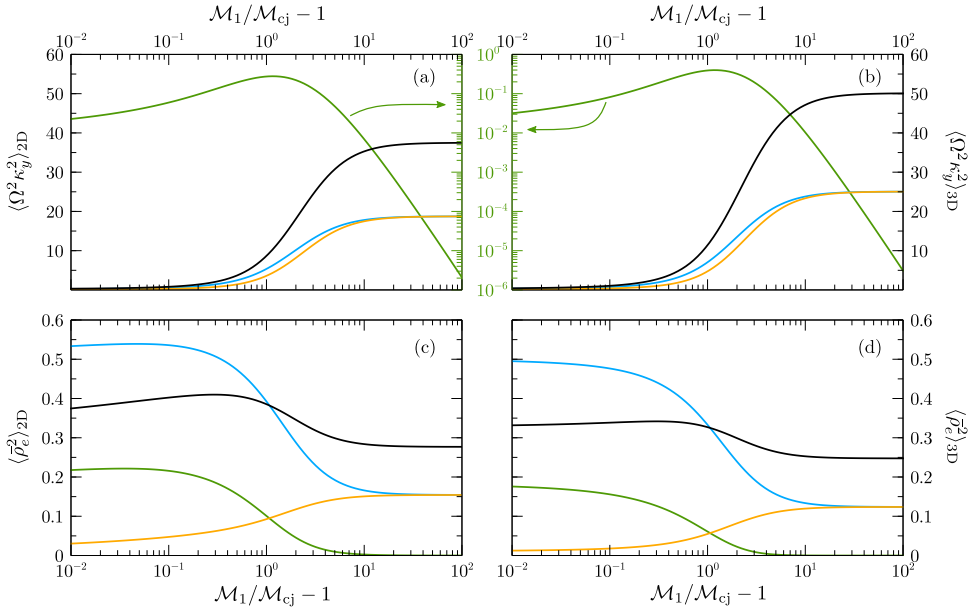

Figure 3.5: Averaged square vorticity (a-b) and square entropic density (c-d) in 2D (a and c) and 3D (b and d) geometries. Computations are shown as a function of the overdrive parameter $\mathcal{M}_1/\mathcal{M}_{cj} - 1$ for $\gamma = 1.2$, $Q = 1$, and $|W| \gg |H|$ (——), $|H| \gg |W|$ (——), $W = H$ (——) and $W = -H$ (——).

density perturbations, negative correlations provide higher amplitudes for the vorticity perturbations downstream. It resembles the findings in Sinha [65], where the baroclinic torque due to a mean pressure gradient has an appreciable effect for non-zero entropic fluctuations in the upstream flow. As shown in Fig. 3.3, the highly overdriven limit for $|W| \gg |H|$ doubles the value for $|W| = |H|$.

Regarding the change in the entropic heterogeneities due to the detonation passage (in terms of the dimensionless variables measured with the bulk density), it is observed that overdrive modifies the hierarchy of the dominant contributions in the generation of entropy. For weak overdrives, $\mathcal{M}_1/\mathcal{M}_{cj} - 1 \ll 1$, negative correlations render the highest levels of entropy, while positive correlations yield the lowest. For $\mathcal{M}_1/\mathcal{M}_{cj} \gg 1$, these contributions merge to the same asymptotic value, yielding half of that for $|W| \gg |H|$. The highest and lowest levels of entropy are obtained for $|W| \gg |H|$ and $|H| \gg |W|$, respectively, in the highly overdriven limit.

The results shown in Figs. 3.3 to 3.5 are qualitatively similar to those obtained previously for the interaction of detonations with random vorticity perturbations [223,

224, 228, 232]. However, a detailed comparison requires taking into account the diverse criteria used for normalization in different investigations. For isotropic vorticity fields, the upstream perturbed velocity field was scaled in Jackson et al. [228] and Huete et al. [232] with the speed of sound downstream from the detonation, which always increases with the detonation intensity. If it had been scaled with the upstream sound speed, the results would have shown how the downstream perturbations decay with the overdrive to become negligibly small for strongly overdriven detonations. In strong-shock conditions, upstream perturbations in density and heat-release will dominate the turbulence generation across the detonation wave. In this particular case, the turbulence amplification factors measure how much turbulence is generated for any convective perturbation of the fuel mass fraction of order $\epsilon/\sqrt{W^2+H^2}$. When W and/or H are large, the allowed fuel mass fraction perturbations must be much smaller than the corresponding density and/or heat-release perturbations. This condition relaxes when W and H are of order unity or less. According to Table 3.1, the value of W is of order unity for light hydrocarbons and reasonably small for acetylene, while the value of H is very sensitive to mixture conditions, being of order unity or less only in the vicinity of the heat release peak.

3.3.3 Turbulence scales characterization

Previous results refer to far-field mean values, which are independent of the shape of energy spectrum, on condition that it is isotropic. The analysis is valid at a distance sufficiently far from the detonation wave, where the vanishing contribution of the acoustic energy can be neglected. Close to the detonation wave, however, the decaying pressure contribution should be taken into account as described in Eq. (C.18) in the Appendix C for monochromatic perturbations.

Near-field contributions are studied in detail in [65, 67, 70] for inert-shocks in canonical turbulent flows. To illustrate this effect, the emphasis is placed here on the near-field acoustic energy, which can be expressed as the sum of the non-vanishing and the vanishing contributions, namely $\langle\bar{p}^2\rangle^{\mathrm{total}}(x_s)=\langle\bar{p}^2\rangle^{\mathrm{non-van}}+\langle\bar{p}^2\rangle^{\mathrm{van}}(x_s)$, where $x_s=u_2t-x$ measures the distance from the detonation pointing backwards. The former, which is associated with high-frequency perturbations, is explicitly given in Eq. (3.28), while the decaying contribution is given by low-frequency disturbances in the following form:

$$\langle\bar{p}^2\rangle^{\mathrm{van}}(x_s)=\frac{\int_0^\infty\left[\int_{\theta_c}^{\pi/2}\left(\mathbb{P}_{l1}^2+\mathbb{P}_{l2}^2\right)\mathrm{e}^{-2\sigma(\theta)\Lambda\ k_o x_s}\sin\theta\mathrm{d}\theta\right]\epsilon(\Lambda)^2\Lambda^2\ \mathrm{d}\Lambda}{\int_0^\infty\epsilon(\Lambda)^2\Lambda^2\ \mathrm{d}\Lambda} \tag{3.29}$$

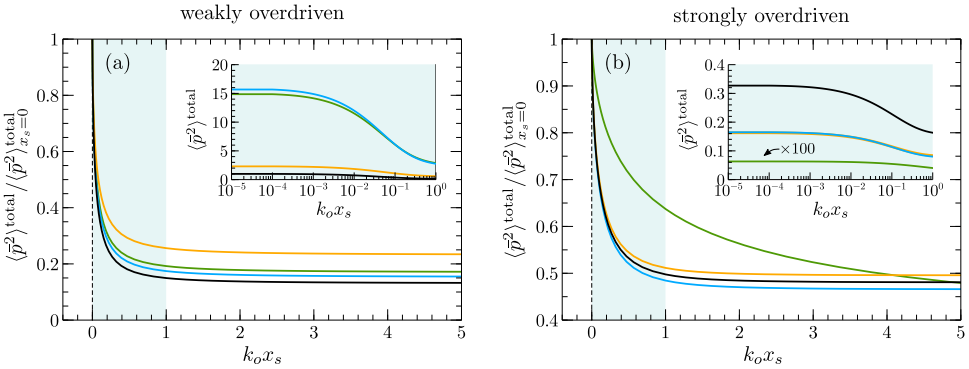

Figure 3.6: Three-dimensional total acoustic energy $\langle \bar{p}^2 \rangle^{\text{total}} / \langle \bar{p}^2 \rangle^{\text{total}}_{x_s=0}$ as a function of the scaled distance $k_o x_s$. Computations are given for $\gamma = 1.2$, $Q = 1$, weakly overdriven detonations $\mathcal{M}_1 = 1.001\mathcal{M}_{\text{cj}}$ (a), and strongly overdriven detonations $\mathcal{M}_1 = 5\mathcal{M}_{\text{cj}}$ (b). The distinguished cases include $|W| \gg |H|$ (——), $|H| \gg |W|$ (——), $W = H$ (——) and $W = -H$ (——). The function $\langle \bar{p}^2 \rangle^{\text{total}}$ is shown in the insets for the same conditions.

for a three dimensional isotropic spectrum $\epsilon(\Lambda)$ that is written in terms of the reduced wavenumber amplitude $\Lambda = k/k_o$. The function $\sigma(\theta)$, given in Eq. (C.19), defines the spatial decay rate along the dimensionless spatial coordinate $k_o x_s$. The decay rate depends on the form of the energy spectrum, which ultimately shapes the contribution of the different mode angles θ.

The reduced acoustic energy $\langle \bar{p}^2 \rangle^{\text{total}} / \langle \bar{p}^2 \rangle^{\text{total}}_{x_s=0}$ is shown in Fig. 3.6 as a function of the scaled distance $k_o x_s$. The functions are computed for $|W| \gg |H|$ (black lines), $|H| \gg |W|$ (green lines), $W = H$ (orange lines), and $W = -H$ (blue lines). Weakly overdriven detonations are displayed in panel (a) for $\mathcal{M}_1 = 1.001\mathcal{M}_{\text{cj}}$ and strongly overdriven detonations are shown in panel (b) for $\mathcal{M}_1 = 5\mathcal{M}_{\text{cj}}$. Except for the case $|H| \gg |W|$ in Fig. 3.6(b), which has been amplified by a factor of 100 in the inset, the decay rate is not significantly affected by the type of perturbation upstream.

It takes a distance $x_s \sim k_o^{-1}$ for the acoustic energy to reach the asymptotic plateau corresponding to the far-field contribution. For weakly overdriven detonations, negative correlations exhibit the highest value of acoustic energy in the near-field, in contrast to the far-field solution where perturbations of the type $|H| \gg |W|$ render slightly higher values. On the other hand, upstream flows dominated by density perturbations $|W| \gg |H|$ produce the highest acoustic energy in the whole spatial domain. In general, the vanishing contribution $\langle \bar{p}^2 \rangle^{\text{van}}$ has a relatively low influence on the total pressure field for $k_o x_s \gtrsim 1$. Notice that near-field profiles are computed for purely inviscid flows. Depending on the particular conditions, there may exist another contribution coming

from viscous dissipation that may not be neglected, as noted in Quadros et al. [67] and Sethuraman et al. [70].

To gain further insight into the properties of the turbulent flow that emerges far downstream the detonation wave, the one-dimensional power spectra of the different variables can be evaluated through the integral functions

$$\Phi_p(k_x) = N k_x^{-5/3} \int_0^{\pi/2} \mathbb{P}^2(\theta) \frac{\sin^3\theta}{\cos^5\theta \left(k_x^{-2} + 1 + \tan^2\theta\right)^{17/6}} \, \mathrm{d}\theta, \tag{3.30}$$

$$\Phi_u(k_x) = N k_x^{-5/3} \int_0^{\pi/2} \mathbb{U}^2(\theta) \frac{\sin^3\theta}{\cos^5\theta \left(k_x^{-2} + 1 + \tan^2\theta\right)^{17/6}} \, \mathrm{d}\theta, \tag{3.31}$$

$$\Phi_v(k_x) = N k_x^{-5/3} \int_0^{\pi/2} \mathbb{V}^2(\theta) \frac{\sin^3\theta}{\cos^5\theta \left(k_x^{-2} + 1 + \tan^2\theta\right)^{17/6}} \, \mathrm{d}\theta, \tag{3.32}$$

$$\Phi_\rho(k_x) = N k_x^{-5/3} \int_0^{\pi/2} \mathbb{D}^2(\theta) \frac{\sin^3\theta}{\cos^5\theta \left(k_x^{-2} + 1 + \tan^2\theta\right)^{17/6}} \, \mathrm{d}\theta, \tag{3.33}$$

provided that the three-dimensional von Kármán model is applicable, as in Ribner [82] and Jackson et al. [228], which translates into considering turbulence spectra of the form $\epsilon(k_x, k_y)^2 \sim k_y^2/(1 + k_x^2 + k_y^2)^{17/6}$. The normalization parameter is chosen to satisfy

$$N^{-1} = \int_{-\infty}^{\infty} \int_0^{\infty} \frac{k_y^2}{\left(1 + k_x^2 + k_y^2\right)^{17/6}} \, k_y \, \mathrm{d}k_y \mathrm{d}k_x. \tag{3.34}$$

Previous investigations on the interaction of turbulence with adiabatic shocks have reported that large-scale turbulence is amplified to a greater extent than small-scale motions [250]. A similar behavior is observed with detonations when they travel in isotropic vorticity flows [228] or isotropic entropic-density flows, as the example considered here for $|W| \gg |H|$. This phenomenon is readily observed in the black curves plotted in Fig. 3.7, where the power spectra Φ_p, Φ_u, Φ_v, and Φ_ρ are represented as a function of the longitudinal wavenumber k_x for $\gamma = 1.2$, $\mathcal{M}_1 = 1.2\mathcal{M}_{\mathrm{cj}}$, $Q = 1$, and for $|W| \gg |H|$ (black lines), $|H| \gg |W|$ (green lines), $W = H$ (orange lines) and $W = -H$ (blue lines). In the presence of upstream density perturbations W with values of H that are either negligible or of the same order, the curves exhibit a similar pattern, and the case $|W| \gg |H|$ results in the highest values along with the negatively correlated cases $W = -H$. As a result of the destructive interference, positive correlations yield lower values in most of the domains for each spectrum. The case $|H| \gg |W|$ results in the lowest intensity for the two velocity spectra in all the domains

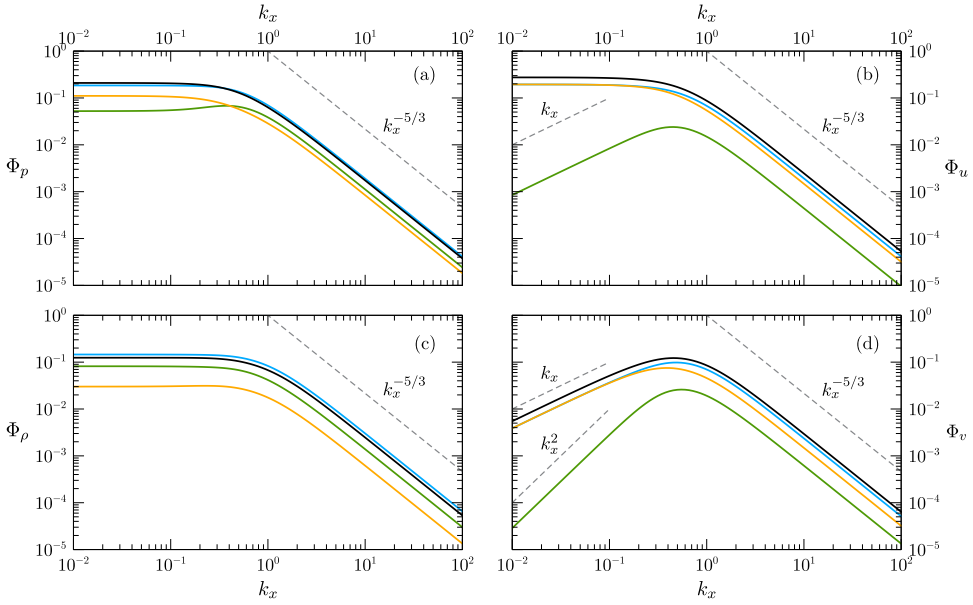

Figure 3.7: One-dimensional power spectra of the pressure (a), density (c), and longitudinal and transverse velocity components (b and d, respectively). Computations are shown as a function of the wavenumber k_x for $\gamma = 1.2$, $\mathcal{M}_1 = 1.2\mathcal{M}_{\mathrm{cj}}$, $Q = 1$, and $|W| \gg |H|$ (——), $|H| \gg |W|$ (——), $W = H$ (——) and $W = -H$ (——).

and for the pressure spectrum for small wave numbers only. Regarding this large-scale limit, it is noticeable that curves of Φ_u approach a plateau as k_x decreases except for the case $|H| \gg |W|$, where the spectrum decreases as k_x^{-1}. Curves for Φ_v decrease as k_x is reduced in all cases; however, the isochoric case shows a higher slope k_x^{-2}. Regarding Φ_p and Φ_ρ, they reach plateaus in the large-scale limit for any combination of W and H. With respect to the small-scale regime, all contributions obey the von Kármán decay law $k_x^{-5/3}$. Although these conclusions apply for $\mathcal{M}_1 = 1.2\mathcal{M}_{\mathrm{cj}}$, they can be extrapolated to higher overdrives. On the other hand, the weakly overdriven limit should be discussed separately, as the acoustic part may change the ranking of the most important contributions.

Aside from the fact that viscosity and molecular diffusion are not accounted for in the model—in which case the spectra would become time-dependent functions after the passage of the detonation [65, 73]—, the small-scale regime must be taken with caution as the thin-detonation hypothesis may not be fulfilled. Therefore, the properties of the turbulent flow behind the detonation front predicted by the linear interaction theory should be further extended to include the effects of finite reaction lengths [223, 224] and

non-linear contributions [63, 214, 237, 248]. The latter is unavoidable if multi-phase environments are under consideration [219, 220]. However, there are some aspects predicted by the model that deserve particular attention. When a detonation wave or a reactive shock is considered, the possibility of having different heat releases across the detonation wave due to non-perfect mixing should not be neglected. This effect plays a leading role in the turbulence generation process of acoustic type in the CJ condition. As a result, the turbulent flow downstream cannot be assumed to be isobaric, as reasonably done for inert shocks. For detonations, the dilatational part of the velocity gradient tensor cannot be neglected when the correlations between the corresponding invariants are employed to characterize the topology of the turbulent flow.

3.4 Corrections to Rankine-Hugoniot equations and propagation speed

The analysis presented above demonstrates how a non-uniform fresh mixture that exhibits weak fuel mass fraction deviations perturbs the detonation front surface, thereby creating additional disturbances in the burnt gas. The deposition of rotational/acoustic velocity perturbations in the downstream flow along with the amplification of the entropic fluctuations comes with a price in the overall RH relations. In particular, changes are expected in the jump conditions given the averaged downstream magnitudes with respect to the case of uniform mixtures with the same averaged upstream properties [234]. As a direct consequence, the averaged propagation speed of the detonation wave will also be affected, as previously noted for inert shocks [235, 236].

The goal of this section is to predict these changes and to provide analytical expressions, which are similar to those reported in Velikovich et al. [236] in terms of the parameters characterizing the detonation front. Then, the non-uniformity parameter

$$\bar{\epsilon} = \sqrt{1 - \frac{\langle Y_1 \rangle^2}{\langle Y_1^2 \rangle}} \tag{3.35}$$

is introduced to characterize the average fuel mass fraction fluctuations. Although it may vary from 0 to 1, the upper limit corresponding to infinite density gradients as those present in multi-phase flow, the use of the linear model previously presented forces it to be much smaller than unity and therefore equal to $\sqrt{\langle \delta Y_1^2 \rangle}$ in Eq. (3.2).

3.4.1 Averaged turbulent Rankine-Hugoniot jump equations

The changes in the RH relations are given by second-order corrections in the form

$$\frac{\langle \rho_2 \rangle}{\langle \rho_1 \rangle} = \mathcal{R}\left(1 + \bar{\epsilon}^2 \delta\mathcal{R}\right), \quad \frac{\langle p_2 \rangle}{p_1} = \mathcal{P}\left(1 + \bar{\epsilon}^2 \delta\mathcal{P}\right), \quad \frac{\langle u_2 \rangle}{u_1} = \frac{1}{\mathcal{R}}\left(1 + \bar{\epsilon}^2 \delta\mathcal{U}\right), \tag{3.36}$$

provided that the flow perturbations can be written as the breakdown of averaged and local deviation contributions, e.g., $\rho_2 = \langle \rho_2 \rangle \left(1 + \bar{\epsilon}\bar{\rho}\right)$ for the burnt-gas density field. To illustrate this, Fig. 3.8 (left) sketches the effect of the second-order corrections to the post-detonation RH values. Hollow circles represent the initial conditions, which may differ if second-order average values are non-zero. The blue and orange filled circles indicate the one-dimensional and turbulent post-detonation conditions, respectively. The vector $(\delta\mathcal{V}, \delta\mathcal{P})$, with $\delta\mathcal{V} = -\delta\mathcal{R}$ standing for the correction to the specific volume, is defined to characterize the relative deviations of the post-detonation RH state on the $(V/V_1, p/p_1)$-plane. The right panel shows the vector $(\delta\mathcal{V}, \delta\mathcal{P})$ as computed from the theory presented below for the same conditions given in Fig. 3.9, namely, $\gamma = 1.2$, $\mathcal{M}_1 = 1.2\mathcal{M}_{\text{cj}}$ and $Q = 1$. In this case, both pressure and density corrections are negative in the whole domain, yet the values differ significantly depending on the particular values of W and H. Note also that in agreement with the results of Sec. 3.3, perturbations weaken for $|H| \gg W$ and intensify for $|H| \ll W$.

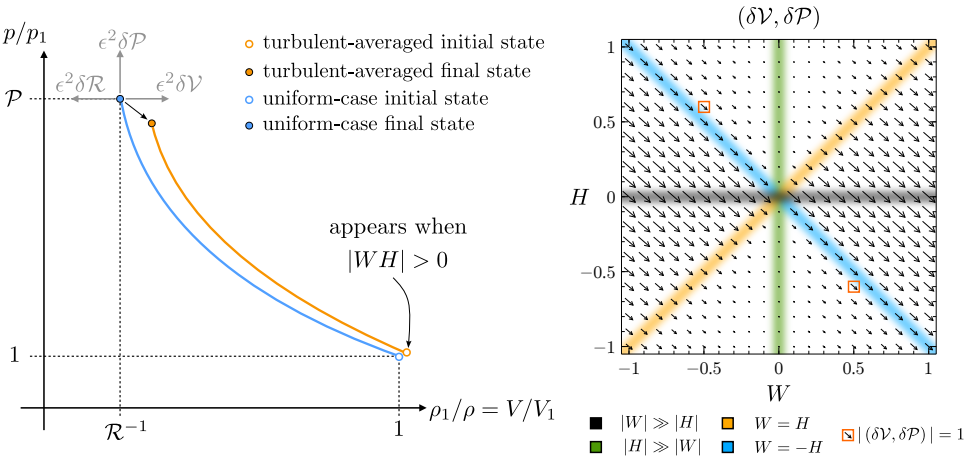

Figure 3.8: Left: Sketch for the Rankine-Hugoniot curves. In blue the one-dimensional curve and in orange the second-order-averaged curve. Right: Computations for $\gamma = 1.2$, $\mathcal{M}_1 = 1.2\mathcal{M}_{\text{cj}}$, $Q = 1$, $H = [-1 : 1]$ and $W = [-1 : 1]$.

Corrections to the RH jump conditions due to weak turbulence are derived from the lowest non-vanishing order, i.e., the non-linear second-order terms describing the interaction between the different perturbation modes and their self-interactions. The natures of rotational and entropic modes are similar as they are both carried along with the fluid. Thus, they correlate and provide rotational-entropic and rotational-rotational second-order corrections. By contrast, acoustic waves are uncorrelated with the entropic and rotational perturbations. Consequently, second-order corrections can be decomposed into entropic-rotational and acoustic-acoustic terms separately.

The entropic-rotational correlations enter only as second-order corrections as the first-order of the random-phase oscillating terms vanishes. Conversely, acoustic perturbations play a two-fold role in the global contribution. The first role, which is akin to entropic-rotational modes, is given by second-order corrections to the mass, momentum, and energy fluxes across the detonation front. The second role stems from the fact that acoustic waves shift the average values of the flow variables in the second-order of the sound amplitude. Further details of the analytical derivation of the distinguished contributions can be withdrawn from Velikovich et al. [236] and references therein, particularly the supplemental material, as well as in Refs. [251–253].

As a result of the second-order corrections to the mass, momentum, and energy fluxes across the detonation wave, the downstream pressure, density, and streamwise velocity suffer the corresponding corrections $\delta\mathcal{P}_\mathrm{f}$, $\delta\mathcal{R}_\mathrm{f}$, and $\delta\mathcal{U}_\mathrm{f}$, where the subscript f is used to denote changes due to flux corrections. These corrections can be obtained from the averaged turbulent conservation equations, namely

$$\langle \rho_1 u_1 \rangle = \langle \rho_2 u_2 \rangle, \tag{3.37a}$$

$$\langle p_1 + \rho_1 u_1^2 \rangle = \langle p_2 + \rho_2 u_2^2 \rangle, \tag{3.37b}$$

$$\Big\langle \frac{\gamma}{\gamma-1} p_1 u_1 + \frac{1}{2}\rho_1 u_1^3 + \rho_1 u_1 q_1 \Big\rangle = \Big\langle \frac{\gamma}{\gamma-1} p_2 u_2 + \frac{1}{2}\rho_2 u_2 \left(u_2^2 + v_2^2\right) \Big\rangle, \tag{3.37c}$$

which provide, with use made of Eq. (3.36) and knowing that first-order entropic and rotational corrections give null average contributions, the following second-order relationships:

$$\delta\mathcal{R}_\mathrm{f} + \delta\mathcal{U}_\mathrm{f} + \mathcal{M}_2^{-1}\langle l_\mathrm{f} \rangle = 0, \tag{3.38a}$$

$$\delta\mathcal{P}_\mathrm{f} + \gamma\mathcal{M}_2^2\left(\delta\mathcal{R}_\mathrm{f} + 2\delta\mathcal{U}_\mathrm{f}\right) + \gamma\langle m_\mathrm{f} \rangle = 0, \tag{3.38b}$$

$$\mathcal{M}_2^2\delta\mathcal{R}_\mathrm{f} + \left(3\mathcal{M}_2^2 + \frac{2}{\gamma-1}\right)\delta\mathcal{U}_\mathrm{f} + \frac{2}{\gamma-1}\delta\mathcal{P}_\mathrm{f} + \frac{2}{(\gamma-1)\mathcal{M}_2}\langle n_\mathrm{f} \rangle = q_\mathrm{wh}, \tag{3.38c}$$

where the factor

$$q_{\mathrm{wh}} = \frac{4Q\mathcal{M}_2^2\mathcal{R}^2}{(\gamma^2-1)\mathcal{M}_1^2}\langle\bar{\rho}_1\bar{q}_1\rangle = \frac{4Q\mathcal{R}}{(\gamma^2-1)\mathcal{P}}\frac{WH}{W^2+H^2} \tag{3.39}$$

appears due to the existence of two non-vanishing second-order sources of perturbations upstream. The factor q_{wh} vanishes for flows with uniform density or constant heat-release given that first-order averages of entropic disturbances do not provide net contributions. The terms $\langle l_{\mathrm{f}}\rangle$, $\langle m_{\mathrm{f}}\rangle$, and $\langle n_{\mathrm{f}}\rangle$ represent the dimensionless second-order turbulent corrections to the mass, streamwise momentum, and energy fluxes, respectively. As mentioned above, the terms split into entropic-rotational (subscript er) and acoustic-acoustic (subscript aa) contributions to yield the following:

$$\langle l_{\mathrm{f}}\rangle = \langle l_{er}\rangle + \langle l_{aa}\rangle = \langle\bar{\rho}_e\bar{u}_r\rangle - \frac{\gamma+1}{4}\mathcal{M}_2\langle\bar{p}^2\rangle, \tag{3.40a}$$

$$\langle m_{\mathrm{f}}\rangle = \langle m_{er}\rangle + \langle m_{aa}\rangle = 2\mathcal{M}_2\langle\bar{\rho}_e\bar{u}_r\rangle + \langle\bar{u}_r^2\rangle - \frac{(\gamma-1)\mathcal{M}_2^2+3-\gamma}{4}\langle\bar{p}^2\rangle + \langle\bar{u}_a^2\rangle, \tag{3.40b}$$

$$\begin{aligned}\langle n_{\mathrm{f}}\rangle = \langle n_{er}\rangle + \langle n_{aa}\rangle = {}& \frac{\mathcal{M}_2(\gamma-1)}{2}\left[3\langle\bar{u}_r^2\rangle + \langle\bar{v}_r^2\rangle + 3\mathcal{M}_2\langle\bar{\rho}_e\bar{u}_r\rangle\right] \\ & - \frac{(\gamma+1)\mathcal{M}_2}{8}\left[(\gamma-1)\mathcal{M}_2^2 + 2(2-\gamma)\right]\langle\bar{p}^2\rangle + (\gamma-1)\mathcal{M}_2\langle\bar{u}_a^2\rangle \\ & - (\gamma-1)\langle\bar{p}\bar{u}_a\rangle,\end{aligned} \tag{3.40c}$$

where $\langle\bar{u}_r^2\rangle$, $\langle\bar{u}_a^2\rangle$, $\langle\bar{v}_r^2\rangle$, and $\langle\bar{p}^2\rangle$ have been previously defined in Eqs. (3.24), (3.25) and (3.28). The averages $\langle\bar{\rho}_e\bar{u}_r\rangle$ and $\langle\bar{p}\bar{u}_a\rangle = \langle\bar{\rho}_a\bar{u}_a\rangle$ are second-order contributions that have not been previously introduced. As noted in (3.24), (3.25) and (3.28), these parameters can be written in terms of integral expressions for two-dimensional and three-dimensional upstream isotropic spectra, namely

$$\begin{aligned}\langle\bar{\rho}_e\bar{u}_r\rangle_{2\mathrm{D}} &= -\frac{2}{\pi}\int_0^{\theta_c}\mathbb{D}_{e,h}\mathbb{U}_{r,h}\,\mathrm{d}\theta - \frac{2}{\pi}\int_{\theta_c}^{\pi/2}\left[\mathbb{D}_{e,l1}\mathbb{U}_{r,l1} + \mathbb{D}_{e,l2}\mathbb{U}_{r,l2}\right]\,\mathrm{d}\theta, \\ \langle\bar{\rho}_e\bar{u}_r\rangle_{3\mathrm{D}} &= -\int_0^{\theta_c}\mathbb{D}_{e,h}\mathbb{U}_{r,h}\sin\theta\,\mathrm{d}\theta - \int_{\theta_c}^{\pi/2}\left[\mathbb{D}_{e,l1}\mathbb{U}_{r,l1} + \mathbb{D}_{e,l2}\mathbb{U}_{r,l2}\right]\sin\theta\,\mathrm{d}\theta,\end{aligned} \tag{3.41}$$

and

$$\langle\bar{p}\bar{u}_a\rangle_{2\mathrm{D}} = \frac{2}{\pi}\int_0^{\theta_c}\mathbb{P}_h\mathbb{U}_a\,\mathrm{d}\theta, \quad \langle\bar{p}\bar{u}_a\rangle_{3\mathrm{D}} = \int_0^{\theta_c}\mathbb{P}_h\mathbb{U}_a\sin\theta\,\mathrm{d}\theta \tag{3.42}$$

for the entropic-rotational contribution to the mass flux and the projected acoustic

contribution to the energy flux, respectively. The amplitudes of the entropic density and the streamwise rotational velocity are given in Eq. (C.22) and (C.29), respectively, and the negative sign arises from the opposite direction between the flow and the orientation of the detonation front. Finally, the amplitude of the pressure perturbations $\mathbb{P}_h$ together with $\mathbb{U}_a = \mathbb{P}_h \kappa_a/\omega_a$ is given in Eq. (C.9). It is readily observed that $\langle \bar{\rho}_e \bar{u}_r \rangle$ is directly associated to the far-field convective energy flux, which is studied in detailed in [67, 70] for different types of spectra in canonical shock-turbulence scenarios.

The post-shock density, pressure, and streamwise velocity component exhibit second-order changes due to the presence of the acoustic wave field. The dual temporal-spatial averaging that is conveniently applied to this problem is similar to time averaging performed in the reference frame with the gas at rest. The averaging must be computed in the Eulerian reference system at a fixed position relative to the detonation front. Therefore, as a direct consequence of the shift in the acoustic waves, there exists an additional contribution in the burnt-gas properties, namely

$$\delta\mathcal{R}_\mathrm{b} = -\frac{\gamma+1}{4}\langle \bar{p}^2 \rangle, \quad \delta\mathcal{P}_\mathrm{b} = -\frac{\gamma(3-\gamma)}{4}\langle \bar{p}^2 \rangle, \quad \delta\mathcal{U}_\mathrm{b} = \frac{1}{\mathcal{M}_2}\langle \bar{p}\bar{u}_a \rangle, \tag{3.43}$$

where the subscript b denotes changes in the background downstream properties due to random-phase acoustic perturbations. The ultimate corrections to the RH jump conditions are given by the sum of the contributions due to the turbulent fluxes (subscript f) and background corrections induced by the acoustic field (subscript b). With use made of Eqs. (3.38), (3.40) and (3.43), the turbulent corrections to the RH conditions read as follows:

$$\delta\mathcal{R} = \delta\mathcal{R}_\mathrm{f} + \delta\mathcal{R}_\mathrm{b} = \frac{1}{1-\mathcal{M}_2^2}\left[\frac{\mathcal{M}_2^2(\gamma+3)-2}{2\mathcal{M}_2}\langle l_\mathrm{f}\rangle - \gamma\langle m_\mathrm{f}\rangle + \frac{1}{\mathcal{M}_2}\langle n_\mathrm{f}\rangle - \frac{\gamma-1}{2}q_\mathrm{wh}\right] - \frac{\gamma+1}{4}\langle \bar{p}^2 \rangle, \tag{3.44}$$

$$\delta\mathcal{P} = \delta\mathcal{P}_\mathrm{f} + \delta\mathcal{P}_\mathrm{b} = \frac{\gamma}{1-\mathcal{M}_2^2}\left[\frac{\mathcal{M}_2\left[\mathcal{M}_2^2(\gamma-1)+2\right]}{2}\langle l_\mathrm{f}\rangle - \left[\mathcal{M}_2^2(\gamma-1)+1\right]\langle m_\mathrm{f}\rangle + \mathcal{M}_2\langle n_\mathrm{f}\rangle - \frac{\mathcal{M}_2^2(\gamma-1)}{2}q_\mathrm{wh}\right] - \frac{\gamma(3-\gamma)}{4}\langle \bar{p}^2 \rangle, \tag{3.45}$$

$$\delta\mathcal{U} = \delta\mathcal{U}_\mathrm{f} + \delta\mathcal{U}_\mathrm{b} = \frac{-1}{1-\mathcal{M}_2^2}\left[\frac{\mathcal{M}_2(\gamma+1)}{2}\langle l_\mathrm{f}\rangle - \gamma\langle m_\mathrm{f}\rangle + \frac{1}{\mathcal{M}_2}\langle n_\mathrm{f}\rangle - \frac{\gamma-1}{2}q_\mathrm{wh}\right] + \frac{1}{\mathcal{M}_2}\langle \bar{p}\bar{u}_a \rangle. \tag{3.46}$$

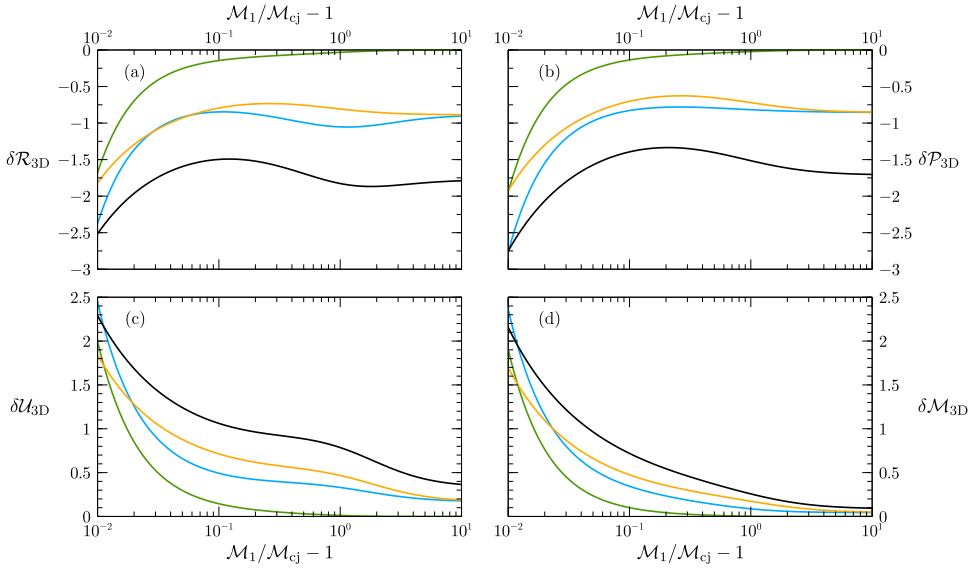

Figure 3.9: Three-dimensional second-order correction to the RH jump conditions (a) $\delta\mathcal{R}$, (b) $\delta\mathcal{U}$, (c) $\delta\mathcal{P}$, and (d) $\delta\mathcal{M}$ as a function of the overdrive parameter $\mathcal{M}_1/\mathcal{M}_{\rm cj}-1$. Computations correspond to $\gamma=1.2$, $Q=1$, and $|W|\gg|H|$ (——), $|H|\gg|W|$ (——), $W=H$ (——) and $W=-H$ (——).

Associated to the turbulence-induced changes in the RH jump conditions, the Mach number of the burnt gas fluid particles is also modified according to

$$\delta\mathcal{M}=\frac{\mathcal{M}_1}{\sqrt{\mathcal{R}\mathcal{P}}}\left(\delta\mathcal{U}+\frac{1}{2}\delta\mathcal{R}-\frac{1}{2}\delta\mathcal{P}\right). \tag{3.47}$$

Computations of $\delta\mathcal{R}$, $\delta\mathcal{P}$, $\delta\mathcal{U}$, and $\delta\mathcal{M}$ are represented in Fig. 3.9 as a function of the overdrive parameter $\mathcal{M}_1/\mathcal{M}_{\rm cj}-1$ for three-dimensional isotropic perturbations with $\gamma=1.2$, and $Q=1$. The four distinguished cases include $|W|\gg|H|$ (black lines), $|H|\gg|W|$ (green lines), $W=H$ (orange lines), and $W=-H$ (blue lines). Density and pressure corrections, $\delta\mathcal{R}$ and $\delta\mathcal{P}$, are always negative, and the amplitude of the second-order corrections weakens with the overdrive and approaches an asymptotic constant value that is null only when $W=0$, which is consistent with previous turbulence generation functions. A qualitative representation of the combined effect of $\delta\mathcal{P}$ and $\delta\mathcal{R}$ is shown in Fig. 3.8 (right) in terms of the vector $(\delta\mathcal{V},\delta\mathcal{P})$, with $\delta\mathcal{V}=-\delta\mathcal{R}$. The post-detonation velocity and corresponding Mach number curves go in the opposite direction because $\delta\mathcal{U}$ and $\delta\mathcal{M}$ exhibit positive values in all cases. For the conditions chosen in Fig. 3.9, perturbations involving only density changes result in the strongest corrections,

while those involving only variations in heat-release yield the weakest corrections far from the CJ condition. Positive and negative correlations, on the other hand, yield intermediate values for the second-order corrections.

3.4.2 Detonation propagation speed

The averaged turbulent properties of the post-detonation state differ from those of the unperturbed, i.e., one-dimensional case. Second-order corrections for density, pressure, and velocity must be accounted for to properly describe the burnt-gas state. In real conditions, depending on the experimental setup, boundary conditions may impose different restrictions to the burnt-gas flow. For example, a highly overdriven detonation formed by a piston-driven shock traveling into the reactive mixture forces the velocity of the burnt gas particles to be equal to the piston velocity, $u_p = u_1 - u_2$, in steady state. Then, along with the velocity variation of the expelled burnt gas $\delta\mathcal{U}$, a detonation propagation speed correction must occur to satisfy the boundary condition, i.e., $\delta\langle u_p\rangle = 0 = \delta u_1 - \bar{\epsilon}^2 u_2 \delta\mathcal{U}$, which yields

$$\delta\mathcal{S}|_{\delta\langle u_p\rangle=0} = \frac{1}{\bar{\epsilon}^2}\left.\frac{\delta u_1}{u_1}\right|_{\delta\langle u_p\rangle=0} = \frac{1}{\mathcal{R}}\delta\mathcal{U}, \tag{3.48}$$

where $\delta\mathcal{S}$ is an order-of-unity function that characterizes the correction of the detonation propagation speed. According to the results shown in Fig. 3.9, where $\delta\mathcal{U}$ is positive, the accommodated velocity of the detonation is therefore increased. Except for weakly overdriven detonations, where negative correlated perturbations $W = -H$ render the strongest correction, the case corresponding to dominant density perturbations $W \gg H$ is the case where the detonation would move faster compared to the homogeneous case.

Another canonical possibility is that total pressure (including corrections) must remain invariant. For this to be true, $\delta\langle p_2\rangle = 0 = p_2\bar{\epsilon}^2\delta\mathcal{P} + (\mathrm{d}p_2)/(\mathrm{d}u_1)\delta u_1$ and the detonation propagation speed must be adapted according to

$$\delta\mathcal{S}|_{\delta\langle p_2\rangle=0} = \frac{1}{\bar{\epsilon}^2}\left.\frac{\delta u_1}{u_1}\right|_{\delta\langle p_2\rangle=0} = -\frac{\mathcal{P}}{\mathcal{M}_1}\left(\frac{\mathrm{d}\mathcal{P}}{\mathrm{d}\mathcal{M}_1}\right)^{-1}\delta\mathcal{P}, \tag{3.49}$$

where $(\mathrm{d}\mathcal{P})/(\mathrm{d}\mathcal{M}_1) > 0$ and $\delta\mathcal{P} < 0$, according to Fig. 3.9. Then, the constant-pressure boundary condition also predicts a positive second-order correction to the propagation speed, which aligns with the previous boundary condition. These considerations oppose the initially imposed isolated-wave boundary condition. For Eqs. (3.48) and (3.49) to be true along with the isolated condition, the influence of the coupling

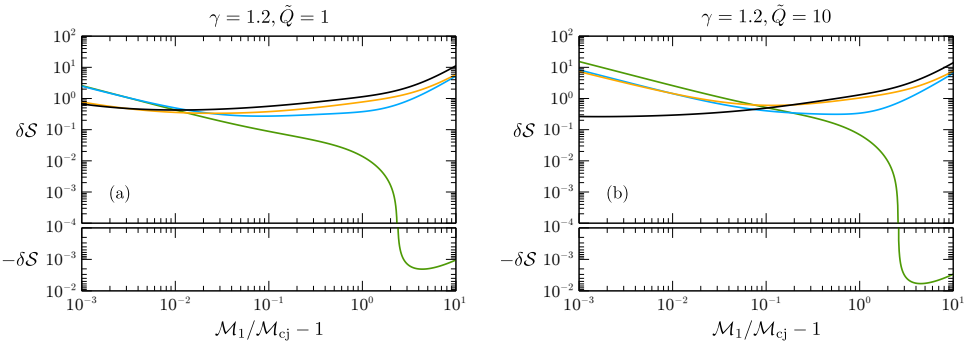

Figure 3.10: Three-dimensional second-order correction of the detonation propagation velocity $\delta\mathcal{S}$, according to (3.50), as a function of the overdrive parameter $\mathcal{M}_1/\mathcal{M}_{\rm cj} - 1$. Computations are provided for $\gamma = 1.2$, $\tilde{Q} = 1$ (a) and $\tilde{Q} = 10$ (b) evaluated for $|W| \gg |H|$ (——), $|H| \gg |W|$ (——), $W = H$ (——) and $W = -H$ (——).

surface must be sufficiently far away from the detonation for the asymptotic oscillating regime to be achieved before the reflections come into play. Certainly, more complex scenarios may require non-canonical boundary conditions to be imposed. For example, for a detonation moving along a tube with the back extreme being open, the boundary condition should be given by the corresponding matching of the far-field non-reflective condition with the acoustics inside the channel because both velocity and pressure variations are non-zero $\delta\langle u_p\rangle \neq \delta\langle p_2\rangle \neq 0$ downstream.

Regarding detonations traveling close to the CJ velocity, $1 - \mathcal{M}_2 \ll 1$, the closure is given by imposing $\delta\langle\mathcal{M}_2\rangle = 0$, i.e., not admitting variations in the post-detonation Mach number as the reacting gas expands up to its maximum value $\mathcal{M}_2 = 1$. Since the corresponding second-order correction to the RH conditions predicts variations in the flow velocity u_2 and in the speed of sound a_2, the detonation propagation velocity must provide $\delta\langle\mathcal{M}_2\rangle = 0 = \bar{\epsilon}^2\delta\mathcal{M} + (\mathrm{d}\mathcal{M}_2)/(\mathrm{d}u_1)\delta u_1$, and then

$$\delta\mathcal{S}|_{\delta\langle\mathcal{M}_2\rangle=0} = \frac{1}{\bar{\epsilon}^2}\left.\frac{\delta u_1}{u_1}\right|_{\delta\langle\mathcal{M}_2\rangle=0} = -\frac{1}{\sqrt{\mathcal{R}\mathcal{P}}}\left(\frac{\mathrm{d}\mathcal{M}_2}{\mathrm{d}\mathcal{M}_1}\right)^{-1}\left(\delta\mathcal{U} + \frac{1}{2}\delta\mathcal{R} - \frac{1}{2}\delta\mathcal{P}\right). \tag{3.50}$$

The variation of the propagation speed is studied through the order-of-unity factor $\delta\mathcal{S}$ as a function of the overdrive $\mathcal{M}_1/\mathcal{M}_{\rm cj} - 1$, reduced heat release $\tilde{Q}$, and specific heat ratio γ in Figs. 3.10 to 3.12, respectively. To properly isolate the effects, heat release is conveniently redefined with the thermal enthalpy upstream $\tilde{Q} = q_1/(c_{p_1}T_1)$, which relates to $Q = \tilde{Q}(\gamma+1)/2$ in the former definition.

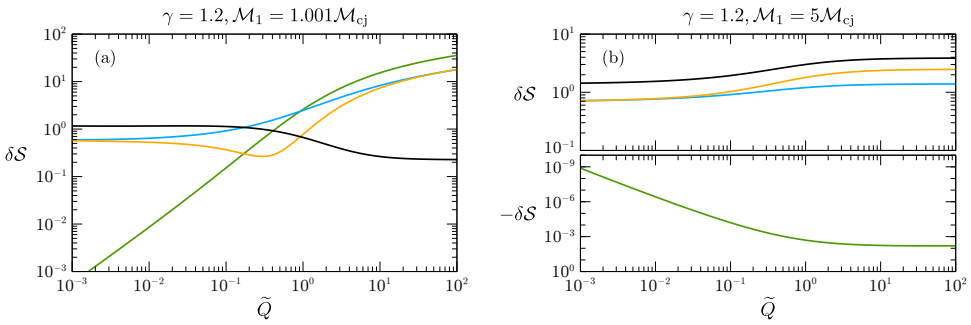

Figure 3.11: Three-dimensional second-order correction of the detonation propagation velocity $\delta\mathcal{S}$, according to (3.50), as a function of the dimensionless heat release $\tilde{Q}$. Computations are shown for $\gamma = 1.2$, weak-overdrives as $\mathcal{M}_1 = 1.001\mathcal{M}_{cj}$ (a) and strong-overdrives as $\mathcal{M}_1 = 5\mathcal{M}_{cj}$ (b). $|W| \gg |H|$ (——), $|H| \gg |W|$ (——), $W = H$ (——) and $W = -H$ (——).

Figure 3.10 shows the variation of the detonation propagation velocity given by Eq. (3.50) as a function of $\mathcal{M}_1/\mathcal{M}_{cj} - 1$ for three-dimensional isotropic perturbations, $\gamma = 1.2$, $\tilde{Q} = 1$ (a) and $\tilde{Q} = 10$ (b). The four distinguished cases include $|W| \gg |H|$ (black lines), $|H| \gg |W|$ (green lines), $W = H$ (orange lines) and $W = -H$ (blue lines). For strongly overdriven detonations, dominant density perturbations induce the highest amplification to the propagation velocity. For iso-density mixtures, $|H| \gg |W|$, the correction of the propagation speed becomes negative for sufficiently overdriven detonations, thereby resulting in a slower propagation speed. However, this effect can be effectively neglected in view of its amplitude. Increasing the value of $\tilde{Q}$ results in higher values of $\delta\mathcal{S}$ for weakly overdriven detonations, except for $|W| \gg |H|$. Weakly overdriven detonations are dominated by heat-release perturbations, where the case $|H| \gg |W|$ predicts the highest amplification.

The effect of heat release is better analyzed in Fig. 3.11, where the function $\delta\mathcal{S}$ is computed as a function of $\tilde{Q}$ for weakly overdriven (a) and strongly overdriven (b) detonations. The panel on the left shows that weakly overdriven detonations in heterogeneous mixtures tend to move faster for any value of $\tilde{Q}$. Regarding the type of mixture, higher heat release is associated with smaller amplification for $|W| \gg |H|$, while the opposite is found for $|H| \gg |W|$. Intermediate mixture properties $W = H$ and $W = -H$ present in-between values. For strongly overdriven detonations (b), heat release amplifies the propagation speed when density perturbations are not negligible. However, a negative correction is found for iso-density mixtures dominated by heat-release perturbations $|H| \gg |W|$; However, the order of magnitude, which is significantly smaller, predicts a negligible correction to the propagation speed.

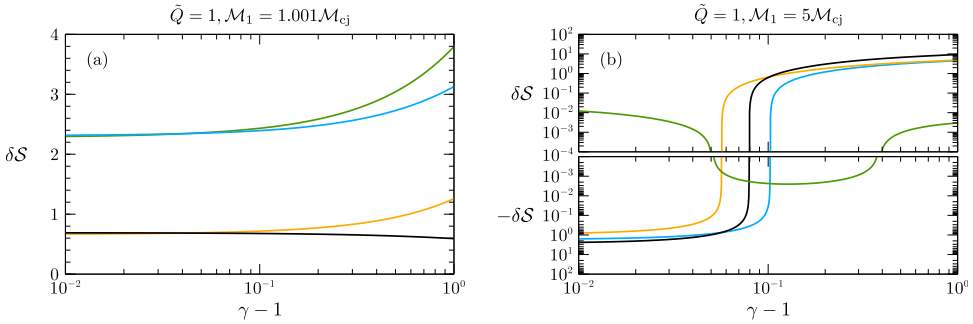

Figure 3.12: Three-dimensional second-order correction of the detonation propagation velocity $\mathcal{S}$, according to (3.50), as a function of the adiabatic constant as $\gamma - 1$. Computations are given for $\tilde{Q} = 1$, weak-overdrives as $\mathcal{M}_1 = 1.001\mathcal{M}_{cj}$ (a) and strong-overdrives as $\mathcal{M}_1 = 5\mathcal{M}_{cj}$ (b). Computations are evaluated for $|W| \gg |H|$ (——), $|H| \gg |W|$ (——), $W = H$ (——) and $W = -H$ (——).

The effect of the specific heats ratio γ is displayed in Fig. 3.12, where the factor $\delta\mathcal{S}$ is computed as a function of $\gamma - 1$ for weakly overdriven (a) and strongly overdriven (b) detonations. In agreement with previous figures, the former shows an always-positive velocity correction. When density perturbations dominate the upstream flow, the reduction of γ results in a higher propagation speed, but this trend reverses when heat-release perturbations are included. Overdriven detonations, on the other hand, exhibit a less intuitive picture. For values of γ between 1.1 and 1.4, the cases of utmost interest, results are qualitatively similar to those obtained previously for $\gamma = 1.2$, where the case $|H| \gg |W|$ predicts minor negative corrections to the propagation speed, and the cases $|W| \gg |H|$ and $|W| = |H|$ predict positive order-of-unity values of $\delta\mathcal{S}$.

Based on the analysis performed in the previous section, where the relative weight of the different types of perturbations in the burnt gas has been computed, it can be concluded that CJ-detonations moving in heterogeneous mixtures are governed by acoustic-type turbulent fluctuations in the burnt gas when net heat release is not negligible. Consequently, these factors are highly influenced by the heat-release variations derived from the upstream heterogeneities, with the correlation with density perturbations playing a dominant role in the formation of turbulent structures downstream. These results are in qualitative agreement with previous numerical simulations [215, 216]; However, the numerical setup is not completely compatible with the assumptions made in this theoretical model. Spatial inhomogeneities are introduced by collecting the energy sources into discretized reactive layers and into reactive square-based prisms, both of which are spatially separated by inert regions ($\bar{\epsilon} \sim 1$). They found that the average

wave propagation velocity is greater, up to 10%, than the CJ velocity of the equivalent homogeneous medium when the characteristic scale of the perturbations is greater than the inherent reaction zone length. The wave in CJ conditions speeds up when the specific heat ratio decreases. In agreement with linear theory, when the amplitude of the upstream heterogeneity increases, the propagation speed also increases.

3.5 Conclusions

In this chapter, an analytical description of the linear interaction of a planar thin detonation front with a heterogeneous mixture of gases has been presented. The weak deviation of the fuel mass fraction with respect to the homogeneous case provides two sources of perturbations to the reactive Rankine-Hugoniot equations: the relative density changes associated with the different density of the upstream gas mixture W and the relative heat-release changes induced by the dependence of the heat release with the fuel mass fraction H. The combination of the two strongly impacts the detonation response, and major differences in the perturbations are generated in the burnt gas associated with the corresponding relation between the two types of perturbations. This notion suggests that heat-release changes across the detonation must be addressed when modeling the interaction with non-perfect reactive mixtures, which places the equivalence ratio as a pivotal parameter in the analysis.

The results presented for all quantities of interest can be particularly useful in analysing the linear response of detonations to weak disturbances for conditions that render the basic planar solution stable provided that the characteristic sizes of the disturbances are much larger than the detonation thickness. For the interaction with a single-frequency perturbation field, the long-time amplitude of the perturbations can be written in terms of the characteristic oscillation frequency of the detonation front. Neutral conditions associated with the absence of pressure perturbations at the oscillating detonation or fully planar propagating detonations occur for distinguished conditions of reactive mixture associated to the density and heat release variations, W and H, respectively.

Fourier superposition for two- and three-dimensional isotropic fields are used to obtain integral formulae for the amplification of the kinetic energy, enstrophy, and density fluctuations in the burnt gas. The effects of the propagation Mach number, overdrive, and mixture properties through W and H are identified, and the latter plays a key role in the intensity of the turbulence generation. Regarding the type of upstream mixture, density perturbations dominate the turbulence generation for moderate-to-high over-

drives, while heat release variations become relevant for weak overdrives. As a direct result, heat-release variations make the acoustic contribution the same order as the rotational and entropic perturbations. Therefore, linear interaction analysis suggests that the turbulent flow downstream cannot be assumed to be isobaric, and the dilatational part of the velocity gradient tensor cannot be neglected in CJ conditions. This conclusion deserves further analysis by means of high-accuracy numerical simulations.

Turbulence generation provides second-order corrections to the averaged Rankine-Hugoniot jump conditions. While the pressure and density ratios are lower in the whole range of the parametric space, the post-detonation Mach number is amplified. This is consistent because the turbulence corrections are translated into a strong flow expansion, thereby exerting additional momentum on the leading shock. As a direct implication, the propagation of the detonation front traveling in heterogeneous mixtures differs from that in homogeneous mixtures with the same averaged upstream properties. How intense this deviation is, depends on the effective boundary condition in the burnt-gas flow. However, regardless of the closure expression (externally-imposed pressure, velocity or Mach number), the propagation speed is higher than that in the equivalent homogeneous case in the vast majority of cases, which agrees with previous results obtained numerically [214–216, 238]. The second-order correction to the propagation speed is determined by the type of turbulence generated downstream. For overdriven detonations, the downstream acoustic contribution plays a subdominant role in favor of rotational-entropic disturbances, while the contrary applies for weakly overdriven detonations, for which the effect of upstream heat-release variations is of utmost importance.

4 Thermochemical effects on hypersonic shock waves with turbulent flows

> *Science cannot solve the ultimate mystery of nature. And that is because, in the last analysis, we ourselves are part of nature and therefore part of the mystery that we are trying to solve.*
>
> **— Max Planck**

Contents

Summary

In this chapter, the interaction between a weakly turbulent free stream and a hypersonic shock wave is investigated theoretically by using linear interaction analysis (LIA). The formulation is developed in the limit in which the thickness of the thermochemical nonequilibrium region downstream of the shock, where relaxation toward vibrational and chemical equilibrium occurs, is assumed to be much smaller than the characteristic size of the shock wrinkles caused by turbulence. Modified Rankine-Hugoniot jump conditions that account for dissociation and vibrational excitation are derived and employed in a Fourier analysis of a shock interacting with three-dimensional isotropic vortical disturbances. This provides the modal structure of the post-shock gas arising from the interaction, along with integral formulas for the amplification of enstrophy, concentration variance, turbulent kinetic energy (TKE), and turbulence intensity across the shock. Besides confirming known endothermic effects of dissociation and vibrational excitation in decreasing the mean post-shock temperature and velocity, these LIA results indicate that the enstrophy, anisotropy, intensity, and TKE of the fluctuations are much more amplified through the shock than in the thermochemically frozen case. Additionally, the turbulent Reynolds number is amplified across the shock at hypersonic Mach numbers in the presence of dissociation and vibrational excitation, as opposed to the attenuation observed in the thermochemically frozen case. These results suggest that turbulence may persist and get augmented across hypersonic shock waves despite the high post-shock temperatures. Furthermore, we demonstrate the robustness and accuracy of this work by comparing it with the Combustion Toolbox (described in Chapter 2), which employs the NASA's 9 coefficient polynomials fits to evaluate the thermodynamic functions. Results are in excellent agreement between the two approaches, while significant differences are observed due to the electronic excitation at very high temperatures.

4.1 Introduction

Strong shock waves participate in a number of problems in physics, including the dynamics of high-energy interstellar medium [42–45], the explosions of giant stars [46–49], the fusion of matter in inertial-confinement devices [50–52], and the ignition of combustible mixtures by lasers [53, 54]. In addition to those, an important contemporary problem of relevance for aeronautical and astronautical engineering is the aerothermodynamics of hypersonic flight [55, 56]. In hypersonics, similarly to the aforementioned problems, the intense compression of the gas through the shock waves generated by

the fuselage leads to high temperatures that can activate complex thermochemical phenomena [254]. In particular, at high Mach numbers of up to approximately 25 in the terrestrial atmosphere, corresponding to sub-ionizing, sub-orbital stagnation enthalpies of up to approximately 15-30 MJ/kg depending on altitude, vibrational excitation and air dissociation are the dominant thermochemical phenomena typically observed in the gas downstream of shock waves around hypersonic flight systems.

Turbulence can also play an important role at the high Mach numbers mentioned above, particularly in low-altitude hypersonic flight because of the correspondingly larger Reynolds numbers of the airflow around the fuselage [144, 255, 256]. However, the way in which turbulence influences the thermomechanical loads and the thermochemistry around hypersonic flight systems remains largely unknown. To compound this problem, experiments in the area of hypersonic turbulence are curtailed by the exceedingly large flow powers required to move gases at sufficiently high Mach and Reynolds numbers in order to observe shock waves simultaneously with turbulence and thermochemistry. Additionally, the airflow in most ground facilities is poisoned with weak free-stream turbulence that interacts with the shock waves enveloping the test article. The fluctuations in the post-shock gases induced by this interaction oftentimes lead to artificial transition to turbulence in hypersonic boundary layers in wind-tunnel experiments [257].

Most early work on the interaction of shock waves with turbulence have been limited to calorically perfect gases in boundary layers [258–267], and isotropic free streams [268–272]. Large-scale numerical simulations, including direct numerical simulations (DNS) [61–76], large eddy simulations (LES) [77–79], and Reynolds-averaged Navier-Stokes simulations (RANS) [273, 274], have been the pacing item for those investigations. Nonetheless, the rapid progress in large-scale numerical simulations during the last decades has not abated the fundamental role that theoretical analyses have played in understanding shock/turbulence interactions (STI) by providing closed-form solutions. In problems dealing with shock waves propagating in turbulent free streams, as in the problem treated in the present study, the most successful theoretical approach has been the linear interaction analysis (LIA) pioneered by Ribner [80–82].

Under the assumption that turbulence is comprised of small linear fluctuations that can be separated using Kovásznay's decomposition into vortical, entropic, and acoustic modes [83], LIA describes their two-way coupled interaction with the shock by using linearized Rankine-Hugoniot jump conditions coupled with the linearized Euler equations in the post-shock gas. The resulting formalism describes the wrinkles induced by turbulence on the shock and the corresponding Kovásznay's compressible turbulence modes radiated by the interaction toward the downstream gas.

Despite its simplicity and limitations, LIA has not only provided a valuable insight into the underlying physical processes of STI, but has also worked sufficiently well for predicting the amplification of the turbulent kinetic energy (TKE) that is commonly used for bench-marking numerical simulations [63–65].

However, there exist known discrepancies between LIA and numerical simulations in the way that TKE is distributed among the diagonal components of the Reynolds stress tensor. For instance, LIA yields a smaller (larger) amplification of TKE associated with streamwise (transverse) velocity fluctuations relative to that observed in numerical simulations (see Section 5.4). These discrepancies are typically attributed to the fact that LIA treats the shock as a discontinuity, in that DNS results are observed to converge to those obtained by LIA when the ratio of the numerical shock thickness to the Kolmogorov length scale becomes sufficiently small [66, 68, 71].

In this study, an extension that incorporates thermochemical effects of vibrational excitation and gas dissociation is made to the standard LIA previously applied to calorically perfect gases [80–82, 275]. As in the standard LIA, the following conditions must be satisfied: (a) the root-mean-square (rms) of the velocity fluctuations u_ℓ needs to be much smaller than the speed of sound in both pre-shock and post-shock gases; (b) the amplitude of the streamwise displacement of the distorted shock from its mean position ξ_s needs to be much smaller than the upstream integral size of the turbulence ℓ; and (c) the eddy turnover time ℓ/u_ℓ needs to be much smaller than the molecular diffusion time ℓ^2/ν based on the kinematic viscosity ν, or equivalently, the turbulent Reynolds number $Re_\ell = u_\ell \ell/\nu$ needs to be large.

In addition to the conditions (a-c) stated above, the incorporation of thermochemical effects requires that the characteristic size of the shock wrinkles, which is of the same order as ℓ, needs to be much larger than the thickness ℓ_T of the thermochemical nonequilibrium region behind the shock, as depicted in Fig. 4.1. For instance, the value of ℓ_T behind a Mach-14 normal shock at a pressure equivalent to 45 km of altitude is approximately 1 cm (see page 503 in Ref. [276]), in consonance with the values obtained in Sec. 5.3.3 for a Mach-10 at different flight altitudes by solving one-dimensional direct numerical simulations with the HTR solver [277–279] using a two-temperature model.

In this thermochemical nonequilibrium region, the gas relaxes toward vibrational and chemical equilibrium in an intertwined manner, in that the vibrational energy of the molecules and their dissociation probability are coupled [254, 280]. The value of ℓ_T is approximately given by the mean post-shock velocity multiplied by the sum of the characteristic time scales of dissociation and vibrational relaxation. Since both of these characteristic time scales depend inversely on pressure and exponentially on the inverse

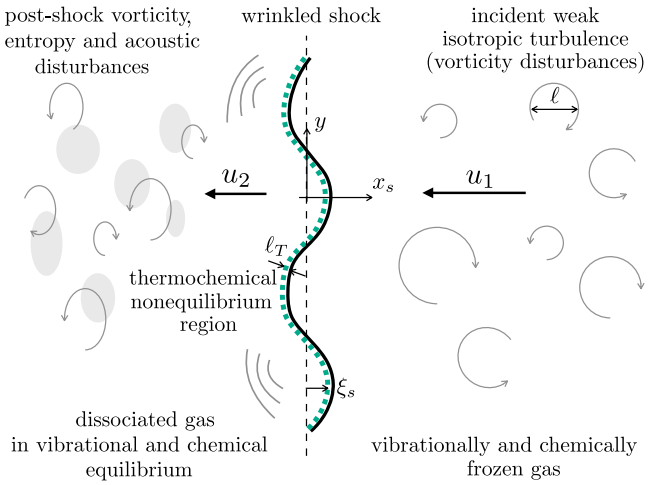

Figure 4.1: Sketch of the model problem: a normal shock wave interacts with a hypersonic free stream of weak isotropic turbulence (velocities are shown in the shock reference frame).

of the temperature, the veracity of the approximation $\ell_T/\ell \ll 1$ in practical hypersonic systems is expected to improve as the flight Mach number increases and the altitude decreases.

The LIA results provided in this study yield integral formulas for the amplification of the enstrophy, composition variance and TKE as a function of the post-shock Mach number, the density ratio and the normalized inverse of the slope of the Hugoniot curve. The latter undergoes a change in sign at high Mach numbers due to the thermochemical effects. As a result, at Mach numbers larger than approximately 13 in the conditions tested here, a local decrement (increment) in post-shock pressure – due, for instance to shock wrikling –, engenders an increment (decrement) in post-shock density.

This peculiar structure of the Hugoniot curve at hypersonic Mach numbers is found to strongly amplify turbulence in the post-shock gas, where most of the TKE is observed to be contained in transverse velocity fluctuations of the vortical mode. For instance, the present LIA results in a maximum TKE amplification factor of approximately 2, whereas this value drops close to 1.8 when the gas is assumed to be thermochemically frozen (i.e., diatomic calorically perfect) and close to 1.85 when the vibrational excitation is considered.

The remainder of this study is structured as follows. The Rankine-Hugoniot jump conditions across the shock are derived in Sec. 4.2 accounting for dissociation and vibrational excitation in the post-shock gas. A linearized formulation of the problem

is presented in Sec. 4.3 for the interaction of a normal shock with monochromatic vorticity disturbances. A Fourier analysis is carried out in Sec. 4.4 to address the interaction of a normal shock with weak isotropic turbulence composed of multiple and linearly superposed vorticity modes. A one-to-one comparison with the Combustion Toolbox (CT) is conducted in Sec. 4.5 to test the accuracy of the theoretical results, and discrepancies due to the electronic excitation are discussed. Lastly, conclusions are given in Sec. 4.6.

4.2 Rankine-Hugoniot jump conditions with vibrational excitation and gas dissociation

Consider first the problem of an undisturbed, normal shock wave in a cold, inviscid, irrotational, single-component gas consisting of symmetric diatomic molecules. The pre-shock density, pressure, temperature, specific internal energy, and flow velocity in the reference frame of the shock are denoted, respectively, as ρ_1, p_1, T_1, e_1 and u_1. The corresponding flow variables in the post-shock gas are denoted as ρ_2, p_2, T_2, e_2, and u_2.

4.2.1 Conservation equations across the shock

In the reference frame attached to the shock front, the conservation equations of mass, momentum, and enthalpy across the shock are

$$\rho_1 u_1 = \rho_2 u_2, \tag{4.1a}$$

$$p_1 + \rho_1 u_1^2 = p_2 + \rho_2 u_2^2, \tag{4.1b}$$

$$e_1 + p_1/\rho_1 + u_1^2/2 = e_2 + p_2/\rho_2 + u_2^2/2 + q_d, \tag{4.1c}$$

respectively. In this formulation, the symbol q_d denotes a positive quantity that represents the net change of specific chemical enthalpy caused by the gas dissociation reaction

$$\mathrm{A_2} \rightleftharpoons \mathrm{A} + \mathrm{A}, \tag{4.2}$$

with $\mathrm{A_2}$ being a generic molecular species and A its dissociated atomic counterpart. In particular, q_d can be expressed as

$$q_d = \alpha R_{g,\mathrm{A_2}} \Theta_d, \tag{4.3}$$

where R_{g,A_2} is the gas constant based on the molecular weight of A_2, and Θ_d is the characteristic dissociation temperature. In addition, the variable α is the degree of dissociation defined as the ratio of the mass of dissociated A atoms to the total mass of the gas, or equivalently, the mass fraction of A atoms.

Equations (4.1a) to (4.1c) are supplemented with the ideal-gas equations of state in the pre-shock gas

$$p_1/\rho_1 = R_{g,\mathrm{A}_2} T_1 \tag{4.4}$$

and in the post-shock gas

$$p_2/\rho_2 = (1+\alpha) R_{g,\mathrm{A}_2} T_2. \tag{4.5}$$

Additionally, the specific internal energy in the pre-shock gas e_1 is given by the translational and rotational components

$$e_1 = (5/2) R_{g,\mathrm{A}_2} T_1, \tag{4.6}$$

whereas in the post-shock gas e_2 requires consideration of translational, rotational, and vibrational degrees of freedom along with mixing between molecular and atomic species, which gives

$$e_2 = R_{g,\mathrm{A}_2} T_2 \left[3\alpha + (1-\alpha) \left(\frac{5}{2} + \frac{\Theta_v/T_2}{\mathrm{e}^{\Theta_v/T_2} - 1} \right) \right], \tag{4.7}$$

where Θ_v is the characteristic vibrational temperature. The first term inside the square brackets in (4.7), proportional to the dissociation degree α, corresponds to the translational contribution of the monatomic species. The second term, proportional to the factor $1-\alpha$, includes the translational, rotational and vibrational contributions of the molecular species, where it has been assumed that the rotational degrees of freedom are fully activated and the molecules vibrate as harmonic oscillators.

The formulation is closed with the chemical-equilibrium condition downstream of the shock, namely [281]

$$\frac{\alpha^2}{1-\alpha} = \mathcal{G} m \Theta_r \left(\frac{m k_B}{4\pi\hbar^2} \right)^{3/2} \frac{\sqrt{T_2}}{\rho_2} \mathrm{e}^{-\frac{\Theta_d}{T_2}} \left(1 - \mathrm{e}^{-\frac{\Theta_v}{T_2}} \right), \tag{4.8}$$

where Θ_r is the characteristic rotational temperature, m is the atomic mass of A, k_B is the Boltzmann's constant, $\hbar$ is the reduced Planck's constant, and $\mathcal{G} = (Q^a_{\mathrm{el}})^2 / Q^{aa}_{\mathrm{el}}$ is a ratio of electronic partition functions of A atoms (Q^a_{el}) and A_2 molecules (Q^{aa}_{el}). Upon neglecting the variations of the specific internal energy with temperature due to

	H_2	O_2	N_2	F_2	I_2	Cl_2
Θ_r [K]	87.53	2.08	2.87	1.27	0.0538	0.0346
Θ_v [K]	6338	2270	3390	1320	308	805
Θ_d [K]	51973	59500	113000	18633	17897	28770
$\mathcal{G}$	$2^2/1$	$9^2/3$	$4^2/1$	$4^2/1$	$4^2/1$	$4^2/1$
m[kg] $\times 10^{26}$	0.16735	2.6567	2.3259	3.1548	21.072	5.8871

Table 4.1: Rotational (Θ_r), vibrational (Θ_v), and dissociation (Θ_d) characteristic temperatures, along with the factor $\mathcal{G}$ and the atomic mass m of relevant molecular gases.

electronic excitation, the electronic partition functions in $\mathcal{G}$ can be approximated as the ground-state degeneracy factors. Nonetheless, in the context of the initial mixture consisting solely of diatomic oxygen, it is important to note that the dissociation of molecular oxygen into its monatomic form only occurs at temperatures greater than ~ 2500 K considering atmospheric pressure. Therefore, the effect of the two lowest excitation states of monatomic oxygen (D.25a) must be taken into account, as they are activated at these temperatures. Consequently, $Q_{\mathrm{el}}^{\mathrm{O}} \sim 9$, which is almost twice its ground-state value $Q_{\mathrm{el}}^{\mathrm{O}} \sim 5$. Typical values of Θ_r, Θ_v, Θ_d, $\mathcal{G}$, and m are provided in Table 4.1 for a wide range of molecular gases.

4.2.2 Dimensionless formulation

A dimensionless formulation of the problem can be written by introducing the dimensionless parameters

$$B = \frac{\mathcal{G} m \Theta_r T_1^{1/2}}{\rho_1} \left(\frac{m k_B}{4\pi\hbar^2} \right)^{3/2}, \quad \beta_d = \frac{\Theta_d}{T_1}, \quad \beta_v = \frac{\Theta_v}{T_1}, \tag{4.9}$$

along with the pressure, temperature, and density jumps

$$\mathcal{P} = p_2/p_1, \quad \mathcal{T} = T_2/T_1, \quad \mathcal{R} = \rho_2/\rho_1 \tag{4.10}$$

across the shock. In the expressions below, the solution for a vibrationally and chemically frozen gas (i.e., a calorically perfect diatomic gas) is recovered by taking the limits $\beta_v \to \infty$ and $\beta_d \to \infty$ (or $\alpha \to 0$).

Using these definitions, the dimensionless Rayleigh line

$$\mathcal{P} = 1 + \frac{7}{5}\mathcal{M}_1^2 \left(1 - \frac{1}{\mathcal{R}} \right), \tag{4.11}$$

which relates $\mathcal{P}$ and $\mathcal{R}$, is obtained by combining the mass and momentum conservation equations (4.1a) and (4.1b). In (4.11), the symbol $\mathcal{M}_1$ denotes the pre-shock Mach number defined as

$$\mathcal{M}_1 = u_1/a_1, \tag{4.12}$$

where $a_1 = \sqrt{(7/5)R_{g,\mathrm{A}_2}T_1}$ is the speed of sound of the pre-shock gas. Regardless of the value of $\mathcal{M}_1$, the Rayleigh line always emanates from the pre-shock state, $\mathcal{P} = 1$ and $\mathcal{R} = 1$, as a straight line with negative slope in the $\{\mathcal{R}^{-1}, \mathcal{P}\}$ plane.

In contrast, since the post-shock gas is calorically imperfect, its Mach number

$$\mathcal{M}_2 = \frac{u_2}{a_2} = \frac{\mathcal{M}_1}{\mathcal{R}}\frac{a_1}{a_2} \tag{4.13}$$

requires a more elaborate calculation of the speed of sound, namely

$$a_2^2 = \frac{p_2}{\rho_2^2}\frac{\left.\dfrac{\partial p_2}{\partial T_2}\right|_{\rho_2}}{\left.\dfrac{\partial (e_2+q_d)}{\partial T_2}\right|_{\rho_2}} - \frac{\left.\dfrac{\partial p_2}{\partial T_2}\right|_{\rho_2}\left.\dfrac{\partial (e_2+q_d)}{\partial \rho_2}\right|_{T_2}}{\left.\dfrac{\partial (e_2+q_d)}{\partial T_2}\right|_{\rho_2}} + \left.\frac{\partial p_2}{\partial \rho_2}\right|_{T_2}. \tag{4.14}$$

Upon substituting Eqs. (4.5) and (4.7) into (4.14), the expression

$$\frac{a_2^2}{a_1^2} = \frac{5\mathcal{T}}{7}\left[1+\alpha+\alpha_R+(1+\alpha+\alpha_T)\times \frac{2(1+\alpha)-\alpha_R\left(1-2\bar{e}_{\mathrm{vib}}+2\beta_d/\mathcal{T}\right)}{5+\alpha+2(1-\alpha)\bar{e}_{\mathrm{vib}}^2\mathrm{e}^{-\beta_v/\mathcal{T}}+\alpha_T\left(1-2\bar{e}_{\mathrm{vib}}+2\beta_d/\mathcal{T}\right)}\right] \tag{4.15}$$

is obtained, where

$$\bar{e}_{\mathrm{vib}} = \frac{\beta_v/\mathcal{T}}{\mathrm{e}^{\beta_v/\mathcal{T}}-1} \tag{4.16}$$

is the dimensionless component of the specific internal energy corresponding to vibrational excitation in equilibrium. Additionally, the coefficients α_R and α_T in Eq. (4.15) are given by

$$\alpha_R = \mathcal{R}\left.\frac{\partial\alpha}{\partial\mathcal{R}}\right|_{\mathcal{T}} = -\frac{\alpha(1-\alpha)}{2-\alpha}, \tag{4.17}$$

$$\alpha_T = \mathcal{T}\left.\frac{\partial\alpha}{\partial\mathcal{T}}\right|_{\mathcal{R}} = -\alpha_R\left[\frac{1}{2}+\frac{\beta_d}{\mathcal{T}}\frac{1-\left(1+\frac{\beta_v}{\beta_d}\right)\mathrm{e}^{-\beta_v/\mathcal{T}}}{1-\mathrm{e}^{-\beta_v/\mathcal{T}}}\right]. \tag{4.18}$$

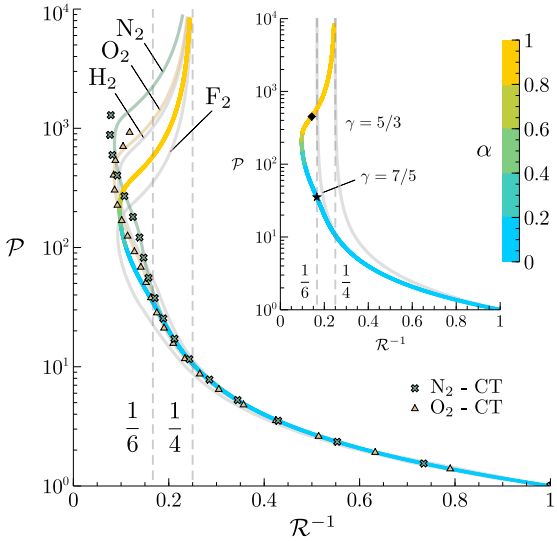

Figure 4.2: Hugoniot curves for different molecular gases at pre-shock temperature $T_1 = 300$ K and pressure $p_1 = 1$ atm [grey lines: present formulation; symbols: numerical results obtained with the Combustion Toolbox (CT) code [23] including electronic excitation and ionization], along with the Hugoniot curve of a gas with $B = 10^4$, $\beta_v = 10$, and $\beta_d = 100$ (line colored by the degree of dissociation). The latter is compared in the inset with the Hugoniot curves of a calorically perfect monatomic gas (grey line corresponding to $\gamma = 5/3$) and a calorically perfect diatomic gas (grey line corresponding to $\gamma = 7/5$).

Equation (4.15), along with definitions (4.16) to (4.18), determine the post-shock Mach number defined in (4.13). The equations of state (4.4) and (4.5) can be combined into a single equation as

$$\mathcal{P} = (1 + \alpha)\mathcal{R}\mathcal{T}. \tag{4.19}$$

Upon substituting Eqs. (4.4) to (4.7) into the conservation equations (4.1a) to (4.1c) and using the normalizations (4.9) and (4.10), the relation

$$\mathcal{T} = \frac{6 - \mathcal{R}^{-1} - 2\alpha\beta_d - 2(1-\alpha)\beta_v / \left(\mathrm{e}^{\beta_v/\mathcal{T}} - 1\right)}{2(\alpha + 3) - \mathcal{R}(1 + \alpha)} \tag{4.20}$$

is obtained between α, $\mathcal{R}$, and $\mathcal{T}$. Lastly, the problem is closed by rewriting the chemical-equilibrium condition (4.8) in dimensionless form using Eqs. (4.9) and (4.10) as

$$\frac{\alpha^2}{1-\alpha} = B\mathrm{e}^{-\beta_d/\mathcal{T}} \frac{\sqrt{\mathcal{T}}}{\mathcal{R}} \left(1 - \mathrm{e}^{-\beta_v/\mathcal{T}}\right), \tag{4.21}$$

which provides an additional relation between α, $\mathcal{R}$, and $\mathcal{T}$. In particular, given the

	H_2	O_2	N_2	F_2	I_2	Cl_2
$B \times 10^{-4}$	0.8332	8.4535	5.6622	3.9581	2.8944	0.2749
$\beta_v \times 10^{-1}$	2.1127	0.7567	1.13	0.44	0.1027	0.2683
$\beta_d \times 10^{-2}$	1.7324	1.9833	3.7667	0.6211	0.5966	0.959

Table 4.2: Dimensionless parameters B, β_v, and β_d for relevant molecular gases at pre-shock temperature $T_1 = 300$ K and pressure $p_1 = 1$ atm.

dimensionless parameters β_v, β_d, and B, the combination of Eqs. (4.19) to (4.21) provides the Hugoniot curve $\mathcal{P} = \mathcal{P}(\mathcal{R}^{-1})$, which in the present case is a laborious implicit function that is evaluated numerically and is shown in Fig. 4.2. As a result, given a pre-shock Mach number $\mathcal{M}_1$, the post-shock state is completely determined by the intersection of the Hugoniot curve and the Rayleigh line Eq. (4.11).

4.2.3 The turning point in the Hugoniot curve at hypersonic Mach numbers

It is worth discussing some peculiarities of the Hugoniot curve that is obtained by including dissociation and vibrational excitation in the post-shock gas, since they are of some relevance for the STI problem studied in Secs. 4.3 and 4.4.

The main panel in Fig. 4.2 shows Hugoniot curves in grey color for H_2, O_2, N_2, and F_2 using the simple theory provided above particularized for the parameters B, β_v, and β_d listed in Table 4.2. As shown in Fig. 4.2, the curves for O_2 and N_2 are in excellent agreement with the more complex numerical calculations obtained with the Combustion Toolbox (see Chapter 2). The latter incorporates variations of the specific heat with temperature due to both vibrational and electronic excitation through the NASA polynomials [128] as well as the ionization of the species. Consequently, there are differences at very high temperatures and pressures due to the electronic excitation and ionization, which are not considered in this theoretical study. Nevertheless, for the sake of completeness, an extension of the mathematical framework presented in this study is provided in Appendix D, which includes the effects of electronic excitation and ionization.

To narrow down the exposition, the main panel in Fig. 4.2 also shows a Hugoniot curve colored by the degree of dissociation and obtained using the representative values[1] $B = 10^4$, $\beta_v = 10$, and $\beta_d = 100$. This is a particular choice of values that nonetheless approximately captures the order of magnitude of these parameters observed among the different gases listed in Table 4.2. However, it is important to remark that the value of B depends strongly on upstream conditions. For instance, at an altitude of 30 km above sea level ($T_1 = 226.51$ K and $p_1 = 1.181 \cdot 10^{-2}$ atm), B reaches $O(10^6)$, which is two orders of magnitude higher than the tested conditions in this study.

The inset in Fig. 4.2 shows that the Hugoniot curve starts departing significantly from that of a calorically perfect diatomic gas [corresponding to an adiabatic coefficient $\gamma = 7/5$ and a maximum density ratio $\mathcal{R} = (\gamma + 1)/(\gamma - 1) = 6$] at a rather modest degree of dissociation $\alpha \sim 1\%$ attained at $\mathcal{M}_1 \sim 5$. Despite the smallness of this crossover value of α, large changes in chemical enthalpy occur because of the large bond-dissociation specific energy of most relevant species (e.g., approximately 15 MJ/kg for O_2). As a result, $\alpha \sim 1\%$ renders $\alpha\beta_d = O(1)$ in Eq. (4.20), which represents a balance between the heat absorbed by dissociation q_d and the pre-shock internal energy e_1 in the conservation equation (4.1c). As α is further increased, q_d becomes of the same order as e_2, and the departure from calorically perfect behavior becomes increasingly more pronounced.

As α becomes increasingly closer to unity, which requires the kinetic energy of the pre-shock gas to be increasingly larger than q_d (or equivalently, it requires the pre-shock Mach number $\mathcal{M}_1$ to be increasingly larger than $\sqrt{\beta_d}$), the slope of the Hugoniot curve undergoes a change in sign and turns inwards toward larger specific volumes. For the parameters investigated in Fig. 4.2, the turning point occurs at $\alpha \simeq 0.6$, where $\mathcal{T} \simeq 13$ (corresponding to 3900 K when $T_1 = 300$ K), $\mathcal{M}_1 \simeq 13$, and $\mathcal{R} \simeq 10$, the latter being 1.7-times (2.5-times) the density ratio of a calorically perfect diatomic (monatomic) gas. There, the inverse of the slope of the Hugoniot curve normalized with the slope of the Rayleigh line,

$$\Gamma = -\left(\frac{p_2 - p_1}{1/\rho_1 - 1/\rho_2}\right)\frac{\mathrm{d}(1/\rho_2)}{\mathrm{d}p_2} = \frac{7}{5}\frac{\mathcal{M}_1^2}{\mathcal{R}^2}\left(\frac{\partial \mathcal{P}}{\partial \mathcal{R}}\right)^{-1}, \tag{4.22}$$

attains a zero value. The role of Γ in the description of the STI problem will be addressed in Secs. 4.3 and 4.4.

[1] In the original manuscript, there was an error in the order of magnitude provided for B. Although all the analysis is accurately conducted, the value $B = O(10^6)$ does not correspond to sea level conditions ($T_1 = 300$ K and $p_1 = 1$ atm) as stated. Instead, this value aligns with results obtained at an altitude of 30 km above sea level, which falls within the range of operating conditions of hypersonic flights.

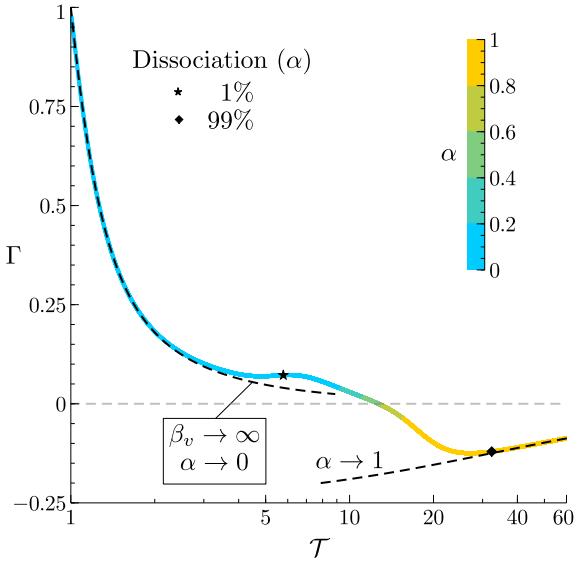

Figure 4.3: Normalized inverse of the slope of the Hugoniot curve Γ as a function of the temperature jump across the shock $\mathcal{T}$ for $B = 10^4$, $\beta_v = 10$, and $\beta_d = 100$ (line colored by the degree of dissociation). Dashed lines represent asymptotic limits for a calorically perfect diatomic gas ($\beta_v \to \infty$ and $\alpha \to 0$), and for a highly dissociated gas ($\alpha \to 1$).

As shown in Fig. 4.3, the value of Γ becomes negative along the upper branch of the Hugoniot curve beyond the turning point $\Gamma = 0$. Along that branch, an increment (decrement) in post-shock pressure induces a decrement (increment) in post-shock density. For the parameters tested here, the value Γ in the upper branch of the Hugoniot curve is always larger than the critical values for the onset of (a) shock instabilities associated with multi-wave [282, 283] and multi-valued [284, 285] solutions, and (b) D'yakov-Kontorovich pseudo-instabilities associated with the spontaneous emission of sound [49, 286–289]. Similar characteristics of the Hugoniot curve have been observed elsewhere for shocks subjected to endothermicity [289–293].

4.2.4 Limit behavior in the post-shock gas

Typical distributions of the density ratio $\mathcal{R}$, the post-shock Mach number $\mathcal{M}_2$ and the pre-shock Mach number $\mathcal{M}_1$ are provided in Fig. 4.4 as a function of the temperature ratio $\mathcal{T}$. The curves also show the limit behavior for $\alpha \to 0$ and $\beta_v \to \infty$ (corresponding to a calorically perfect diatomic gas at low temperatures), and for $\alpha \to 1$ (corresponding to a fully dissociated gas at high temperatures). Additionally, the first

limit can be extended for $\alpha \to 0$ and $\beta_v = \theta_v/T_1$ (corresponding to a diatomic gas with full vibrational excitation). Some insight into these limits is provided below.

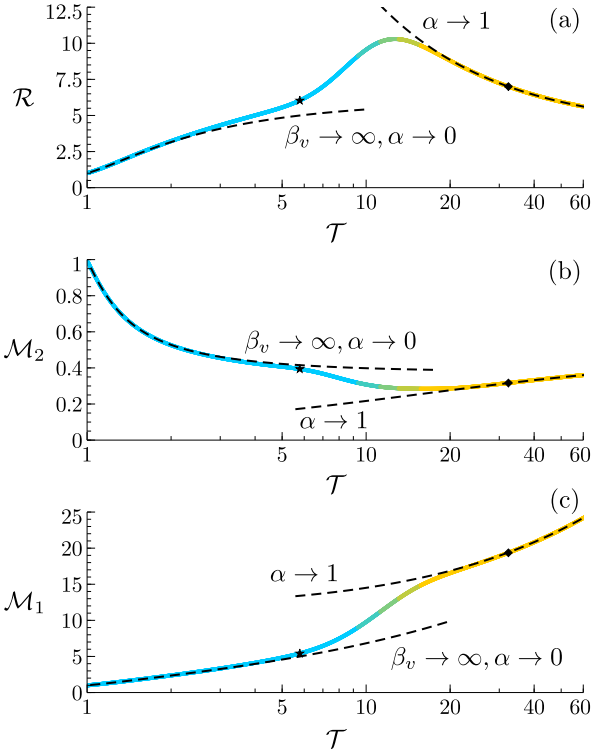

Figure 4.4: Distributions of (a) density jump $\mathcal{R}$, (b) post-shock Mach number $\mathcal{M}_2$, and (c) pre-shock Mach number $\mathcal{M}_1$ as a function of the temperature jump $\mathcal{T}$ for $B = 10^4$, $\beta_v = 10$, and $\beta_d = 100$ (lines colored by the degree of dissociation; refer to Fig. 4.3 for a colorbar). Dashed lines represent asymptotic limits for a calorically perfect diatomic gas ($\beta_v \to \infty$ and $\alpha \to 0$), and for a highly dissociated gas ($\alpha \to 1$).

In Fig. 4.4(a), the low-temperature limit of the density ratio corresponds to the standard Rankine-Hugoniot jump condition for a calorically perfect diatomic gas,

$$\mathcal{R} \sim 3\left(1 - \frac{1}{\mathcal{T}}\right)\left[1 + \sqrt{1 + \frac{\mathcal{T}}{9\left(\mathcal{T} - 1\right)^2}}\right], \tag{4.23}$$

which can be derived by taking the limits $\alpha \to 0$ and $\beta_v \to \infty$ in Eq. (4.20). In this low-temperature limit, the normalized slope of the Hugoniot curve becomes $\Gamma \sim \mathcal{M}_1^{-2}$, as indicated in Fig. 4.3. As previously mentioned, this limit can be extended to account

also vibrational excitation by setting $\alpha \to 0$ and remaining β_v in (4.20), providing

$$\mathcal{R} \sim \left[3\left(1-\frac{1}{\mathcal{T}}\right)+\bar{e}_{\mathrm{vib}}\right]\left(1+\sqrt{1+\frac{1}{\mathcal{T}\left[3\left(1-\mathcal{T}^{-1}\right)+\bar{e}_{\mathrm{vib}}\right]^2}}\right), \tag{4.24}$$

with $\bar{e}_{\mathrm{vib}}$ given by Eq. (4.16). Note that (4.24) simplies to (4.23) for $\beta_v \to \infty$. Due to its similar value with the calorically perfect approximation, the vibrational excitation limit is not shown in the present study. Additional insights regarding this matter are expounded upon in Sec. 4.5.

In the opposite limit, when the post-shock gas is hot and almost fully dissociated, $\alpha \to 1$, the density jump and the normalized slope of the Hugoniot curve become

$$\mathcal{R} \sim \frac{\beta_d + 4\mathcal{T} - 3 + \sqrt{(\beta_d + 4\mathcal{T} - 3)^2 + 2\mathcal{T}}}{2\mathcal{T}}, \tag{4.25}$$

and

$$\Gamma \sim -\frac{7\mathcal{M}_1^2\left(\mathcal{R}-4\right)^2}{5\mathcal{R}^2(8\beta_d - 23)}, \tag{4.26}$$

respectively, with $\beta_d > 23/8$ in the conditions tested here. At very high Mach numbers $\mathcal{M}_1 \gg \sqrt{\beta_d}$, when $\beta_d/\mathcal{T} \ll 1$, Eq. (4.25) simplifies to $\mathcal{R} \sim 4$ in the first approximation, whereas Eq. (4.26) yields very small and negative values of Γ. Remarkably, unlike $\mathcal{R}$, $\mathcal{M}_1$, and $\mathcal{M}_2$, the normalized inverse of the slope Γ is not bounded by its asymptotic limits at low and high Mach numbers. The relevance of this property for the problem of STI will be discussed in Secs. 4.3 and 4.4.

The results mentioned above for $\alpha \to 1$ indicate that the post-shock gas increasingly resembles a monatomic calorically perfect gas (corresponding to an adiabatic coefficient $\gamma = 5/3$) at infinite Mach numbers, an effect that can also be visualized in Fig. 4.2 as the Hugoniot curve asymptotes the abscissa $\mathcal{R}^{-1} \sim 1/4$. However, this limit is of little practical relevance because it would require such exceedingly high temperatures that additional effects like electronic excitation, radiation, and ionization would have to be included in the formulation, thereby invalidating these considerations. Further insights into these additional phenomena are given in Sec. 4.5 (electronic excitation), and Chapter 5 and Appendix D (electronic excitation and ionization).

4.3 The interaction of a hypersonic shock wave with an incident monochromatic vorticity wave

For small-amplitude velocity fluctuations and vanishing turbulent Mach numbers, the free-stream turbulence in the pre-shock gas can be represented as a linear superposition of Kovásznay's three-dimensional vorticity modes, which are solutions of the incompressible Euler equations [83, 249]. This section addresses the interaction of the shock with a single one of those vorticity modes.

4.3.1 Laboratory, shock and post-shock reference frames

Three reference frames are used in the analysis. Whereas the spanwise and transverse axes of all the frames coincide, the streamwise axis differs depending on whether the frames are attached to the laboratory (x), the mean shock front (x_s) or the mean absolute post-shock gas motion (x_c).

In the laboratory reference frame, the streamwise coordinate is denoted by x and is attached to the bulk of the pre-shock gas, which is at rest on average. In contrast, in the shock reference frame, which corresponds to the one visualized in Fig. 4.1, the streamwise coordinate x_s moves at the mean shock velocity $\langle u_1 \rangle$, and is therefore defined by the relation $x_s = x - \langle u_1 \rangle t$ in terms of the time coordinate t. The integral formulation of the conservation equations across the shock can be readily written in the shock reference frame, as done in Sec. 4.2. Whereas the incident vorticity wave remains stationary in space in the laboratory frame, it becomes a wave traveling at velocity $\langle u_1 \rangle$ toward the shock in the shock reference frame.

In the reference frame moving with the post-shock gas, the streamwise coordinate x_c moves with the post-shock mean absolute velocity $\langle u_1 \rangle - \langle u_2 \rangle$, and is therefore defined as $x_c = x - (\langle u_1 \rangle - \langle u_2 \rangle)t$. In this frame, the vorticity and entropy fluctuations in the post-shock gas are stationary in space, which facilitates the description of the problem, as shown below.

4.3.2 Orientation and form of the incident vorticity wave

Anticipating that the pre-shock turbulence is isotropic, there is no privileged direction of the wavenumber vector $\boldsymbol{k}$, and therefore the amplitude of the vorticity modes

depend exclusively on $k = |\boldsymbol{k}|$. Similarly, because of this isotropy, there is no preferred wavenumber-vector orientation relative to the shock surface. In principle, this would require the formulation of a three-dimensional problem to describe the interaction. However, a simple rotation of the reference frame can transform the problem into a two-dimensional one, as described below (see also Refs. [61, 232, 275]).

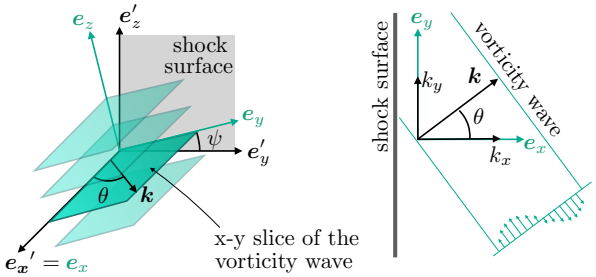

Figure 4.5: Simplification of a three-dimensional problem of a shock interacting with an arbitrarily oriented vorticity wave to a two-dimensional problem by rotating the reference frame around the streamwise axis.

For an incident wavenumber vector arbitrarily oriented in space at latitude and longitude angles θ and φ, respectively, the reference frames described in Sec. 4.3.1 can be rotated counterclockwise around x by an angle equal to the longitudinal inclination of the incident wave ψ, as indicated in Fig. 4.5. In this way, the interaction problem becomes two-dimensional, in that all variations with respect to z are zero.

Using the aforementioned rotation, the wavenumber-vector components in the streamwise and transverse directions are

$$k_x = k\cos\theta, \quad k_y = k\sin\theta, \tag{4.27}$$

respectively, with $k_z = 0$ by construction. Similarly, in the laboratory reference frame, the vorticity vector of the incident wave in the pre-shock gas can be expressed as

$$\boldsymbol{\varpi_1} = (\delta\boldsymbol{\varpi_1})\mathrm{e}^{\mathrm{i}(k_x x + k_y y)}, \tag{4.28}$$

with

$$\begin{gathered}\delta\varpi_{x,1} = -\varepsilon k\langle a_2\rangle\sin\theta\cos\varphi, \quad \delta\varpi_{y,1} = \varepsilon k\langle a_2\rangle\cos\theta\cos\varphi, \\ \delta\varpi_{z,1} = -\varepsilon k\langle a_2\rangle\sin\varphi,\end{gathered} \tag{4.29}$$

being the vorticity amplitude in each direction. In this formulation, $\langle a_2\rangle$ denotes the mean speed of sound in the post-shock gas, and ε is a dimensionless velocity fluctuation

amplitude, which is small in the linear theory, $\varepsilon \ll 1$. The vorticity of the incident wave engenders a fluctuation velocity field in the pre-shock gas given by

$$\mathbf{v_1} = (\delta \mathbf{v_1}) \mathrm{e}^{\mathrm{i}(k_x x + k_y y)}, \tag{4.30}$$

whose amplitude is

$$\delta u_1 = \varepsilon \langle a_2 \rangle \sin\theta \sin\varphi, \quad \delta v_1 = -\varepsilon \langle a_2 \rangle \cos\theta \sin\varphi, \quad \delta \varpi_1 = \varepsilon \langle a_2 \rangle \cos\varphi, \tag{4.31}$$

in the x, y, and z directions, respectively. Specifically, the z-component of the fluctuation velocity vector is uniform along z. This component will not be carried any further in the analysis, since it is transmitted unaltered through the shock because of the conservation of tangential momentum. Note also that Eqs. (4.28) and (4.30) are related by the definition of the vorticity $\boldsymbol{\varpi_1} = \boldsymbol{k} \times \mathbf{v_1}$. Furthermore, the velocity field (4.30) and (4.31) is one that satisfies the incompressibility relation $\boldsymbol{k} \cdot \mathbf{v_1} = 0$. Lastly, implicit in the definitions given above is that the incident vorticity wave is inviscid, or equivalently, that the pre-shock Reynolds number of the fluctuation, $2\pi|\mathbf{v}_1|/(k\nu_1)$, is infinitely large.

To illustrate the analysis, a particular form of the pre-shock vorticity fluctuation corresponding to the inviscid Taylor-Green vortex

$$\varpi_{z,1}(x,y) = \varepsilon_u \langle a_2 \rangle \left(\frac{k^2}{k_y}\right) \cos(k_x x) \sin(k_y y) \tag{4.32}$$

is employed in the numerical results highlighted below, with $\varpi_{x,1} = \varpi_{y,1} = 0$. The corresponding streamwise and transverse components of the velocity fluctuations in the pre-shock gas are given by

$$u_1(x,y) = \varepsilon_u \langle a_2 \rangle \cos(k_x x) \cos(k_y y), \tag{4.33a}$$

$$v_1(x,y) = \varepsilon_u \langle a_2 \rangle \left(\frac{k_x}{k_y}\right) \sin(k_x x) \sin(k_y y), \tag{4.33b}$$

respectively. In this formulation, ε_u is the amplitude of the pre-shock streamwise velocity fluctuations

$$\varepsilon_u = \varepsilon \sin\theta \sin\varphi, \tag{4.34}$$

with $\varepsilon_u \ll 1$ in the linear theory.

4.3.3 Linearized formulation of the interaction problem

In this linear theory, the vorticity and the streamwise and transverse velocity components in the post-shock gas reference frame are expanded to first order in ε_u as

$$\varpi = \varepsilon_u k_y \langle a_2^2 \rangle \bar{\varpi}, \quad u = \varepsilon_u \langle a_2 \rangle \bar{u}, \quad v = \varepsilon_u \langle a_2 \rangle \bar{v}, \tag{4.35}$$

respectively, with $\bar{\varpi}$, $\bar{u}$, and $\bar{v}$ being the corresponding dimensionless fluctuations. The post-shock pressure and density can be similarly expressed as

$$p = \langle p_2 \rangle + \varepsilon_u \langle \rho_2 \rangle \langle a_2 \rangle^2 \bar{p}, \quad \rho = \langle \rho_2 \rangle (1 + \varepsilon_u \bar{\rho}), \tag{4.36}$$

with $\bar{p}$ and $\bar{\rho}$ being the dimensionless fluctuations of pressure and density, respectively. The brackets indicate time-averaged quantities, which are given by the solution obtained in Sec. 4.2. In this way, all fluctuations are defined to have a zero time average.

Assuming that the Reynolds number of the post-shock fluctuations is infinitely large, the expansions given by Eqs. (4.35) and (4.36) can be employed in writing the linearized Euler conservation equations of mass, streamwise momentum, transverse momentum, and energy as

$$\frac{\partial \bar{\rho}}{\partial \tau} + \frac{\partial \bar{u}}{\partial \bar{x}_c} + \frac{\partial \bar{v}}{\partial \bar{y}} = 0, \tag{4.37a}$$

$$\frac{\partial \bar{u}}{\partial \tau} + \frac{\partial \bar{p}}{\partial \bar{x}_c} = 0, \tag{4.37b}$$

$$\frac{\partial \bar{v}}{\partial \tau} + \frac{\partial \bar{p}}{\partial \bar{y}} = 0, \tag{4.37c}$$

$$\frac{\partial \bar{p}}{\partial \tau} = \frac{\partial \bar{\rho}}{\partial \tau}, \tag{4.37d}$$

in the reference frame moving with the post-shock gas, in the same manner as in Section 3.2.3. In this notation, the space and time coordinates have been nondimensionalized as

$$\bar{x}_c = k_y x_c, \quad \bar{y} = k_y y, \quad \tau = k_y \langle a_2 \rangle t. \tag{4.38}$$

The linearized Euler equations (4.37) can be combined into a single, two-dimensional periodically-symmetric wave equation

$$\frac{\partial^2 \bar{p}}{\partial \tau^2} = \frac{\partial^2 \bar{p}}{\partial \bar{x}_c^2} + \frac{\partial^2 \bar{p}}{\partial \bar{y}^2} \tag{4.39}$$

for the post-shock pressure fluctuations. Equation (4.39) is integrated for $\tau \geq 0$ within the spatiotemporal domain bounded by the leading reflected sonic wave traveling upstream, $\bar{x}_c = -\tau$, and the shock front moving downstream $\bar{x}_c = \mathcal{M}_2 \tau$, with $\mathcal{M}_2 = \langle u_2 \rangle / \langle a_2 \rangle$.

The boundary condition at the shock front is derived from the linearized Rankine-Hugoniot jump conditions assuming that (a) the thickness of the thermochemical non-equilibrium region ℓ_T is significantly less than the inverse of the transverse wavenumber k_y^{-1}; and (b) the displacement of the shock $\xi_s = \xi_s(y,t)$ from its mean, flat shape (see Fig. 4.1) is considerably smaller than k_y^{-1}. In these limits, at any transverse coordinate $\bar{y}$, the Rayleigh-Hugoniot jump conditions can be applied at the mean shock front location $\bar{x}_c = \mathcal{M}_2 \tau$, and can be linearized about the mean thermochemical-equilibrium post-shock gas state $\mathcal{P}$, $\mathcal{R}$, $\mathcal{T}$, $\mathcal{M}_2$, and α calculated in Sec. 4.2, thereby yielding

$$\frac{\partial \bar{\xi}_s}{\partial \tau} = \frac{\mathcal{R}\,(1-\Gamma)}{2\mathcal{M}_2\,(\mathcal{R}-1)} \bar{p}_s - \bar{u}_1, \tag{4.40a}$$

$$\bar{u}_s = \frac{1+\Gamma}{2\mathcal{M}_2} \bar{p}_s + \bar{u}_1, \tag{4.40b}$$

$$\bar{v}_s = \bar{v}_1 - \mathcal{M}_2\,(\mathcal{R}-1)\,\frac{\partial \bar{\xi}_s}{\partial \bar{y}}, \tag{4.40c}$$

$$\bar{\rho}_s = \frac{\Gamma}{\mathcal{M}_2^2} \bar{p}_s. \tag{4.40d}$$

In Eq. (4.40), $\bar{\xi}_s = k_y \xi_s / \varepsilon_u$ is the dimensionless shock displacement, whereas $\bar{p}_s$, $\bar{\rho}_s$, $\bar{u}_s$ and $\bar{v}_s$ are, respectively the dimensionless fluctuations of pressure, density, streamwise velocity and transverse velocity immediately downstream of the shock front, where thermochemical equilibrium is reached in the limit $k_y \ell_T \ll 1$. In these relations, $\bar{u}_1 = u_1 / (\varepsilon_u \langle a_2 \rangle)$ and $\bar{v}_1 = v_1 / (\varepsilon_u \langle a_2 \rangle)$ are the normalized components of the pre-shock velocity field (4.30) engendered by the incident wave described in Sec. 4.3.2. Note that, at the turning point of the Hugoniot curve ($\Gamma = 0$), the compression of the gas exerted by the shock is isochoric in the near field, and therefore leads to vanishing density fluctuations immediately downstream of the shock, as prescribed by the linearized jump condition (4.40d).

The flow is periodic in the transverse direction $\bar{y}$. As a result, the terms involving partial derivatives with respect to $\bar{y}$ in Eqs. (4.37a), (4.37c), (4.39) and (4.40c) can be easily calculated from the transverse functional form of the post-shock flow variables given the incident vorticity wave (4.32). In particular, it can be shown that the fluctuations $\bar{p}$, $\bar{u}$, and $\bar{\xi}_s$ are proportional to $\cos(\bar{y})$, whereas $\bar{v}$ is proportional to $\sin(\bar{y})$.

These prefactors are henceforth omitted in the analysis, but should be brought back when reconstructing the full solution from the dimensionless fluctuations.

The initial conditions required to solve Eq. (4.39) assume that the shock is initially flat, $\bar{\xi}_s = \bar{v}_s = 0$ at $\tau = 0$. Correspondingly, the initial values of the fluctuations of pressure and streamwise velocity immediately downstream of the shock must satisfy the relation $\bar{u}_s + \bar{p}_s = 0$ at $\tau = 0$, as prescribed by the first acoustic wave traveling upstream $x_c = -\tau$. This gives a pressure fluctuation $\bar{p}_s = -2\mathcal{M}_2/(1 + \Gamma + 2\mathcal{M}_2)$ immediately downstream of the shock front at $\tau = 0$.

The linearized problem(4.39), along with its boundary and initial conditions provided above, describe the fluctuations in the post-shock gas in the LIA framework. Remarkably, this problem can be integrated using the mean post-shock flow obtained from the analytical formulation provided in Sec. 4.2, as done in the remainder of this study, or by considering a mean post-shock flow obtained numerically with more sophisticated thermochemistry.

For instance, instead of the formulation presented in Sec. 4.2, a zero-dimensional chemical equilibrium code like the Combustion Toolbox (presented in Chapter 2) could be used to calculate numerically the mean post-shock conditions, as it will be shown in Sec. 4.5 incorporating (a) different models for the variations of the specific heats such as the NASA polynomials [128], which include both vibrational and electronic excitation, and (b) additional chemical effects such as ionization (a proper analysis with more complex phenomena is addressed for air in Chapter 5). This can be understood by noticing that Eq. (4.39), along with its boundary and initial conditions, depend only on the following dimensionless parameters: the mean density jump $\mathcal{R}$, the mean post-shock Mach number $\mathcal{M}_2$, and the inverse of the slope of the Hugoniot curve Γ, all of which can be computed numerically solving a zero-dimensional shock wave subject to arbitrary thermochemistry.

4.3.4 Far-field and long-time asymptotic analysis

Following the same procedure as in Appendix C (for detonations with inhomogeneities in the fuel mass fraction), at long times $t \gg (k_y \langle a_2 \rangle)^{-1}$, the solution to the wave equation (4.39), subject to the boundary conditions described in Sec. 4.3.3, yields the pressure fluctuations

$$\bar{p}_s = \begin{cases} \Pi_{l1} \cos(\omega\tau) + \Pi_{l2} \sin(\omega\tau) & \text{if } \zeta \leq 1 \\ \Pi_s \cos(\omega\tau) & \text{if } \zeta \geq 1 \end{cases} \tag{4.41}$$

behind the shock. In this formulation, $\omega = \zeta\sqrt{1-\mathcal{M}_2^2}$ is the dimensionless frequency, where ζ is a frequency parameter defined as

$$\zeta = \frac{\mathcal{M}_2\mathcal{R}}{\sqrt{1-\mathcal{M}_2^2}}\left(\frac{k_x}{k_y}\right), \tag{4.42}$$

with $k_x/k_y = 1/|\tan\theta|$. Cases with $\zeta \leq 1$ correspond to sufficiently small streamwise wavenumbers, $k_x \leq k_y(\sqrt{1-\mathcal{M}_2^2})/(\mathcal{M}_2\mathcal{R})$, whereas the opposite (sufficiently large streamwise wavenumbers) holds for $\zeta \geq 1$. The corresponding amplitudes of the pressure wave (4.41) are

$$\Pi_{l1} = -\frac{(1-\mathcal{R}^{-1})(\sigma_b\zeta^2-\sigma_c)}{\zeta^2(1-\zeta^2)+(\sigma_b\zeta^2-\sigma_c)^2}\left(\zeta^2 - \frac{\mathcal{R}\mathcal{M}_2^2}{1-\mathcal{M}_2^2}\right), \tag{4.43a}$$

$$\Pi_{l2} = \frac{(1-\mathcal{R}^{-1})\zeta\sqrt{1-\zeta^2}}{\zeta^2(1-\zeta^2)+(\sigma_b\zeta^2-\sigma_c)^2}\left(\zeta^2 - \frac{\mathcal{R}\mathcal{M}_2^2}{1-\mathcal{M}_2^2}\right), \tag{4.43b}$$

$$\Pi_{s} = -\frac{(1-\mathcal{R}^{-1})}{\zeta\sqrt{\zeta^2-1}+\sigma_b\zeta^2-\sigma_c}\left(\zeta^2 - \frac{\mathcal{R}\mathcal{M}_2^2}{1-\mathcal{M}_2^2}\right), \tag{4.43c}$$

where σ_b and σ_c are auxiliary factors defined as

$$\sigma_b = \frac{1+\Gamma}{2\mathcal{M}_2}, \quad \sigma_c = \frac{\mathcal{M}_2\mathcal{R}}{1-\mathcal{M}_2^2}\left(\frac{1-\Gamma}{2}\right). \tag{4.44}$$

To describe the far-field post-shock gas, it is convenient to split the fluctuations of velocity, pressure and density into their acoustic (a), vortical (r), and entropic (e) components as

$$\bar{u}(\bar{x}_c,\tau) = \bar{u}_a(\bar{x}_c,\tau) + \bar{u}_r(\bar{x}_c), \tag{4.45a}$$

$$\bar{v}(\bar{x}_c,\tau) = \bar{v}_a(\bar{x}_c,\tau) + \bar{v}_r(\bar{x}_c), \tag{4.45b}$$

$$\bar{p}(\bar{x}_c,\tau) = \bar{p}_a(\bar{x}_c,\tau), \tag{4.45c}$$

$$\bar{\rho}(\bar{x}_c,\tau) = \bar{\rho}_a(\bar{x}_c,\tau) + \bar{\rho}_e(\bar{x}_c). \tag{4.45d}$$

The acoustic pressure wave emerging from Eq. (4.39) is of the form $\bar{p}_a \sim \mathrm{e}^{\pm\mathrm{i}(\omega_a\tau-\kappa_a\bar{x}-\bar{y})}$, where ω_a and κ_a are the dimensionless acoustic frequency and longitudinal wavenumber reduced with a_2k_y and k_y, respectively, which are related as

$$\omega_a^2 = \kappa_a^2 + 1. \tag{4.46}$$

In the shock reference frame $\bar{x} = \mathcal{M}_2\tau$, the oscillation frequency at shock front, ω, is

related to the post-shock Mach number as $\omega = \omega_a - \mathcal{M}_2\kappa_a$. Upon substituting this relation into Eq. (4.46), the expressions

$$\kappa_a = \frac{\mathcal{M}_2\omega \pm \sqrt{\omega^2 - 1 + \mathcal{M}_2^2}}{1 - \mathcal{M}_2^2}, \tag{4.47a}$$

$$\omega_a = \frac{\omega \pm \mathcal{M}_2\sqrt{\omega^2 - 1 + \mathcal{M}_2^2}}{1 - \mathcal{M}_2^2}, \tag{4.47b}$$

are obtained. In (4.47), the solution corresponding to the positive sign in front of the square root must be excluded since it represents nonphysical acoustic waves whose amplitude increases exponentially with distance downstream of the shock when $\omega < (1 - \mathcal{M}_2^2)^{1/2}$.

Different forms of the solution arise depending on the value of the dimensionless frequency ω. At frequencies $\omega < (1 - \mathcal{M}_2^2)^{1/2}$, or equivalently $\zeta < 1$, the amplitude of the acoustic pressure decreases exponentially with distance downstream of the shock. On the other hand, for $\omega > (1 - \mathcal{M}_2^2)^{1/2}$, or $\zeta > 1$, the acoustic pressure becomes a constant-amplitude wave,

$$\bar{p}(\bar{x}_c, \tau) = \Pi_s \cos(\omega_a\tau - \kappa_a\bar{x}_c), \tag{4.48}$$

which corresponds to a downstream-traveling sound wave for $\kappa_a < 0$ (or $\omega < 1$), and to an upstream-traveling sound wave for $\kappa_a > 0$ ($\omega > 1$), both cases being referenced to the post-shock gas reference frame. In this case, the acoustic modes of the density, temperature, and velocities are

$$\bar{\rho}_a(\bar{x}_c, \tau) = \Pi_s \cos(\omega_a\tau - \kappa_a\bar{x}_c), \tag{4.49a}$$

$$\bar{T}_a(\bar{x}_c, \tau) = \Theta_a \cos(\omega_a\tau - \kappa_a\bar{x}_c), \tag{4.49b}$$

$$\bar{u}_a(\bar{x}_c, \tau) = \mathcal{U}_a \cos(\omega_a\tau - \kappa_a\bar{x}_c), \tag{4.49c}$$

$$\bar{v}_a(\bar{x}_c, \tau) = \mathcal{V}_a \sin(\omega_a\tau - \kappa_a\bar{x}_c), \tag{4.49d}$$

respectively, where $\bar{T} = (T - \langle T_2\rangle)/(\varepsilon_u\langle T_2\rangle)$ is the dimensionless post-shock temperature fluctuation.

The amplitudes of the acoustic modes of the streamwise and transverse velocity fluctuations in Eq. (4.49) are proportional to the amplitude of the acoustic pressure, $\mathcal{U}_a/\Pi_s = \kappa_a/\omega_a$ and $\mathcal{V}_a/\Pi_s = 1/\omega_a$, as prescribed by second and third equations in (4.37). Similarly, the amplitude of the acoustic mode of the post-shock temperature

fluctuations can be expressed relative to Π_s as

$$\Theta_a/\Pi_s = \frac{2(1+\alpha) - \alpha_R\,(1 - 2\bar{e}_{\mathrm{vib}} + 2\beta_d/\mathcal{T})}{5 + \alpha + 2(1-\alpha)\bar{e}_{\mathrm{vib}}^2 \mathrm{e}^{-\beta_v/\mathcal{T}} + \alpha_T\,(1 - 2\bar{e}_{\mathrm{vib}} + 2\beta_d/\mathcal{T})}, \tag{4.50}$$

with $\bar{e}_{\mathrm{vib}}$, α_R, and α_T being defined in Eqs. (4.16) to (4.18), respectively. Note that (4.50) simplifies to $\Theta_a/\Pi_s \sim \gamma - 1$ in both the calorically perfect diatomic gas limit ($\alpha \to 0$ and $\beta_v \to \infty$, for which $\gamma \to 7/5$) and in the fully dissociated gas limit ($\alpha \to 1$, for which $\gamma \to 5/3$). On the other hand, in the limit with vibrational excitation ($\alpha \to 0$ and $\beta_v = \theta_v/T_1$, for which $\gamma \to 7/5$) we have $\Theta_a/\Pi_s \sim (\gamma-1)/[1+(\gamma-1)\bar{e}_{\mathrm{vib}}^2 \mathrm{e}^{-\beta_v/\mathcal{T}}]$.

The entropic mode of the density fluctuations is determined by the linearized Rankine-Hugoniot jump condition (4.40d) after subtracting the acoustic mode

$$\bar{\rho}_e(\bar{x}_c) = \frac{\Gamma}{\mathcal{M}_2^2}\bar{p}_s(\tau = \bar{x}_c/\mathcal{M}_2) - \bar{\rho}_a(\bar{x}_c, \tau = \bar{x}_c/\mathcal{M}_2) \tag{4.51}$$

to give

$$\bar{\rho}_e(\bar{x}_c \gg 1) = \begin{cases} \Delta_{l1}\cos(\kappa_e \bar{x}_c) + \Delta_{l2}\sin(\kappa_e \bar{x}_c) & \text{if } \zeta \le 1 \\ \Delta_s \cos(\kappa_e \bar{x}_c) & \text{if } \zeta \ge 1 \end{cases} \tag{4.52}$$

in the asymptotic far field. In (4.52), $\kappa_e = \mathcal{R}k_x/k_y$ is a dimensionless wavenumber, and $\Delta_j = (\Gamma\mathcal{M}_2^{-2} - 1)\Pi_j$ is a fluctuation amplitude that depends on ζ through the pressure amplitudes Π_{l1}, Π_{l2}, and Π_s defined in (4.43). Since the pre-shock gas contains only vortical velocity fluctuations, all entropic modes are generated at the shock.

The entropic density fluctuations $\bar{\rho}_e$ are related to the entropic temperature fluctuations

$$\bar{T}_e(\bar{x}_c \gg 1) = -\frac{1 + \alpha + \alpha_R}{1 + \alpha + \alpha_T}\bar{\rho}_e(\bar{x}_c), \tag{4.53}$$

and both $\bar{\rho}_e$ and $\bar{T}_e$ induce entropic fluctuations in the degree of dissociation, as shown in (4.8). As a result, the thermochemical equilibrium state in the post-shock gas fluctuates depending on the local shock curvature. Specifically, there exist fluctuations of the concentrations of the chemical species A and A_2 in the post-shock gas that are in phase with the entropic modes of density and temperature fluctuations. The normalized fluctuation of the degree of dissociation is

$$\begin{aligned} \bar{\alpha}(\bar{x}_c \gg 1) = \frac{\alpha - \langle\alpha\rangle}{\varepsilon_u} &= \alpha_R\bar{\rho}_e(\bar{x}_c) + \alpha_T\bar{T}_e(\bar{x}_c) \\ &= \frac{(\alpha_R - \alpha_T)(1+\alpha)}{1 + \alpha + \alpha_T}\bar{\rho}_e(\bar{x}_c). \end{aligned} \tag{4.54}$$

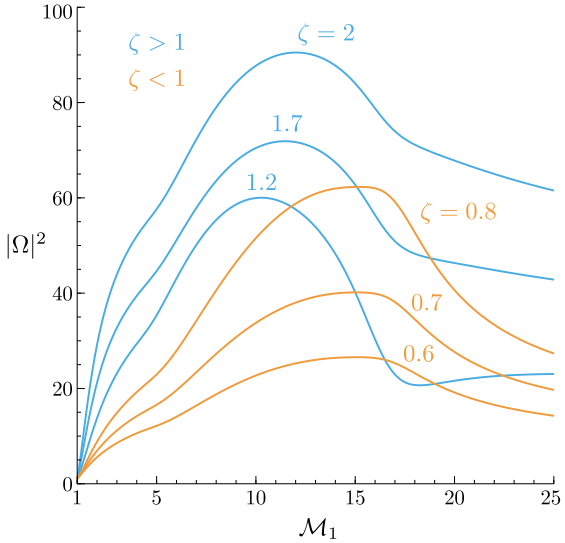

Figure 4.6: Square of the vorticity amplitude $|\Omega|^2$ as a function of the pre-shock Mach number $\mathcal{M}_1$ for $B = 10^4$, $\beta_v = 10$, $\beta_d = 100$, and six different values of the frequency parameter: $\zeta = 0.6$, 0.7, 0.8, 1.2, 1.7, and 2.

In a similar manner, the vorticity fluctuations $\bar{\varpi}$ defined in (4.35) can be expressed in terms of ζ as

$$\bar{\varpi}(\bar{x}_c \gg 1) = \begin{cases} \Omega_l \cos(\kappa_r \bar{x}_c + \phi_r) & \text{if } \zeta \leq 1 \\ \Omega_s \cos(\kappa_r \bar{x}_c) & \text{if } \zeta \geq 1 \end{cases} \tag{4.55}$$

where, as found in the entropic perturbation field, the dimensionless rotational wavenumber is simply given by the compressed upstream wavenumber ratio $\kappa_r = \kappa_e = \mathcal{R}k_x/k_y$. The amplitudes are

$$\Omega_l = \sqrt{(\Omega_1 + \Omega_2 \Pi_{l1})^2 + (\Omega_2 \Pi_{l2})^2}, \tag{4.56a}$$

$$\Omega_s = \Omega_1 + \Omega_2 \Pi_s, \tag{4.56b}$$

where $\Omega_1 = \mathcal{R}(1 + k_x^2/k_y^2)$ quantifies the amplification of the pre-shock vorticity as a direct result of the shock compression and $\Omega_2 = (\mathcal{R} - 1)(1 - \Gamma)/(2\mathcal{M}_2)$ measures the vorticity production by the discontinuity front rippling. The corresponding phase for $\zeta < 1$ is given by $\tan \phi_r = \Omega_2 \Pi_{l2}/(\Omega_1 + \Omega_2 \Pi_{l1})$, which is different to that associated to entropic fluctuations $\tan \phi_e = \Pi_{l2}/\Pi_{l1}$.

Figure 4.6 shows the value of $|\Omega|^2$ as a function of the shock strength $\mathcal{M}_1$ for six arbitrary values of the frequency parameter ζ. Three of them pertain to the long-wavelength regime $\zeta < 1$ ($\Omega = \Omega_l$) and the other three to the short-wavelength regime

$\zeta > 1$ ($\Omega = \Omega_s$). It is found that the shape of the curve qualitatively changes depending on the wavelength regime. For instance, when compared to interactions with frequency $\zeta < 1$, cases for $\zeta > 1$ render curves with wider peaks and whose location corresponds to lower Mach numbers.

The streamwise and transverse components of the vortical mode of the velocity read

$$\bar{u}_r(\bar{x}_c \gg 1) = \mathcal{U}_r \cos(\kappa_r \bar{x}_c + \phi_r), \tag{4.57a}$$

$$\bar{v}_r(\bar{x}_c \gg 1) = \mathcal{V}_r \sin(\kappa_r \bar{x}_c + \phi_r), \tag{4.57b}$$

where the phase angle is $\phi_r = 0$ for $\zeta > 1$. The amplitudes are proportional to the vorticity fluctuations as

$$\mathcal{U}_r = \frac{1}{1+\kappa_r^2}\Omega = \frac{\mathcal{M}_2^2}{\mathcal{M}_2^2 + (1-\mathcal{M}_2^2)\,\zeta^2}\Omega, \tag{4.58a}$$

$$\mathcal{V}_r = \frac{\kappa_r}{1+\kappa_r^2}\Omega = \frac{\zeta \mathcal{M}_2 \sqrt{1-\mathcal{M}_2^2}}{\mathcal{M}_2^2 + (1-\mathcal{M}_2^2)\,\zeta^2}\Omega, \tag{4.58b}$$

where Ω depends on frequency, as shown in Eq. (4.56) and Fig. 4.6.

4.4 The interaction of a hypersonic shock wave with weak isotropic turbulence

The weak isotropic turbulence in the pre-shock gas can be represented by a linear superposition of incident vorticity waves whose amplitudes ε vary with the wavenumber in accord with an isotropic energy spectrum $E(k) = \varepsilon^2(k)$. The root mean square (rms) of the velocity and vorticity fluctuations in the pre-shock gas can be calculated by invoking the isotropy assumption, which states that the probability the incident wave has of having orientation angles ranging from θ to $\theta + d\theta$, and from φ to $\varphi + d\varphi$, is proportional to the solid angle $\sin\theta \mathrm{d}\theta \mathrm{d}\varphi/(4\pi)$. This assumption provides the expressions

$$\frac{\langle u_1'^2 \rangle}{\varepsilon^2 \langle a_2 \rangle^2} = \frac{1}{3}, \quad \frac{\langle v_1'^2 \rangle}{\varepsilon^2 \langle a_2 \rangle^2} = \frac{1}{6}, \quad \frac{\langle \varpi_1'^2 \rangle}{\varepsilon^2 \langle a_2 \rangle^2} = \frac{1}{2} \tag{4.59}$$

for the pre-shock rms velocity fluctuations, and

$$\frac{\langle \varpi_{x,1}'^2 \rangle}{\varepsilon^2 k^2 \langle a_2 \rangle^2} = \frac{1}{3}, \quad \frac{\langle \varpi_{y,1}'^2 \rangle}{\varepsilon^2 k^2 \langle a_2 \rangle^2} = \frac{1}{6}, \quad \frac{\langle \varpi_{z,1}'^2 \rangle}{\varepsilon^2 k^2 \langle a_2 \rangle^2} = \frac{1}{2} \tag{4.60}$$

for the pre-shock vorticity fluctuations. In this section, a linear analysis is performed to calculate the variations of the rms of the velocity and vorticity fluctuations across the shock.

4.4.1 Amplifications of turbulent kinetic energy, turbulence intensity, and turbulent Reynolds number across the shock

The analysis begins by expressing pre-shock components of the velocity fluctuation modulus as

$$|u_2'| = a_2\varepsilon|\bar{u}_a + \bar{u}_r|\sin\theta\sin\varphi, \tag{4.61a}$$
$$|v_2'| = a_2\varepsilon|\bar{v}_a + \bar{v}_r|\sin\theta\sin\varphi, \tag{4.61b}$$
$$|w_2'| = |w_1'|, \tag{4.61c}$$

where the acoustic and vortical modes of the dimensionless velocity fluctuations in the far field are given in Eqs. (4.49) and (4.57). The relations between the modes of the streamwise and transverse velocity fluctuations are provided by the irrotationality condition $\bar{v}_a = \kappa_a\bar{u}_a$ for the acoustic mode, and by the solenoidal condition $k_y\bar{v}_r = \mathcal{R}k_x\bar{u}_r$ for the vortical mode.

The TKE amplification factor across the shock wave is defined as

$$\begin{aligned} K &= \frac{\langle u_2'^2\rangle + \langle v_2'^2\rangle + \langle w_2'^2\rangle}{\langle u_1'^2\rangle + \langle v_1'^2\rangle + \langle w_1'^2\rangle} = \frac{\langle u_2'^2\rangle + \langle v_2'^2\rangle}{\varepsilon^2\langle a_2\rangle^2} + \frac{1}{2} \\ &= \frac{1}{2}\left[\int_0^{\pi/2}\left(\bar{u}^2 + \bar{v}^2\right)\sin^3\theta\mathrm{d}\theta + 1\right], \end{aligned}$$

where use of Eq. (4.59) has been made. Furthermore, K can also be decomposed linearly into acoustic and vortical modes as $K = K^a + K^r$, with

$$K^a = \frac{1}{3}\int_1^\infty \left(\mathcal{U}_a^2 + \mathcal{V}_a^2\right)\mathrm{P}(\zeta)\mathrm{d}\zeta = \frac{1}{3}\int_1^\infty \Pi_s^2\mathrm{P}(\zeta)\mathrm{d}\zeta, \tag{4.62a}$$
$$K^r = \frac{1}{2} + \frac{1}{3}\int_0^\infty \left(\mathcal{U}_r^2 + \mathcal{V}_r^2\right)\mathrm{P}(\zeta)\mathrm{d}\zeta. \tag{4.62b}$$

The entropic mode does not contain any kinetic energy, since entropy fluctuations are decoupled from velocity fluctuations in the inviscid linear limit. In Eq. (4.62), $\mathrm{P}(\zeta)$ is a

probability-density distribution given by

$$\mathrm{P}(\zeta) = \frac{3}{2} \frac{\mathcal{M}_2^4 \mathcal{R}^4 \sqrt{1-\mathcal{M}_2^2}}{\left[\mathcal{M}_2^2 \mathcal{R}^2 + \zeta^2 \left(1-\mathcal{M}_2^2\right)\right]^{5/2}}, \tag{4.63}$$

which satisfies the normalization $\int_0^\infty \mathrm{P}(\zeta)\mathrm{d}\zeta = 1$. In addition, the velocity amplitudes $\mathcal{U}_a$, $\mathcal{U}_r$, $\mathcal{V}_a$, and $\mathcal{V}_r$ are obtained using the long-time far-field asymptotic expressions Eqs. (4.49) and (4.58). The lower integration limit of K^a is $\zeta = 1$ since the acoustic mode decays exponentially with distance downstream of the shock in the long-wave regime $\zeta < 1$. However, the integral $1/3 \int_0^1 (\Pi_{l1}^2 + \Pi_{l1}^2)\mathrm{P}(\zeta)\mathrm{d}\zeta$ needs to be added to K^a when evaluating the solution in the near field $\bar{x}_s - \bar{x}_c \ll 1$.

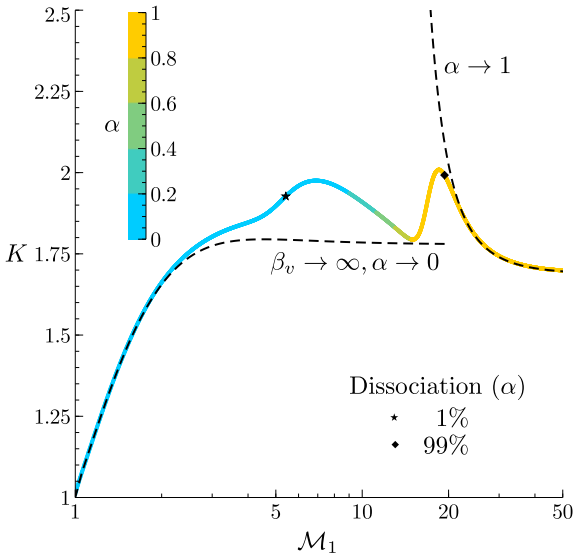

Figure 4.7: TKE amplification factor K as a function of the pre-shock Mach number $\mathcal{M}_1$ for $B = 10^4$, $\beta_v = 10$, and $\beta_d = 100$ (line colored by the degree of dissociation). Dashed lines correspond to limit behavior of K calculated using the asymptotic expressions (4.23) and (4.25) for small and high Mach numbers, respectively.

Figure 4.7 shows the TKE amplification factor K, given by the sum of the acoustic and vortical contributions in Eq. (4.62), as a function of the pre-shock Mach number $\mathcal{M}_1$. Similarly to the results observed in Sec. 4.2, the onset of vibrational excitation at $\mathcal{M}_1 \sim 3$ begins to produce small departures of K from the thermochemically frozen result corresponding to a diatomic calorically perfect gas. These departures are exacerbated as the degree of dissociation increases, and become significant even at small values of α of order 1% at $\mathcal{M}_1 \sim 5$, where K significantly departs from the curve

predicted in the thermochemically frozen limit corresponding to a diatomic calorically perfect gas. The latter was shown to plateau at $K = 1.78$ for $\mathcal{M}_1 \gg 1$ in early work [62, 275], whereas the present study indicates that such plateau does not exist when thermochemical effects at hypersonic Mach numbers are accounted for.

The resulting curve of K in Fig. 4.7 is non-monotonic and contains two peaks in the hypersonic range of Mach numbers. This behavior cannot be guessed by a simple inspection of the post-shock density and Mach number shown in Fig. 4.4. Instead, the non-monotonicity of K is related to the strong dependence of the enstrophy amplification on the wavenumber. Specifically, the vortical mode of the velocity fluctuation, which is shown below to be the most energetic, is proportional to the post-shock vorticity amplitude Ω given in Eq. (4.56), which peaks at different pre-shock Mach numbers depending on the frequency parameter ζ, as shown in Fig. 4.6.

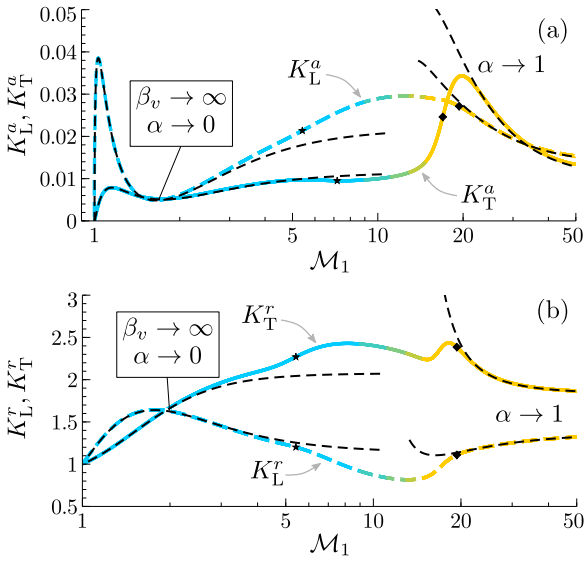

Figure 4.8: (a) Acoustic and (b) vortical modes of the streamwise (K_{L}) and transverse (K_{T}) components of the TKE amplification factor as a function of the pre-shock Mach number $\mathcal{M}_1$ for $B = 10^4$, $\beta_v = 10$, and $\beta_d = 100$ (lines colored by the degree of dissociation; refer to Fig. 4.7 for a colorbar). Dashed lines correspond to limit behavior of K_{L} and K_{T} calculated using the asymptotic expressions(4.23) and (4.25) for small and high Mach numbers, respectively.

The two peaks render a similar local maximum. The first peak of K reaches a value of 1.97 and occurs at $\mathcal{M}_1 \sim 7$, where $\alpha \sim 6\%$. In contrast, the second peak occurs at a Mach number of $\mathcal{M}_1 \sim 18$, where dissociation is almost complete and

yields a value of $K \sim 2$. Note that these peaks are approximately 10% higher than the value predicted in the thermochemically frozen limit. At very large Mach numbers $\mathcal{M}_1 > 40$, in the fully dissociated regime, K asymptotes to the value $K \sim 1.69$ predicted for monatomic calorically perfect gases. However, as discussed in Sec. 4.2.4, this limit has to be interpreted with caution because additional thermochemical effects not included here, such as ionization and electronic excitation, play an important role at those extreme Mach numbers. These effects will be addressed in Sec. 4.5 for the electronic excitation and in Chapter 5 for both the electronic excitation and ionization in a multi-species mixture. Additionally, Appendix D extends the theoretical framework described in Sec. 4.2 to account for the electronic excitation and ionization in monatomic and diatomic gases.

Most of the TKE produced across the shock belongs to transverse velocity fluctuations of the vortical mode. To see this, consider the decomposition of the TKE amplification factor into longitudinal (K_L) and transverse (K_T) components as

$$K = \frac{1}{3}(K_\mathrm{L} + 2K_\mathrm{T}), \tag{4.64}$$

with

$$K_\mathrm{L} = \underbrace{\int_1^\infty \mathcal{U}_a^2 \mathrm{P}(\zeta)\mathrm{d}\zeta}_{K_\mathrm{L}^a} + \underbrace{\int_0^\infty \mathcal{U}_r^2 \mathrm{P}(\zeta)\mathrm{d}\zeta}_{K_\mathrm{L}^r}, \tag{4.65a}$$

kinetic energy of the longitudinal acoustic mode — kinetic energy of the longitudinal vortical mode

$$K_\mathrm{T} = \underbrace{\frac{1}{2}\int_1^\infty \mathcal{V}_a^2 \mathrm{P}(\zeta)\mathrm{d}\zeta}_{K_\mathrm{T}^a} + \underbrace{\frac{3}{4} + \frac{1}{2}\int_0^\infty \mathcal{V}_r^2 \mathrm{P}(\zeta)\mathrm{d}\zeta}_{K_\mathrm{T}^r}. \tag{4.65b}$$

kinetic energy of the transverse acoustic mode — kinetic energy of the transverse vortical mode

The contribution of the acoustic mode to K_L and K_T yields negligible TKE over the entire range of Mach numbers, as shown in Fig. 4.8(a). In contrast, the contribution of the vortical mode is significant. Whereas the longitudinal TKE of the vortical mode K_L^r dominates over the transverse one K_T^r at supersonic Mach numbers, it plunges below K_T^r at hypersonic Mach numbers around the turning point of the Hugoniot curve. The value of K_T^r peaks at $\mathcal{M}_1 \sim 18$ with $K_\mathrm{T}^r \sim 2.4$, as observed in Fig. 4.8(b). This peak is responsible for the peak in K observed in Fig. 4.7 at the same Mach number, thereby indicating that most the TKE there is stored in vortical gas motion in the transverse direction.

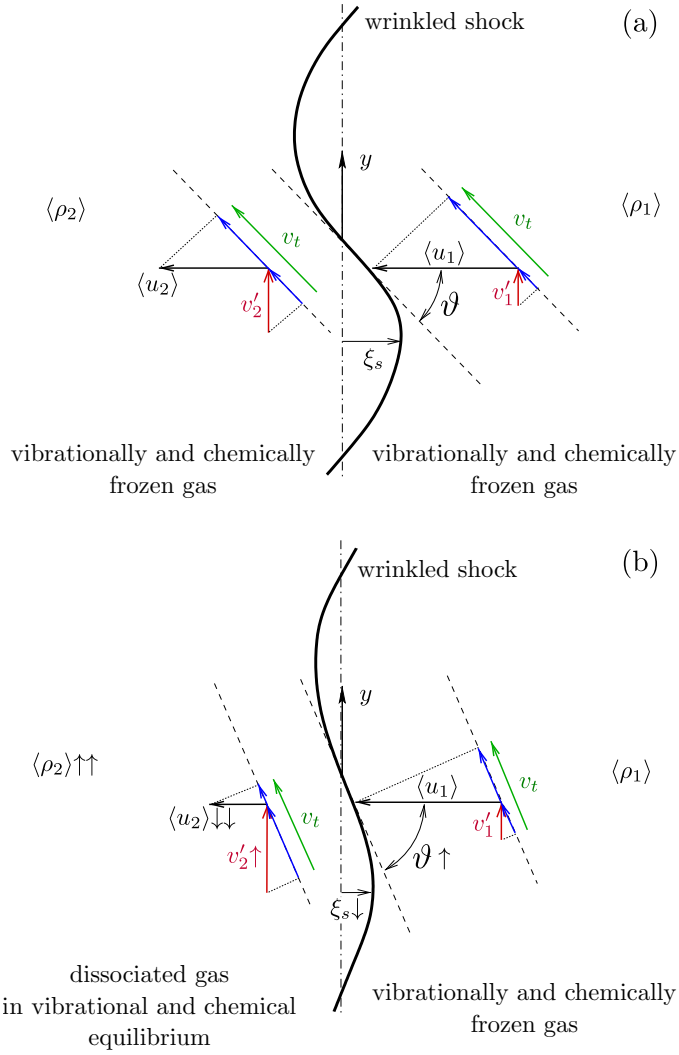

Figure 4.9: Schematics of the mechanism of TKE amplification for (a) thermochemically frozen (i.e., diatomic calorically perfect) post-shock gas, and (b) thermochemically equilibrated post-shock gas, both panels simulating the same pre-shock conditions. The flow is from right to left. The magnitude of the shock displacement and velocity perturbations have been exaggerated for illustration purposes.

The mechanism whereby high-temperature thermochemistry augments the TKE across the shock in this LIA framework is explained by the linearized Rankine-Hugoniot jump condition (4.40c) and is schematically shown in Fig. 4.9. In particular, the conservation of the tangential velocity across the wrinkled shock requires

$$\begin{aligned} v_t &= \langle u_1 \rangle \cos\vartheta + v_1' \sin\vartheta \\ &= \langle u_2 \rangle \cos\vartheta + v_2' \sin\vartheta, \end{aligned} \tag{4.66}$$

where $\vartheta = \pi/2 + \arctan(\partial\xi_s/\partial y)$ is a local shock incidence angle whose departures from $\pi/2$ are of order ε_u, since $k_y\xi_s = O(\varepsilon_u)$ in this linear theory. The streamwise velocity fluctuations u_1' and u_2' have been neglected in writing Eq. (4.66), since their multiplication by $\cos\beta$ is smaller by a factor of order ε_u relative to the other terms. Equation (4.66) yields the transverse post-shock velocity fluctuation

$$v_2' = v_1' - (\langle u_1 \rangle - \langle u_2 \rangle) \frac{\partial \xi_s}{\partial y}, \tag{4.67}$$

which represents the dimensional counterpart of the linearized Rankine-Hugoniot jump condition (4.40c). In (4.67), $\partial\xi_s/\partial y < 0$ in both configurations sketched in Fig. 4.9. Note that Eq. (4.67) holds independently of whether the gas is thermochemically frozen or equilibrated. However, the thermochemistry influences (4.67) by flattening the shock front (i.e., by decreasing $\partial\xi_s/\partial y$) while strongly decreasing the mean post-shock velocity $\langle u_2 \rangle = \langle u_1 \rangle / \mathcal{R}$, with the latter effect prevailing over the former. As a result, v_2' and its associated kinetic energy K_T are larger relative to those observed in a diatomic calorically perfect gas.

The TKE amplification, along with the aforementioned decrease in the mean post-shock velocity $\langle u_2 \rangle$ caused by the thermochemical effects, also lead to a strong amplification of the turbulence intensity across the shock. Specifically, the ratio of post- to pre-shock turbulence intensities

$$\frac{\mathcal{I}_2}{\mathcal{I}_1} = \frac{u_{\ell,2}/\langle u_2 \rangle}{u_{\ell,1}/\langle u_1 \rangle} = K^{1/2}\mathcal{R} \tag{4.68}$$

is found to peak at the turning point of the Hugoniot curve ($\alpha \simeq 0.6$, $\mathcal{T} \simeq 13$, $\mathcal{M}_1 \simeq 13$, and $\mathcal{R} \simeq 10$) with a value $\mathcal{I}_2/\mathcal{I}_1 \simeq 14$, as shown in Fig. 4.10(a). This is in contrast to the maximum value $\mathcal{I}_2/\mathcal{I}_1 \simeq 8$ predicted by the theory of calorically perfect gases.

Although the theory presented above is formulated in the inviscid limit, the ratio of

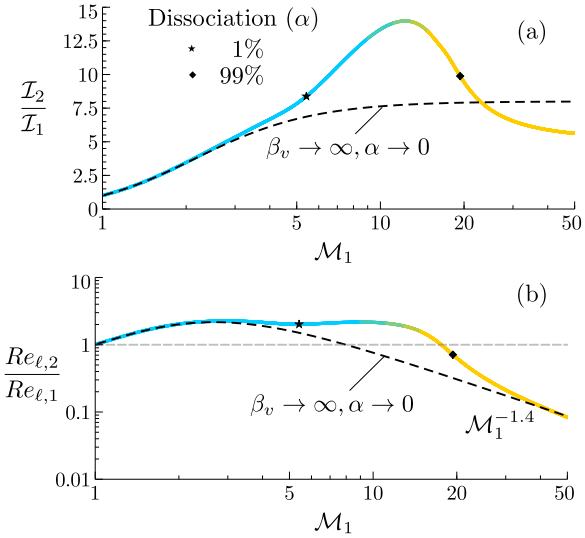

Figure 4.10: Amplification of (a) turbulence intensity and (b) turbulent Reynolds number across the shock as a function of the pre-shock Mach number $\mathcal{M}_1$ for $B = 10^4$, $\beta_v = 10$, and $\beta_d = 100$ (lines colored by the degree of dissociation; refer to Fig. 4.7 for a colorbar). The dashed lines correspond to the values of $\mathcal{I}_2/\mathcal{I}_1$ and $Re_{\ell,2}/Re_{\ell,1}$ calculated assuming that the post-shock gas is thermochemically frozen (i.e., diatomic calorically perfect).

post- to pre-shock turbulent Reynolds numbers

$$\frac{Re_{\ell,2}}{Re_{\ell,1}} = \frac{u_{\ell,2}\ell_2/\nu_2}{u_{\ell,1}\ell_1/\nu_1} = \frac{K^{1/2}}{\mathcal{T}^{0.7}}\sqrt{\frac{2\mathcal{R}^2+1}{3}} \tag{4.69}$$

is a finite quantity that can be calculated. In the last term of (4.69), use has been made of the fact that the only wavenumber that is distorted through the shock is the longitudinal one, which changes from k_x in the pre-shock fluctuations to $k_x\mathcal{R}$ in the post-shock ones. Additionally, the molecular viscosity is assumed to vary with temperature raised to the power of 0.7.

Remarkably, the vortical post-shock fluctuations downstream of the hypersonic shock are not only much more intense than those upstream, but they also have a higher turbulent Reynolds number $Re_{\ell,2} > Re_{\ell,1}$, as shown in Fig. 4.10(b). Similarly to the turbulence intensities, the maximum ratio of turbulent Reynolds numbers across the shock is reached at the turning point of the Hugoniot curve ($\alpha \simeq 0.6$, $\mathcal{T} \simeq 13$, $\mathcal{M}_1 \simeq 13$, and $\mathcal{R} \simeq 10$) with a value of $Re_{\ell,2}/Re_{\ell,1} \simeq 2.3$. In contrast, the theory of calorically perfect gases predicts an attenuation of the turbulent Reynolds number

at those conditions. When thermochemical effects are accounted for, the amplification of the turbulent Reynolds number lasts until $\mathcal{M}_1 \simeq 18$, beyond which the increase in post-shock temperature and the decrease in post-shock density make $Re_{\ell,2}/Re_{\ell,1}$ to plummet below unity.

In summary, the increase of transverse velocity fluctuations of the vortical mode across the shock is responsible for the TKE amplification in this linear theory. In addition, the results indicate that the TKE is more amplified when dissociation and vibrational excitation are accounted for at high Mach numbers. In the conditions tested here, the post-shock fluctuations resulting at hypersonic Mach numbers can be -at most- 14-times more intense and can have -at most- a 2.3-times larger turbulent Reynolds number than the pre-shock fluctuations.

4.4.2 Amplifications of anisotropy, enstrophy, and variances of density and degree of dissociation across the shock

The weak isotropic turbulence in the pre-shock gas becomes anisotropic as it traverses the shock wave. An anisotropy factor that quantifies this change can be defined as [275]

$$\Psi = \frac{\langle \bar{v}^2 \rangle + \langle \bar{w}^2 \rangle - 2\langle \bar{u}^2 \rangle}{\langle \bar{v}^2 \rangle + \langle \bar{w}^2 \rangle + 2\langle \bar{u}^2 \rangle} = 1 - \frac{2K_{\mathrm{L}}}{K_{\mathrm{L}} + K_{\mathrm{T}}}, \tag{4.70}$$

with $-1 \leq \Psi \leq 1$. The cases $\Psi = -1$ and 1 represent anisotropic turbulent flows dominated by longitudinal and transverse velocity fluctuations, respectively. In contrast, $\Psi = 0$ corresponds to an isotropic turbulent flow, $K_{\mathrm{T}} = K_{\mathrm{L}} = K$. Figure 4.11 shows that dissociation and vibrational excitation dissociation lead to larger anisotropy factors in the post-shock gas compared to the thermochemically frozen (diatomic calorically perfect) case in the relevant range of hypersonic Mach numbers up to the fully-dissociated gas limit.

The vortical motion downstream of the shock is quantified by the enstrophy amplification factor

$$W = \frac{\langle \varpi'^2_{x,2} \rangle + \langle \varpi'^2_{y,2} \rangle + \langle \varpi'^2_{z,2} \rangle}{\langle \varpi'^2_{x,1} \rangle + \langle \varpi'^2_{y,1} \rangle + \langle \varpi'^2_{z,1} \rangle} = \frac{1}{3} + \frac{2}{3} W_{\perp}, \tag{4.71}$$

where use of Eq. (4.60) and of the invariance of the normal vorticity across the shock has been made. In (4.71), $W_{\perp}$ is the enstrophy amplification factor in the transverse direction

$$W_{\perp} = \frac{1}{3} + \frac{2}{3} \frac{\langle \varpi'^2_{y,2} \rangle + \langle \varpi'^2_{z,2} \rangle}{\langle \varpi'^2_{y,1} \rangle + \langle \varpi'^2_{z,1} \rangle} = \frac{\mathcal{R} + 3W_z}{4}, \tag{4.72}$$

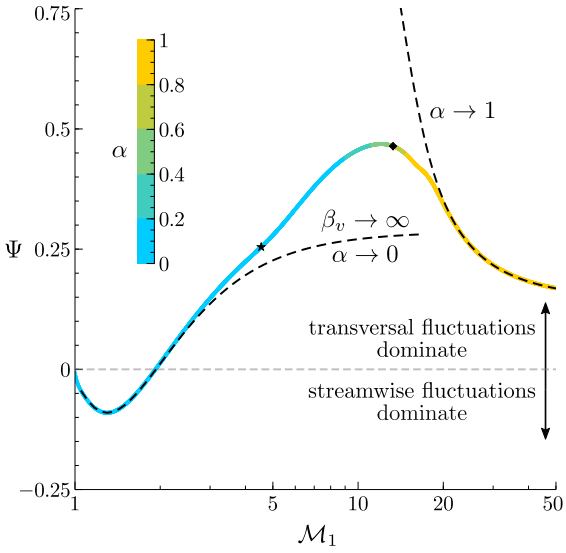

Figure 4.11: Anisotropy factor Ψ as a function of the pre-shock Mach number $\mathcal{M}_1$ for $B = 10^4$, $\beta_v = 10$, and $\beta_d = 100$ (line colored by the degree of dissociation). Dashed lines correspond to limit behavior of Ψ calculated using the asymptotic expressions (4.23) and (4.25) for small and high Mach numbers, respectively.

with

$$W_z = \frac{\langle \varpi'^2_{z,2} \rangle}{\langle \varpi'^2_{z,1} \rangle} = \int_0^\infty \Omega^2 \frac{\mathcal{R}^2 \mathcal{M}_2^2 \, \mathrm{P}(\zeta)}{\mathcal{R}^2 \mathcal{M}_2^2 + (1 - \mathcal{M}_2^2)\zeta^2} \mathrm{d}\zeta \tag{4.73}$$

being the amplification factor of the rms of the $z-$component of the vorticity. Equation (4.73) includes the asymptotic amplitudes defined in (4.56) and the relation

$$\sin^2 \theta(\zeta) \mathrm{P}(\zeta) = \frac{3}{2} \frac{\mathcal{M}_2^6 \mathcal{R}^6 \sqrt{1 - \mathcal{M}_2^2}}{\left[\mathcal{M}_2^2 \mathcal{R}^2 + \zeta^2 \left(1 - \mathcal{M}_2^2\right)\right]^{7/2}}. \tag{4.74}$$

The enstrophy amplification factor W is provided in Fig. 4.12 as a function of the pre-shock Mach number. Unlike Fig. 4.7 for K, the curve of W displays only one maxima, but the differences with respect to the thermochemically frozen case are much larger for W. This peak of W is dominated by the increase of short-wavelength vorticity, as shown in Fig. 4.6, and it represents an amplification of nearly 2.5-times the enstrophy predicted by the theory of calorically perfect gases.

Whereas the pre-shock density is uniform because of the vortical character of the incident modes, the density in the post-shock gas fluctuates due to both acoustic and

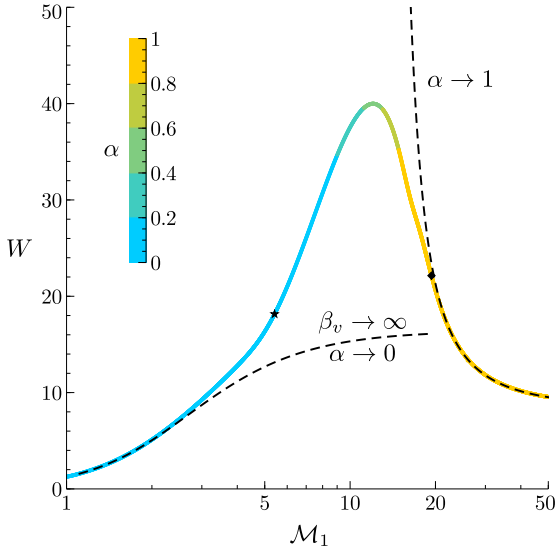

Figure 4.12: Enstrophy W as a function of the pre-shock Mach number $\mathcal{M}_1$ for $B = 10^4$, $\beta_v = 10$, and $\beta_d = 100$ (line colored by the degree of dissociation). Dashed lines correspond to limit behavior of W calculated using the asymptotic expressions (4.23) and (4.25) for small and high Mach numbers, respectively.

entropic modes generated by the shock wrinkles. To investigate these fluctuations, consider the normalized density variance

$$\frac{\langle \rho_2'^2 \rangle}{\langle \rho_2^2 \rangle} = (G^a + G^e) \int_0^\infty E(k) k^2 \mathrm{d}k, \tag{4.75}$$

which depends on the integral of the energy spectrum E over the entire wavenumber space. The prefactors G^a and G^e represent density-variance components induced by acoustic and entropic modes, respectively, and are given by

$$G^a = K^a, \tag{4.76a}$$

$$G^e = \left(\Gamma \mathcal{M}_2^{-2} - 1\right)^2 \int_0^1 \left(\Pi_{l1}^2 + \Pi_{l2}^2\right) \mathsf{P}(\zeta) \mathrm{d}\zeta + \left(\Gamma \mathcal{M}_2^{-2} - 1\right)^2 \int_1^\infty \Pi_s^2 \mathsf{P}(\zeta) \mathrm{d}\zeta, \tag{4.76b}$$

where use of Eq. (4.52) has been made. Figure 4.13(a) shows that, while the vortical fluctuations across the shock are increased by dissociation, the density variance induced by the entropic mode is small for $\mathcal{M}_1 \lesssim 10$ but increases sharply thereafter up to

$\mathcal{M}_1 \sim 18$, where it achieves a maximum value. As observed by comparing Figs. 4.8(b) and 4.13(a), the acoustic prefactor G^a is found to be negligible compared to the entropic one G^e.

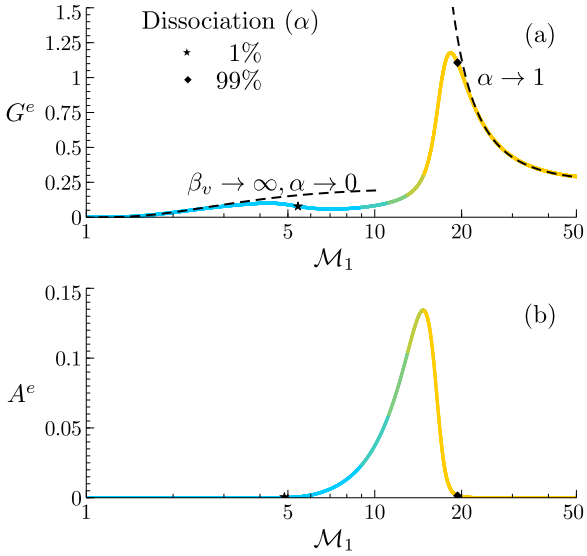

Figure 4.13: Entropic prefactors of (a) the post-shock density variance and (b) the post-shock degree of dissociation as a function of the pre-shock Mach number $\mathcal{M}_1$ for $B = 10^4$, $\beta_v = 10$, and $\beta_d = 100$ (lines colored by the degree of dissociation; refer to Fig. 4.12 for a colorbar). Dashed lines correspond to limit behavior of G^e and A^e calculated using the asymptotic expressions (4.23) and (4.25) for small and high Mach numbers, respectively.

Whereas the Rankine-Hugoniot jump condition (4.40d) evaluated at the turning point of the Hugoniot curve $\Gamma = 0$ indicates that the density fluctuations immediately downstream of the shock are zero, the entropic prefactor in Fig. 4.13(a) at $\mathcal{M}_1 \simeq 13$ (where Γ vanishes) leads to a non-zero density variance. The two results can be reconciled by noticing that the formulation in Eq. (4.76) and the approximation $G^e \gg G^a$ are applicable only to the far field downstream of the shock. In contrast, the acoustic mode needs to be retained near the shock. Specifically, the post-shock density fluctuations in the near field vanish as $\Gamma \to 0$ because of destructive interference between the acoustic and entropic modes. In contrast, the entropic mode dominates in the far field, leading to non-zero post-shock density fluctuations.

The entropic component of the density variance engenders a variance of the degree of dissociation given by

$$\langle \alpha'^2 \rangle = A^e \int_0^\infty E(k) k^2 \mathrm{d}k, \tag{4.77}$$

where

$$A^e = \frac{(\alpha_R - \alpha_T)^2(1+\alpha)^2}{(1+\alpha+\alpha_T)^2} G^e \tag{4.78}$$

is the corresponding prefactor. Figure 4.13 (b) shows that A^e attains a maximum value at $\mathcal{M}_1 \sim 15$, and becomes negligible both in absence of dissociation and when dissociation is complete.

4.5 Comparison with the Combustion Toolbox

In Fig. 4.2, we observed a generally good agreement between the theoretical framework presented in Sec. 4.2 and the numerical results obtained with the Combustion Toolbox (CT) that benefited from the vertical logarithmic scale. To properly evaluate the accuracy and limitations of the approach, we have obtained the RH relations from CT instead of solving (4.19) to (4.21). This allows to incorporate a more comprehensive set of effects, such as electronic excitation of species, as well as anharmonicity (deviation from harmonic oscillator), vibration-rotation coupling and nonrigid rotation for diatomic and polyatomic gases [294]. By examining the similarities and discrepancies between the two approaches, we can identify the limitations associated with neglecting these additional effects.

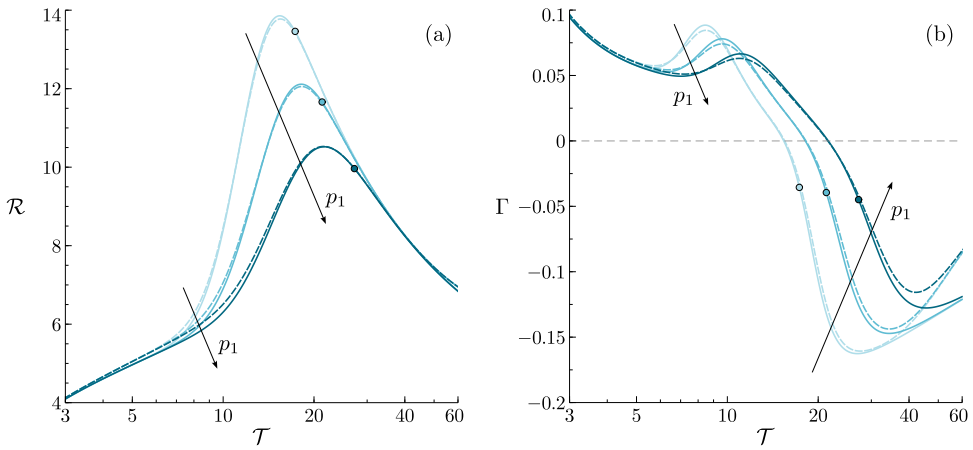

Figure 4.14: Comparison of the theoretical results (solid lines) with the numerical results obtained with the Combustion Toolbox (dashed lines) for diatomic hydrogen (H_2): density ratio $\mathcal{R}$ (a) and the normalized inverse of the slope of the Hugoniot curve Γ (b) for a wide range of temperature ratios $\mathcal{T}$ and different upstream pressures $p_1 = (0.01, 0.1, 1)$ atm.

In general, there is an excellent agreement for the density ratio $\mathcal{R}$ between this work and CT across the evaluated range of temperature ratios $\mathcal{T}$ [see Fig. 4.14(a)], with minor discrepancies of $\sim 3\%$ and $\sim 1\%$ observed around $\mathcal{T} \sim 9$ and $\mathcal{T} \sim 50$, respectively. However, it is worth noting that in the latter region, even a small error in the density ratio of $\sim 1\%$ leads to strong deviations of 30% in the normalized inverse of the slope of the Hugoniot curve Γ [see Fig. 4.14(b)] due to the sensitivity of the first derivative involved in its calculation.

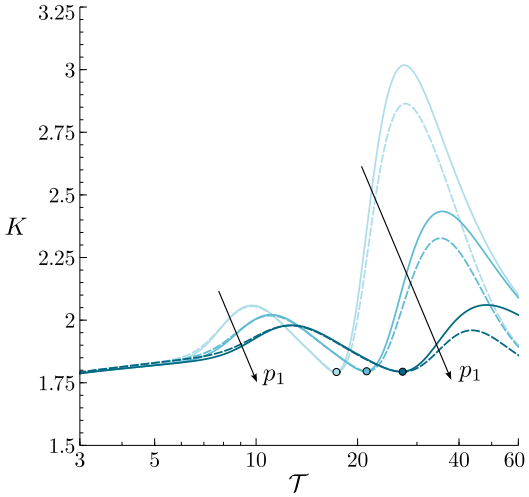

Figure 4.15: Comparison of the theoretical results (solid lines) with the numerical results obtained with the Combustion Toolbox (dashed lines) for the TKE amplification factor. Calculations are carried out for diatomic hydrogen (H_2) over a wide range of temperature ratios $\mathcal{T}$, with $T_1 = 300$ K, and different upstream pressures $p_1 = (0.01, 0.1, 1)$ atm.

Figure 4.15 presents the TKE amplification K across the shock as a function of the temperature ratio $\mathcal{T}$. The qualitative behavior remains consistent with the findings depicted in Fig. 4.7, revealing again two distinct peaks. The valley between these local maxima is indicated by a circle. The range of values preceding this point is referred to as region I, while the subsequent values comprise region II. In region I, we observe an excellent agreement between the calculated TKE amplification and the values obtained with CT, with a maximum error of approximately 2%. However, in region II the values of K are 10% higher compared to the results obtained with CT across all tested pressures. Lower discrepancies are observed for the amplification of the turbulent intensity and turbulent Reynolds number due to the factor $K^{1/2}$, as detailed in Fig. 4.16.

These findings emphasize important considerations for future research. Firstly, the exclusion of electronic excitation in the current approach can lead to notable devia-

tions, particularly for molecules with multiple electrons in the subshell [295–298]. As temperature and pressure increase, the impact of electronic excitation becomes more significant, as evident in region II. Secondly, the assumption of diatomic molecules behaving as harmonic oscillators may not hold at very high temperatures [295]. At such elevated temperatures, diatomic molecules exhibit anharmonic behavior due to the coupling between molecular vibration and rotation, necessitating a more sophisticated model to accurately describe their thermodynamic properties [126, 281, 294, 299–302].

It is worth noting that the contribution of diatomic molecules to the internal energy is influenced by a factor of $(1-\alpha)$, indicating that the effects of anharmonicity and vibrational-rotational coupling are primarily responsible of the discrepancies observed in region I. Conversely, deviations in region II predominantly stem from electronic excitation, playing a dominant role at very high temperatures. The maximum errors attributed to each region are approximately 3% and 10%, respectively.

Although our results align well with the CT, the discrepancies observed around $\mathcal{T} \sim 9$ and $\mathcal{T} \sim 50$ underscore the importance of considering electronic excitation, anharmonicity, and vibrational and rotational coupling in future theoretical studies pertaining to the high-temperature behavior of gases. In Chapter 5, CT will be employed to extend the theoretical analysis presented in this study to also multi-species mixtures and species' ionization.

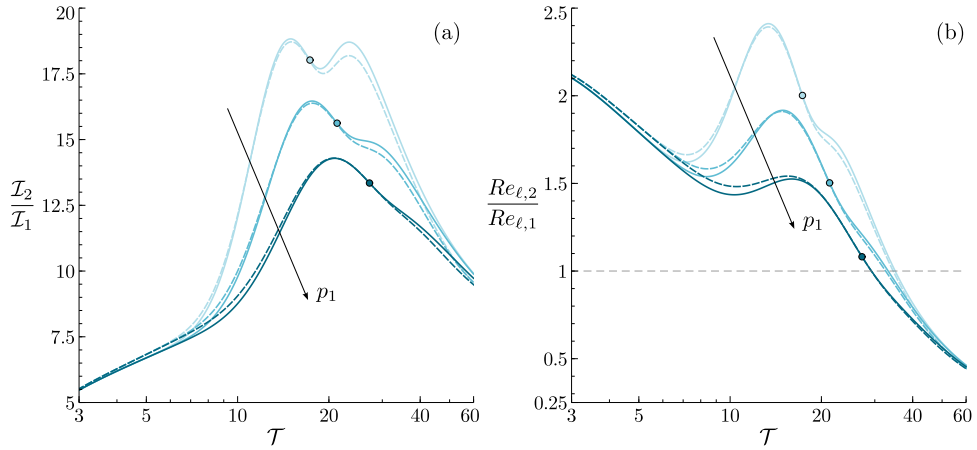

Figure 4.16: Comparison of the theoretical results (solid lines) with the numerical results obtained with the Combustion Toolbox (dashed lines) for the amplification of the turbulent intensity (a) and the turbulent Reynolds number (b). Calculations are carried out for diatomic hydrogen (H_2) over a wide range of temperature ratios $\mathcal{T}$, with $T_1 = 300$ K, and different upstream pressures $p_1 = (0.01, 0.1, 1)$ atm.

4.6 Conclusions

In this chapter, the interaction between a hypersonic shock wave and weak isotropic turbulence has been addressed using LIA. Contrary to previous studies of shock/turbulence interactions (STI) focused on calorically perfect gases, the results provided here account for endothermic thermochemical effects of vibrational excitation and gas dissociation enabled by the high post-shock temperatures. Important approximations used in this theory are that the thickness of the thermochemical non-equilibrium region trailing the shock front is small compared to the characteristic size of the shock wrinkles, and that all fluctuations in the flow are small relative to the mean.

The results presented here indicate that the thermochemical effects act markedly on the solution in a number of important ways with respect to the results predicted by the theory of calorically perfect gases:

(a) Significant departures from calorically-perfect-gas behavior can be observed in the solution even at modest degrees of dissociation of 1%, corresponding to Mach 5 and therefore to the beginning of the hypersonic range. This is because the associated bond-dissociation energies of typical molecules are large. As a result, the chemical enthalpy invested in dissociation in the post-shock gas can easily surpass the pre-shock thermal energy and become of the same order as the pre-shock kinetic energy.

(b) A turning point in the Hugoniot curve is observed at approximately Mach 13 and 70% degree of dissociation, leading to a significant increase of the mean post-shock density of approximately 12 times its pre-shock value, representing nearly twice the maximum density jump predicted by the theory of calorically perfect gases.

(c) The aerothermodynamic behavior of the post-shock gas changes fundamentally around the turning point in the Hugoniot curve. As the Mach number increases above 13, positive fluctuations of streamwise velocity engender positive pressure fluctuations in the post-shock gas that are accompanied by negative density fluctuations. In this way, the local post-shock density and pressure are anticorrelated, although the shock remains stable to corrugations in all operating conditions tested here.

(d) The amplification of TKE is larger than that observed in calorically perfect gases. Whereas the streamwise velocity fluctuations across the shock are decreased,

the transverse ones are greatly increased (i.e., much more than in a diatomic calorically perfect gas). This phenomenon can be explained in the linear theory by using the conservation of tangential momentum, which elicits larger transverse velocity fluctuations as a result of the increase in post-shock density that occurs due to dissociation and vibrational excitation. This effect also leads to a much more significant increase of anisotropy and enstrophy across the shock than that observed in a diatomic calorically perfect gas.

(e) Most of the amplified content of TKE is stored in vortical velocity fluctuation modes in the post-shock gas. The trend of the TKE amplification factor with the pre-shock Mach number is non-monotonic and involves two local maxima of similar value, one equal to 1.97 at Mach 6 (corresponding to a degree of dissociation of 6%) and a second one equal to 2 at Mach 18 (corresponding to a degree of dissociation larger than 99%). The second peak increases sharply at lower pressures (higher altitudes).

(f) The turbulence intensity and turbulent Reynolds number increase across the shock and reach maximum amplification factors of 16 and 2.7, respectively, both occurring at the turning point of the Hugoniot curve (approximately Mach 13 and degree of dissociation of 60%). The maximum amplification factor of the turbulence intensity is twice the one attainable in a diatomic calorically perfect gas. The amplification of the turbulent Reynolds number observed here is in contrast with the attenuation predicted by the theory of calorically perfect gases at hypersonic Mach numbers.

(g) The density variance in the post-shock gas is almost exclusively generated by entropic modes radiated by the shock wrinkles and is approximately 5 times the value predicted for calorically perfect gases. Similarly, the shock front generates entropic fluctuations of the concentration of atomic species that might be relevant for applications in supersonic combustion if the post-shock gas is going to be employed to oxidize the fuel [55, 303].

(h) The electronic excitation plays a significant role in the TKE amplification diminishing the maximum value by 10% for the conditions tested. This is because part of the kinetic energy is employed to move the electrons between the valence shell of the species. Lower deviations are observed for the amplification of turbulent intensity and turbulent Reynolds number. The calculations were carried out using the Combustion Toolbox and stated the limitations of not modeling the electronic excitation, anharmonicity, and vibrational-rotational coupling.

The LIA predictions for the overall TKE amplification factor in calorically perfect gases have been previously found to be in fair agreement with numerical simulations [61, 63, 64, 75] and experiments [270]. However, the way LIA predicts the amplified TKE to be partitioned in the streamwise and transverse directions has not been as successful. In particular, computational and experimental studies at supersonic Mach numbers have often reported Reynolds stress tensors with dominant streamwise contributions, this being an effect typically attributed to convective non-linearities and molecular transport [75]. Whether these discrepancies subside or persist at hypersonic Mach numbers is an open question of research.

The theoretical results provided here indicate amplified levels of post-shock fluctuation energies that could perhaps be unexpected at first, because of the high post-shock temperatures prevailing at hypersonic Mach numbers. These findings would greatly benefit from comparisons with simulations and experiments in future studies.

This theory could be extended to include additional phenomena such as: (a) non-equilibrium vibrational relaxation and finite-rate dissociation [254, 304–306]; (b) multi-component gas mixtures (particularly O_2 and N_2 for STI in air); (c) compressibility and anisotropy in the pre-shock turbulence; (d) the effects of walls downstream of the shock to address modal resonance in high-temperature inviscid shock layers around hypersonic projectiles; and (e) electronic excitation, radiation, and ionization in the post-shock gas for hypersonic flows at orbital stagnation enthalpies. Points (b) and (e), except for the radiation, are addressed in the next Chapter 5 by using the Combustion Toolbox presented in Chapter 2. Additionally, the mathematical framework described in Sec. 4.2 is extended in Appendix D considering the electronic excitation and ionization of monatomic and diatomic gases, separately.

5 Linear theory of hypersonic shocks interacting with turbulence in air

Contents

Summary

In this chapter, the interaction between a weakly turbulent free stream of air and a hypersonic shock wave is investigated theoretically by using linear interaction analysis (LIA). The perturbation-free jump conditions across the shock are computed using the Combustion Toolbox presented in Chapter 2, an in-house thermochemical code capable of capturing high-temperature phenomena such as dissociation, electronic excitation, ionization, and recombination in multi-species ideal gas mixtures, which are found to be dominant effects in hypersonic shocks in air. The formulation is developed in the limit in which the thickness of the thermochemical nonequilibrium region is assumed to be much smaller than the characteristic size of the shock wrinkles caused by turbulence. Similarly to our previous work described in Chapter 4, which only accounted for vibrational and dissociation effects of single-species diatomic gases, the LIA results presented here for air indicate that the enstrophy, anisotropy, intensity, and turbulent kinetic energy (TKE) of the fluctuations are more amplified through the shock than in the thermochemical frozen case. Moreover, the turbulent Reynolds number is also amplified across the shock at hypersonic Mach numbers in the presence of dissociation and vibrational excitation, as opposed to the attenuation observed in the thermochemical frozen case. Multi-species

effects reshape the TKE curve by rendering two maxima that fit fairly well within the O_2 and N_2 dissociation processes. Lastly, the TKE amplification factor is compared with direct numerical simulations.

5.1 Introduction

Hypersonic technologies have been investigated for more than six decades, but their attention has grown in the last decade due to the significant raise of geopolitical tensions among major powers [307]. In fact, the number of publications on hypersonics has been steadily increasing since the early 1980s due to its renewed relevance in aeronautical, astronautical, and military applications [308]. As a broad statement, we refer to hypersonic flows when the characteristic flow speed is sufficiently high that in its interaction with the vehicle (from which the relative speed is measured) a significant amount of kinetic is transformed into thermal energy, thereby involving changes in the molecular structure of the gas. In atmospheric air, where molecular oxygen and nitrogen dominate the composition, this transition is found to occur when the Mach number is greater than 5.

Ubiquitous to the high-Mach character of the flow is the presence of shock waves that sharply change the aerothermal properties of the air, along with the boundary layers that shape the flow around the fuselage of the vehicle. Both shocks and boundary layers slow down the flow velocity with the associated increase in thermal energy. In particular, when the temperature is sufficiently high, powerful inter-molecular collisions bring into play modes of intramolecular energy storage (vibrational modes) that are effectively quiescent in standard thermodynamic conditions [309]. When inter-molecular collisions turn very violent, i.e., when the flow Mach number is further increased, such collisions can ultimately lead to molecular dissociation, electronic excitation, and ionization. Although the molecular description associated with high-Mach flows is well understood since the 1960s (see Refs. [281, 310, 311]), their coupled interaction with complex flow structures is still open and subject to intense study. Within this category lies the shock/turbulence interaction (STI) problem, which is of paramount importance in low-altitude hypersonic flight because of the correspondingly larger Reynolds numbers of the airflow around the fuselage and/or at the air intake of supersonic combustion ramjets [312].

Many studies have been devoted to the interaction of shock waves with turbulent flows below the hypersonic threshold, starting with experimental works on the interaction of shocks with turbulent boundary layers [258–261] and isotropic turbulent

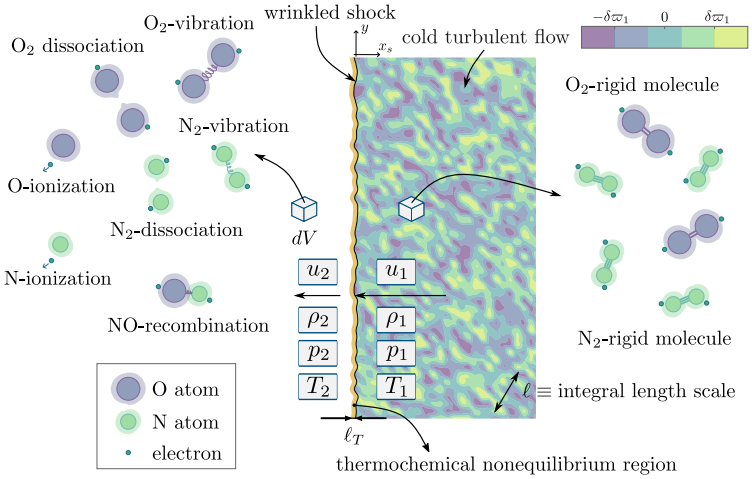

Figure 5.1: Sketch of the interaction of a planar shock wave with an isotropic vorticity field in air, where post-shock high-temperature phenomena is included.

flows [268–270]. The strongly arduous conditions that shock-related experiments demand, place numerical computations as an excellent alternative to gain understanding of the complex linear and nonlinear mechanisms involved, see Refs. [61–68, 70–73, 75–79, 273, 313–322]. From the theoretical point of view, the most popular approach is the so-called linear interaction analysis (LIA), pioneered by Ribner [80–82] and extended later by Wouchuk et al. [275] to address the initial value problem (transient behavior of the interaction). Regardless of the approach, and although there are some discrepancies in the form of the post-shock Reynolds stress tensor, all studies agree in that the mean velocity perturbations increase across the shock wave and the level of turbulence increases monotonically with the Mach number. For example, for a Mach number ~ 2 the turbulence kinetic energy across the shock grows a factor ~ 1.6. If the air is considered a calorically perfect gas, this value asymptotically approaches ~ 1.8 as the shock Mach number grows. This is no longer true in hypersonic conditions, as demonstrated in the previous chapter. Molecular transformations change, among others, the mass compression ratio and the post-shock Mach number, thereby affecting the intensity of the downstream perturbations.

The present chapter aims to investigate high-temperature effects in the interaction of hypersonic shocks with turbulent air, as depicted in Fig. 5.1. In this respect, this work is a natural extension of Chapter 4 that made use of LIA to study the amplification of turbulence across hypersonic shocks moving in single-species diatomic gases, since air comprises a multi-species mixture and the reaction processes are richer. The

model assumes that turbulence is comprised of small linear vorticity fluctuations and that downstream perturbations can be separated using Kovásznay's decomposition into vortical, entropic, and acoustic modes. Then, normal-mode analysis is used to compute the amplitude of the post-shock perturbation modes as a function of the shock properties [81]. The analysis demands the linearization of the Rankine–Hugoniot (RH) relations, computed in a preceding step using the Combustion Toolbox (see Chapter 2). This is a recently developed thermochemical code that includes, among others, routines to accurately solve processes involving strong changes in the dynamic pressure, such as steady state detonations and shock waves that involve transformation in the molecular structure of the gas. We refer to Fig. 5.2 below, where the RH curve and the shock Mach numbers are computed and compared against the ideal thermochemically frozen flow with $\gamma = 1.4 =$ constant.

Here, unlike in the previous Chapter 4, which addressed single-species symmetric diatomic gases, a more detailed model is required to take into account the dissociation and recombination into multi-species gases (monatomic, diatomic, and polyatomic species). By contrast, the current approach benefits from including more complex effects beyond recombination into multi-species gases, such as electronic excitation and ionization, thereby increasing the range of the application of the theory to Mach numbers beyond 10. Furthermore, to expose the limits of LIA, a one-to-one comparison of the turbulent kinetic energy with previous direct numerical simulations (DNS) is included.

In addition to the standard assumptions of LIA, namely, that velocity perturbations must be much smaller than the corresponding speed of sound, the incorporation of thermochemical effects requires that the characteristic size of the shock wrinkles be much larger than the thickness of the thermochemical nonequilibrium region behind the shock. The accuracy of this approximation in practical hypersonic systems is expected to improve as the flight Mach number increases and the flight altitude decreases, since temperature behind the shock increases with the Mach number, and the upstream density increases at lower altitudes, which promotes inter-molecular collisions to reach thermochemical equilibrium in a shorter time.

This chapter is organized as follows. A brief description of the mathematical framework presented in the previous chapter is included in Secs. 5.2 and 5.3.1 for completeness. An analysis of the amplification of TKE, turbulent intensity, and turbulent Reynolds number across the shock is provided in Sec. 5.3.2. Flight altitude effects in the TKE amplification factor are included Sec. 5.3.3. In Sec. 5.4, a comparison of the components of the TKE amplification factor with a collection of DNS data from the past two decades is presented. Final conclusions are given in Sec. 5.5.

5.2 Base flow variables across the shock

As in the previous chapter, consider first the problem of an undisturbed, normal shock wave in a cold, inviscid, irrotational air stream. The pre-shock density, pressure, flow velocity, and enthalpy in the reference frame of the shock are denoted, respectively, as ρ_1, p_1, u_1, and h_1. The corresponding flow variables in the post-shock gas are denoted as ρ_2, p_2, u_2, and h_2. The corresponding RH relations are

$$p_2 = p_1 + \rho_1 u_1^2 \left(1 - \frac{\rho_1}{\rho_2}\right) \qquad \text{and} \qquad h_2 = h_1 + \frac{u_1^2}{2}\left[1 - \left(\frac{\rho_1}{\rho_2}\right)^2\right] \tag{5.1}$$

provided that mass flow rate per unit area is conserved across the shock, $\rho_1 u_1 = \rho_2 u_2$. These equations must be supplemented with the ideal-gas equation of state (EoS) $p = \rho R_g T$, where T is the temperature of the fluid particles and R_g is the gas constant of the mixture. Anticipating that air is not a calorically perfect gas in the high-Mach number regime and that irreversible molecular transformations occur behind the shock, the gas enthalpy must be correspondingly modeled to account for these inelastic processes. In our case, h is modeled with the use made of the NASA 9-coefficient polynomials database [128], which ranges up to 20000 K, with the internal energy given by $e = h - p/\rho$ and the speed of sound squared by

$$a^2 = \left(\frac{\partial e}{\partial T}\bigg|_\rho\right)^{-1}\left(\frac{p}{\rho^2}\frac{\partial p}{\partial T}\bigg|_\rho - \frac{\partial p}{\partial T}\bigg|_\rho \frac{\partial e}{\partial \rho}\bigg|_T\right) + \frac{\partial p}{\partial \rho}\bigg|_T, \tag{5.2}$$

to be used in the definition of the upstream $\mathcal{M}_1 = u_1/a_1$ and downstream $\mathcal{M}_2 = u_2/a_2$ Mach numbers ahead and behind the shock.

When the incoming flow temperature and Mach number are sufficiently low, the air behaves as a calorically perfect ideal gas with frozen composition, and the enthalpy, internal energy, and speed of sound squared are only functions of temperature that can be expressed as

$$h = \frac{\gamma}{\gamma - 1}\frac{p}{\rho}, \qquad e = \frac{1}{\gamma - 1}\frac{p}{\rho}, \qquad \text{and} \qquad a^2 = \gamma\frac{p}{\rho} \tag{5.3}$$

in terms of the pressure to density ratio $p/\rho = R_g T$. This allows writing the momentum conservation equation and energy conservation equation in (5.1) with use made of the identities $\rho_1 u_1^2/p_1 = \gamma \mathcal{M}_1^2$ and $u_1^2/h_1 = (\gamma - 1)\mathcal{M}_1^2$, respectively. However, this is found to be inaccurate for pre-shock Mach numbers exceeding roughly 5, i.e., in

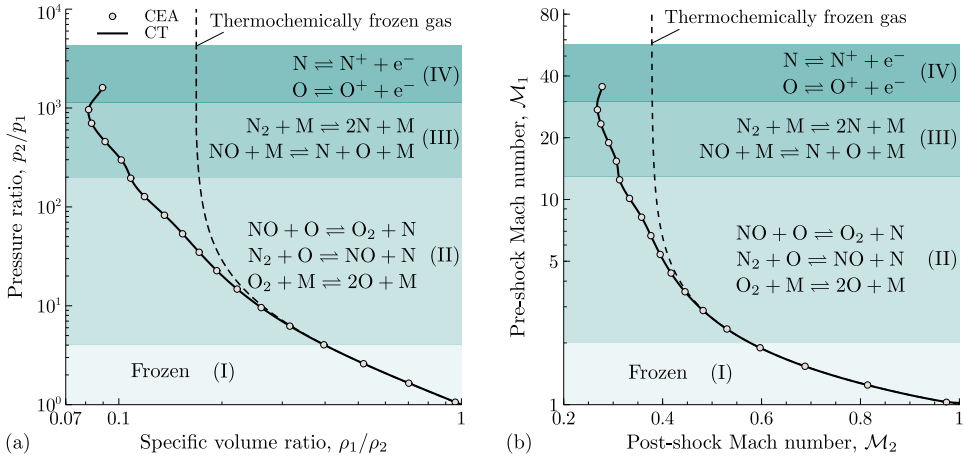

Figure 5.2: Log-log RH curve (a) and log-log upstream Mach number as a function of the downstream Mach number (b) for normal shocks propagating in air at $T_1 = 300$ K and $p_1 = 1$ atm; solid line: Combustion Toolbox (CT); dashed line: thermochemical frozen gas approximation; circles: results by CEA code [10]; Roman numerals: regions with the dominant reactions labeled.

the hypersonic flow regime. An illustrative example is provided on the left panel of Fig. 5.2, where the Hugoniot curve (p_2/p_1 vs. ρ_1/ρ_2) is plotted for normal shocks in air with pre-shock conditions: $T_1 = 300$ K, $p_1 = 1$ atm, and volume % composition $\{N_2, O_2, Ar, CO_2\} = \{78.08, 20.95, 0.9365, 0.0319\}$. Full equilibrium calculations have been carried out with the Combustion Toolbox assuming a 39-species mixture and using NASA's 9-coefficient polynomials. The results are compared with the analytical solution obtained for a thermochemically frozen gas. It is seen that, due to the endothermicity of the dissociation processes, a significantly higher compression ratio is achieved compared to that in the thermochemically frozen case.

Figure 5.2(b) shows the upstream Mach number $\mathcal{M}_1 = u_1/a_1$ vs. downstream Mach number $\mathcal{M}_2 = u_2/a_2$ for the same conditions. Both panels exhibit a similar behavior, with both the post-shock specific volume and Mach number decreasing significantly below their frozen flow values because of the further increase in density and decrease in velocity. This trend finishes after a clear turning point associated with the change in the mean molecular structure. At some degree of dissociation, endothermic effects are no longer dominant, and the balance of diatomic molecules vs. monoatomic species shifts to the latter. This lowers the theoretical maximum compression ratio $d+1$ from 6 to 4, with d standing for the degrees of freedom of the species involved ($d = 5$ for rigid diatomic molecules and $d = 3$ for single atoms). Roman numerals have been used

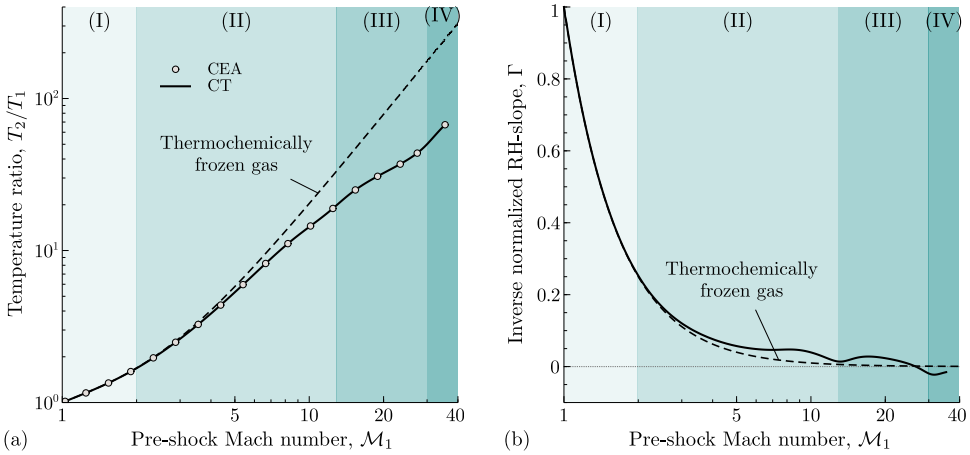

Figure 5.3: Log-log temperature jump (a) and log-linear normalized RH-slope parameter (b) as a function of the upstream Mach number for normal shocks propagating in air at $T_1 = 300$ K and $p_1 = 1$ atm.; solid line: Combustion Toolbox (CT); dashed line: thermochemical frozen gas approximation; circles: results by CEA code [10]; Roman numerals: regions with the dominant reactions labeled in Fig. 5.2.

in Fig. 5.2 to identify the dominant reactions in the different Mach regimes, starting with oxygen dissociation (region II), followed by nitrogen dissociation (region III), whose dissociation temperature is roughly twice that of oxygen, and finishing with their first ionization (region IV). Results have been compared with NASA's Chemical Equilibrium with Applications (CEA) code [10], showing excellent agreement in all cases.

To complete the analysis of the base-flow variables across the shock, the dependence of the temperature jump $\mathcal{T} = T_2/T_1$ and the normalized RH-slope parameter

$$\Gamma = -\frac{p_2 - p_1}{1/\rho_1 - 1/\rho_2}\left(\frac{\mathrm{d}(1/\rho_2)}{\mathrm{d}p_2}\right)_{\mathrm{H}} = u_2^2\left(\frac{\partial \rho_2}{\partial p_2}\right)_{\mathrm{H}}, \tag{5.4}$$

are computed as a function of the pre-shock Mach number $\mathcal{M}_1$. As shown in Fig. 5.3, the value of Γ becomes negative along the upper branch of the Hugoniot curve beyond the turning point $\Gamma = 0$. Along that branch, an increment (decrement) in post-shock pressure induces a decrement (increment) in post-shock density. The role of Γ in the description of the shock/turbulence interaction problem will be addressed in next section.

5.3 Linear interaction analysis

5.3.1 Mono-frequency perturbations

The problem formulation follows the linear analysis detailed in the previous chapter. A summary of the most important steps is given below for completeness, but the detailed description is given in Chapter 4. As shown there, the analytical development gives the exact values of the disturbance patterns generated behind the shock for a single-mode vorticity field, including explicit expressions for the distributions of density, pressure, and velocity. Anticipating that the isotropic turbulent flow can be constructed by direct weighted superposition of mono-frequency vorticity perturbations, the first part of the analysis considers only the interaction with a single-mode vorticity field. The upstream flow is made of weak rotational perturbations given by

$$u_1(x,y) = \varepsilon_u \langle a_2 \rangle \cos(k_x x) \cos(k_y y), \tag{5.5a}$$

$$v_1(x,y) = \varepsilon_u \langle a_2 \rangle \left(\frac{k_x}{k_y}\right) \sin(k_x x) \sin(k_y y). \tag{5.5b}$$

In this formulation, $\langle a_2 \rangle$ denotes the mean speed of sound in the post-shock gas, and ε_u is a dimensionless pre-shock streamwise velocity fluctuation amplitude, which is small in the linear theory, $\varepsilon_u \ll 1$. Correspondingly, the vorticity field reads as

$$\varpi_{z,1}(x,y) = \varepsilon_u \langle a_2 \rangle \left(\frac{k^2}{k_y}\right) \cos(k_x x) \sin(k_y y). \tag{5.6}$$

The angle θ of the shear layer relative to the shock propagation direction is given by $k_x/k_y = 1/|\tan\theta|$.

The vorticity, the streamwise and the transverse velocity components in the post-shock gas reference frame

$$\varpi = \varepsilon_u k_y \langle a_2^2 \rangle \overline{\varpi}, \quad u = \varepsilon_u \langle a_2 \rangle \overline{u}, \quad v = \varepsilon_u \langle a_2 \rangle \overline{v}, \tag{5.7}$$

are proportional to ε_u in the first-order, where $\overline{\varpi}$, $\overline{u}$, and $\overline{v}$ are the corresponding dimensionless fluctuations. The post-shock pressure and density can be similarly expressed as

$$p = \langle p_2 \rangle + \varepsilon_u \langle \rho_2 \rangle \langle a_2 \rangle^2 \overline{p}, \quad \rho = \langle \rho_2 \rangle (1 + \varepsilon_u \overline{\rho}), \tag{5.8}$$

with $\overline{p}$ and $\overline{\rho}$ the dimensionless fluctuations of pressure and density, respectively. The

brackets indicate time-averaged quantities, which are given by the solution obtained in the previous section. In this way, all fluctuations are defined to have a zero time average. Assuming that the Reynolds number of the post-shock fluctuations is infinitely large, the expansions Eqs. (5.7) and (5.8) can be employed in writing the linearized Euler conservation equations of mass, streamwise momentum, transverse momentum, and energy. They can be combined into a single, two-dimensional periodically-symmetric wave equation

$$\frac{\partial^2 \overline{p}}{\partial \tau^2} = \frac{\partial^2 \overline{p}}{\partial \overline{x}_c^2} + \frac{\partial^2 \overline{p}}{\partial \overline{y}^2} \tag{5.9}$$

for the post-shock pressure fluctuations in the reference frame moving with the post-shock gas. In this notation, the space and time coordinates have been nondimensionalized as follows

$$\overline{x}_c = k_y x_c, \quad \overline{y} = k_y y, \quad \tau = k_y \langle a_2 \rangle t, \tag{5.10}$$

where x_c refers to the streamwise coordinate measured in a reference co-coming with the compressed gas.

The boundary condition at the shock front is obtained from the linearized Rankine-Hugoniot jump conditions assuming that (a) the thickness of the thermochemical nonequilibrium region ℓ_T is much smaller than the inverse of the transverse wavenumber k_y^{-1}; and (b) the displacement of the shock $\xi_s = \xi_s(y,t)$ from its mean, flat shape is much smaller than k_y^{-1}. In these limits, at any transverse coordinate $\overline{y}$, the Rayleigh-Hugoniot jump conditions can be applied at the mean shock front location $\overline{x}_c = \mathcal{M}_2 \tau$, and can be linearized about the mean thermochemical-equilibrium post-shock gas state $\mathcal{P} = p_2/p_1$, $\mathcal{R} = \rho_2/\rho_1$, $\mathcal{T} = T_2/T_1$, and $\mathcal{M}_2$ calculated in Sec. 5.2, thereby yielding

$$\frac{\partial \overline{\xi}_s}{\partial \tau} = \frac{\mathcal{R}\,(1-\Gamma)}{2\mathcal{M}_2\,(\mathcal{R}-1)} \overline{p}_s - \overline{u}_1, \tag{5.11a}$$

$$\overline{u}_s = \frac{1+\Gamma}{2\mathcal{M}_2} \overline{p}_s + \overline{u}_1, \tag{5.11b}$$

$$\overline{v}_s = \overline{v}_1 - \mathcal{M}_2\,(\mathcal{R}-1)\,\frac{\partial \overline{\xi}_s}{\partial \overline{y}}, \tag{5.11c}$$

$$\overline{\rho}_s = \frac{\Gamma}{\mathcal{M}_2^2} \overline{p}_s. \tag{5.11d}$$

In the above equations $\overline{\xi}_s = k_y \xi_s / \varepsilon_u$ is the dimensionless shock displacement, whereas $\overline{p}_s$, $\overline{\rho}_s$, $\overline{u}_s$, and $\overline{v}_s$ are, respectively, the dimensionless fluctuations of pressure, density, streamwise velocity and transverse velocity immediately downstream of the shock front, where thermochemical equilibrium is reached in the limit $k_y \ell_T \ll 1$. In these relations,

$\overline{u}_1 = u_1/(\varepsilon_u\langle a_2\rangle)$ and $\overline{v}_1 = v_1/(\varepsilon_u\langle a_2\rangle)$ are the normalized components of the pre-shock velocity field engendered by the incident wave. Note that at the turning point of the Hugoniot curve ($\Gamma = 0$), the compression of the gas exerted by the shock is isochoric in the near field, and therefore leads to vanishing density fluctuations immediately downstream of the shock, as prescribed by the linearized jump condition given in Eq. (5.11d).

The initial value problem is solved by integrating Eq. (5.9) for $\tau \geq 0$, within the spatiotemporal domain bounded by the leading reflected sonic wave traveling upstream, $\overline{x}_c = -\tau$, and the shock front moving downstream $\overline{x}_c = \mathcal{M}_2\tau$, with $\mathcal{M}_2 = \langle u_2\rangle/\langle a_2\rangle$. It provides the transient evolution of the shock response along with the flow disturbances in the post-shock gas. However, the result of utmost interest is the long-time response, whose results are used in a Fourier analysis of the shock interaction with a three-dimensional isotropic vorticity field.

To describe the far-field post-shock gas, it is convenient to split the fluctuations of velocity, pressure and density into their acoustic (a), vortical (r), and entropic (e) components as

$$\overline{u}(\overline{x}_c,\tau) = \overline{u}_a(\overline{x}_c,\tau) + \overline{u}_r(\overline{x}_c), \tag{5.12a}$$
$$\overline{v}(\overline{x}_c,\tau) = \overline{v}_a(\overline{x}_c,\tau) + \overline{v}_r(\overline{x}_c), \tag{5.12b}$$
$$\overline{p}(\overline{x}_c,\tau) = \overline{p}_a(\overline{x}_c,\tau), \tag{5.12c}$$
$$\overline{\rho}(\overline{x}_c,\tau) = \overline{\rho}_a(\overline{x}_c,\tau) + \overline{\rho}_e(\overline{x}_c). \tag{5.12d}$$

The acoustic pressure wave emerging from Eq. (5.9) is of the form $\sim \mathrm{e}^{\pm\mathrm{i}(\omega_a\tau - \kappa_a\overline{x} - \overline{y})}$, where ω_a and κ_a are the dimensionless acoustic frequency and longitudinal wavenumber reduced with a_2k_y and k_y, respectively, which are related as $\omega_a^2 = \kappa_a^2 + 1$. The mono-frequency character of the asymptotic solution can be used to associate the acoustic frequency with the shock oscillation frequency through $\omega = \omega_a - \mathcal{M}_2\kappa_a$, which finally yields

$$\kappa_a = \frac{\mathcal{M}_2\omega \pm \sqrt{\omega^2 - 1 + \mathcal{M}_2^2}}{1 - \mathcal{M}_2^2}, \qquad \text{and} \qquad \omega_a = \frac{\omega \pm \mathcal{M}_2\sqrt{\omega^2 - 1 + \mathcal{M}_2^2}}{1 - \mathcal{M}_2^2}, \tag{5.13}$$

for the acoustic wavenumber and frequency, respectively. On the other hand, the rotational and entropic perturbations are steady functions $\sim \mathrm{e}^{-\pm\mathrm{i}(\mathcal{R}\overline{x} + \overline{y})}$. The corresponding amplitudes of the acoustic and rotational contributions to the velocity field are ultimate functions of $\mathcal{M}_2$, $\mathcal{R}$, Γ, and $\theta = \tan^{-1}(k_x/k_y)$. Their explicit form can be found in Sec. 4.3.4 in Chapter 4.

5.3.2 Amplification of turbulent kinetic energy, turbulent intensity, and turbulent Reynolds number across the shock

The weak isotropic turbulence in the pre-shock gas can be represented by a linear superposition of incident vorticity waves whose amplitudes ε vary with the wavenumber in accord with an isotropic energy spectrum $E(k) = \varepsilon^2(k)$. The root mean square of the velocity and vorticity fluctuations in the pre-shock gas can be calculated by invoking the isotropy assumption, which states that the probability that the incident wave has a given orientation is proportional to the solid angle.

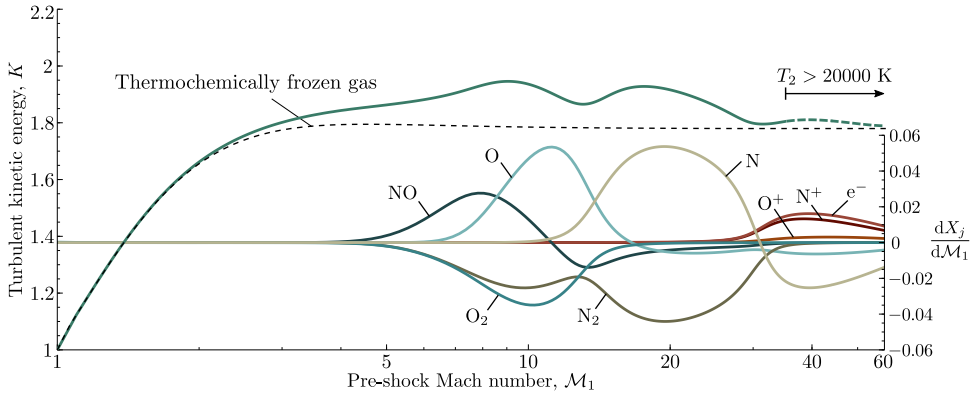

Figure 5.4: TKE amplification factor K as a function of the pre-shock Mach number $\mathcal{M}_1$ (upper green line) for normal shocks propagating in low turbulence intensity air at $T_1 = 300$ K and $p_1 = 1$ atm. The dashed line corresponds to the thermochemical frozen gas approximation. The inset represents the rate of change of the molar fractions with the pre-shock Mach number $\mathrm{d}X_j/\mathrm{d}\mathcal{M}_1$ for the most relevant species in the mixture.

The TKE amplification factor across the shock wave is a magnitude of utmost interest in the interaction of shock waves with turbulence. It is defined as

$$K = \frac{\langle u'^2_2 \rangle + \langle v'^2_2 \rangle + \langle w'^2_2 \rangle}{\langle u'^2_1 \rangle + \langle v'^2_1 \rangle + \langle w'^2_1 \rangle}, \tag{5.14}$$

where $\langle u'^2 \rangle$ denotes the averaged value of the perturbation kinetic energy associated with velocity component u. By performing the theoretical analysis described in Chapter 4, with the details omitted here for brevity, the value of K can be expressed as an integral formula—corresponding to an isotropically weighted sum of contributions of the vorticity perturbations impinging on the planar shock—that ultimately depends on the post-shock properties: mass compression ratio ρ_2/ρ_1, post-shock Mach number

$\mathcal{M}_2$, and a non-dimensional parameter that accounts for the RH-slope Γ, which are computed with the aid of the Combustion Toolbox (described in Chapter 2). In our case, we have a multi-species mixture of gases composed mainly of O_2 and N_2, which have different characteristic dissociation temperatures.

The resulting curve for K as a function of the pre-shock Mach number $\mathcal{M}_1$ (green line) is shown in Fig. 5.4. The curve exhibits two distinguished peaks corresponding to regions (II) and (III) of Fig. 5.2. The non-monotonicity of K is dictated by the behavior of the vorticity generation across the shock, since acoustic turbulent kinetic energy is negligible in hypersonic conditions. This effect, not shown explicitly in this work, was analyzed in detail in the previous Chapter 4. Two main effects are found to govern the post-shock perturbation flow: the mass compression ratio, whose amplification via endothermicity increases the flow deflection and the generation of transverse kinetic energy; and the RH-slope, which is sensitive to the different internal processes that take place within the non-equilibrium region. The latter is found to be associated with the rate of change of the molar fractions with the pre-shock Mach number $\mathrm{d}X_j/\mathrm{d}\mathcal{M}_1$ for the most important species in the mixture, which is also represented in Fig. 5.4. This is in line with Bottin's observation [295] on the specific heat at constant pressure c_p, where the author attributed the c_p local maxima to the dissociation processes of O_2 and N_2, and their ionization (discussed below), respectively. A simple form to verify the isolated contribution of the dissociation and ionization of species is to *ad hoc* freeze some of them. For example, when freezing the dissociation and recombination of N_2, the first peak of the K-curve still corresponds the peak of $|\mathrm{d}X_\mathrm{O}/\mathrm{d}\mathcal{M}_1| \sim |\mathrm{d}X_{\mathrm{O}_2}/\mathrm{d}\mathcal{M}_1|$. Under such conditions, higher temperatures are reached due to the absence of the endothermic effects of N_2 dissociation. The ionization of atomic oxygen occurs at lower Mach numbers, exhibiting the corresponding peak in the TKE curve.

Another effect that has not been included in our model, although it deserves further attention, is the second (and subsequent) ionization processes of atomic oxygen and nitrogen, expected to occur at temperatures above 20000 K. To highlight the limitation of the NASA's polynomials employed in this work, a dashed line has been used when showing the computations of TKE amplification factor in Fig. 5.4. By extrapolating (linearly) the correlation between the sensitivity of dissociation and ionization with the Mach number, we can anticipate that further ionization phenomena (appropriately described in Ref. [302]) will lead to additional lower-amplitude peaks in the K vs. $\mathcal{M}_1$ curve.

Figure 5.5 provides the amplification of the turbulent intensity $\mathcal{I}_2/\mathcal{I}_1$ and the turbulent Reynolds number $Re_{\ell,2}/Re_{\ell,1}$ across the shock as a function of $\mathcal{M}_1$ under identical

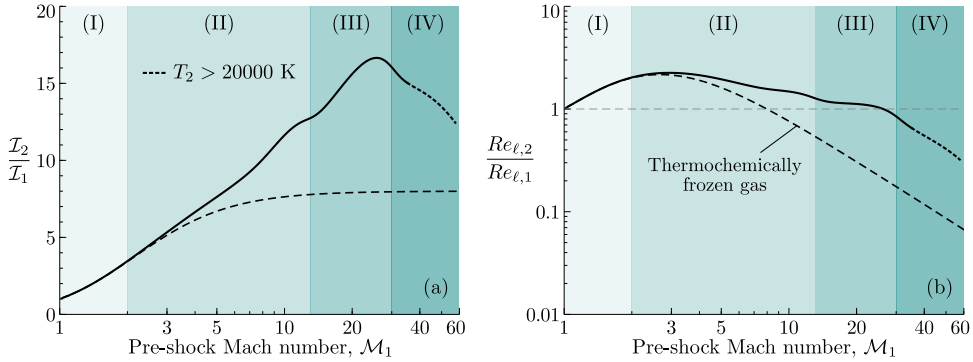

Figure 5.5: Amplification of the turbulent intensity $\mathcal{I}_2/\mathcal{I}_1$ (a) and the turbulent Reynolds number $Re_{\ell,2}/Re_{\ell,1}$ (b) across the shock as a function of $\mathcal{M}_1$ for air (solid line) at $T_1 = 300$ K and $p_1 = 1$ atm. The dashed line corresponds to the thermochemical frozen gas approximation. Roman numerals: regions with the dominant reactions labeled in Fig. 5.2.

conditions. Consistent with the findings in the preceding chapter, the turbulent intensity ratio $\mathcal{I}_2/\mathcal{I}_1$ exhibits a sharp increase in regions II and III as species dissociate [see Fig. 5.5(a)]. For instance, for $\mathcal{M}_1 = 10$ the turbulent intensity is 1.5-times higher than the value obtained with the thermochemically frozen approximation, while at $\mathcal{M}_1 \simeq 26$ where the maximum amplification occurs, it doubles the value $\mathcal{I}_2/\mathcal{I}_1 \simeq 8$ predicted. This maxima corresponds with the turning point of the Hugoniot curve ($\Gamma = 0$, $\mathcal{T} \simeq 42$, and $\mathcal{R} \simeq 12$). For $\mathcal{M}_1 > 26$, the turbulence intensity start to decrease; however, it is expected to remain higher compared to the linear extrapolation due to additional species dissociation, ionization, and recombination not considered in this study. A similar trend is observed for the turbulent Reynolds number, shown in Fig. 5.5(b).

5.3.3 Flight altitude effects

The flight envelope of hypersonic air-breathing vehicles presents lower and upper altitude limits beyond which the vehicle can not be flown. The lowest altitude limit is constrained by structural aircraft capabilities, while the highest altitude is imposed by the engine combustion requisites that demand a minimum amount of oxygen to operate. Briefly speaking, a cruise hypersonic aircraft must fly between 15–30 km at Mach-5 and 30–45 km at Mach-15 [323]. Then, since atmospheric properties are susceptible to altitude changes of the order of 10 km, it is natural to wonder how this effect modifies the turbulent kinetic energy amplification factor computed above. Prior to the computation of the function K vs. $\mathcal{M}_1$, it is convenient to recall an assumption underlying the

LIA: the thickness ℓ_T of the thermochemical nonequilibrium region behind the shock must be much smaller than the characteristic size of the shock wrinkles, which is of the same order as the integral length scale of the free stream turbulence ℓ. Thus, to properly assess the assumption $\ell \gg \ell_T$, we must evaluate the characteristic length of the chemical nonequilibrium region as a function of the flight altitude for a representative flight Mach number, say $\mathcal{M}_1 = 10$. To this end, we use the Hypersonic Task-based Research (HTR) solver [277–279].

The HTR solver is a high-order Navier–Stokes solver targeted towards direct numerical simulations of chemically-reactive compressible turbulent flows. In particular, we utilize a recent update of the HTR solver [324] which describes thermochemical nonequilibrium via a two-temperature model [254]. In this type of model, the thermochemical nonequilibrium region is modeled using two temperatures, namely T, which characterizes the translational and rotational energy modes of the chemical species in the gas, and T_{ve}, which refers to the vibrational and electronic excitation. The dissociation rate constants are evaluated at the geometric mean temperature $\sqrt{TT_{ve}}$. The chemistry of air (79% N_2, 21% O_2) is modeled with a 5-species mixture $\{N_2, O_2$ NO, O, N$\}$ using NASA's 9-coefficient polynomials. The interested reader is referred to Refs. [277–279, 324] for further details on the numerical code. The calculations are carried out in a one-dimensional computational domain discretized with 1200 grid points. Supersonic inflow conditions are imposed at the upstream boundary, while the downstream boundary features a characteristic multi-component non-reflecting outflow boundary condition [325]. Calculations are advanced in time with a constant time step that implies a Courant number CFL ~ 0.1, until steady state is reached.

The numerical results are displayed in the insets of Fig. 5.6, where the upstream pressure (left subplot) is presented as a function of the distance from the shock for $\mathcal{M}_1 = 10$ and different flight altitudes in the International Standard Atmosphere (ISA). The right subplot represents the temperature profile of the nonequilibrium zone at an altitude of 10 km above mean sea level. The characteristic relaxation length ℓ_T, shown as a diamond symbol, is found to growth from $\sim 10^{-4}$ m to $\sim 10^{-2}$ m when the flight altitude increases from 0 to 30 km. As a result, the minimum characteristic length of the turbulent eddies that can be described using the LIA increases correspondingly with the flight altitude. During the climb and acceleration segment, the value of ℓ_T is expected to decrease as the Mach number increases (since the post-shock temperature increases with the Mach number) and to increase as the altitude increases (because of the exponential pressure drop with altitude), the latter being the expected dominant contribution. This is better analyzed by looking at Fig. 5.6(b), which shows the temperature and pressure profiles in the ISA model. First, the temperature decreases

linearly in the troposphere (from sea level to 11 km), it remains roughly constant at the lower layer of the stratosphere (from 11 km to 20 km), and finally increases again until reaching the mesosphere at 50 km of altitude. By contrast, the pressure exhibits a monotonous power-law decay with altitude that becomes exponential in the constant temperature layer from 11 km to 20 km.

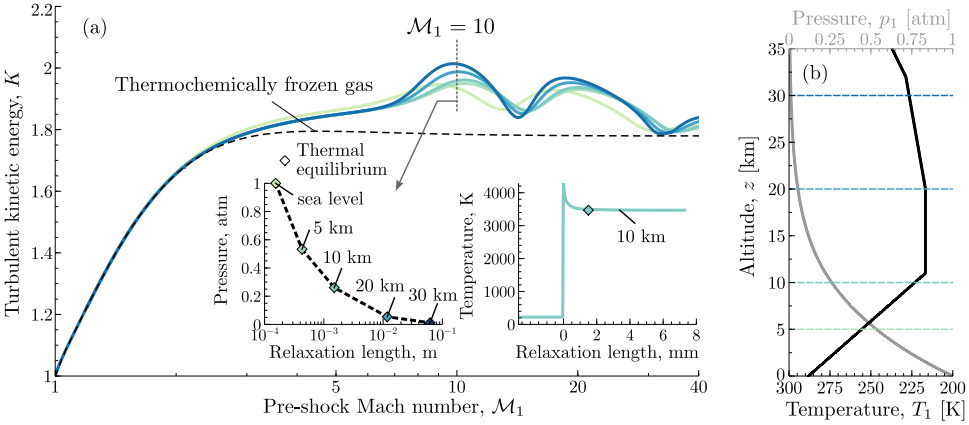

Figure 5.6: TKE amplification factor K as a function of the pre-shock Mach number $\mathcal{M}_1$ at different flight altitudes (0, 5, 10, 20, and 30 km) above sea level in the ISA model (a) and the corresponding temperature-pressure vs. altitude profiles (b). The curve for the lowest altitude (0 km) corresponds to conditions indicated in Fig. 5.4. The dashed line corresponds to the thermochemically frozen gas approximation. The insets represent the variation of the pressure (left) and temperature (right; translational and rotational) with the relaxation length as obtained from one-dimensional direct numerical simulations with the HTR solver [277–279] using a two-temperature model.

Going back to the TKE amplification factor, we refer again to Fig. 5.6, which shows the variation of K with the pre-shock Mach number $\mathcal{M}_1$ for five different flight altitudes: 0, 5, 10, 20, and 30 km above sea level. It is seen that the qualitative picture remains the same, with small changes associated with the variation of the upstream conditions with altitude. Roughly, endothermic effects are found to increase the value of K in the whole Mach number domain. Also, the higher the altitude the stronger the peaks in the amplification of the turbulent kinetic energy. It must be emphasized that K measures the amplification of the TKE, so that evaluation of the total turbulent intensity requires information on the upstream turbulent flow, which is also expected to change with altitude. This was already commented in Sec. 4.5, but focusing solely on evaluating the results at different pressures. In this case, lower (higher) pre-shock temperatures shift the curves to the right (left), which means that it is required a higher (lower) pre-shock velocity to achieve similar conditions.

The variation of the flight altitude may also affect the integral length scale of the upstream turbulence, making the conditions imposed by LIA ($\ell_T \ll \ell$) less likely to occur. The effect of turbulent perturbations with a characteristic length of the order of the thermochemical relaxation length is out of the scope of this work, but it could be investigated using direct numerical simulations, as done by Kerkar and Ghosh [319]. They find out that chemical reactions within the nonequilibrium region enhance the production of turbulence, primarily due to the amplification of streamwise velocity perturbations, as opposed to the laterally dominating turbulence predicted by LIA.

5.4 Comparison with direct numerical simulations

In the previous section, we examined the influence of upstream conditions, such as temperature and pressure, on the TKE amplification ratio. We have seen that under the isotropic-spectrum and weak-disturbance assumptions, the reduces to providing information on the upstream thermochemical state and the shock strength. However, in the context of direct numerical simulations, where the upstream flow must be explicitly defined, it becomes essential to incorporate information about the turbulence properties. This is usually characterized by the turbulent Mach number $\mathcal{M}_t$ that characterizes the turbulent intensity and the Taylor-scale Reynolds number Re_λ. Therefore, in the LIA conducted before, it is neglected the inherent non-linear terms associated with the shock/turbulence interaction, which implies $\mathcal{M}_t \ll 1$ (linearity) and $Re_\lambda \to \infty$ (inviscid limit). This consideration allowed us to obtain explicit analytical formulae for post-shock turbulence using LIA. We refer to [320, 326] for the extension to weakly non-linear perturbations.

In this section, we will examine and compare the far-field results obtained through the LIA with DNS conducted under the assumption of a perfect gas EoS and constant specific heat. However, accurately determining the precise value from the DNS data for direct comparison with the LIA results can be challenging because the shock-capturing method typically involves numerical dissipation factors that have an impact on the turbulence simulation. A sample is offered in Fig. 5.7, where a schematic view of a 3D direct numerical simulation in the XY-plane is displayed. It is evident that the turbulent fluctuations decrease as we move along the streamwise direction. As a result, when considering sufficiently long distances, the turbulence will be effectively dissipated, leading to an associated increase in thermal energy.

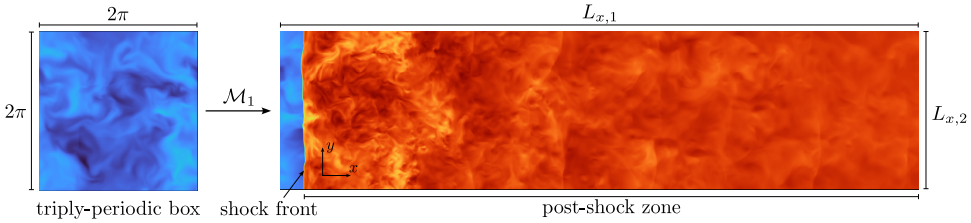

Figure 5.7: A schematic of a 3D direct numerical simulation in the XY-plane showcasing isotropic turbulence generated by a triply periodic box and advecting at a mean Mach number $\mathcal{M}_1$ toward the shock/turbulence interaction domain. This figure corresponds to ongoing research utilizing the HTR solver [277–279].

To define the far-field solution in the DNS, several works (see Refs. [72, 76] and references therein) take advantage of the non-monotonic behavior of the streamwise Reynolds stress (R_{11}). In particular, the position at which the streamwise Reynolds stress peaks, typically normalized with its corresponding upstream value ($R_{11}/R_{11,1}$, equivalent to our K_L in the linear regime), is the position at which the comparison is carried out. This is depicted in Fig. 5.8. To conduct the STI simulation, a turbulence generator is employed, usually a triply-periodic box with dimensions $2\pi \times 2\pi \times 2\pi$, where forced homogeneous isotropic turbulence (HIT) is computed. The velocity, pressure, and temperature are then advected to the STI domain using the Taylor hypothesis. A gradual decay occurs due to dissipation until it reaches the shock location, denoted as x_1. This implies that the amplification factors should be based on turbulent properties specifically at this location. Due to the strong compression, a prominent peak appears at x_s in the factor K_L (similarly found in the transverse component K_T) as a result of fluctuations in the shock position. This peak does not represent the actual turbulent kinetic energy and is intentionally excluded from the vertical axis range limits. Following the peak, a local minimum is observed at $x_{2'}$. From that point onwards, there is a gradual increase in turbulent kinetic energy, which is typically associated with a transfer from the acoustic field to the velocity fluctuations. This effect becomes less pronounced as we move away from the shock. Additionally, the contribution of dissipation effects, which are always present, is found to compensate for the increasing value of K_L at the location x_2, where the maximum value is observed. This value is commonly used for comparison purposes.

Alternatively, one can extrapolate the K_L and K_T components of the turbulent kinetic energy back to the average shock position x_s, as suggested by Larsson & Lele [63]. This approach aims to minimize the influence of viscosity effectively. Figures 5.7 and 5.8 have been obtained using the HTR solver [277–279], which is a Navier–Stokes solver purpose-built for conducting direct numerical simulations of hypersonic flows charac-

terized by high enthalpies. It is specifically designed to account for the complex effects arising from non-calorically perfect gases. These results correspond to ongoing research and have not been included in the analysis.

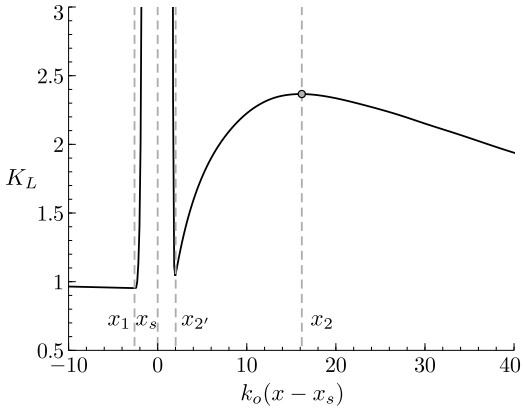

Figure 5.8: Distribution of the streamwise $K_L(x)$ components of the TKE amplification factor considering a thermochemically frozen gas. The symbol represents the location considered as far-field. Calculations carried out for a pre-shock Mach number $\mathcal{M}_1 = 5$, turbulent Mach number $\mathcal{M}_t = 0.2$, Taylor-scale Reynolds number $Re_\lambda = 40$, and considering a thermochemical frozen gas. The spatial variable $(x - x_s)$ is normalized with the energy-peak wavenumber $k_o = 8$. This figure corresponds to ongoing research utilizing the HTR solver [277–279].

It is important to note that LIA results are derived from Reynolds-averaged statistics. On the other hand, DNS of compressible flows commonly employs Favre-averaged statistics. This choice is primarily due to the convenience it offers in dealing with the convective term of the Navier-Stokes equations. The derived solutions from LIA for the streamwise K_L and transverse K_T components of the TKE amplification (see (4.65a) and (4.65b), respectively) are compared against DNS data in Fig. 5.9. The solid line represents the theoretical results obtained with LIA considering thermochemical effects, while the dashed line provides the widely used thermochemically frozen gas approximation. Results have been compared in a log-linear scale as a function of the factor $(\mathcal{M}_1 - 1)$ for better visualization. The data collected from other numerical simulations are denoted by different symbols (see caption of Fig. 5.9 for reference), maintaining the notation of Refs. [72, 76]. This data is compound of a wide variety of calculations: $\mathcal{M}_1 \in [1.1, 6]$, $\mathcal{M}_t \in [0.02, 0.54]$, and $Re_\lambda \in [10, 74]$ as described in Table 5.1 (for further details we refer to their respectively works). The hollow symbols represent results obtained using HIT, while the filled symbols correspond with spatially developed turbulence (SDT). The latter approach allows the interaction between the fluctuations and the mean flow. This procedure resembles a larger streamwise component of velocity

variance compared to the transverse components (slightly anisotropic flow), similar to the conditions found in wind tunnel tests [72, 327].

The two components of the total kinetic energy K, namely longitudinal K_L and transverse K_T, are amplified in most of the region tested. In particular, at pre-shock Mach numbers up to $\mathcal{M}_1 \sim 2$, most of the TKE produced across the shock belongs to rotational modes of the streamwise velocity fluctuations (the acoustic contribution is negligible in the far field as discussed in the previous chapter; see Fig. 4.8 for reference). However, for $\mathcal{M}_1 \gtrsim 2$, K_L plunges below K_T and the transverse component dominates, reaching its first peak around $\mathcal{M}_1 \sim 10$. This value is approximately 15% higher than the obtained with the thermochemically frozen approximation.

Source	$\mathcal{M}_1$	$\mathcal{M}_t$	Re_λ	Symbol
Lee et al. [61, 77]	1.2, 2, 3	0.102-0.11	14.9-19.7	▷
Mahesh et al. [62]	1.29	0.14	19.1	△
Larsson et al. [63, 64]	1.28-6	0.05-0.56	39-74	▽
Ryu & Livescu [66]	1.1-2.2	0.02-0.27	10-45	∗
Chen & Donzis [72, 76]	1.1, 1.2, 1.4	0.05-0.54	10-65	○,●,□,■,◇

Table 5.1: Summary of several computational works in canonical shock/turbulence interaction, further details in their original works.

From these results, we have constructed the total TKE amplification factor according to Eq. (4.64), namely $K = 1/3(K_L + 2K_T)$, as shown in Fig. 5.10. Here, we have also included the DNS data from Larsson & Lele [63] and Larsson et al. [64] (red symbol), where the authors artificially removed viscous dissipation by doing an extrapolation to infinite Reynolds number (see Eq. (3.4) from [64]). It is found that, in contrast to the values obtained for the TKE components K_L and K_T, the results provided for the TKE amplification factor are much closer to the LIA prediction. As expected, the DNS results approximate LIA prediction when $\mathcal{M}_t \ll 1$ and $Re_\lambda \to \infty$. Specifically, there is a larger dependence with $\mathcal{M}_t$ in comparison with Re_λ. Therefore, similar values are obtained when there is sufficient separation of scales between the characteristic size of the smallest eddies and the shock thickness. However, when the transverse component dominate for $\mathcal{M}_1 \gtrsim 2.5$, the anisotropy predicted by LIA ($K_T > K_L$) is totally opposite to the DNS ($K_L > K_T$). It appears that the nonlinear terms compensate for each other in the computation of K, somehow providing an answer beyond what LIA can explain. Further explanations pertain to the energy transfer occurring from the acoustic field in the longitudinal direction. This phenomenon leads to DNS predictions for K_L being

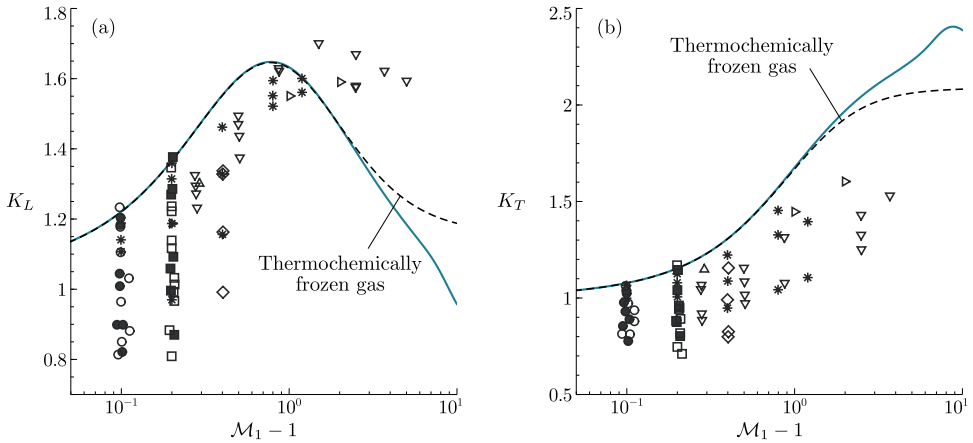

Figure 5.9: Streamwise K_L (a) and transverse K_T (b) components of the TKE amplification factor as a function of $\mathcal{M}_1 - 1$ (solid line). The dashed line corresponds to the values of K_L and K_T calculated assuming that the post-shock gas is thermochemically frozen. The symbols represent direct numerical simulations (DNS) from other studies: Lee et al. [61, 77] (▷), Mahesh et al. [62] (△), Larsson & Lele [63] and Larsson et al. [64] (▽), Ryu & Livescu [66] (∗), and Chen & Donzis [72, 76] (○,●,□,■,◇). The DNS data has been collected from Refs. [72, 76] maintaining their original notation.

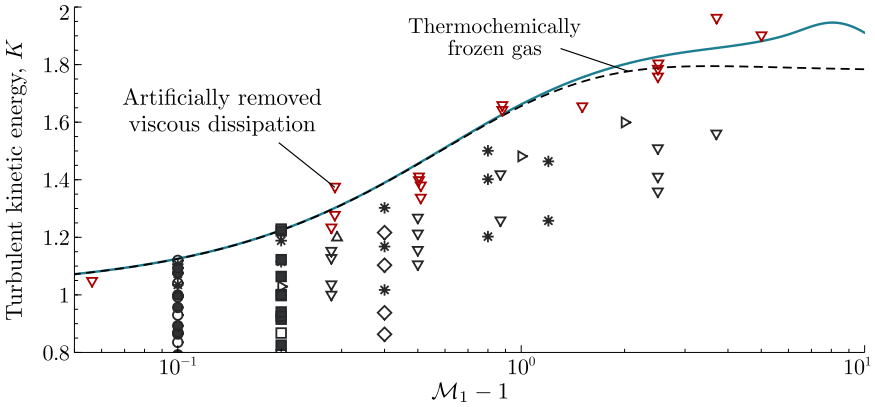

Figure 5.10: TKE amplification factor K as a function of $\mathcal{M}_1 - 1$ (solid line). The dashed line corresponds to the value of K assuming that the post-shock gas is thermochemically frozen. The symbols represent direct numerical simulations (DNS) from other studies: Lee et al. [61, 77] (▷), Mahesh et al. [62] (△), Larsson & Lele [63] and Larsson et al. [64] (▽), Ryu & Livescu [66] (∗), and Chen & Donzis [72, 76] (○,●,□,■,◇). The red-hollow triangles (▽) represent the values from Larsson et al. [64] with artificially removed viscous dissipation. The black symbols have been computed according to Eq. (4.64) maintaining the notation from Refs. [72, 76].

higher than those provided by LIA when $\mathcal{M}_1 \gtrsim 2.5$. In addition, the simplified thickless treatment of shocks in LIA promotes the generation of transverse disturbances due to the total conservation of transverse velocity. Previous studies also confirm the convergence between LIA and DNS when the turbulent Mach number approaches zero [66, 72]. To address this, Donzis [316] proposed a novel parameter, denoted as $\mathcal{K} = \mathcal{M}_t/[\sqrt{Re_\lambda}(\mathcal{M}_1 - 1)]$, based on similarity arguments concerning the instantaneous shock thickness. This parameter represents the ratio of the Kolmogorov length scale to the laminar shock thickness and effectively collapses all the available data regarding the streamwise component of the TKE amplification factor [64].

5.5 Conclusions

This chapter presents the study of the interaction between a hypersonic shock wave and a weakly turbulent free stream of air by using LIA. The perturbation-free jump conditions across the shock were determined using the Combustion Toolbox, which was introduced in Chapter 2. This thermochemical code is designed to accurately capture high-temperature phenomena, including dissociation, electronic excitation, ionization, and recombination in multi-species gas mixtures. These effects have been identified as dominant factors in hypersonic shocks in air. The present study is a natural continuation of the previous Chapter 4, which focused solely on the analysis of vibrational and dissociation effects in single-species diatomic gases.

The amplification of TKE of hypersonic shocks in air is larger than that observed in calorically perfect gases. Because of the fast-reaction limit assumed in this analysis, the streamwise velocity fluctuations across the shock are reduced, and the transverse ones are largely increased (i.e., much more than in a diatomic calorically perfect gas). Most of the amplified content of TKE is stored in vortical velocity fluctuation modes in the post-shock gas. Two well-distinguished peaks in the TKE amplification factor have been identified to the dissociation processes of the major species in the mixture. Furthermore, the intensity of the TKE changes with the flight altitude, although the qualitative picture of its dependence on the shock Mach number remains alike, with endothermic effects increasing the turbulence intensity. Lastly, to validate the results obtained using LIA, a comparison is made with available DNS data from previous studies, which assume the calorically perfect gas approximation. It is observed that the DNS results align with the predictions of LIA when the turbulent Mach number is significantly smaller than 1, and the Taylor-scale Reynolds number tends to infinity. However, further numerical investigations considering the calorically imperfect gas approximation are necessary to

analyze the results with thermochemical phenomena activated, particularly for Mach numbers exceeding 5.

Future work on this topic will involve a detailed one-to-one comparison of LIA prediction and direct numerical simulation (DNS) of shock/turbulence interactions. In particular, the foreseen calculations will be targeted toward cases where the thermochemical relaxation length scales are increasingly similar to the turbulence characteristic lengths. The objective of these future studies will be to provide a more thorough assessment of the limit in which LIA can accurately predict the amplification of turbulent kinetic energy through the shock.

6 Conclusions and Perspectives

Recent advancements in scientific and technological fields such as combustion, aerospace engineering, and astrophysics have highlighted the critical need for accurate, robust, and efficient numerical codes capable of predicting complex mixtures' chemical composition and properties at chemical equilibrium. In response to this demand, this thesis includes the development and validation of a novel open-source thermochemical code. On the other hand, the research conducted in this thesis also focuses on the theoretical investigation of reactive and non-reactive shocks propagating through non-homogeneous conditions. Specifically, it explores detonations with inhomogeneities in the upstream fuel mass fraction and examines the interaction of strong shocks with turbulent flows considering the associated high-temperature thermochemical effects, which play a dominant role in hypersonic conditions.

The following Sec. 6.1 provides a more detailed summary of the specific conclusions and contributions of this thesis. Lastly, some perspectives on future work are given in Sec. 6.2.

6.1 Contributions of this work

Chapter 2 introduced the Combustion Toolbox (CT), an open-source thermochemical code for calculating equilibrium states in gaseous reacting systems. CT has been developed from scratch in MATLAB and designed with a modular architecture, making it both user- and developer-friendly. The tool features a comprehensive suite of algorithms, ranging from fundamental chemical equilibrium problems to complex computations of steady shock and detonation waves for a variety of flow configurations, as well as rocket engine performance predictions. Additionally, CT is equipped with an advanced Graphic User Interface that encapsulates most of the built-in functions, providing users with a convenient operating experience. The full-package have been validated against established state-of-the-art codes: NASA's Chemical Equilibrium with Applications (CEA) [10], Cantera [41] within Caltech's Shock and Detonation Toolbox (SD-Toolbox) [40, 118], and the Thermochemical Equilibrium Abundances (TEA) code [18]. The results demonstrated excellent agreement between CT and these codes,

with CT showcasing superior computational performance in terms of cost and time when compared to Caltech's SD-Toolbox and TEA. Interested users can access the CT website at https://combustion-toolbox-website.readthedocs.io for additional support, documentation, and illustrative examples. CT is actively maintained and readily available on GitHub at https://github.com/AlbertoCuadra/combustion_toolbox. While CT's primary focus lies in addressing combustion problems involving the formation of condensed-phase species, its capabilities extend beyond this realm. It can be employed to calculate atmospheric compositions of gaseous exoplanets, analyze ablation processes, study hypersonic shocks, and investigate detonations. CT has been utilized in all of the studies presented in this thesis, demonstrating its reliability and versatility. Furthermore, CT's unique GUI has proven beneficial for educational purposes in undergraduate and graduate degrees over the past four years, resulting in an overall improvement in the learning process. Future studies will explore the educational benefits of CT in detail and provide comprehensive insights.

In Chapter 3, a theoretical study on detonations propagating through non-homogeneous fuel mixtures was presented using linear interaction analysis (LIA). The work highlights the significance of considering density and heat-release changes across the detonation when modeling the interaction with non-perfect reactive mixtures, with the equivalence ratio emerging as a crucial parameter in the analysis. Here, the transfer functions required to relate the upstream fuel mass fraction inhomogeneities with the burnt-gas perturbations are included via normal mode analysis (see appendix C). These results allow to derive the integral formulae for the turbulent kinetic energy, sonic energy, averaged vorticity, and entropy production rates using Fourier superposition for two- and three-dimensional isotropic fields. The effects of various factors, including the propagation Mach number, overdrive, and mixture properties, are identified, with heat-release variations playing a pivotal role in the intensity of turbulence generation. Furthermore, the study investigates the deviation of detonation propagation in heterogeneous gaseous mixtures compared to the homogeneous case with equivalent averaged upstream properties. The research shows that turbulence corrections lead to lower pressure and density ratios but an amplified post-detonation Mach number. The propagation speed in non-homogeneous mixtures is generally higher than in homogeneous mixtures, which agrees with previous results obtained numerically [214–216, 238]. The effective boundary condition influences the intensity of this deviation in the burnt-gas flow. Overall, the contributions of this work shed light on the intricate behavior of detonations traveling through non-homogeneous gaseous mixtures, emphasizing the importance of density and heat-release variations in the turbulence generation downstream of the detonation front.

In Chapters 4 and 5, the focus is on the interaction of hypersonic shocks with turbulent flows using LIA. The results presented here account for endothermic thermochemical effects enabled by high post-shock temperatures, contrasting with previous studies that focused on calorically perfect gases. Important approximations used in this theory are that the thickness of the thermochemical non-equilibrium region downstream the shock front is small compared to the characteristic size of the shock wrinkles, and that all fluctuations in the flow are small relative to the mean. In particular, the theoretical framework in Chapter 4 described the vibration and dissociation of single-diatomic species while also including transfer functions for upstream vortical disturbances. Utilizing Fourier superposition for three-dimensional isotropic fields, integral formulas are derived for enstrophy, concentration variance, turbulent kinetic energy (TKE), and turbulence intensity across the shock. Besides confirming known endothermic effects of dissociation and vibrational excitation in decreasing the mean post-shock temperature and velocity, these LIA results indicate that the enstrophy, anisotropy, intensity, and TKE of the fluctuations are much more amplified through the shock than in the thermochemically frozen case. Furthermore, the turbulent Reynolds number is also amplified across the shock at hypersonic Mach numbers in the presence of dissociation and vibrational excitation, in contrast to the attenuation observed in the thermochemically frozen case. These findings suggest that turbulence may persist and intensify across hypersonic shock waves despite the high post-shock temperatures. The robustness and accuracy of this work are demonstrated by comparing it with the Combustion Toolbox (described in Chapter 2), which employs NASA's 9 coefficient polynomial fits to evaluate thermodynamic functions. Excellent agreement is observed between the two approaches, with notable differences arising from electronic excitation at very high temperatures. An extension of the mathematical framework that accounts for electronic excitation and ionization is detailed in Appendix D.

In Chapter 5, the perturbation-free jump conditions across the shock are computed using the Combustion Toolbox, considering dissociation, electronic excitation, ionization, and recombination in multi-species ideal gas mixtures. These effects are found to be dominant in hypersonic shocks in air. Similar to the results in Chapter 4, the LIA results for air demonstrate that the enstrophy, anisotropy, intensity, and TKE of the fluctuations are more amplified through the shock compared to the thermochemically frozen case. The turbulent Reynolds number is also amplified across the shock at hypersonic Mach numbers in the presence of dissociation and vibrational excitation, contrary to the attenuation observed in the thermochemically frozen case. Multi-species effects reshape the TKE curve, exhibiting two maxima corresponding to O_2 and N_2 dissociation processes. The intensity of the TKE varies with flight altitude, but the qualitative

dependence on the shock Mach number remains consistent, with endothermic effects increasing the turbulence intensity. Lastly, the TKE amplification factor is compared with direct numerical simulations (DNS) from previous studies, which assume the calorically perfect gas approximation. The DNS results align with the predictions of LIA when the turbulent Mach number is significantly smaller than 1, and the Taylor-scale Reynolds number tends to infinity. However, further numerical investigations considering the calorically imperfect gas approximation are necessary to analyze the results with activated thermochemical phenomena, especially for Mach numbers exceeding 5.

6.2 Future work and perspectives

This thesis presented the development and validation of the Combustion Toolbox, showcasing its promising results. However, CT is an ongoing research project. In future versions of the code, we aim to introduce additional functionalities that will significantly expand its potential and scope. One of the key areas for improvement is the incorporation of non-ideal equations of state, which is currently under implementation, and the extension to multi-phase systems. Additionally, we aim to extend the database of the Combustion Toolbox to include species transport properties. Another feature that we are currently exploring, is the extension of the range of validity for certain species within the database, which will require to incorporate their second and subsequent ionizations, see Refs. [296, 302, 328]. By doing so, CT will be able to accurately handle extreme temperatures and pressures up to 100 000 K and 100 atm, respectively, which is crucial for modeling high-enthalpy processes. In terms of computational efficiency, we are also considering using MEX functions in the kernel of the code to combine C++ and MATLAB for calculating chemical equilibrium at defined temperature and pressure/volume, which is anticipated to improve the speed of the code substantially.

The theoretical analysis employed in this thesis focused on utilizing the isolated assumption as the boundary condition downstream of the shock wave to solve the linearized Euler equations. However, it is important to acknowledge that more realistic scenarios may require the inclusion of different types of boundary conditions. For example, when a rigid piston is considered, the sound waves emitted by the rippled shock will be reflected on the downstream surface that drives the shock, undoubtedly influencing the downstream perturbations. In addition, the problem discussed in Chapter 3 can be further generalized to include perturbations in the adiabatic index. In certain scenarios, these perturbations can have a comparable impact, particularly when dealing with similar-density mixtures near the heat release peak, characterized by low values of

both W and H simultaneously. Lastly, the Combustion Toolbox can also be used to facilitate the theoretical analysis by solving the perturbation-free jump conditions across the shock.

As discussed in Chapter 4, the theoretical framework presented can be extended to include additional phenomena such as: (a) non-equilibrium vibrational relaxation and finite-rate dissociation [254, 304–306]; (b) multi-component gas mixtures (particularly O_2 and N_2 for STI in air); (c) compressibility and anisotropy in the pre-shock turbulence; (d) the effects of walls downstream of the shock to address modal resonance in high-temperature inviscid shock layers around hypersonic projectiles; and (e) electronic excitation, radiation, and ionization in the post-shock gas for hypersonic flows at orbital stagnation enthalpies. Points (b) and (e), except for the radiation, were addressed numerically in Chapter 5 by using CT. While not presented in this thesis, ongoing research in collaboration with Christopher Williams (Stanford University) and Professor Mario Di Renzo (University of Salento and Stanford University) involves conducting direct numerical simulations (DNS) using the HTR solver [277–279] to investigate the interaction of hypersonic shocks with turbulent flows. The foreseen calculations will be targeted toward cases where the thermochemical relaxation length scales are increasingly similar to the turbulence characteristic lengths. The objective of these future studies will be to provide a more thorough assessment of the limit in which LIA can accurately predict the amplification of turbulent kinetic energy through the shock.

Acknowledgments

This work was partially supported by Madrid Government (Comunidad de Madrid-Spain) under the Multiannual Agreement with UC3M (H2SFE-CM-UC3M), by FEDER/Ministerio de Ciencia, Innovación y Universidades – Agencia Estatal de Investigación Projects (PID2019-108592RB-C41), and by UC3M – Financial Aids of the Doctoral School for Participation in Conferences and Mobility of Doctoral Students. The author thank Christopher Williams and Professor Mario Di Renzo for their contributions during the research process. Additionally, the author wants to thank Javier Rico for his critical feedback on the thesis introduction.

A Thermodynamic data

This appendix describes the calculation of the thermochemical properties of an ideal gas mixture required in the Combustion Toolbox (see Chapter 2).

A.1 Polynomials

The equilibrium computations carried out by CT rely on NASA's 9-coefficient polynomial fits, which provide the thermodynamic data of the individual species, including the molar specific heat at constant pressure, enthalpy, and entropy as a function of temperature in dimensionless form

$$\frac{C_p^\circ}{R} = a_1 T^{-2} + a_2 T^{-1} + a_3 + a_4 T + a_5 T^2 + a_6 T^3 + a_7 T^4, \tag{A.1a}$$

$$\frac{H^\circ}{RT} = -a_1 T^{-2} + a_2 T^{-1} \ln T + a_3 + a_4 T/2 + a_5 T^2/3 + a_6 T^3/4 + a_7 T^4/5 + a_8/T, \tag{A.1b}$$

$$\frac{S^\circ}{R} = -a_1 T^{-2}/2 - a_2 T^{-1} + a_3 \ln T + a_4 T + a_5 T^2/2 + a_6 T^3/3 + a_7 T^4/4 + a_9, \tag{A.1c}$$

where the a_i are the specific heat temperature coefficients for $i = 1, \ldots, 7$ and the two integration constants required for the computation of enthalpy and entropy for $i = 8, 9$. Depending on the species, the fits range from 50 K to 20000 K and are typically divided into two or three temperature ranges. The implemented thermodynamic database is a combination of NASA's [128] and Burcat's (Third Millennium) [129] databases.

As discussed in Sec. 2.2, when the temperature falls outside the range covered by the employed thermodynamic fits, CT employs a linear extrapolation instead of including higher order terms in the polynomials (A.1). This allows extending the range of validity of the thermodynamic data available, as demonstrated in Fig. D.1. A similar approach has been conducted by Stock et al. [122]. However, it is important to note that this extrapolation is only valid within a narrow temperature range and may not be applicable

to temperatures that significantly exceed this range. Therefore, alternative approaches are required to model such cases properly (e.g., see Refs. [302, 328]).

To compute the dimensionless Gibbs free energy G°/RT from NASA's polynomials, we use the following expression

$$G^\circ/RT = H^\circ/RT - S^\circ/R, \tag{A.2}$$

or equivalently

$$\begin{aligned}\frac{G^\circ}{RT} = &-a_1T^{-2}/2 + a_2T^{-1}(1+\ln T) + a_3(1-\ln T) - a_4T/2 \\ &- a_5T^2/6 - a_6T^3/12 - a_7T^4/20 + a_8/T - a_9.\end{aligned}$$

This data is collected from the `thermo_CT.inp` file and next formatted into a more accessible structure (*DB_master*) with the built-in function `generate_DB_master.m`. Then, for faster data access, we generate a new database (*DB*) that contains *griddedInterpolant* objects that allows the evaluation of the thermodynamic functions at a given temperature. CT implements routines that facilitate the evaluation of these functions. Thus, obtaining the value of the previous functions for methane CH_4 at 3000 K is as simple as follows:

```
cp0 = species_cp('CH4', 3000, self.DB)
h0  = species_h0('CH4', 3000, self.DB)
s0  = species_s0('CH4', 3000, self.DB)
g0  = species_g0('CH4', 3000, self.DB)
```

returning the values in J/(mol-K) for c_p°, in kJ/mol for h° and g°, and in kJ/(mol-K) for s°.

A.2 Properties of an ideal gas mixture

The thermodynamic properties of a mixture at equilibrium require the evaluation of the contributions of the individual species contained in the mixture, as described in the previous subsection. Due to the mixing process, these properties change when solids, liquids, or gases are considered. Therefore, CT computes them considering a linear mixing rule. In this case, the enthalpy, internal energy, entropy, and Gibbs energy of

the mixture read, respectively:

$$h = \sum_{j \in \mathbf{S}} n_j H_j^\circ, \tag{A.3a}$$

$$e = h - nRT, \tag{A.3b}$$

$$s = \sum_{j \in \mathbf{S}} n_j S_j^\circ - R \sum_{j \in \mathbf{S^G}} n_j \ln\left(\frac{n_j p}{n}\right), \tag{A.3c}$$

$$g = h - Ts, \tag{A.3d}$$

where $n = \sum_{j \in \mathbf{S^G}} n_j$ represents the total number of moles in the gas phase. By differentiating Eq. (A.3a) with respect to n_j and T at constant p, we obtain the specific heat at constant pressure

$$c_p = \sum_{j \in \mathbf{S}} n_j C_{p,j}^\circ + \sum_{j \in \mathbf{S^G}} n_j \frac{H_j^\circ}{T} \left(\frac{\partial \ln n_j}{\partial \ln T}\right)_p + \sum_{j \in \mathbf{S^C}} \frac{H_j^\circ}{T} \left(\frac{\partial n_j}{\partial \ln T}\right)_p, \tag{A.4}$$

defined as the sum of the frozen contribution (first term) and the reaction contribution (the remainder). The partial derivatives $(\partial \ln n_j/\partial T)_p$ and $(\partial n_j/\partial T)_p$ are obtained using the solution of the Jacobian matrix $\mathbf{J}$ obtained at equilibrium (see Ref. [10] for more details.). On the other hand, by differentiating Eq. (A.3b) with respect to n_j and T at constant v, we get the specific heat at constant volume

$$c_v = c_p + nR \left(\frac{\partial \ln v}{\partial \ln T}\right)_p^2 \left(\frac{\partial \ln v}{\partial \ln p}\right)_T^{-1} \tag{A.5}$$

and from the ideal gas EoS we obtain the partial derivatives

$$\left(\frac{\partial \ln v}{\partial \ln T}\right)_p = 1 + \left(\frac{\partial \ln n}{\partial \ln T}\right)_p, \tag{A.6a}$$

$$\left(\frac{\partial \ln v}{\partial \ln p}\right)_T = -1 + \left(\frac{\partial \ln n}{\partial \ln p}\right)_T. \tag{A.6b}$$

Lastly, the speed of sound a is defined as

$$a^2 = \frac{p}{\rho} \left(\frac{\partial \ln p}{\partial \ln \rho}\right)_s, \tag{A.7}$$

with

$$\gamma_s = \left(\frac{\partial \ln p}{\partial \ln \rho}\right)_s = -\gamma \left(\frac{\partial \ln v}{\partial \ln p}\right)_T^{-1}, \tag{A.8}$$

where the subscript s denotes constant entropy and $\gamma = c_p/c_v$ is the specific heat ratio.

Combustion Toolbox calculates all these quantities with the function `compute_properties.m`, but first, it is necessary to fill the property matrix

$$\mathbf{M_0} = \begin{bmatrix} h_{f,1} & e_{f,1} & W_1 & \text{phase}_1 & n_1 & h_1^\circ & c_{p,1}^\circ & s_1^\circ \\ h_{f,2} & e_{f,2} & W_2 & \text{phase}_2 & n_2 & h_2^\circ & c_{p,2}^\circ & s_2^\circ \\ \vdots & \vdots & \vdots & \vdots & \vdots & \vdots & \vdots & \vdots \\ h_{f,\text{NS}} & e_{f,\text{NS}} & W_\text{NS} & \text{phase}_\text{NS} & n_\text{NS} & h_\text{NS}^\circ & c_{p,\text{NS}}^\circ & s_\text{NS}^\circ \end{bmatrix} \tag{A.9}$$

containing the necessary thermodynamic parameters of all the species in the system required to calculate the thermodynamic properties of the mixture. These are the enthalpy of formation h_f, the internal energy of formation e_f, the molecular mass W, and the phase, which is zero or one depending if the species is in gas or condensed phase, respectively, the number of moles n, the enthalpy h°, the specific heat at constant pressure c_p°, and the entropy s°. Note that the first four columns are constants; however, the following columns change with temperature and pressure, i.e., the chemical equilibrium state. These values are filled with the routines `set_species_initialize.m` and `set_species.m`, respectively.

B Code examples of the Combustion Toolbox

In Chapter 2, we have presented the Combustion Toolbox[1], its capabilities, and the type of problems that can be solved with the first version of the code. Each problem has to be called with a specific abbreviation, as demonstrated in line 11 of Listing B.1. For example, for the thermochemical equilibrium module CT-EQUIL, these are:

- TP: equilibrium at specified temperature and pressure.
- HP: equilibrium at constant enthalpy and pressure.
- SP: equilibrium at constant entropy and pressure.
- TV: equilibrium at specified temperature and volume.
- EV: equilibrium at constant internal energy and volume.
- SV: equilibrium at constant entropy and volume.

As one may expect, constant parameters imply that the value, e.g., enthalpy of the HP problem, is the same for the initial (mix1) and final mixture (mix2). However, there are problems where it is necessary to use specific values. To do this, using the same example, we can proceed as follows:

```
1 function mix2 = example(mix1, h, p)
2     mix1.h = h;
3     mix2 = equilibrate(self, mix1, p);
4 end
```

solving the HP problem for a defined enthalpy in kJ and pressure in bar. By using a function, we can avoid the use of an auxiliary variable to store the actual value of mix1.

[1]To access the latest documentation of the Combustion Toolbox, including tutorials, examples, and detailed code descriptions, please visit the official website https://combustion-toolbox-website.readthedocs.io.

The CT-SD module for shock and detonation calculations contains multiple possible problems, with these abbreviations:

- SHOCK_I: planar shock wave, incident.
- SHOCK_R: planar shock wave, incident and reflected.
- SHOCK_OBLIQUE : oblique shock wave, incident.
- SHOCK_OBLIQUE_R: oblique shock wave, incident and reflected.
- SHOCK_POLAR: shock polar diagrams.
- SHOCK_POLAR_R: shock polar diagrams, incident and reflected.
- SHOCK_IDEAL_GAS: planar shock wave, incident for a fixed adiabatic index.
- DET: Chapman-Jouguet detonation.
- DET_R: Chapman-Jouguet detonation, incident and reflected.
- DET_OBLIQUE: oblique detonation.
- DET_POLAR: detonation polar diagrams.
- DET_OVERDRIVEN: over-driven detonation.
- DET_OVERDRIVEN_R: over-driven detonation, incident and reflected.
- DET_UNDERDRIVEN: under-driven detonation.
- DET_UNDERDRIVEN_R: under-driven detonation, incident and reflected.

For further details on how to introduce the additional inputs required for each problem, the reader is referred to the *examples* folder or the website. As two illustrative examples, Listing B.2 shows the snippet of the code necessary to obtain the shock polar diagrams of Fig. 2.6, and Listing B.3 displays an example of the report prompted in the command window after computing an oblique shock in air, at a given pre-shock Mach number and deflection angle.

The calculations of the IAC and FAC models in the CT-ROCKET module are called with the same abbreviation:

- ROCKET: rocket engine performance under ideal conditions,

and the model is specified by setting the variable `FLAG_IAC` (in `ProblemDescription.m`) to true or false, corresponding with the IAC and FAC models, respectively. This is shown in Listing B.4. Note that, in this case, the temperature of the cryogenic reactants has not been specified because CT directly assigns the temperature corresponding to their boiling points. For calculations assuming frozen chemistry (post-combustion), the `FLAG_FROZEN` attribute of the *Problem Description* must be set to true (by default, it is set to false).

```
% Initialization
self = App('Soot formation extended');
% Set initial conditions
self = set_prop(self, 'TR', 300, 'pR', 1);
self = set_prop(self, 'phi', 0.5:0.05:4);
self.PD.S_Fuel = {'C2H2_acetylene'};
self.PD.S_Oxidizer = {'N2', 'O2'};
self.PD.ratio_oxidizers_O2 = [79, 21]/21;
% Additional inputs
self = set_prop(self, 'pP', 1);
% Solve problem
self = solve_problem(self, 'HP');
% Display results (plots)
post_results(self);
```

Listing B.1: Snippet of the code necessary to reproduce the case shown in Fig. 2.13 using the desktop environment.

```
% Initialization
self = App('Air_ions');
% Set initial conditions
self = set_prop(self, 'TR', 300);
self = set_prop(self, 'pR', 1.01325);
self.PD.S_Oxidizer = {'N2', 'O2', 'Ar'};
self.PD.ratio_oxidizers_O2 = [78, 21, 1]/21;
% Additional inputs
self = set_prop(self, 'M1', 2:2:14);
% Tuning properties
self.TN.N_points_polar = 300;
% Solve problem
self = solve_problem(self, 'SHOCK_POLAR');
% Display results (plots)
post_results(self);
```

Listing B.2: Snippet of the code necessary to reproduce the case shown in Fig. 2.6 using the desktop environment.

```
1  ------------------------------------------------------------------------
2  Problem type: SHOCK_OBLIQUE  | phi =  NaN
3  ------------------------------------------------------------------------
4                  |     STATE 1      |     STATE 2-W    |     STATE 2-S
5  T [K]           |        300.0000  |       1233.3991  |       1525.1611
6  p [bar]         |          1.0132  |         20.9924  |         28.2923
7  r [kg/m3]       |          1.1768  |          5.9302  |          6.4635
8  h [kJ/kg]       |          1.8585  |       1019.1807  |       1371.9119
9  e [kJ/kg]       |        -84.2432  |        665.1911  |        934.1900
10 g [kJ/kg]       |      -2057.6172  |      -8236.8991  |     -10334.2938
11 s [kJ/(kg-K)]   |          6.8649  |          7.5045  |          7.6754
12 W [g/mol]       |         28.9697  |         28.9699  |         28.9702
13 (dlV/dlp)T [-]  |                  |         -1.0000  |         -1.0000
14 (dlV/dlT)p [-]  |                  |          1.0000  |          1.0000
15 cp [kJ/(kg-K)]  |          1.0044  |          1.1844  |          1.2333
16 gamma [-]       |          1.4001  |          1.3198  |          1.3032
17 gamma_s [-]     |          1.4001  |          1.3198  |          1.3032
18 sound vel [m/s] |        347.2019  |        683.5102  |        755.2816
19 u [m/s]         |       1736.0094  |        989.2476  |        523.1743
20 Mach number [-] |          5.0000  |          1.4473  |          0.6927
21 ------------------------------------------------------------------------
22 PARAMETERS
23 min wave  [deg] |                  |         11.5370  |         11.5370
24 wave angle[deg] |                  |         56.9743  |         75.8636
25 deflection[deg] |                  |         40.0000  |         40.0000
26 ------------------------------------------------------------------------
27 STATE 1                Xi [-]
28 N2                  7.8000e-01
29 O2                  2.1000e-01
30 Ar                  1.0000e-02
31 MINORS[+48]         0.0000e+00
32
33 TOTAL               1.0000e+00
34 ------------------------------------------------------------------------
35 STATE 2-W              Xi [-]
36 N2                  7.7987e-01
37 O2                  2.0986e-01
38 Ar                  1.0000e-02
39 NO                  2.4927e-04
40 NO2                 1.6587e-05
41 N2O                 7.8179e-08
42 O                   4.9856e-09
43 O3                  1.1427e-10
44 NO3                 2.2089e-11
45 N2O3                5.2354e-13
46 MINORS[+41]         0.0000e+00
47
48 TOTAL               1.0000e+00
49 ------------------------------------------------------------------------
50 STATE 2-S              Xi [-]
51 N2                  7.7931e-01
52 O2                  2.0928e-01
53 Ar                  1.0000e-02
54 NO                  1.3710e-03
55 NO2                 3.6374e-05
56 O                   4.8812e-07
57 N2O                 4.4256e-07
58 O3                  1.9535e-09
59 NO3                 1.2256e-10
60 N2O3                4.7846e-12
61 N                   1.8984e-14
62 MINORS[+40]         0.0000e+00
63
64 TOTAL               1.0000e+00
65 ------------------------------------------------------------------------
```

Listing B.3: Results shown in MATLAB's command window after solving an oblique shock for air (78% N_2, 21% O_2, and 1% Ar) at standard conditions ($T_1 = 300$ K, $p_1 = 1$ atm), pre-shock Mach number $\mathcal{M}_1 = 5$, and deflection angle $\theta = 40$ deg. The states 1, 2-W, and 2-S denote initial state, weak solution, and strong solution, respectively.

```
% Initialization
self = App('Hydrogen_L');
% Set initial conditions
self = set_prop(self, 'pR', 101.325);
self = set_prop(self, 'phi', 0.5:0.05:4)
self.PD.S_Fuel = {'H2bLb'};
self.PD.S_Oxidizer = {'O2bLb'};
self.PD.FLAG_IAC = false;
self.PD.FLAG_FROZEN = false;
% Additional inputs
self = set_prop(self, 'Aratio_c', 2);
self = set_prop(self, 'Aratio', 3);
% Solve problem
self = solve_problem(self, 'ROCKET');
% Display results (plots)
post_results(self);
```

Listing B.4: Snippet of the code necessary to partially reproduce the case shown in Fig. 2.12 using the desktop environment.

C Normal mode analysis

In this appendix, we describe the normal mode analysis required in Chapter 3 to describe the propagation of planar detonation fronts through heterogeneous mixtures of reactive gases consisting of random fluctuations in the fuel mass fraction.

Computations of the turbulence kinetic energy, along with the second-order corrections to the Rankine-Hugoniot jump conditions and detonation propagation speed, call for the amplitudes of the flow variables in the burnt gas. These amplitudes, provided by the corresponding transfer functions across the detonation front for a given upstream perturbation, can be analytically derived by means of the Laplace Transform functions, as shown in Huete et al. [229, 232]. However, as the interest is placed in the long-time dynamics, normal mode analysis offers a simpler form to obtain the asymptotic amplitudes of the burnt-gas perturbations. Thus, assuming that upstream perturbations are described by Eqs. (3.13) and (3.14), the asymptotic far-field amplitudes for the pressure, density and velocity functions can be written as follows:

$$\bar{p}(\bar{x},\bar{y},\tau) = \mathbb{P}_a \mathrm{e}^{\mathrm{i}(\kappa_a \bar{x} - \omega_a \tau)} \mathrm{e}^{\mathrm{i}\kappa_y \bar{y}}, \tag{C.1a}$$

$$\bar{\rho} = \bar{\rho}_a(\bar{x},\bar{y},\tau) + \bar{\rho}_e(\bar{x},\bar{y}) = \left[\mathbb{D}_a \mathrm{e}^{\mathrm{i}(\kappa_a \bar{x} - \omega_a \tau)} + \mathbb{D}_e \mathrm{e}^{\mathrm{i}\kappa_e \bar{x}}\right] \mathrm{e}^{\mathrm{i}\kappa_y \bar{y}}, \tag{C.1b}$$

$$\bar{u} = \bar{u}_a(\bar{x},\bar{y},\tau) + \bar{u}_r(\bar{x},\bar{y}) = \left[\mathbb{U}_a \mathrm{e}^{\mathrm{i}(\kappa_a \bar{x} - \omega_a \tau)} + \mathbb{U}_r \mathrm{e}^{\mathrm{i}\kappa_r \bar{x}}\right] \mathrm{e}^{\mathrm{i}\kappa_y \bar{y}}, \tag{C.1c}$$

$$\bar{v} = \bar{v}_a(\bar{x},\bar{y},\tau) + \bar{v}_r(\bar{x},\bar{y}) = \left[\mathbb{V}_a \mathrm{e}^{\mathrm{i}(\kappa_a \bar{x} - \omega_a \tau)} + \mathbb{V}_r \mathrm{e}^{\mathrm{i}\kappa_r \bar{x}}\right] \mathrm{e}^{\mathrm{i}\kappa_y \bar{y}}, \tag{C.1d}$$

where the acoustic (subscript a), entropic (subscript e), and rotational (subscript r) contributions are easily recognized. The spatial and temporal acoustic frequencies are κ_a and ω_a, respectively, and the rotational/entropic spatial frequency is $\kappa_r = \kappa_e = \mathcal{R}\kappa_x$.

While the value of the amplitudes must be solved with the aid of the linearized RH equations given in Eq. (3.17), the spatial and temporal frequencies are readily obtained

by introducing the normal mode functions in the linear Euler equations (3.16)

$$-\omega_a \mathbb{D}_a + \kappa_a \mathbb{U}_a + \kappa_y \mathbb{V}_a = 0, \tag{C.2a}$$
$$-\omega_a \mathbb{U}_a + \kappa_a \mathbb{P}_a = 0, \tag{C.2b}$$
$$-\omega_a \mathbb{V}_a + \kappa_y \mathbb{P}_a = 0, \tag{C.2c}$$
$$\mathbb{P}_a - \mathbb{D}_a = 0, \tag{C.2d}$$

thereby yielding the adiabatic dispersion relationship, $\omega_a^2 = \kappa_a^2 + \kappa_y^2$, of the flow perturbations in the burnt gas. As a result of the Doppler effect, the frequency seen by the detonation front is $\omega = \omega_a - \mathcal{M}_2 \kappa_a$ when there is a single excitation frequency in the upstream heterogeneous flow (isolated and stable detonation assumption). This is used to give

$$\kappa_a = \frac{\mathcal{M}_2 \omega - \sqrt{\omega^2 - \kappa_y^2 \left(1 - \mathcal{M}_2^2\right)}}{1 - \mathcal{M}_2^2}, \tag{C.3}$$

$$\omega_a = \frac{\omega - \mathcal{M}_2 \sqrt{\omega^2 - \kappa_y^2 \left(1 - \mathcal{M}_2^2\right)}}{1 - \mathcal{M}_2^2}, \tag{C.4}$$

as the characteristic spatial and temporal frequencies of the downstream acoustic field.

When these parameters are real, the frequency ω_a is always positive, while the wavenumber κ_a can be either positive or negative depending on whether the frequency of oscillation ω is smaller or larger than κ_y. Thus, from Eq. (C.1) it is observed that $\kappa_a > 0$ corresponds to right-traveling waves, while left-traveling waves prevail for $\kappa_a < 0$. In a laboratory frame where the upstream flow remains static, the latter condition refers to the case where the sound waves escaping from the detonation front surmount the velocity of the burnt-gas fluid particles and propagate downstream. The other distinguished case occurs when the values of κ_a and ω_a become imaginary, thereby yielding an exponential decay of the acoustic disturbances behind the front, a non-radiating condition that holds whenever $\omega < \kappa_y (1 - \mathcal{M}_2^2)^{1/2}$. In the opposite case, the detonation is said to be in the radiation regime, a condition that is hard to meet when there is no external excitation, as shown in Huete & Vera [207].

Direct combination of the linearized RH equations with the inviscid-inert Euler equations in the burnt-gas state gives the dispersion relation

$$\begin{aligned}\left[\omega_a^2 \left(\sigma_b + \mathcal{M}_2\right) - \kappa_a \omega_a \left(\mathcal{M}_2^2 + 2\mathcal{M}_2 \sigma_b + 1\right) + \kappa_a^2 \mathcal{M}_2 \left(\mathcal{M}_2 \sigma_b + 1\right)\right. \\ \left. - \kappa_y^2 \left(1 - \mathcal{M}_2^2\right) \sigma_c\right] \mathbb{P}_a = \mu \left[\omega^2 - \kappa_y^2 \left(1 - \mathcal{M}_2^2\right) \sigma_d\right]\end{aligned} \tag{C.5}$$

for the pressure fluctuations at the detonation front, where

$$\sigma_b = \frac{1+\Gamma}{2\mathcal{M}_2}, \quad \sigma_c = \frac{\mathcal{M}_2\mathcal{R}}{1-\mathcal{M}_2^2}\left(\frac{1-\Gamma}{2}\right), \\ \sigma_d = \frac{\mathcal{M}_2^2\mathcal{R}}{1-\mathcal{M}_2^2}\frac{(\mathcal{R}+\Delta-2)\,W-(1-\Delta)\,H}{(\mathcal{R}-\Delta)\,W+(1-\Delta)\,H}, \tag{C.6}$$

and the function

$$\mu = \frac{\mathcal{M}_2\left[(\mathcal{R}-\Delta)\,W+(1-\Delta)\,H\right]}{2\sqrt{W^2+H^2}} \tag{C.7}$$

accounts for the effective amplitude of the upstream excitation.

By employing normal mode analysis, the long-time dynamics of the pressure perturbation can be written as a piece-wise function of the high-frequency (sub-index h) and low-frequency (sub-indices l_1 and l_2) contributions

$$\begin{aligned} \bar{p}_2(\tau \gg 1) &= \mathbb{P}_h \mathrm{e}^{-\mathrm{i}\omega\tau+\mathrm{i}\kappa_y\bar{y}} && \text{for} \quad \omega \geq \kappa_y(1-\mathcal{M}_2^2)^{1/2}, \\ \bar{p}_2(\tau \gg 1) &= \sqrt{\mathbb{P}_{l_1}^2+\mathbb{P}_{l_2}^2}\,\mathrm{e}^{-\mathrm{i}(\omega\tau+\phi_a)+\mathrm{i}\kappa_y\bar{y}} && \text{for} \quad \omega \leq \kappa_y(1-\mathcal{M}_2^2)^{1/2}, \end{aligned} \tag{C.8}$$

with the phase $\tan\phi_a = \mathbb{P}_{l_2}/\mathbb{P}_{l_1}$ and the corresponding amplitudes $\mathbb{P}_h$, $\mathbb{P}_{l_1}$, and $\mathbb{P}_{l_2}$ given by

$$\mathbb{P}_h = \frac{\mu\left(\zeta^2-\sigma_d\right)}{\zeta\sqrt{\zeta^2-1}+\sigma_b\zeta^2-\sigma_c}, \tag{C.9a}$$

$$\frac{\mathbb{P}_{l_1}}{(\sigma_b\zeta^2-\sigma_c)} = \frac{-\mathbb{P}_{l_2}}{\zeta\sqrt{1-\zeta^2}} = \frac{\mu\left(\zeta^2-\sigma_d\right)}{\zeta^2(1-\zeta^2)+\left(\sigma_b\zeta^2-\sigma_c\right)^2}, \tag{C.9b}$$

with use made of the normalized dimensionless frequency

$$\zeta = \frac{\omega}{\kappa_y\sqrt{1-\mathcal{M}_2^2}} = \frac{\mathcal{M}_2\mathcal{R}}{\sqrt{1-\mathcal{M}_2^2}}\frac{1}{\tan\theta} = \frac{\mathcal{M}_2\mathcal{R}}{\sqrt{1-\mathcal{M}_2^2}}\left(\frac{\kappa_x}{\kappa_y}\right). \tag{C.10}$$

It is readily seen that the critical frequency $\omega = \kappa_y(1-\mathcal{M}_2^2)^{1/2}$ corresponds to $\zeta = 1$ and to the critical angle

$$\tan\theta_c = \frac{\mathcal{M}_2\mathcal{R}}{\sqrt{1-\mathcal{M}_2^2}}. \tag{C.11}$$

Inspection of the above equations provides conditions where the detonation travels through the monochromatic heterogeneous mixture without generating any pressure

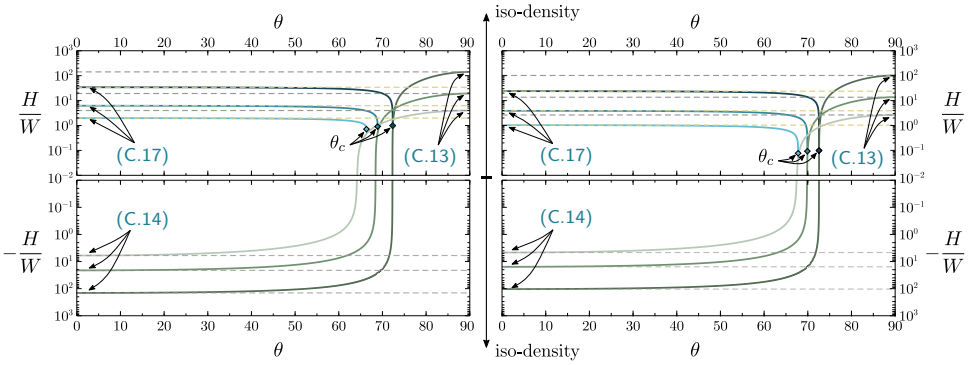

Figure C.1: Iso-curves $\mathbb{P}_a = 0$ (light-to-dark green as the incident Mach number increases) and $\mathbb{X} = 0$ (light-to-dark blue as the incident Mach number increases) as a function of the correlation factor H/W and the incident angle $\theta = \tan^{-1}(k_y/k_x)$ for $\gamma = 1.2, \mathcal{M}_1 = (1.2, 2, 5) \times \mathcal{M}_{\text{cj}}$ and $Q = 1$ (left) and $Q = 10$ (right).

perturbations behind it, $\bar{p}_2 = 0$. These conditions are obtained by analysing the right-hand side of Eq. (C.5), which becomes identically zero when upstream heat-release and density changes are correlated in the following form:

$$\left.\frac{H}{W}\right|^{\mathbb{P}_a=0} = -\frac{(\mathcal{R}-\Delta)\,\omega^2 - \mathcal{M}_2^2\mathcal{R}\,(\mathcal{R}+\Delta-2)\,\kappa_y^2}{(1-\Delta)\left(\omega^2 + \mathcal{M}_2^2\mathcal{R}\kappa_y^2\right)}. \tag{C.12}$$

When this condition is met, the detonation oscillates in mechanical equilibrium and no pressure perturbations are generated, a situation often referred to as a neutral condition. It is seen that H/W is not an exclusive property of the detonation, as it also depends on the excitation frequency ω/k_y. This dependence is computed in Fig. C.1 (a) as a function of the incident wave angle θ. Very large values of $|H/W|$ are representative of iso-density gas mixtures, while values of $|H/W| \ll 1$ represent situations close to the peak in the heat release-fuel mass fraction diagram, which is usually placed in slightly rich mixtures. For slow-frequency oscillations, $\omega/\kappa_y \ll 1$ or $\theta \sim 90°$, the detonation behaves neutrally if

$$\left.\frac{H}{W}\right|^{\mathbb{P}_a=0}_{\pi/2-\theta\ll 1} = \frac{\mathcal{R}+\Delta-2}{1-\Delta}, \tag{C.13}$$

which represents a positive correlation between the changes in density and heat release. On the other hand, high-frequency perturbations $\omega \gg \kappa_y$ can render a neutral state

only in negatively-correlated conditions, namely

$$\left.\frac{H}{W}\right|_{\theta\ll 1}^{\mathbb{P}_a=0} = -\frac{\mathcal{R}-\Delta}{1-\Delta}. \tag{C.14}$$

Both limiting conditions tend to infinity in the strongly overdriven limit as $\Delta \sim 1 - O(\mathcal{M}_2/\mathcal{M}_{\mathrm{cj}})$. This implies that natural stability is not possible in inert shocks where variations in heat release are effectively negligible.

Similarly, the amplitude of the perturbations of the detonation front is computed using Eq. (3.17a) to yield

$$\begin{aligned} \xi_2(\tau \gg 1) &= \mathbb{X}_h \mathrm{e}^{-\mathrm{i}\omega\tau + \mathrm{i}\kappa_y \bar{y}} && \text{for} \quad \omega \geq \kappa_y (1-\mathcal{M}_2^2)^{1/2}, \\ \xi_2(\tau \gg 1) &= \sqrt{\mathbb{X}_{l_1}^2 + \mathbb{X}_{l_2}^2}\, \mathrm{e}^{-\mathrm{i}(\omega\tau+\phi_\xi) + \mathrm{i}\kappa_y \bar{y}} && \text{for} \quad \omega \leq \kappa_y (1-\mathcal{M}_2^2)^{1/2}, \end{aligned} \tag{C.15}$$

where $\tan\phi_\xi = \mathbb{X}_{l_2}/\mathbb{X}_{l_1}$ and the functions $\mathbb{X}_h$, $\mathbb{X}_{l_1}$, and $\mathbb{X}_{l_2}$ can be explicitly written, with the aid of Eq. (3.17a), as a function of the pressure function

$$\mathbb{X}_h = \frac{\mathcal{M}_2 \mathcal{R}}{\zeta\,(\mathcal{R}-1)\sqrt{1-\mathcal{M}_2^2}} \left[\frac{1-\Gamma}{2\mathcal{M}_2^2} \mathbb{P}_h - \frac{(\mathcal{R}+\Delta-2)\,W - (1-\Delta)\,H}{2\sqrt{W^2+H^2}} \right], \tag{C.16a}$$

$$\mathbb{X}_{l_1} = \frac{\mathcal{M}_2 \mathcal{R}}{\zeta\,(\mathcal{R}-1)\sqrt{1-\mathcal{M}_2^2}} \left[\frac{1-\Gamma}{2\mathcal{M}_2^2} \mathbb{P}_{l_1} - \frac{(\mathcal{R}+\Delta-2)\,W - (1-\Delta)\,H}{2\sqrt{W^2+H^2}} \right], \tag{C.16b}$$

$$\mathbb{X}_{l_2} = -\frac{\mathcal{M}_2 \mathcal{R}}{\zeta\,(\mathcal{R}-1)\sqrt{1-\mathcal{M}_2}} \frac{1-\Gamma}{2\mathcal{M}_2} \mathbb{P}_{l_2}. \tag{C.16c}$$

The neutral condition for the wrinkled detonation front, $\mathbb{X} = 0$, can also be computed, and is shown in Fig. C.1 in blue colours. Asymptotic planar detonations occur in the high-frequency regime, for $\theta < \theta_c$, with the correlation value that predicts $\mathbb{X} = 0$ approaching the case for $\mathbb{P}_a = 0$ when $\theta \sim \theta_c$; however, they cannot occur simultaneously. In the high-frequency limit $\omega \gg \kappa_y$ the correlation factor reaches an asymptotic value given by

$$\left.\frac{H}{W}\right|_{\theta\ll 1}^{\mathbb{X}=0} = \frac{(\mathcal{R}-1)(\mathcal{M}_2+\Gamma)}{(1-\Delta)(1+\mathcal{M}_2)} - 1, \tag{C.17}$$

which, unlike the case for $\mathbb{P} = 0$, is positive. Along the blue curves, the detonation front is negligibly distorted, while dimensionless pressure perturbations are of the order of ϵ.

As the detonation propagates through the heterogeneous mixture, various types of perturbations are generated downstream. As shown in Eq. (C.1), the terms can be decomposed into acoustic, rotational and entropic fluctuations [83, 249], with the former taking the form of adiabatic traveling waves. The values of κ_a and ω_a turn out to be imaginary for $\omega \leq \kappa_y(1-\mathcal{M}_2^2)^{1/2}$, which translates into an effectively null acoustic contribution in the far-field burnt gas. This is readily seen in a reference frame attached to the detonation front $\bar{x}_s = \mathcal{M}_2\tau - \bar{x}$, which provides the following pressure field

$$\bar{p}(\bar{x}_s,\bar{y},\tau) = \sqrt{\mathbb{P}_{l_1}^2+\mathbb{P}_{l_2}^2}\,\mathrm{e}^{-\mathrm{i}\omega\left(\tau+\bar{x}_s\frac{\mathcal{M}_2}{1-\mathcal{M}_2^2}+\phi_a\right)+\mathrm{i}\kappa_y\bar{y}}\mathrm{e}^{-\sigma(\theta)\bar{x}_s} \tag{C.18}$$

for low-frequency oscillations, where

$$\sigma(\theta) = \frac{\sqrt{(1-\mathcal{M}_2^2)\sin^2\theta - \mathcal{M}_2^2\mathcal{R}^2\cos^2\theta}}{1-\mathcal{M}_2^2} \tag{C.19}$$

defines the spatial decay rate that varies from 0 (for $\theta = \theta_c$) to $1/\sqrt{1-\mathcal{M}_2^2}$ (for $\theta = \pi/2$). It is observed that the maximum decay rate increases as the overdrive decreases. For $\omega \geq \kappa_y(1-\mathcal{M}_2^2)^{1/2}$, the pressure field in the burnt gas is given by

$$\bar{p}(\bar{x},\bar{y},\tau) = \mathbb{P}_h\mathrm{e}^{-\mathrm{i}(\omega_a\tau-\kappa_a\bar{x})+\mathrm{i}\kappa_y\bar{y}}, \tag{C.20}$$

where the amplitude corresponds to that at the detonation front, as in Eq. (C.8). The isentropic density variations induced by the acoustic radiation are $\mathbb{D}_a = \mathbb{P}_h$, as dictated by Eq. (C.2d). Similarly, the associated velocity perturbations of the sonic wave emitted by the detonation can be computed with the aid of Eqs. (C.2b) and (C.2c), which gives $\mathbb{U}_a = \mathbb{P}_h\kappa_a/\omega_a$ and $\mathbb{V}_a = \mathbb{P}_h\kappa_y/\omega_a$ for the longitudinal and transverse contributions, respectively.

The acoustic velocity perturbations, which reach the far field only for $\zeta > 1$ ($\theta < \theta_c$), are shown in Fig. C.2 in the form of log-polar plots of $|\mathbb{U}_a|$ (left panels) and $|\mathbb{V}_a\tan\theta|$ (right panels) as functions of the incident wave angle θ. The results are computed for $\gamma = 1.2$, $\mathcal{M}_1 = 1.01\mathcal{M}_{\mathrm{cj}}$ (a-b), $\mathcal{M}_1 = 1.2\mathcal{M}_{\mathrm{cj}}$ (c-d) and $\mathcal{M}_1 = 2\mathcal{M}_{\mathrm{cj}}$ (e-f) and show curves corresponding to $|W| \gg |H|$ (black lines), $|H| \gg |W|$ (green lines), $W = H$ (orange lines) and $W = -H$ (blue lines).

Computations show that the radiated acoustic energy is very sensitive to the ratio between W and H, specially for weak overdrives. For example, when density variations are negligible, $|H| \gg |W|$, the acoustic perturbations are one order of magnitude smaller for finite overdrives, but they are non-negligible for $\mathcal{M}_1 = 1.01\mathcal{M}_{\mathrm{cj}}$. It is also observed that positive correlations $W = H$ lead to more intense acoustic perturbations than

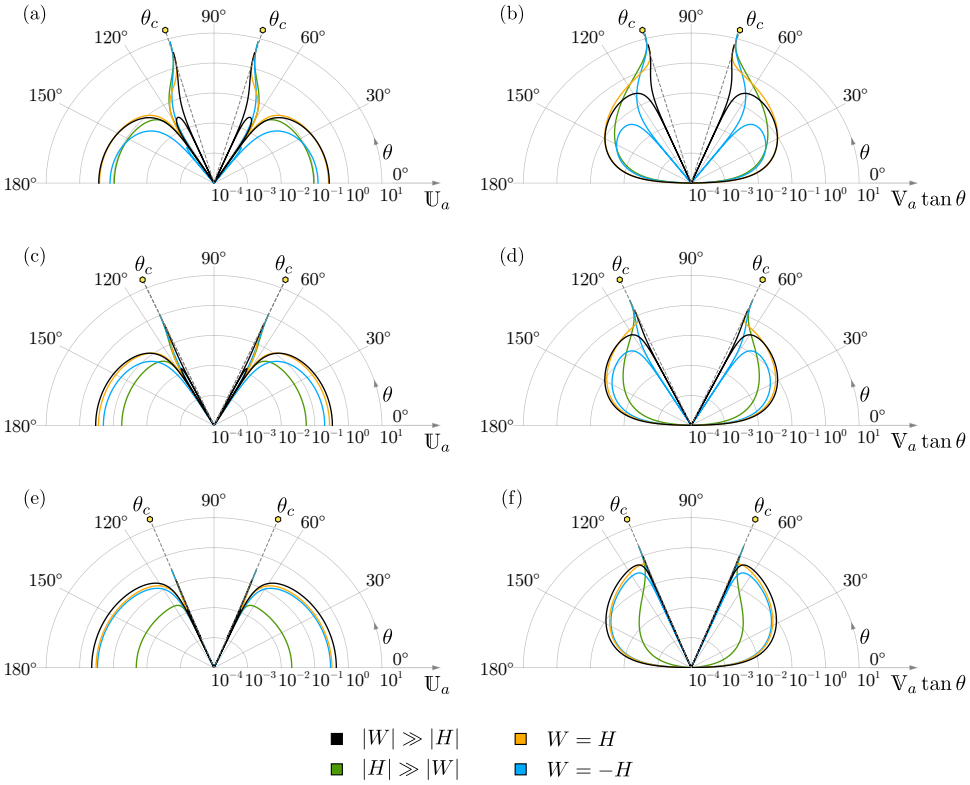

Figure C.2: Log-polar plot for $|\mathbb{U}_a|$ (a, c, and e) and $|\mathbb{V}_a \tan\theta|$ (b, d, and f) as functions of the incident wave angle $\theta = \tan^{-1}(k_y/k_x)$ for $\gamma = 1.2, \mathcal{M}_1 = 1.01\mathcal{M}_{\text{cj}}$ (a-b), $\mathcal{M}_1 = 1.2\mathcal{M}_{\text{cj}}$ (c-d), $\mathcal{M}_1 = 2\mathcal{M}_{\text{cj}}$ (e-f), $Q = 1$, and $|W| \gg |H|$ (——), $|H| \gg |W|$ (——), $W = H$ (——) and $W = -H$ (——).

negative correlations $W = -H$, but with the increase of overdrive both tend to the same value. In all cases, the maximum acoustic intensity is generated when $\theta \sim \theta_c$. It is also found that $|\mathbb{U}_a|$ and $|\mathbb{V}_a \tan\theta|$ become null when $\mathbb{P} = 0$, a condition met when Eq. (C.12) is satisfied. The intermediate angle at which acoustic perturbations cancel out approaches θ_c when the overdrive increases, as observed in Fig. C.1.

Along with the acoustic field, the oscillating detonation front is a source of entropy and vorticity disturbances. The former

$$\begin{aligned} \bar{\rho}_e(\bar{x} \gg 1, \bar{y}) &= \mathbb{D}_{e,h} \mathrm{e}^{\mathrm{i}\kappa_e \bar{x} + \mathrm{i}\kappa_y \bar{y}} && \text{for} \quad \omega \geq \kappa_y (1 - \mathcal{M}_2^2)^{1/2}, \\ \bar{\rho}_e(\bar{x} \gg 1, \bar{y}) &= \sqrt{\mathbb{D}_{e,l_1}^2 + \mathbb{D}_{e,l_2}^2}\, \mathrm{e}^{\mathrm{i}(\kappa_e \bar{x} + \phi_e) + \mathrm{i}\kappa_y \bar{y}} && \text{for} \quad \omega \leq \kappa_y (1 - \mathcal{M}_2^2)^{1/2}, \end{aligned} \tag{C.21}$$

where $\tan\phi_e = \mathbb{D}_{e,l_2}/\mathbb{D}_{e,l_1}$ and $\kappa_e = \mathcal{R}\kappa_x$, is easily evaluated by subtracting the acoustic contribution in the RH equation (3.17c). The corresponding amplitudes are

$$\mathbb{D}_{e,h} = \frac{\Gamma - \mathcal{M}_2^2}{\mathcal{M}_2^2} \mathbb{P}_h + \frac{\Delta W - (1 - \Delta) H}{\sqrt{W^2 + H^2}}, \tag{C.22a}$$

$$\mathbb{D}_{e,l_1} = \frac{\Gamma - \mathcal{M}_2^2}{\mathcal{M}_2^2} \mathbb{P}_{l_1} + \frac{\Delta W - (1 - \Delta) H}{\sqrt{W^2 + H^2}}, \tag{C.22b}$$

$$\mathbb{D}_{e,l_2} = \frac{\Gamma - \mathcal{M}_2^2}{\mathcal{M}_2^2} \mathbb{P}_{l_2}, \tag{C.22c}$$

for the high frequency (short wavelength) and low frequency (long wavelength) regimes, respectively.

The dimensionless vorticity function $\Omega(\bar{x}, \bar{y})\kappa_y = \partial\bar{v}/\partial\bar{x} - \partial\bar{u}/\partial\bar{y}$ is computed by calculating the vorticity generated by the first-order perturbations on the corrugated front, namely,

$$\frac{\partial \bar{v}}{\partial \bar{x}} - \frac{\partial \bar{u}}{\partial \bar{y}} = -\frac{(1 - \Gamma)(\mathcal{R} - 1)}{2\mathcal{M}_2} \frac{\partial \bar{p}_2}{\partial \bar{y}} + \frac{\mathcal{M}_2 (\mathcal{R} - 1)}{2} \frac{(\mathcal{R} + \Delta) W - (1 - \Delta) H}{\sqrt{W^2 + H^2}} \frac{\partial\, \delta Y_1}{\partial \bar{y}}, \tag{C.23}$$

where the functions $\bar{p}_2$ and δY_1 are evaluated at the detonation front $\tau = \bar{x}/\mathcal{M}_2$. The vorticity generated remains constant in the absence of diffusive effects, thereby yielding

$$\begin{aligned} \Omega(\bar{x} \gg 1, \bar{y}) &= \mathbb{O}_h \mathrm{e}^{\mathrm{i}\kappa_r \bar{x} + \mathrm{i}\kappa_y \bar{y}} && \text{for} \quad \omega \geq \kappa_y (1 - \mathcal{M}_2^2)^{1/2}, \\ \Omega(\bar{x} \gg 1, \bar{y}) &= \sqrt{\mathbb{O}_{l_1}^2 + \mathbb{O}_{l_2}^2}\, \mathrm{e}^{\mathrm{i}(\kappa_r \bar{x} + \phi_r) + \mathrm{i}\kappa_y \bar{y}} && \text{for} \quad \omega \leq \kappa_y (1 - \mathcal{M}_2^2)^{1/2}, \end{aligned} \tag{C.24}$$

for the far-field vorticity, where $\tan\phi_r = \mathbb{O}_{l_2}/\mathbb{O}_{l_1}$ and $\kappa_r = \kappa_e = \mathcal{R}\kappa_x$.

The corresponding amplitudes of the associated short and long wavelengths are

$$\mathbb{O}_h = \frac{(1-\Gamma)(\mathcal{R}-1)}{2\mathcal{M}_2}\mathbb{P}_h - \frac{\mathcal{M}_2(\mathcal{R}-1)}{2}\frac{(\mathcal{R}+\Delta)W-(1-\Delta)H}{\sqrt{W^2+H^2}}, \tag{C.25a}$$

$$\mathbb{O}_{l_1} = \frac{(1-\Gamma)(\mathcal{R}-1)}{2\mathcal{M}_2}\mathbb{P}_{l_1} - \frac{\mathcal{M}_2(\mathcal{R}-1)}{2}\frac{(\mathcal{R}+\Delta)W-(1-\Delta)H}{\sqrt{W^2+H^2}}, \tag{C.25b}$$

$$\mathbb{O}_{l_2} = \frac{(1-\Gamma)(\mathcal{R}-1)}{2\mathcal{M}_2}\mathbb{P}_{l_2}. \tag{C.25c}$$

The related steady-rotational velocity perturbations, which are isobaric in the linear limit, are governed by

$$\frac{\partial^2\bar{u}_r}{\partial\bar{x}^2}+\frac{\partial^2\bar{u}_r}{\partial\bar{y}^2}=-\frac{\partial\Omega}{\partial\bar{y}} \qquad \text{and} \qquad \frac{\partial^2\bar{v}_r}{\partial\bar{x}^2}+\frac{\partial^2\bar{v}_r}{\partial\bar{y}^2}=-\frac{\partial\Omega}{\partial\bar{x}}, \tag{C.26}$$

which provide the following far-field velocity functions for the longitudinal and transverse contributions, respectively

$$\begin{aligned}
&\bar{u}_r(\bar{x}\gg 1,\bar{y}) = \mathbb{U}_{r,h}\mathrm{e}^{\mathrm{i}\kappa_r\bar{x}+\mathrm{i}\kappa_y\bar{y}} && \text{for} \quad \omega \geq \kappa_y(1-\mathcal{M}_2^2)^{1/2},\\
&\bar{u}_r(\bar{x}\gg 1,\bar{y}) = \sqrt{\mathbb{U}_{r,l_1}^2+\mathbb{U}_{r,l_2}^2}\,\mathrm{e}^{\mathrm{i}(\kappa_r\bar{x}+\phi_r)+\mathrm{i}\kappa_y\bar{y}} && \text{for} \quad \omega \leq \kappa_y(1-\mathcal{M}_2^2)^{1/2},
\end{aligned} \tag{C.27}$$

and

$$\begin{aligned}
&\bar{v}_r(\bar{x}\gg 1,\bar{y}) = \mathbb{V}_{r,h}\mathrm{e}^{\mathrm{i}\kappa_r\bar{x}+\mathrm{i}\kappa_y\bar{y}} && \text{for} \quad \omega \geq \kappa_y(1-\mathcal{M}_2^2)^{1/2},\\
&\bar{v}_r(\bar{x}\gg 1,\bar{y}) = \sqrt{\mathbb{V}_{r,l_1}^2+\mathbb{V}_{r,l_2}^2}\,\mathrm{e}^{\mathrm{i}(\kappa_r\bar{x}+\phi_r)+\mathrm{i}\kappa_y\bar{y}} && \text{for} \quad \omega \leq \kappa_y(1-\mathcal{M}_2^2)^{1/2},
\end{aligned} \tag{C.28}$$

with the corresponding amplitudes proportional to the vorticity amplitude $\mathbb{O}_j$ through

$$\mathbb{U}_{r,j} = \frac{\mathbb{O}_j}{1+(\kappa_r/\kappa_y)^2} = \frac{\mathbb{O}_j\mathcal{M}_2^2}{\mathcal{M}_2^2+\zeta^2(1-\mathcal{M}_2^2)} = \mathbb{V}_{r,j}\frac{\kappa_y}{\kappa_r} = \mathbb{V}_{r,j}\frac{\mathcal{M}_2}{\zeta\sqrt{1-\mathcal{M}_2^2}}. \tag{C.29}$$

The subscript j may refer to the sub-indices h or l_1 and l_2 for high frequency and low-frequency contributions, respectively, as noted in previous equations.

The computed amplitudes of the rotational velocity perturbations are presented in Fig. C.3 as a function of the polar coordinate θ, with the left and right plots corresponding to $|\mathbb{U}_r|$ and $|\mathbb{V}_r\tan\theta|$, respectively. As in Fig. C.2, the results are obtained for $\gamma = 1.2$, $\mathcal{M}_1 = 1.01\mathcal{M}_{\mathrm{cj}}$ (a-b), $\mathcal{M}_1 = 1.2\mathcal{M}_{\mathrm{cj}}$ (c-d) and $\mathcal{M}_1 = 2\mathcal{M}_{\mathrm{cj}}$ (e-f) and show curves corresponding to $|W| \gg |H|$ (black lines), $|H| \gg |W|$ (green lines),

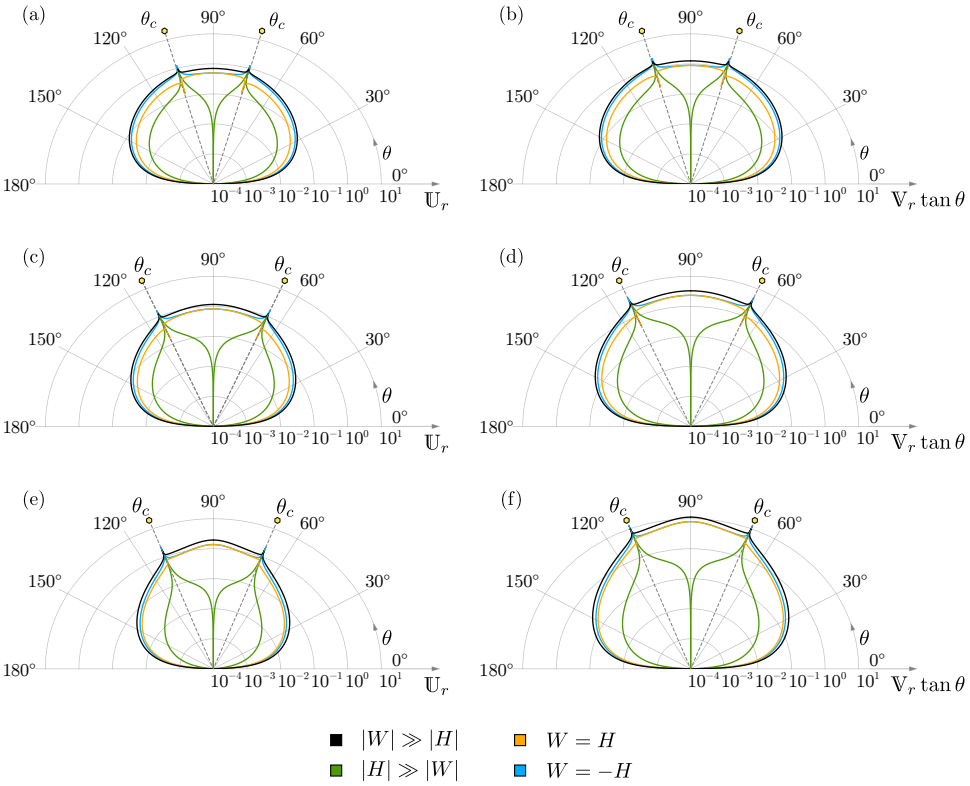

Figure C.3: Log-polar plot for $|\mathbb{U}_r|$ (a, c, and e) and $|\mathbb{V}_r \tan\theta|$ (b, d, and f) as functions of the incident wave angle $\theta = \tan^{-1}(k_y/k_x)$ for $\gamma = 1.2, \mathcal{M}_1 = 1.01\mathcal{M}_{\text{cj}}$ (a-b), $\mathcal{M}_1 = 1.2\mathcal{M}_{\text{cj}}$ (c-d), $\mathcal{M}_1 = 2\mathcal{M}_{\text{cj}}$ (e-f), $Q = 1$, and $|W| \gg |H|$ (——), $|H| \gg |W|$ (——), $W = H$ (——) and $W = -H$ (——).

$W = H$ (orange lines) and $W = -H$ (blue lines). It can be inferred that considering $|W| > 0$ amplifies the rotational perturbations in most of the domain for all degrees of overdrive, a finding that contrasts with the acoustic contribution. It is also observed that increasing the detonation intensity (by increasing the overdrive, see lower panel) amplifies the transverse part but barely changes the streamwise contribution. As expected, the maximum rotational intensity is produced close to the critical angle θ_c where all amplitudes peak. Aside from the trivial conditions determined by $\theta = 0°$ or $180°$, null rotational contribution, i.e., $|\mathbb{U}_r| = 0$ and $|\mathbb{V}_r \tan\theta| = 0$, are found to occur for transverse stratified gases, i.e., $\theta = 90°$, with similar density and outside of the heat-release peak.

The above results provide the dependence of the post-detonation perturbation amplitudes $\mathbb{P}(\theta)$, $\mathbb{D}(\theta)$, $\mathbb{O}(\theta)$, $\mathbb{U}(\theta)$ and $\mathbb{V}(\theta)$ for the pressure, density, vorticity and velocity variables, respectively, as a function of the incident angle $\theta = \tan^{-1}(k_y/k_x)$. They give the amplitudes of the perturbations in the asymptotic far field when the oscillating detonation reaches the constant-amplitude regime governed by the external single-frequency excitation. This case is representative of scenarios where the upstream spectrum is dominated by a single characteristic frequency k, something that is not expected to occur in heterogeneous gaseous mixtures, but rather in multi-phase environments involving water sprays [219, 220] or fuel sprays [208]. The model presented here cannot be directly applied to these conditions since in them density gradients cannot be linearized, and non-linear terms cannot be neglected. In general, specially in cases where the heterogeneities arise from the mixing of gaseous reactants as is considered here, the perturbations in the resulting mixture show a wide range of length scales. Then, the use of probability distribution functions is required to compute the flow perturbation variables downstream, as noted in Sec. 3.3.

D Ionization effects on the Rankine-Hugoniot jump relationships

This appendix is an extension of the mathematical framework of Sec. 4.2 in Chapter 4, where the Rankine-Hugoniot (RH) relations were defined using statistical thermodynamics. Here, the RH jump conditions include in addition to the previous thermochemical effects (rotation, translation, vibration, and dissociation), electronic excitation and ionization of the species. Specific formulae for monatomic and diatomic gases is included.

D.1 Monatomic gas

The simplest case consists of a single-species monatomic gas, where vibrational or dissociation effects cannot occur. In this section we provide the RH jump relations along with their asymptotic frozen and fully ionized gas limits.

D.1.1 Conservation equations across the shock

Similar to the previous chapters, let us begin by considering the scenario of an undisturbed, normal shock wave in a single-component gas consisting of single atoms, which is cold, inviscid, and irrotational. In this case, the pre-shock density, pressure, temperature, specific internal energy, and flow velocity in the shock's reference frame are represented by ρ_1, p_1, T_1, e_1, and u_1, respectively. On the other hand, the corresponding flow variables in the post-shock gas are denoted as ρ_2, p_2, T_2, e_2, and u_2.

In the reference frame attached to the shock front, the conservation equations of mass, momentum, and enthalpy across the shock are

$$\rho_1 u_1 = \rho_2 u_2, \tag{D.1a}$$

$$p_1 + \rho_1 u_1^2 = p_2 + \rho_2 u_2^2, \tag{D.1b}$$

$$e_1 + \frac{p_1}{\rho_1} + \frac{1}{2}u_1^2 = e_2 + \frac{p_2}{\rho_2} + \frac{1}{2}u_2^2 + q_i, \tag{D.1c}$$

respectively. The formulation employs the symbol q_i to represent the net change of specific internal energy caused by ionization of the gas through the following reaction

$$\mathrm{A} \rightleftharpoons \mathrm{A}^{+} + \mathrm{e}^{-}. \tag{D.2}$$

Here, A represents the neutral atom, A^{+} denotes the corresponding positive ion, and e^{-} refers to the free electron. The energy employed in ionizing the gas is directly proportional to the ionization temperature

$$q_i = \eta_{\mathrm{A}} R_{g,\mathrm{A}} \Theta_{\mathrm{A}} \tag{D.3}$$

where $\eta_{\mathrm{A}} = n_{\mathrm{e}}/(n_{\mathrm{A}} + n_{\mathrm{A}^{+}})$ is the degree of ionization, measures as the relative concentration of electrons n_{e} with respect to the concentration of atoms n_{A} and ions $n_{\mathrm{A}^{+}}$. Assuming that upstream the gas is sufficiently cold to neglect ionization effects, the pressure is readily given by

$$p_1 = R_{g,\mathrm{A}} \rho_1 T_1, \tag{D.4}$$

while downstream pressure must account for the electron contribution in the form

$$p_2 = (1 + \eta_{\mathrm{A}})\, R_{g,\mathrm{A}} \rho_2 T_2. \tag{D.5}$$

The conservation equations complete upon determination of the internal energy state functions, namely

$$e_1 = \frac{3}{2} R_{g,\mathrm{A}} T_1, \tag{D.6}$$

and

$$e_2 = \frac{3}{2} R_{g,\mathrm{A}} T_2 (1 + \eta_{\mathrm{A}}), \tag{D.7}$$

which are associated with the conditions upstream and downstream of the shock, respectively. It is worth noting that only the translational component of the atoms' kinetic energy is taken into account.

The problem formulation is considered complete once the equilibrium condition for the concentrations of electrons and ions is determined. This condition is given by the Saha equation

$$\frac{\eta_{\mathrm{A}}^2}{1 - \eta_{\mathrm{A}}} = \mathcal{G}_{\mathrm{A}} m_{\mathrm{A}} \left(\frac{m_{\mathrm{e}} k_B}{2\pi\hbar^2} \right)^{3/2} \frac{T_2^{3/2}}{\rho_2} \mathrm{e}^{-\frac{\Theta_{\mathrm{A}}}{T_2}}. \tag{D.8}$$

where m_{A} is the atomic mass of the atom (which can be taken invariant in ionized conditions), m_{e} is the atomic mass of the electron, and Θ_{A} is the corresponding ionization

temperature. The equilibrium condition (D.8) involves the Boltzmann constant k_B and the reduced Plank's constant $\hbar$. In addition, the factor $\mathcal{G}$ includes information on the electronic partition functions of the mixture species: electrons, ions, and atoms, which can be approximated as the ground state degeneracy factors (Appendix D.2 explains how to model the electronic excitation). The values of Θ_A, $\mathcal{G}$, and m_A for different gases are provided in Table D.1.

D.1.2 Dimensionless formulation

Upstream properties are conveniently used to rewrite the problem in terms of dimensionless parameters:

$$B_\mathrm{A} = \mathcal{G}_\mathrm{A} \frac{m_A T_1^{2/3}}{\rho_1} \left(\frac{m_\mathrm{e} k_B}{2\pi\hbar^2} \right)^{3/2}, \quad \beta_A = \frac{\Theta_\mathrm{A}}{T_1}, \tag{D.9}$$

which are later employed in the nondimensional formulation of the problem. For example, the combination of the conservation equations (D.1a) to (D.1c) and the Saha equilibrium condition (D.8), render

$$\mathcal{T} = \frac{4 - \mathcal{R}^{-1} - 2\eta_\mathrm{A}\beta_\mathrm{A}}{(4-\mathcal{R})(1+\eta_\mathrm{A})}, \tag{D.10a}$$

$$\frac{\eta_\mathrm{A}^2}{1-\eta_\mathrm{A}} = B_\mathrm{A} \frac{\mathcal{T}^{3/2}}{\mathcal{R}} \mathrm{e}^{-\beta_\mathrm{A}/\mathcal{T}}, \tag{D.10b}$$

where $\mathcal{T} = T_2/T_1$ and $\mathcal{R} = \rho_2/\rho_1$ are the temperature and density ratios, respectively. Equations (D.10a) and (D.10b) describe downstream properties in terms of a single jump condition imposed by the shock intensity. For instance, if the temperature jump $\mathcal{T}$ is specified as an input variable, then $\mathcal{R}$ and η_A can be completely determined. If, on the other hand, pressure jump $\mathcal{P} = p_2/p_1$ is known, then the EoS

$$\mathcal{P} = (1+\eta_\mathrm{A})\,\mathcal{R}\mathcal{T} \tag{D.11}$$

must be used to complete the system. Additionally, the relationship with the shock Mach number $\mathcal{M}_1 = u_1/a_1$, where $a_1 = \sqrt{(5/3)R_{g,\mathrm{A}}T_1}$ represents the speed of sound in the gas before the shock, can be derived by directly combining the conservation equations for mass and momentum using:

$$\mathcal{P} = 1 + \frac{5}{3}\mathcal{M}_1^2 \left(1 - \frac{1}{\mathcal{R}} \right). \tag{D.12}$$

D.1.3 Asymptotic frozen and fully ionized gas limits

In the same fashion as in Sec. 4.2.4, the distribution of the density ratio $\mathcal{R}$ have two well distinguished limits, as depicted in Fig. D.1. The first limit is obtained at sufficiently low temperatures, where the monatomic gas has not started the ionization process yet. Thus, when $\eta_{\mathrm{A}} \to 0$, the density ratio can be approximated as

$$\mathcal{R} \sim \frac{2(\mathcal{T}-1)+\sqrt{4\mathcal{T}^2-7\mathcal{T}+4}}{\mathcal{T}}, \tag{D.13}$$

corresponding with the solution for a calorically perfect monatomic gas. In the opposite limit, at very high temperatures we have $\eta_{\mathrm{A}} \to 1$, which renders

$$\mathcal{R} \sim \frac{2\beta_{\mathrm{A}}+4(2\mathcal{T}-1)+\sqrt{8\mathcal{T}+(2\beta_{\mathrm{A}}+8\mathcal{T}-4)^2}}{4\mathcal{T}}. \tag{D.14}$$

Figure D.1 shows the density ratio $\mathcal{R}$ as a function of the temperature ratio $\mathcal{T}$ for two monatomic gases, argon (Ar) and hydrogen (H). The lines are colored by the degree of ionization η_{A}. The dashed lines represent the asymptotic solutions for low and high temperatures given by Eqs. (D.13) and (D.14), respectively. Additionally, the results have been compared with the values obtained using the Combustion Toolbox (see Chapter 2) for the same pre-shock conditions.

It is readily seen the total agreement of the theory with the numerical results (symbols), even at a temperature beyond the limit of NASA's polynomials, i.e., $T_2 > 20000$ K. Note that this is possible because we have cut off the higher orders of the polynomials in the Combustion Toolbox, extending the limit of validity to the close vicinity of the polynomials temperature limit. This particular case matches the entire domain tested because these monatomic gases behave linearly at very high temperatures when there is no interaction with other species.

Not included here for brevity, the density ratio reproduces the values obtained in Mond & Rutkevich [287] and Mond et al. [288]. In the latter, the authors included the electronic excitation in the definition of $\mathcal{G}$. They found that this contribution for monatomic gases with no interaction with other species is negligible, i.e., at chemical equilibrium, the electrons prefer to ionize rather than jump between the valence shell, as seen with the results obtained with the Combustion Toolbox, which considers the electronic excitation of the species.

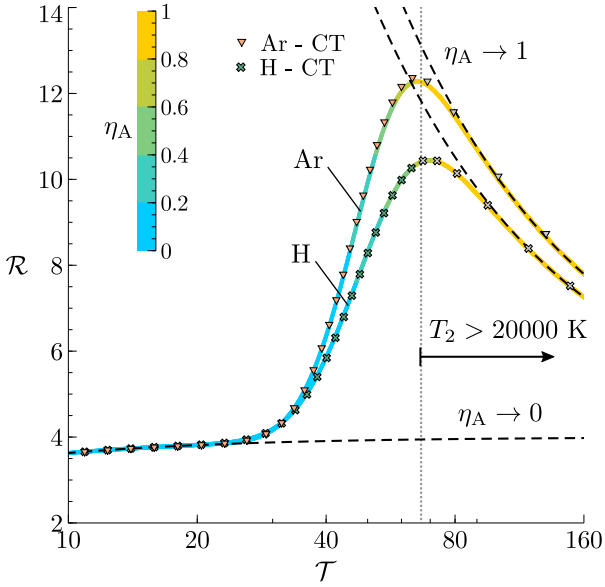

Figure D.1: Distribution of density jump $\mathcal{R}$ as a function of the temperature jump $\mathcal{T}$ for argon (Ar) and hydrogen (H) [lines colored by the degree of ionization]. Dashed lines represent asymptotic limits for a calorically perfect monatomic gas ($\eta_A \to 0$), and for a highly ionized gas ($\eta_A \to 1$). The pre-shock state is defined at $T_1 = 300$ K and $p_1 = 5$ Torr. Symbols represent numerical results obtained with the Combustion Toolbox (in gray using linear extrapolation).

D.2 Diatomic gas

Similarly, we can extend our analysis to a diatomic gas considering a more complex case that accounts for the vibrational and dissociation effects, as well as the electronic excitation and first ionization of the species (monatomic and diatomic). In this section, we will examine the RH jump relations specific to diatomic gases and their asymptotic frozen, vibrational, and fully ionized gas limits.

D.2.1 Conservation equations across the shock

Let us focus on the issue of a strong shock in a diatomic gas. In such a scenario, besides ionization, high-temperature phenomena encompass molecular vibrational excitation and dissociation, which can occur concurrently. Now, the conservation equations read as:

$$\rho_1 u_1 = \rho_2 u_2, \tag{D.15a}$$

$$p_1 + \rho_1 u_1^2 = p_2 + \rho_2 u_2^2, \tag{D.15b}$$

$$e_1 + \frac{p_1}{\rho_1} + \frac{1}{2}u_1^2 = e_2 + \frac{p_2}{\rho_2} + \frac{1}{2}u_2^2 + q_d + q_i, \tag{D.15c}$$

which involves an extra parameter q_d for the overall variation of specific chemical enthalpy induced by the dissociation process. In this scenario, the reactions undergoing behind the shock are

$$\mathrm{A_2} \rightleftharpoons \mathrm{A} + \mathrm{A}, \quad \mathrm{A_2} \rightleftharpoons \mathrm{A_2^+} + \mathrm{e^-}, \quad \mathrm{A} \rightleftharpoons \mathrm{A^+} + \mathrm{e^-}, \tag{D.16}$$

where $\mathrm{A_2}$ refers to a molecular species, while A represents its dissociated atomic counterpart. $\mathrm{A_2^+}$ and $\mathrm{A^+}$ denote the corresponding ions, while $\mathrm{e^-}$ refers to the electron. The energy employed in dissociation, q_d, can be expressed as

$$q_d = \alpha R_{g,\mathrm{A_2}} \Theta_d \tag{D.17}$$

where $R_{g,\mathrm{A_2}}$ is the gas constant based on the molecular weight of $\mathrm{A_2}$ and Θ_d stands for the characteristic dissociation temperature. The parameter $0 < \alpha < 1$ is the degree of dissociation, defined as the ratio of the mass of dissociated A atoms to the total mass of the gas, or equivalently, the mass fraction of A atoms. Ionization, in this case, takes place in both dissociated and non-dissociated molecules, with the whole contribution

being expressed as

$$q_i = \eta_{\mathrm{A}_2}(1-\alpha)R_{g,\mathrm{A}_2}\Theta_{\mathrm{A}_2} + 2\eta_A\alpha R_{g,\mathrm{A}_2}\Theta_A \tag{D.18}$$

where Θ_A and Θ_{A_2} correspond to the characteristic ionization temperatures of the dissociated and non-dissociated species, respectively. The corresponding degree of ionization are measured with $0 < \eta_A < 1$ and $0 < \eta_{\mathrm{A}_2} < 1$, respectively.

Equations (D.15a) to (D.15c) are supplemented with the ideal-gas equations of state in the pre-shock gas

$$p_1 = R_{g,\mathrm{A}_2}\rho_1 T_1 \tag{D.19}$$

and in the post-shock gas

$$p_2 = \left[1 + \alpha + 2\alpha\eta_A + (1-\alpha)\eta_{\mathrm{A}_2}\right] R_{g,\mathrm{A}_2}\rho_2 T_2. \tag{D.20}$$

Additionally, the specific internal energy in the pre-shock gas e_1 is given by the translational and rotational components

$$e_1 = \frac{5}{2}R_{g,\mathrm{A}_2}T_1, \tag{D.21}$$

whereas in the post-shock gas e_2 requires consideration of translational, rotational, vibrational degrees of freedom along with mixing between molecular and atomic species, and the contribution of free electrons, which gives

$$\begin{aligned} e_2 = {} & R_{g,\mathrm{A}_2}T_2\left[3\alpha + (1-\alpha)\left(\frac{5}{2} + \frac{\Theta_v/T_2}{\mathrm{e}^{\Theta_v/T_2}-1}\right)\right] \\ & + R_{g,\mathrm{A}_2}T_2\left[3\alpha\eta_A + \frac{3}{2}(1-\alpha)\eta_{\mathrm{A}_2}\right]. \end{aligned} \tag{D.22}$$

Equation (D.22) contains two square brackets where the first term represents the translational contribution of the monatomic species and is proportional to the dissociation degree α. The second term, proportional to $1-\alpha$, incorporates the translational, rotational, and vibrational contributions of the molecular species. Here, it is assumed that the rotational degrees of freedom are fully activated, and the molecules vibrate as harmonic oscillators with the characteristic vibrational temperature Θ_v. The bottom-line relationship in the equation pertains to the contribution of electrons in both dissociated and non-dissociated molecules, proportional to $\eta_A\alpha$ and to $\eta_{\mathrm{A}_2}(1-\alpha)$, respectively.

The chemical-equilibrium condition downstream of the shock concludes the closure

	H_2	O_2	N_2	H	O	N	Ar
Θ_r [K]	87.53	2.08	2.87	–	–	–	–
Θ_v [K] $\times 10^3$	6.34	2.27	3.39	–	–	–	–
Θ_d [K] $\times 10^4$	5.19	5.95	11.3	–	–	–	–
$\Theta_{A_2,A}$ [K] $\times 10^5$	1.79	1.42	1.81	1.57	1.58	1.69	1.83
m_j [kg] $\times 10^{26}$	0.167	2.66	2.33	0.0835	1.33	1.17	6.63
$\mathcal{G}$ or $\mathcal{G}_A$	$2^2/1$	$9^2/3$	$4^2/1$	2/2	8/9	18/4	11

Table D.1: Rotational (Θ_r), vibrational (Θ_v), dissociation (Θ_d), and ionization (Θ_{A,A_2}) characteristic temperatures, along with the factor $\mathcal{G}$ and the atomic mass m_j of the j species. The electronic partition function of atomic oxygen, $Q_{\mathrm{el}}^{\mathrm{O}}$, includes the first two excitation levels in addition to the ground state.

of the formulation, which is determined separately for the degree of dissociation and the degree of ionization of atoms and ionization of molecules [329]

$$\begin{aligned}
\frac{\alpha^2}{1-\alpha} &= \mathcal{G} m_{\mathrm{A}} \Theta_r \left(\frac{m_{\mathrm{A}} k_B}{4\pi\hbar^2}\right)^{3/2} \frac{T_2^{1/2}}{\rho_2} \mathrm{e}^{-\frac{\Theta_d}{T_2}} \left(1 - \mathrm{e}^{-\frac{\Theta_v}{T_2}}\right), \\
\frac{\eta_{\mathrm{A}}^2}{1-\eta_{\mathrm{A}}} &= \frac{\mathcal{G}_{\mathrm{A}} m_{\mathrm{A}}}{\alpha} \left(\frac{m_{\mathrm{e}} k_B}{2\pi\hbar^2}\right)^{3/2} \frac{T_2^{3/2}}{\rho_2} \mathrm{e}^{-\frac{\Theta_{\mathrm{A}}}{T_2}}, \\
\frac{\eta_{\mathrm{A}_2}^2}{1-\eta_{\mathrm{A}_2}} &= \frac{\mathcal{G}_{\mathrm{A}_2} m_{\mathrm{A}_2}}{1-\alpha} \left(\frac{m_{\mathrm{e}} k_B}{2\pi\hbar^2}\right)^{3/2} \frac{T_2^{3/2}}{\rho_2} \mathrm{e}^{-\frac{\Theta_{\mathrm{A}_2}}{T_2}},
\end{aligned} \tag{D.23}$$

where Θ_r is the characteristic rotational temperature, m is the atomic mass of A, k_B is the Boltzmann's constant, $\hbar$ is the reduced Planck's constant, and $\mathcal{G} = (Q_{\mathrm{el}}^a)^2/Q_{\mathrm{el}}^{aa}$ is a ratio of electronic partition functions of A atoms (Q_{el}^a) and A_2 molecules (Q_{el}^{aa}), whereas $\mathcal{G}_{\mathrm{A}} = 2Q_{\mathrm{el}}^{a^+}/Q_{\mathrm{el}}^a$ and $\mathcal{G}_{\mathrm{A}_2} = 2Q_{\mathrm{el}}^{aa^+}/Q_{\mathrm{el}}^{aa}$ are the electronic partition function of the first ionization of A atoms and A_2 molecules, respectively. The electronic partition function is modeled according to Maxwell-Boltzmann statistics, namely

$$Q_{\mathrm{el}} = \sum_i g_i \mathrm{e}^{\Theta_{\mathrm{el},i}/T}, \tag{D.24}$$

where g_i is the degeneracy factor at the i-th electronic state and $\Theta_{\mathrm{el},i}$ is the electronic characteristic temperature associated. Considering only the ground state is generally sufficient for applications that do not involve very high temperatures. Thus, upon neglecting the variations of the specific internal energy with temperature due to electronic excitation, $\mathcal{G}, \mathcal{G}_{\mathrm{A}}$, and $\mathcal{G}_{\mathrm{A}_2}$ can be approximated as the ground state degeneracy factors, thereby simplifying the analysis and reducing the parameters to the minimum accountable factors. It is important to note that this is not particularly accurate for O and

N^+ due to the low characteristic temperature associated with the two first electronic excitation levels. Thus, $Q_{\mathrm{el}} \sim 9$ should be conveniently used for O and N^+. Typical values of Θ_r, Θ_v, Θ_d, Θ_{A,A_2}, $\mathcal{G}_{A,A_2}$, and m_{A,A_2} are provided in Table D.1 for hydrogen, oxygen, and nitrogen in its atomic and molecular structure, as well as for atomic argon.

As discussed in Section 4.5, significant discrepancies arise if this thermochemical effect is neglected at very high temperatures. In particular, parameters that involve derivatives in their definition [see Fig. 4.14(b)]. In such cases, it becomes necessary to include Eq. (D.24) with a cut-off criterion (e.g., Griem criterion [330]), as the term diverges to infinity for isolated monatomic species. The interested reader is referred to Refs. [295, 296, 302, 331]. Another approach, as a first approximation, is to consider the first excitation states. For example, for O, N, O^+, N^+, O_2, and N_2, respectively, this can also be modeled in a first approximation as [332]

$$Q_{\mathrm{el}}^{\mathrm{O}} = 5 + 3\mathrm{e}^{-\frac{228}{T}} + \mathrm{e}^{-\frac{326}{T}} + 5\mathrm{e}^{-\frac{22800}{T}} + \mathrm{e}^{-\frac{48600}{T}}, \tag{D.25a}$$

$$Q_{\mathrm{el}}^{\mathrm{N}} = 4 + 10\mathrm{e}^{-\frac{27700}{T}} + 6\mathrm{e}^{-\frac{41500}{T}}, \tag{D.25b}$$

$$Q_{\mathrm{el}}^{\mathrm{O}^+} = 4 + 10\mathrm{e}^{-\frac{38600}{T}} + \mathrm{e}^{-\frac{58200}{T}}, \tag{D.25c}$$

$$Q_{\mathrm{el}}^{\mathrm{N}^+} = 1 + 3\mathrm{e}^{-\frac{70.6}{T}} + 5\mathrm{e}^{-\frac{188.9}{T}} + 5\mathrm{e}^{-\frac{22000}{T}} + \mathrm{e}^{-\frac{47000}{T}} + 5\mathrm{e}^{-\frac{67900}{T}}, \tag{D.25d}$$

$$Q_{\mathrm{el}}^{\mathrm{O}_2} = 3 + 2\mathrm{e}^{-\frac{11390}{T}} + \mathrm{e}^{-\frac{18990}{T}}, \tag{D.25e}$$

$$Q_{\mathrm{el}}^{\mathrm{N}_2} = 1. \tag{D.25f}$$

D.2.2 Dimensionless formulation

A dimensionless formulation of the problem can be written by introducing the nondimensional parameters

$$B_d = \mathcal{G}\frac{m_{\mathrm{A}}\Theta_r T_1^{1/2}}{\rho_1}\left(\frac{m_A k_B}{4\pi\hbar^2}\right)^{3/2}, \tag{D.26a}$$

$$B_{\mathrm{A}} = \mathcal{G}_{\mathrm{A}}\frac{m_{\mathrm{A}} T_1^{2/3}}{\rho_1}\left(\frac{m_{\mathrm{e}} k_B}{2\pi\hbar^2}\right)^{3/2}, \tag{D.26b}$$

$$B_{\mathrm{A}_2} = \mathcal{G}_{\mathrm{A}_2}\frac{m_{\mathrm{A}_2} T_1^{2/3}}{\rho_1}\left(\frac{m_{\mathrm{e}} k_B}{2\pi\hbar^2}\right)^{3/2} \tag{D.26c}$$

and

$$\beta_d = \frac{\Theta_d}{T_1}, \quad \beta_v = \frac{\Theta_v}{T_1}, \quad \beta_{\mathrm{A}_2} = \frac{\Theta_{\mathrm{A}_2}}{T_1}. \tag{D.27}$$

Upon substituting Eqs. (D.19) and (D.22) into the conservation equations (D.15a) to (D.15c), and considering the equilibrium relationships for dissociation (D.17) and ionization (D.18) phenomena, we arrive at

$$\mathcal{T} = \frac{6 - \mathcal{R}^{-1} - 2\alpha\beta_d - 2(1-\alpha)\beta_v / \left(\mathrm{e}^{\beta_v/\mathcal{T}} - 1\right) - 4\alpha\eta_{\mathrm{A}}\beta_{\mathrm{A}} - 2(1-\alpha)\eta_{\mathrm{A}_2}\beta_{\mathrm{A}_2}}{2(\alpha+3) - \mathcal{R}(1+\alpha) + (4-\mathcal{R})\left[2\alpha\eta_{\mathrm{A}} + (1-\alpha)\eta_{\mathrm{A}_2}\right]} \tag{D.28}$$

and

$$\frac{\alpha^2}{1-\alpha} = \frac{B\mathcal{T}^{1/2}}{\mathcal{R}}\left(1 - \mathrm{e}^{-\beta_v/\mathcal{T}}\right)\mathrm{e}^{-\beta_d/\mathcal{T}}, \tag{D.29a}$$

$$\frac{\eta_{\mathrm{A}}^2}{1-\eta_{\mathrm{A}}} = \frac{B_{\mathrm{A}}^2\mathcal{T}^{3/2}}{\alpha\mathcal{R}}\mathrm{e}^{-\beta_{\mathrm{A}}/\mathcal{T}}, \tag{D.29b}$$

$$\frac{\eta_{\mathrm{A}_2}^2}{1-\eta_{\mathrm{A}_2}} = \frac{B_{\mathrm{A}_2}^2\mathcal{T}^{3/2}}{(1-\alpha)\mathcal{R}}\mathrm{e}^{-\beta_{\mathrm{A}_2}/\mathcal{T}}, \tag{D.29c}$$

which determine α, η_{A}, η_{A_2}, $\mathcal{R}$, and $\mathcal{T}$, upon condition that information from the shock intensity is externally imposed, say $\mathcal{T}$. The equations of state (D.19) and (D.20) can be combined into a single equation

$$\mathcal{P} = \left[1 + \alpha + 2\alpha\eta_{\mathrm{A}} + (1-\alpha)\eta_{\mathrm{A}_2}\right]\mathcal{R}\mathcal{T} \tag{D.30}$$

for the pressure jump. Additionally, the dimensionless Rayleigh line

$$\mathcal{P} = 1 + \frac{7}{5}\mathcal{M}_1^2\left(1 - \frac{1}{\mathcal{R}}\right), \tag{D.31}$$

which relates $\mathcal{P}$ and $\mathcal{R}$, is used to relate the pressure and density jumps with the pre-shock Mach number $\mathcal{M}_1 = u_1/a_1$, where now $a_1 = \sqrt{(7/5)R_{g,\mathrm{A}_2}T_1}$. In the expressions below, the solution for a vibrationally and chemically frozen gas (i.e., a calorically perfect diatomic gas) is recovered by taking the limits $\beta_v \to \infty$, $\beta_d \to \infty$ (or $\alpha \to 0$), $\beta_{\mathrm{A}} \to \infty$ (or $\eta_{\mathrm{A}} \to 0$), and $\beta_{\mathrm{A}_2} \to \infty$ (or $\eta_{\mathrm{A}_2} \to 0$). Regardless of the value of $\mathcal{M}_1$, the Rayleigh line always emanates from the pre-shock state, $\mathcal{P} = 1$ and $\mathcal{R} = 1$, as a straight line with negative slope in the $\{\mathcal{R}^{-1}, \mathcal{P}\}$ plane.

It is worthwhile to examine certain distinct characteristics of the Hugoniot curve resulting from incorporating dissociation, vibrational excitation, and ionization in the gas after the shock. These features hold significance for the issue of shock-turbulence interaction.

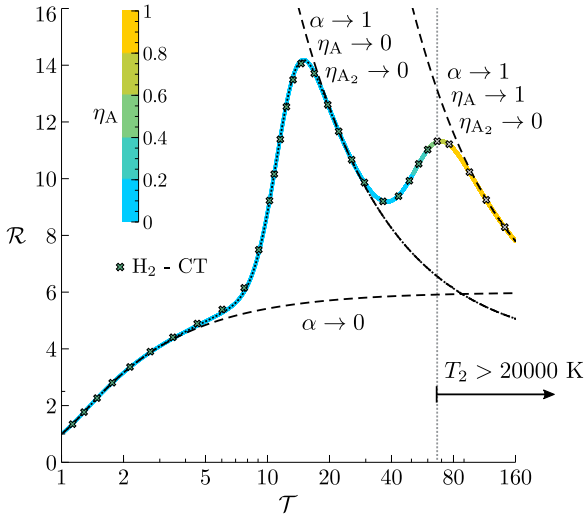

Figure D.2: Distribution of density jump $\mathcal{R}$ as a function of the temperature jump $\mathcal{T}$ for diatomic hydrogen (H_2) [lines colored by the degree of ionization of the monatomic species]. Dashed lines represent asymptotic limits for a calorically perfect diatomic gas ($\eta_A \to 0$), and for a highly ionized gas ($\eta_A \to 1$). The pre-shock state is defined at $T_1 = 300$ K and $p_1 = 5$ Torr. Symbols represent numerical results obtained with the Combustion Toolbox (in gray using linear extrapolation).

D.2.3 Asymptotic frozen, vibrational, and fully ionized gas limits

At low pre-shock Mach numbers, the post-shock temperature is sufficiently low to consider the mixture in thermochemical equilibrium, i.e., $\alpha \to 0$, $\beta_v \to 0$, $\eta_A \to 0$, and $\eta_{A_2} \to 0$, which renders

$$\mathcal{R} \sim 3\left(1 - \frac{1}{\mathcal{T}}\right)\left[1 + \sqrt{1 + \frac{\mathcal{T}}{9\left(\mathcal{T} - 1\right)^2}}\right], \tag{D.32}$$

given in Eq. (4.23). As the temperature increases, the diatomic molecules starts to vibrate obtaining

$$\mathcal{R} \sim \left[3\left(1 - \frac{1}{\mathcal{T}}\right) + \bar{e}_{\text{vib}}\right]\left(1 + \sqrt{1 + \frac{1}{\mathcal{T}\left[3\left(1 - \mathcal{T}^{-1}\right) + \bar{e}_{\text{vib}}\right]^2}}\right), \tag{D.33}$$

for $\alpha \to 0$, $\beta_v \to \theta_v/T_1$, $\eta_A \to 0$, and $\eta_{A_2} \to 0$. Then, the gas starts to dissociate increasing sharply the compression ratio. When the gas is mainly compound of

monatomic species $\alpha \to 1$ (consequently $\eta_{\mathrm{A}_2} \to 0$), but sufficiently low to start to ionize $\eta_{\mathrm{A}} \to 0$, we have

$$\mathcal{R} \sim \frac{\beta_d + 4\mathcal{T} - 3 + \sqrt{(\beta_d + 4\mathcal{T} - 3)^2 + 2\mathcal{T}}}{2\mathcal{T}}, \tag{D.34}$$

which was already given in Eq. (4.25). The strong ionized limit renders the following dependence with the shock temperature jump

$$\mathcal{R} \sim \frac{2\beta_{\mathrm{A}} + \beta_d + 4(2\mathcal{T} - 1) + 1 + \sqrt{4\mathcal{T} + (2\beta_{\mathrm{A}} + \beta_d + 8\mathcal{T} - 3)^2}}{4\mathcal{T}}. \tag{D.35}$$

As displayed in Fig. D.2, the corresponding limits agree very well over their corresponding range of applicability. It suggest their use in more complicated phenomena, as the shock/turbulence interaction problem addressed in Chapter 4.

References

[1] F. Van Zeggeren, S. H. Storey, The Computation of Chemical Equilibria, Cambridge University Press, Cambridge, 1970. 1, 11

[2] S. R. Brinkley, Note on the conditions of equilibrium for systems of many constituents, The Journal of Chemical Physics 14 (9) (1946) 563–564. doi:10.1063/1.1724195. 1, 11

[3] S. R. Brinkley, Calculation of the equilibrium composition of systems of many constituents, The Journal of Chemical Physics 15 (2) (1947) 107–110. doi:10.1063/1.1746420. 1, 11, 12

[4] V. N. Huff, S. Gordon, V. E. Morrell, General method and thermodynamic tables for computation of equilibrium composition and temperature of chemical reactions, NACA Report 1037. 1

[5] W. B. White, S. M. Johnson, G. B. Dantzig, Chemical equilibrium in complex mixtures, The Journal of Chemical Physics 28 (5) (1958) 751–755. doi:10.1063/1.1744264. 1, 11, 12

[6] F. J. Zeleznik, S. Gordon, Calculation of complex chemical equilibria, Industrial & Engineering Chemistry 60 (6) (1968) 27–57. doi:10.1021/ie50702a006. 1, 11, 22

[7] G. Eriksson, Thermodynamic studies of high temperature equilibria III. SOLGAS, a computer program for calculating the composition and heat condition of an equilibrium mixture., Acta Chemica Scandinavica 25 (1971) 2651–2658. 1, 11, 12

[8] W. C. Reynolds, The element potential method for chemical equilibrium analysis: implementation in the interactive program STANJAN, Technical Rept., Dept. of Mechanical Engineering, Stanford University, 1986. 1, 2, 11, 12

[9] M. L. Michelsen, Calculation of multiphase ideal solution chemical equilibrium, Fluid Phase Equilibria 53 (1989) 73–80. doi:10.1016/0378-3812(89)80073-1. 1, 11, 12

[10] S. Gordon, B. J. McBride, Computer program for calculation of complex chemical equilibrium compositions and applications. Part 1: Analysis, No. NAS 1.61:1311. 1, 11, 12, 13, 22, 28, 30, 31, 32, 46, 49, 59, 68, 146, 147, 163, 171

[11] P. Voňka, J. Leitner, Calculation of chemical equilibria in heterogeneous multicomponent systems, Calphad 19 (1) (1995) 25–36. doi:10.1016/0364-5916(95)00004-X. 1, 11, 12

[12] L. Eriksson, CHEPP-A chemical equilibrium program package for Matlab, SAE transactions (2004) 730–741, Available: https://www.jstor.org/stable/44740797. 1, 11, 12

[13] D. V. Nichita, S. Gomez, E. Luna, Multiphase equilibria calculation by direct minimization of Gibbs free energy with a global optimization method, Computers & Chemical Engineering 26 (12) (2002) 1703–1724. doi:10.1016/S0098-1354(02)00144-8. 1, 11, 12

[14] S. B. Pope, The computation of constrained and unconstrained equilibrium compositions of ideal gas mixtures using Gibbs function continuation, Cornell University Report FDA (2003) 03–02. 1, 11, 12

[15] S. B. Pope, Gibbs function continuation for the stable computation of chemical equilibrium, Combustion and Flame 139 (3) (2004) 222–226. doi:10.1016/j.combustflame.2004.07.008. 1, 11, 12

[16] A. Néron, G. Lantagne, B. Marcos, Computation of complex and constrained equilibria by minimization of the Gibbs free energy, Chemical engineering science 82 (2012) 260–271. doi:10.1016/j.ces.2012.07.041. 1, 11, 12

[17] J. B. Scoggins, T. E. Magin, Gibbs function continuation for linearly constrained multiphase equilibria, Combustion and Flame 162 (12) (2015) 4514–4522. doi:10.1016/j.combustflame.2015.08.027. 1, 11, 12, 31

[18] J. Blecic, J. Harrington, M. O. Bowman, TEA: A code calculating thermochemical equilibrium abundances, The Astrophysical Journal Supplement Series 225 (1) (2016) 4 1–14. doi:10.3847/0067-0049/225/1/4. 1, 2, 11, 12, 27, 28, 29, 59, 69, 163

[19] J. Gray, J. Chin, T. Hearn, E. Hendricks, T. Lavelle, J. R. Martins, Chemical-equilibrium analysis with adjoint derivatives for propulsion cycle analysis, Journal of Propulsion and Power 33 (5) (2017) 1041–1052. doi:10.2514/1.B36215. 1, 11, 12

[20] C. Tsanas, E. H. Stenby, W. Yan, Calculation of multiphase chemical equilibrium by the modified RAND method, Industrial & Engineering Chemistry Research 56 (41) (2017) 11983–11995. doi:10.1021/acs.iecr.7b02714. 1, 11, 12

[21] C. Tsanas, E. H. Stenby, W. Yan, Calculation of simultaneous chemical and phase equilibrium by the method of Lagrange multipliers, Chemical Engineering Science 174 (2017) 112–126. doi:10.1016/j.ces.2017.08.033. 1, 11, 12

[22] J. Coatléven, A. Michel, A successive substitution approach with embedded phase stability for simultaneous chemical and phase equilibrium calculations, Computers & Chemical Engineering (2022) 108041doi:10.1016/j.compchemeng.2022.108041. 1, 11, 12

[23] A. Cuadra, C. Huete, M. Vera, Combustion Toolbox: A MATLAB-GUI based open-source tool for solving gaseous combustion problems, version 1.0.0 (2023). doi:10.5281/zenodo.5554911. 1, 11, 12, 68, 106

[24] F. J. Zeleznik, S. Gordon, An analytical investigation of three general methods of calculating chemical-equilibrium compositions, National Aeronautics and Space Administration, 1960. 1, 11

[25] B. J. McBride, Computer program for Calculation of Complex Chemical Equilibrium Compositions and Applications, Vol. 2, NASA Lewis Research Center, 1996. 1, 23

[26] P. S. Bishnu, D. Hamiroune, M. Metghalchi, J. C. Keck, Constrained-equilibrium calculations for chemical systems subject to generalized linear constraints using the NASA and STANJAN equilibrium programs, Combustion Theory and Modelling 1 (3) (1997) 295–312. doi:10.1080/713665325. 2

[27] P. S. Bishnu, D. Hamiroune, M. Metghalchi, Development of constrained equilibrium codes and their applications in nonequilibrium thermodynamics, J. Energy Resour. Technol. 123 (3) (2001) 214–220. doi:10.1115/1.1385517. 2

[28] A. E. Lutz, F. M. Rupley, R. J. Kee, W. Reynolds, E. Meeks, EQUIL: A CHEMKIN implementation of STANJAN for computing chemical equilibria, Reaction Design Inc 6500. 2

[29] E. C. Koch, R. Webb, V. Weiser, Review on thermochemical codes, Tech. rep., NATO-Munitions Safety Information Analysis Center, Brussels, Belgium (2009). 2

[30] W. Fickett, W. C. Davis, Detonation: theory and experiment. 2

[31] C. L. Mader, Detonation properties of condensed explosives computed using the Becker-Kistiakowsky-Wilson equation of state. Report LA-2900, Los Alamos Scientific Laboratory, Los Alamos, NM, USA, 1963. 2, 42

[32] M. Cowperthwaite, W. Zwisler, The JCZ equations of state for detonation products and their incorporation into the TIGER code, in: Sixth Symposium (International) on Detonation, Vol. 162, 1976. 2

[33] K. Tanaka, Detonation properties of high explosives calculated by revised Kihara-Hikita equation of state, in: Proc. Eighth Symposium (International) on Detonation NSWC MP, 1986, pp. 86–194. 2

[34] L. Fried, P. Souers, Cheetah: A next generation thermochemical code, Tech. Rep. UCRL-ID-117240, Lawrence Livermore National Lab.(LLNL), Livermore, CA (United States) (1994). doi:10.2172/95184. 2

[35] L. E. Fried, Cheetah 1.0 users manual, Tech. Rep. UCRL-MA-117541, Lawrence Livermore National Lab., CA (United States) (1994). 2

[36] M. Sućeska, Calculation of detonation parameters by EXPLO5 computer program, Mater. Sci. Forum 465 (2004) 325–330. doi:10.4028/www.scientific.net/msf.465-466.325. 2

[37] M. Suceska, M. Dobrilovic, V. Bohanek, B. Stimac, Estimation of explosive energy output by EXPLO5 thermochemical code, Zeitschrift für anorganische und allgemeine Chemie 647 (4) (2021) 231–238. doi:10.1002/zaac.202000219. 2

[38] F. Charlet, M. L. Turkel, J.-F. Danel, L. Kazandijan, Evaluation of various theoretical equations of state used in calculation of detonation properties, J. Appl. Phys. 84 (1998) 4227–4238. doi:10.1063/1.368640. 2

[39] V. Dubois, N. Desbiens, E. Auroux, New developments of the CARTE thermochemical code: Calculation of detonation properties of high explosives, Chemical Physics Letters 494 (4-6) (2010) 306–311. doi:10.1016/j.cplett.2010.05.093. 2

[40] S. Browne, J. Ziegler, J. E. Shepherd, Numerical solution methods for shock and detonation jump conditions, GALCIT Technical Report FM2018.001 Revised January 2023, California Institute of Technology, Pasadena, CA. 2, 6, 12, 33, 45, 59, 69, 163

[41] D. G. Goodwin, R. L. Speth, H. K. Moffat, B. W. Weber, Cantera: An object-oriented software toolkit for chemical kinetics, thermodynamics, and transport processes, https://www.cantera.org, version 2.5.1 (2021). doi:10.5281/zenodo.4527812. 2, 6, 12, 33, 35, 45, 59, 68, 163

[42] J. Raymond, Shock waves in the interstellar medium, The Astrophysical Journal Supplement Series 39 (1979) 1–27. 3, 98

[43] J. Dove, A. Rusk, P. Cribb, P. Martin, Excitation and dissociation of molecular hydrogen in shock waves at interstellar densities, The Astrophysical Journal 318 (1987) 379–391. doi:10.1086/165375. 3, 98

[44] B. T. Draine, C. F. McKee, Theory of interstellar shocks, Annual Review of Astronomy and Astrophysics 31 (1) (1993) 373–432. doi:10.1146/annurev.aa.31.090193.002105. 3, 98

[45] G. Bisnovatyi-Kogan, S. Silich, Shock-wave propagation in the nonuniform interstellar medium, Reviews of Modern Physics 67 (3) (1995) 661. doi:10.1103/revmodphys.67.661. 3, 98

[46] R. Fernández, C. Thompson, Stability of a spherical accretion shock with nuclear dissociation, The Astrophysical Journal 697 (2) (2009) 1827. doi:10.1088/0004-637x/697/2/1827. 3, 98

[47] R. Fernández, C. Thompson, Dynamics of a spherical accretion shock with neutrino heating and alpha-particle recombination, The Astrophysical Journal 703 (2) (2009) 1464. doi:10.1088/0004-637x/703/2/1464. 3, 98

[48] C. Huete, E. Abdikamalov, D. Radice, The impact of vorticity waves on the shock dynamics in core-collapse supernovae, Monthly Notices of the Royal Astronomical Society 475 (3) (2018) 3305–3323. doi:10.1093/mnras/stx3360. 3, 98

[49] C. Huete, F. Cobos-Campos, E. Abdikamalov, S. Bouquet, Acoustic stability of nonadiabatic high-energy-density shocks, Physical Review Fluids 5 (11) (2020) 113403. doi:10.1103/physrevfluids.5.113403. 3, 98, 109

[50] V. Goncharov, O. Gotchev, E. Vianello, T. Boehly, J. Knauer, P. McKenty, P. Radha, S. Regan, T. Sangster, S. Skupsky, et al., Early stage of implosion in inertial confinement fusion: Shock timing and perturbation evolution, Physics of Plasmas 13 (1) (2006) 012702. doi:10.1063/1.2162803. 3, 98

[51] R. Betti, O. Hurricane, Inertial-confinement fusion with lasers, Nature Physics 12 (5) (2016) 435–448. doi:10.1038/nphys3736. 3, 98

[52] V. Tikhonchuk, Progress and opportunities for inertial fusion energy in europe, Philosophical Transactions of the Royal Society A 378 (2184) (2020) 20200013. doi:10.1098/rsta.2020.0013. 3, 98

[53] A. Munafò, A. Alberti, C. Pantano, J. Freund, M. Panesi, Modeling of laser-induced breakdown phenomena in non-equilibrium plasmas, In 2018 AIAA Aerospace Sciences Meeting (2018) 0171doi:10.2514/6.2018-0171. 3, 98

[54] J. MacArt, J. Wang, P. Popov, J. Freund, Detailed simulation of laser-induced ignition, spherical-flame acceleration, and the origins of hydrodynamic instability, Proceedings of the Combustion Institute 38 (2021) 2341–27. doi:10.1016/j.proci.2020.08.038. 3, 98

[55] J. Urzay, Supersonic combustion in air-breathing propulsion systems for hypersonic flight, Annual Review of Fluid Mechanics 50 (2018) 593–627. doi:10.1146/annurev-fluid-122316-045217. 3, 62, 98, 138

[56] G. V. Candler, Rate effects in hypersonic flows, Annual Review of Fluid Mechanics 51 (2019) 379–402. doi:10.1146/annurev-fluid-010518-040258. 3, 98

[57] R. Huff, F. Schauer, S. A. Boller, M. D. Polanka, M. Fotia, J. Hoke, Exit condition measurements of a radial rotating detonation engine bleed air turbine, in: AIAA Scitech 2019 Forum, 2019, p. 1011. doi:10.2514/6.2019-1011. 3, 62

[58] J. J. Bertin, R. M. Cummings, Fifty years of hypersonics: where we've been, where we're going, Progress in Aerospace Sciences 39 (6-7) (2003) 511–536. doi:10.1016/S0376-0421(03)00079-4. 3

[59] J. J. Bertin, R. M. Cummings, Critical hypersonic aerothermodynamic phenomena, Annu. Rev. Fluid Mech. 38 (2006) 129–157. doi:10.1146/annurev.fluid.38.050304.092041. 3

[60] S. Gu, H. Olivier, Capabilities and limitations of existing hypersonic facilities, Progress in Aerospace Sciences 113 (2020) 100607. doi:10.1016/j.paerosci.2020.100607. 3

[61] S. Lee, S. K. Lele, P. Moin, Interaction of isotropic turbulence with shock waves: effect of shock strength, Journal of Fluid Mechanics 340 (1997) 225–247. doi:10.1017/S0022112097005107. 3, 99, 113, 139, 143, 159, 160

[62] K. Mahesh, S. K. Lele, P. Moin, The influence of entropy fluctuations on the interaction of turbulence with a shock wave, Journal of Fluid Mechanics 334 (1997) 353–379. doi:10.1017/S0022112097004576. 3, 99, 125, 143, 159, 160

[63] J. Larsson, S. K. Lele, Direct numerical simulation of canonical shock/turbulence interaction, Physics of fluids 21 (12) (2009) 126101. doi:10.1063/1.3275856. 3, 85, 99, 100, 139, 143, 157, 159, 160

[64] J. Larsson, I. Bermejo-Moreno, S. K. Lele, Reynolds-and mach-number effects in canonical shock-turbulence interaction, Journal of Fluid Mechanics 717 (2013) 293. doi:10.1017/jfm.2012.573. 3, 99, 100, 139, 143, 159, 160, 161

[65] K. Sinha, Evolution of enstrophy in shock/homogeneous turbulence interaction, Journal of Fluid Mechanics 707 (2012) 74. doi:10.1017/jfm.2012.265. 3, 80, 81, 84, 99, 100, 143

[66] J. Ryu, D. Livescu, Turbulence structure behind the shock in canonical shock–vortical turbulence interaction, Journal of Fluid Mechanics 756 (2014) R1. doi:10.1017/jfm.2014.477. 3, 99, 100, 143, 159, 160, 161

[67] R. Quadros, K. Sinha, J. Larsson, Turbulent energy flux generated by shock/homogeneous-turbulence interaction, Journal of Fluid Mechanics 796 (2016) 113–157. doi:10.1017/jfm.2016.236. 3, 81, 83, 89, 99, 143

[68] D. Livescu, J. Ryu, Vorticity dynamics after the shock–turbulence interaction, Shock Waves 26 (3) (2016) 241–251. doi:10.1007/s00193-015-0580-5. 3, 99, 100, 143

[69] R. Boukharfane, Z. Bouali, A. Mura, Evolution of scalar and velocity dynamics in planar shock-turbulence interaction, Shock Waves 28 (2018) 1117–1141. doi:10.1007/s00193-017-0798-5. 3, 99

[70] Y. P. M. Sethuraman, K. Sinha, J. Larsson, Thermodynamic fluctuations in canonical shock–turbulence interaction: effect of shock strength, Theoretical and Computational Fluid Dynamics 32 (5) (2018) 629–654. doi:10.1007/s00162-018-0468-y. 3, 81, 83, 89, 99, 143

[71] Y. Tian, F. A. Jaberi, D. Livescu, Density effects on post-shock turbulence structure and dynamics, Journal of Fluid Mechanics 880 (2019) 935–968. doi:10.1017/jfm.2019.707. 3, 99, 100, 143

[72] C. H. Chen, D. A. Donzis, Shock–turbulence interactions at high turbulence intensities, Journal of Fluid Mechanics 870 (2019) 813–847. doi:10.1017/jfm.2019.248. 3, 99, 143, 157, 158, 159, 160, 161

[73] Y. P. M. Sethuraman, K. Sinha, Effect of turbulent mach number on the thermodynamic fluctuations in canonical shock-turbulence interaction, Computers & Fluids 197 (2020) 104354. doi:10.1016/j.compfluid.2019.104354. 3, 84, 99, 143

[74] K. Tanaka, T. Watanabe, K. Nagata, Statistical analysis of deformation of a shock wave propagating in a local turbulent region, Physics of Fluids 32 (9) (2020) 096107. doi:10.1063/5.0019784. 3, 99

[75] N. E. Grube, M. P. Martín, Reynolds stress anisotropy in shock/isotropic turbulence interactions, Journal of Fluid Mechanics 913. doi:10.1017/jfm.2020.1070. 3, 99, 139, 143

[76] C. H. Chen, D. A. Donzis, Amplification of transverse reynolds stresses in shock–turbulence interactions, AIAA Journal 60 (11) (2022) 6235–6239. doi:10.2514/1.J061736. 3, 99, 143, 157, 158, 159, 160

[77] S. Lee, S. K. Lele, P. Moin, Direct numerical simulation of isotropic turbulence interacting with a weak shock wave, Journal of Fluid Mechanics 251 (1993) 533–562. doi:10.1017/s0022112093003519. 3, 67, 99, 143, 159, 160

[78] F. Ducros, V. Ferrand, F. Nicoud, C. Weber, D. Darracq, C. Gacherieu, T. Poinsot, Large-eddy simulation of the shock/turbulence interaction, Journal of Computational Physics 152 (2) (1999) 517–549. 3, 99, 143

[79] N. Braun, D. Pullin, D. Meiron, Large eddy simulation investigation of the canonical shock–turbulence interaction, Journal of Fluid Mechanics 858 (2019) 500–535. doi:10.1017/jfm.2018.766. 3, 99, 143

[80] H. S. Ribner, Convection of a pattern of vorticity through a shock wave, NACA Report 1164. 3, 64, 99, 100, 143

[81] H. S. Ribner, Shock-turbulence interaction and the generation of noise, NACA Report 1233. 3, 64, 99, 100, 143, 144

[82] H. S. Ribner, Spectra of noise and amplified turbulence emanating from shock-turbulence interaction, AIAA journal 25 (3) (1987) 436–442. doi:10.2514/3.9642. 3, 64, 83, 99, 100, 143

[83] L. S. Kovasznay, Turbulence in supersonic flow, Journal of the Aeronautical Sciences 20 (10) (1953) 657–674. 3, 73, 99, 112, 184

[84] M. Hasan, M. M. Rahman, Performance and emission characteristics of biodiesel–diesel blend and environmental and economic impacts of biodiesel production: A review, Renewable and Sustainable Energy Reviews 74 (2017) 938–948. doi:10.1016/j.rser.2017.03.045. 4

[85] S. Dey, N. Reang, P. Das, M. Deb, A comprehensive study on prospects of economy, environment, and efficiency of palm oil biodiesel as a renewable fuel, Journal of cleaner production 286 (2021) 124981. doi:10.1016/j.jclepro.2020.124981. 4

[86] C. C. Lee, M.-V. Tran, B. T. Tan, G. Scribano, C. T. Chong, A comprehensive review on the effects of additives on fundamental combustion characteristics and pollutant formation of biodiesel and ethanol, Fuel 288 (2021) 119749. doi:10.1016/j.fuel.2020.119749. 4

[87] P. Benjumea, J. Agudelo, A. Agudelo, Effect of altitude and palm oil biodiesel fuelling on the performance and combustion characteristics of a hsdi diesel engine, Fuel 88 (4) (2009) 725–731. doi:10.1016/j.fuel.2008.10.011. 4

[88] H. Jones, The recent large reduction in space launch cost, in: 48th International Conference on Environmental Systems, 2018, pp. 1–12, Available: http://hdl.handle.net/2346/74082. 4, 47

[89] I. W. Kokkinakis, D. Drikakis, Atmospheric pollution from rockets, Physics of Fluids 34 (5) (2022) 056107. doi:10.1063/5.0090017. 4, 47

[90] D. K. Huzel, Modern engineering for design of liquid-propellant rocket engines, Vol. 147, AiAA, 1992. 4

[91] D. Trache, T. M. Klapötke, L. Maiz, M. Abd-Elghany, L. T. DeLuca, Recent advances in new oxidizers for solid rocket propulsion, Green Chemistry 19 (20) (2017) 4711–4736. doi:10.1039/c7gc01928a. 4

[92] J. Dallas, S. Raval, J. A. Gaitan, S. Saydam, A. Dempster, The environmental impact of emissions from space launches: A comprehensive review, Journal of Cleaner Production 255 (2020) 120209. doi:10.1016/j.jclepro.2020.120209. 4, 47

[93] B. Genevieve, M. Brooks, J. Pitot de la Beaujardiere, L. Roberts, Performance modeling of a paraffin wax/nitrous oxide hybrid rocket motor, in: 49th AIAA Aerospace Sciences Meeting including the New Horizons Forum and Aerospace Exposition, 2011, p. 420. doi:10.2514/6.2011-420. 4

[94] A. S. Gohardani, J. Stanojev, A. Demairé, K. Anflo, M. Persson, N. Wingborg, C. Nilsson, Green space propulsion: Opportunities and prospects, Progress in Aerospace Sciences 71 (2014) 128–149. doi:10.1016/j.paerosci.2014.08.001. 4, 47

[95] B. Genevieve, J. Pitot de la Beaujardiere, M. Brooks, A computational tool for predicting hybrid rocket motor performance, R&D Journal 33 (2017) 56–65. 4

[96] Z. Wang, X. Lin, F. Li, X. Yu, Combustion performance of a novel hybrid rocket fuel grain with a nested helical structure, Aerospace Science and Technology 97 (2020) 105613. doi:10.1016/j.ast.2019.105613. 4

[97] M. B. Padwal, B. Natan, D. Mishra, Gel propellants, Progress in Energy and Combustion Science 83 (2021) 100885. doi:10.1016/j.pecs.2020.100885. 4

[98] J. Scoggins, Development of numerical methods and study of coupled flow, radiation, and ablation phenomena for atmospheric entry, Ph.D. thesis, von Karman Institute for Fluid Dynamics Sint-Genesius-Rode, Belgium (2017). 5

[99] F. S. Milos, D. J. Rasky, Review of numerical procedures for computational surface thermochemistry, Journal of thermophysics and heat transfer 8 (1) (1994) 24–34. doi:10.2514/3.497. 5

[100] B. Helber, C. O. Asma, Y. Babou, A. Hubin, O. Chazot, T. E. Magin, Material response characterization of a low-density carbon composite ablator in high-enthalpy plasma flows, Journal of materials science 49 (2014) 4530–4543. doi:10.1007/s10853-014-8153-z. 5, 30

[101] F. Milos, Y.-K. Chen, F. Milos, Y.-K. Chen, Comprehensive model for multicomponent ablation thermochemistry, in: 35th aerospace sciences meeting and exhibit, 1997, p. 141. doi:10.2514/6.1997-141. 5

[102] F. S. Milos, Y.-K. Chen, Ablation, thermal response, and chemistry program for analysis of thermal protection systems, Journal of Spacecraft and Rockets 50 (1) (2013) 137–149. doi:10.2514/1.a32302. 5

[103] A. Wolszczan, D. A. Frail, A planetary system around the millisecond pulsar PSR1257+ 12, Nature 355 (6356) (1992) 145–147. doi:10.1038/355145a0. 5

[104] N. Madhusudhan, Exoplanetary atmospheres: Key insights, challenges, and prospects, Annual Review of Astronomy and Astrophysics 57 (2019) 617–663. doi:10.1146/annurev-astro-081817-051846. 5, 27

[105] J. P. Gardner, J. C. Mather, M. Clampin, R. Doyon, M. A. Greenhouse, H. B. Hammel, J. B. Hutchings, P. Jakobsen, S. J. Lilly, K. S. Long, et al., The James Webb Space Telescope, Space Science Reviews 123 (2006) 485–606. doi:10.1007/s11214-006-8315-7. 5

[106] B. D. Savage, K. R. Sembach, Interstellar abundances from absorption-line observations with the Hubble Space Telescope, Annual Review of Astronomy and Astrophysics 34 (1) (1996) 279–329. doi:10.1146/annurev.astro.34.1.279. 5

[107] S. Seager, D. Deming, Exoplanet atmospheres, Annual Review of Astronomy and Astrophysics 48 (2010) 631–672. doi:10.1146/annurev-astro-081309-130837. 6

[108] C. Visscher, J. I. Moses, S. A. Saslow, The deep water abundance on Jupiter: New constraints from thermochemical kinetics and diffusion modeling, Icarus 209 (2) (2010) 602–615. doi:10.1016/j.icarus.2010.03.029. 6

[109] P. Mollière, R. van Boekel, J. Bouwman, T. Henning, P.-O. Lagage, M. Min, Observing transiting planets with JWST. Prime targets and their synthetic spectral observations, Astronomy & Astrophysics 600 (2017) A10. doi:10.1051/0004-6361/201629800. 6

[110] M. W. Phillips, P. Tremblin, I. Baraffe, G. Chabrier, N. F. Allard, F. Spiegelman, J. M. Goyal, B. Drummond, E. Hebrard, A new set of atmosphere and evolution models for cool T–Y brown dwarfs and giant exoplanets, Astronomy & Astrophysics 637 (2020) A38. doi:10.1051/0004-6361/201937381. 6

[111] D. Sudarsky, A. Burrows, I. Hubeny, Theoretical spectra and atmospheres of extrasolar giant planets, The Astrophysical Journal 588 (2) (2003) 1121. doi:10.1086/374331. 6

[112] M. S. Marley, A. S. Ackerman, J. N. Cuzzi, D. Kitzmann, Clouds and hazes in exoplanet atmospheres, Comparative climatology of terrestrial planets 1 (2013) 367–391. doi:10.2458/azu_uapress_9780816530595-ch15. 6

[113] X. Yu, C. He, X. Zhang, S. M. Hörst, A. H. Dymont, P. McGuiggan, J. I. Moses, N. K. Lewis, J. J. Fortney, P. Gao, et al., Haze evolution in temperate exoplanet atmospheres through surface energy measurements, Nature Astronomy 5 (8) (2021) 822–831. doi:10.1038/s41550-021-01375-3. 6

[114] M. R. Line, M.-C. Liang, Y. L. Yung, High-temperature photochemistry in the atmosphere of HD 189733b, The Astrophysical Journal 717 (1) (2010) 496. doi:10.1088/0004-637x/717/1/496. 6

[115] R. Hu, S. Seager, Photochemistry in terrestrial exoplanet atmospheres. III. Photochemistry and thermochemistry in thick atmospheres on super Earths and mini Neptunes, The Astrophysical Journal 784 (1) (2014) 63. doi:10.1088/0004-637x/784/1/63. 6

[116] O. Venot, E. Hébrard, M. Agúndez, L. Decin, R. Bounaceur, New chemical scheme for studying carbon-rich exoplanet atmospheres, Astronomy & Astrophysics 577 (2015) A33. doi:10.1051/0004-6361/201425311. 6

[117] S.-M. Tsai, M. Malik, D. Kitzmann, J. R. Lyons, A. Fateev, E. Lee, K. Heng, A comparative study of atmospheric chemistry with VULCAN, The Astrophysical Journal 923 (2) (2021) 264. doi:10.3847/1538-4357/ac29bc. 6

[118] S. Browne, J. Ziegler, N. Bitter, B. Schmidt, J. Lawson, J. E. Shepherd, SD-Toolbox - Numerical Tools for Shock and Detonation Wave Modeling, GALCIT Technical Report FM2018.001 Revised January 2023, California Institute of Technology, Pasadena, CA, https://shepherd.caltech.edu/EDL/PublicResources/sdt. 6, 12, 35, 59, 163

[119] P. Jha, L. Massa, Teaching thermo-chemical equilibrium using a matlab algorithm, Computers in Education Journal 5 (3) (2014) 93–103. 7

[120] G. P. Smith, GRI-Mech 3.0, http://www.me.berkley.edu/gri_mech. 10

[121] J. M. Paz-García, B. Johannesson, L. M. Ottosen, A. B. Ribeiro, J. M. Rodríguez-Maroto, Computing multi-species chemical equilibrium with an algorithm based on the reaction extents, Computers & Chemical Engineering 58 (2013) 135–143. doi:10.1016/j.compchemeng.2013.06.013. 11, 12

[122] J. W. Stock, D. Kitzmann, A. B. C. Patzer, E. Sedlmayr, FastChem: A computer program for efficient complex chemical equilibrium calculations in the neutral/ionized gas phase with applications to stellar and planetary atmospheres, Monthly Notices of the Royal Astronomical Society 479 (1) (2018) 865–874. doi:10.1093/mnras/sty1531. 11, 12, 15, 27, 169

[123] P. Woitke, C. Helling, G. H. Hunter, J. D. Millard, G. E. Turner, M. Worters, J. Blecic, J. W. Stock, Equilibrium chemistry down to 100 K. Impact of silicates and phyllosilicates on the carbon to oxygen ratio, Astronomy & Astrophysics 614 (2018) A1. doi:10.1051/0004-6361/201732193. 11, 12, 27

[124] J. W. Stock, D. Kitzmann, A. B. C. Patzer, FastChem 2: an improved computer program to determine the gas-phase chemical equilibrium composition for arbitrary element distributions, Monthly Notices of the Royal Astronomical Society 517 (3) (2022) 4070–4080. doi:10.1093/mnras/stac2623. 11, 12, 27

[125] W. R. Smith, R. W. Missen, Chemical reaction equilibrium analysis, Wiley, 1982. 11

[126] M. W. Chase, NIST-JANAF thermochemical tables 4th edition, Journal of Physical and Chemical Reference Data, Monograph 9 (1998) 1529–1564. doi:10.1063/1.555994. 11, 28, 136

[127] O. V. Dorofeeva, V. P. Novikov, D. B. Neumann, NIST-JANAF thermochemical tables. I. Ten organic molecules related to atmospheric chemistry, Journal of Physical and Chemical Reference Data 30 (2) (2001) 475–513. doi:10.1063/1.1364518. 11, 28

[128] B. J. McBride, NASA Glenn coefficients for calculating thermodynamic properties of individual species, National Aeronautics and Space Administration, Glenn Research Center, 2002. 11, 13, 15, 16, 20, 32, 35, 107, 117, 145, 169

[129] A. Burcat, B. Ruscic, Third millennium ideal gas and condensed phase thermochemical database for combustion (with update from active thermochemical tables), Tech. rep., Argonne National Lab. (ANL), Argonne, IL (United States) (2005). doi:10.2172/925269. 11, 13, 15, 16, 20, 29, 32, 35, 55, 169

[130] B. Ruscic, R. E. Pinzon, G. Von Laszewski, D. Kodeboyina, A. Burcat, D. Leahy, D. Montoy, A. F. Wagner, Active Thermochemical Tables: thermochemistry for the 21st century, in: Journal of Physics: Conference Series, Vol. 16, IOP Publishing, 2005, p. 078. doi:10.1088/1742-6596/16/1/078. 11, 13, 16

[131] B. Ruscic, D. H. Bross, Chapter 1 - Thermochemistry, in: T. Faravelli, F. Manenti, E. Ranzi (Eds.), Mathematical Modelling of Gas-Phase Complex Reaction Systems: Pyrolysis and Combustion, Vol. 45 of Computer Aided Chemical Engineering, Elsevier, 2019, pp. 3–114. doi:https://doi.org/10.1016/B978-0-444-64087-1.00001-2. 11

[132] J. B. Scoggins, J. Rabinovitch, B. Barros-Fernandez, A. Martin, J. Lachaud, R. L. Jaffe, N. N. Mansour, G. Blanquart, T. E. Magin, Thermodynamic properties of carbon–phenolic gas mixtures, Aerospace Science and Technology 66 (2017) 177–192. doi:10.1016/j.ast.2017.02.025. 11

[133] C. F. Goldsmith, G. R. Magoon, W. H. Green, Database of small molecule thermochemistry for combustion, The Journal of Physical Chemistry A 116 (36) (2012) 9033–9057. doi:10.1021/jp303819e. 11

[134] G. Blanquart, H. Pitsch, Thermochemical properties of polycyclic aromatic hydrocarbons (PAH) from G3MP2B3 calculations, The Journal of Physical Chemistry A 111 (28) (2007) 6510–6520. doi:10.1021/jp068579w. 11

[135] G. Blanquart, P. Pepiot-Desjardins, H. Pitsch, Chemical mechanism for high temperature combustion of engine relevant fuels with emphasis on soot precursors, Combustion and Flame 156 (3) (2009) 588–607. doi:10.1016/j.combustflame.2008.12.007. 11

[136] K. Narayanaswamy, G. Blanquart, H. Pitsch, A consistent chemical mechanism for oxidation of substituted aromatic species, Combustion and Flame 157 (10) (2010) 1879–1898. doi:10.1016/j.combustflame.2010.07.009. 11

[137] G. Blanquart, Effects of spin contamination on estimating bond dissociation energies of polycyclic aromatic hydrocarbons, International Journal of Quantum Chemistry 115 (12) (2015) 796–801. doi:10.1002/qua.24904. 11

[138] J. A. Miller, R. J. Kee, C. K. Westbrook, Chemical kinetics and combustion modeling, Annual Review of Physical Chemistry 41 (1) (1990) 345–387. doi:10.1146/annurev.pc.41.100190.002021. 11

[139] N. Kubota, Propellants and explosives: thermochemical aspects of combustion, John Wiley & Sons, 2015. 11

[140] H. Jiang, J. Liu, S. Luo, W. Huang, J. Wang, M. Liu, Thermochemical non-equilibrium effects on hypersonic shock wave/turbulent boundary-layer interaction, Acta Astronautica 192 (2022) 1–14. doi:10.1016/j.actaastro.2021.12.010. 11

[141] G. V. Candler, R. W. MacCormack, Computation of weakly ionized hypersonic flows in thermochemical nonequilibrium, Journal of Thermophysics and Heat Transfer 5 (3) (1991) 266–273. doi:10.2514/3.260. 11

[142] P. A. Libby, F. A. Williams (Eds.), Turbulent Reacting Flows, Academic Press, New York, 1994. 11

[143] P. Wolański, Detonative propulsion, Proceedings of the Combustion Institute 34 (1) (2013) 125–158. doi:10.1016/j.proci.2012.10.005. 11

[144] M. Di Renzo, J. Urzay, Direct numerical simulation of a hypersonic transitional boundary layer at suborbital enthalpies, Journal of Fluid Mechanics 912 (2021) A29 1–36. doi:10.1017/jfm.2020.1144. 12, 99

[145] V. Raman, S. Prakash, M. Gamba, Nonidealities in rotating detonation engines, Annual Review of Fluid Mechanics 55. doi:10.1146/annurev-fluid-120720-032612. 12

[146] M. Michelsen, Calculation of multiphase equilibrium, Computers & chemical engineering 18 (7) (1994) 545–550. doi:10.1016/0098-1354(93)E0017-4. 12

[147] J. B. Scoggins, V. Leroy, G. Bellas-Chatzigeorgis, B. Dias, T. E. Magin, Mutation++: Multicomponent thermodynamic and transport properties for ionized gases in C++, SoftwareX 12 (2020) 100575. doi:10.1016/j.softx.2020.100575. 12

[148] A. M. Leal, D. A. Kulik, W. R. Smith, M. O. Saar, An overview of computational methods for chemical equilibrium and kinetic calculations for geochemical and reactive transport modeling, Pure and Applied Chemistry 89 (5) (2017) 597–643. doi:10.1515/pac-2016-1107. 12

[149] P. J. Groenen, W. J. Heiser, The tunneling method for global optimization in multidimensional scaling, Psychometrika 61 (3) (1996) 529–550. doi:10.1007/BF02294553. 12

[150] R. Storn, K. Price, Differential evolution–a simple and efficient heuristic for global optimization over continuous spaces, Journal of Global Gptimization 11 (4) (1997) 341–359. doi:10.1023/A:1008202821328. 12

[151] K. V. Price, Differential evolution, in: Handbook of optimization, Springer, 2013, pp. 187–214. doi:10.1007/978-3-642-30504-7_8. 12

[152] J. Sánchez-Monreal, A. Cuadra, C. Huete, M. Vera, SimEx: A tool for the rapid evaluation of the effects of explosions, Applied Sciences 12 (18). doi:10.3390/app12189101. 12, 13, 41

[153] T. Andrews, Computation time comparison between Matlab and C++ using launch windows, Tech. rep., California Polytechnic State University San Luis Obispo, Available: https://digitalcommons.calpoly.edu/aerosp/78 (2012). 14, 60

[154] F. N. Fritsch, R. E. Carlson, Monotone piecewise cubic interpolation, SIAM Journal on Numerical Analysis 17 (2) (1980) 238–246. doi:10.1137/0717021. 15

[155] K. Ram, Git can facilitate greater reproducibility and increased transparency in science, Source code for biology and medicine 8 (1) (2013) 1–8. doi:10.1186/1751-0473-8-7. 18

[156] S. Chacon, B. Straub, Pro git, Apress, 2014. 18

[157] J. D. Blischak, E. R. Davenport, G. Wilson, A quick introduction to version control with Git and GitHub, PLOS computational biology 12 (1) (2016) e1004668. doi:10.1371/journal.pcbi.1004668. 18

[158] Y. Perez-Riverol, L. Gatto, R. Wang, T. Sachsenberg, J. Uszkoreit, F. da Veiga Leprevost, C. Fufezan, T. Ternent, S. J. Eglen, D. S. Katz, et al., Ten simple rules for taking advantage of Git and GitHub (2016). doi:10.1371/journal.pcbi.1004947. 18

[159] G. Brandl, Sphinx documentation, Available: http://sphinx-doc.org/sphinx.pdf. 18

[160] J. Cederberg, M. Mikofski, jcewidex, D. Rosset, I. Lenton, N. Martin, M. Topper, C. Markiewicz, C. Boeddeker, C. Vergari, cleobis, D. Stansby, florianjacob, PekaryGergelyR, H. Leblanc, M.-H. Bleu-Laine, N. N. Oosterhof, R. Zimmerman, ptitrex, sphinx-contrib/matlabdomain: 0.18.0 (Apr. 2023). doi:10.5281/zenodo.7829592. 18

[161] D. P. Bertsekas, Constrained Optimization and Lagrange Multiplier Methods, Academic press, New York, 2014. 20

[162] E. Anderson, Z. Bai, C. Bischof, L. S. Blackford, J. Demmel, J. Dongarra, J. Du Croz, A. Greenbaum, S. Hammarling, A. McKenney, et al., LAPACK users' guide, SIAM, 1999. 22

[163] J. Camberos, J. Moubry, Chemical equilibrium analysis with the method of element potentials, in: 39th Aerospace Sciences Meeting and Exhibit, AIAA paper 2001–873, 2001. doi:10.2514/6.2001-873. 22

[164] B. M. Smirnov, Fundamentals of ionized gases: basic topics in plasma physics, John Wiley & Sons, 2012. 23

[165] J. Sharma, A composite third order Newton–Steffensen method for solving nonlinear equations, Applied Mathematics and Computation 169 (1) (2005) 242–246. doi:10.1016/j.amc.2004.10.040. 27

[166] B. Fegley Jr, K. Lodders, Atmospheric chemistry of the brown dwarf Gliese 229B: Thermochemical equilibrium predictions, The Astrophysical Journal 472 (1) (1996) L37. doi:10.1086/310356. 27

[167] C. Visscher, K. Lodders, B. Fegley Jr, Atmospheric chemistry in giant planets, brown dwarfs, and low-mass dwarf stars. II. Sulfur and phosphorus, The Astrophysical Journal 648 (2) (2006) 1181. doi:10.1086/506245. 27

[168] M. Agúndez, V. Parmentier, O. Venot, F. Hersant, F. Selsis, Pseudo 2D chemical model of hot-Jupiter atmospheres: application to HD 209458b and HD 189733b, Astronomy & Astrophysics 564 (2014) A73. doi:10.1051/0004-6361/201322895. 27

[169] V. Parmentier, M. R. Line, J. L. Bean, M. Mansfield, L. Kreidberg, R. Lupu, C. Visscher, J.-M. Désert, J. J. Fortney, M. Deleuil, et al., From thermal dissociation to condensation in the atmospheres of ultra hot Jupiters: WASP-121b in context, Astronomy & Astrophysics 617 (2018) A110. doi:10.1051/0004-6361/201833059. 27

[170] K. B. Stevenson, J.-M. Désert, M. R. Line, J. L. Bean, J. J. Fortney, A. P. Showman, T. Kataria, L. Kreidberg, P. R. McCullough, G. W. Henry, et al., Thermal structure of an exoplanet atmosphere from phase-resolved emission spectroscopy, Science 346 (6211) (2014) 838–841. doi:10.1126/science.1256758. 27

[171] M. Asplund, N. Grevesse, A. J. Sauval, P. Scott, The chemical composition of the Sun, Annual Review of Astronomy and Astrophysics 47 (2009) 481–522. doi:10.1146/annurev.astro.46.060407.145222. 28

[172] F. Bariselli, A. Frezzotti, A. Hubin, T. E. Magin, Aerothermodynamic modelling of meteor entry flows, Monthly Notices of the Royal Astronomical Society 492 (2) (2020) 2308–2325. doi:10.1093/mnras/stz3559. 30

[173] S.-H. Park, J. N. Laboulais, P. Leyland, S. Mischler, Re-entry survival analysis and ground risk assessment of space debris considering by-products generation, Acta Astronautica 179 (2021) 604–618. doi:10.1016/j.actaastro.2020.09.034. 30

[174] T. Scavo, J. Thoo, On the geometry of Halley's method, The American mathematical monthly 102 (5) (1995) 417–426. doi:doi.org/10.1080/00029890.1995.12004594. 34

[175] H. Hornung, Regular and Mach reflection of shock waves, Annual review of fluid mechanics 18 (1986) 33–58. doi:10.1146/annurev.fl.18.010186.000341. 36

[176] Z. Zhang, C. Wen, W. Zhang, Y. Liu, Z. Jiang, A theoretical method for solving shock relations coupled with chemical equilibrium and its applications, Chinese Journal of Aeronautics 35 (6) (2022) 47–62. doi:10.1016/j.cja.2021.08.021. 37, 44, 45

[177] J. E. Dennis Jr, R. B. Schnabel, Numerical methods for unconstrained optimization and nonlinear equations, SIAM, 1996. 39

[178] M. Cavcar, The international standard atmosphere (ISA), Anadolu University, Turkey 30 (9) (2000) 1–6. 39

[179] R. Zipf Jr, V. Gamezo, M. Sapko, W. Marchewka, K. Mohamed, E. Oran, D. Kessler, E. Weiss, J. Addis, F. Karnack, et al., Methane–air detonation experiments at NIOSH Lake Lynn Laboratory, Journal of Loss Prevention in the Process Industries 26 (2) (2013) 295–301. doi:10.1016/j.jlp.2011.05.003. 42

[180] S. Zhou, H. Ma, S. Chen, Y. Zhong, C. Zhou, Experimental investigation on propagation characteristics of rotating detonation wave with a hydrogen-ethylene-acetylene fuel, Acta Astronautica 157 (2019) 310–320. doi:10.1016/j.actaastro.2019.01.009. 42

[181] W. Strauss, S. JN, Experimental investigation of the detonation properties of hydrogen-oxygen and hydrogen-nitric oxide mixtures at initial pressures up to 40 atmospheres, Combustion and Flame 19 (1972) 141–143. doi:10.1016/s0010-2180(72)80097-x. 42

[182] T. Mogi, S. Horiguchi, Explosion and detonation characteristics of dimethyl ether, Journal of hazardous materials 164 (1) (2009) 114–119. doi:10.1016/j.jhazmat.2008.07.133. 42

[183] Norma UNE 31-002-94: Cálculo de las principales características teóricas de los explosivos, Asociación Española de Normalización UNE, 1994. 42

[184] European Standard EN 13631-15: Explosives for Civil use – High Explosives – Part 15: Calculation of the Thermodynamic Properties, 2005. 42

[185] M. L. Hobbs, M. R. Baer, Nonideal thermoequilibrium calculations using a large product species data base, Shock Waves 2 (3) (1992) 177–187. doi:10.1007/BF01414640. 42

[186] O. Heuzé, Equations of state of detonation products: Influence of the repulsive intermolecular potential, Phys. Rev. A 34 (1) (1986) 428–432. doi:10.1103/PhysRevA.34.428. 42

[187] C. Li, K. Kailasanath, E. S. Oran, Detonation structures behind oblique shocks, Physics of Fluids 6 (4) (1994) 1600–1611. doi:10.1063/1.868273. 42

[188] K. Kailasanath, Review of propulsion applications of detonation waves, AIAA journal 38 (9) (2000) 1698–1708. doi:10.2514/3.14599. 42, 62

[189] J. M. Powers, K. A. Gonthier, Reaction zone structure for strong, weak overdriven, and weak underdriven oblique detonations, Physics of Fluids A: Fluid Dynamics 4 (9) (1992) 2082–2089. doi:10.1063/1.858378. 42

[190] Z. Zhang, Y. Liu, C. Wen, Mechanisms of the destabilized Mach reflection of inviscid oblique detonation waves before an expansion corner, Journal of Fluid Mechanics 940. doi:10.1017/jfm.2022.226. 42

[191] X. Zhuo, D. Gang, P. Zhenhua, G. Mingyue, Standing window of oblique detonation with pathological behaviour, Chinese Journal of Aeronautics 34 (5) (2021) 496–503. doi:10.1016/j.cja.2020.12.005. 45

[192] H. Guo, N. Zhao, H. Yang, S. Li, H. Zheng, Analysis on stationary window of oblique detonation wave in methane-air mixture, Aerospace Science and Technology 118 (2021) 107038. doi:10.1016/j.ast.2021.107038. 45

[193] F. García, M. Nürmberger, R. Torres, J. Crespo, ARION 1 reusable sounding rocket: The new microgravity platform in Europe, Adv. Astronaut. Sci. 1 (1) (2018) 23–30. doi:10.1007/s42423-018-0003-7. 45

[194] M. Grossi, A. Sereno, D. Bianchi, B. Favini, Role of finite-rate kinetics on the performance predictions of solid rocket motor nozzles, in: AIAA SCITECH 2023 Forum, 2023, p. 1314. doi:10.2514/6.2023-1314. 47

[195] H. Fangohr, A comparison of C, MATLAB, and Python as teaching languages in engineering, in: International Conference on Computational Science, Springer, 2004, pp. 1210–1217. doi:10.1007/978-3-540-25944-2_157. 60

[196] D. T. Pratt, J. W. Humphrey, D. E. Glenn, Morphology of standing oblique detonation waves, Journal of Propulsion and Power 7 (5) (1991) 837–845. doi:10.2514/3.23399. 62

[197] S. Frolov, V. Aksenov, V. Ivanov, I. Shamshin, A. Zangiev, Air-breathing pulsed detonation thrust module: Numerical simulations and firing tests, Aerospace Science and Technology 89 (2019) 275–287. doi:10.1016/j.ast.2019.04.005. 62

[198] K. Kailasanath, Recent developments in the research on pulse detonation engines, AIAA journal 41 (2) (2003) 145–159. doi:10.2514/6.2002-470. 62

[199] Q. Meng, N. Zhao, H. Zheng, J. Yang, L. Qi, Numerical investigation of the effect of inlet mass flow rates on H2/air non-premixed rotating detonation wave, International Journal of Hydrogen Energy 43 (29) (2018) 13618–13631. doi:10.1016/j.ijhydene.2018.05.115. 62

[200] M. Short, J. J. Quirk, On the nonlinear stability and detonability limit of a detonation wave for a model three-step chain-branching reaction, Journal of Fluid Mechanics 339 (1997) 89–119. doi:10.1017/S002211209700503X. 63

[201] A. R. Kasimov, D. S. Stewart, On the dynamics of self-sustained one-dimensional detonations: A numerical study in the shock-attached frame, Physics of Fluids 16 (10) (2004) 3566–3578. doi:10.1063/1.1776531. 63

[202] M. I. Radulescu, G. J. Sharpe, C. K. Law, J. H. Lee, The hydrodynamic structure of unstable cellular detonations, Journal of Fluid Mechanics 580 (2007) 31–81. doi:10.1017/S0022112007005046. 63

[203] J. Shepherd, Detonation in gases, Proceedings of the Combustion Institute 32 (1) (2009) 83–98. doi:10.1016/j.proci.2008.08.006. 63

[204] P. Clavin, F. A. Williams, Analytical studies of the dynamics of gaseous detonations, Philosophical Transactions of the Royal Society A: Mathematical, Physical and Engineering Sciences 370 (1960) (2012) 597–624. doi:10.1098/rsta.2011.0345. 63

[205] D. I. Kabanov, A. R. Kasimov, Linear stability analysis of detonations via numerical computation and dynamic mode decomposition, Physics of Fluids 30 (3) (2018) 036103. doi:10.1063/1.5020558. 63

[206] W. Han, C. Wang, C. K. Law, Pulsation in one-dimensional H2–O2 detonation with detailed reaction mechanism, Combustion and Flame 200 (2019) 242–261. doi:10.1016/j.combustflame.2018.11.024. 63

[207] C. Huete, M. Vera, D'Yakov–Kontorovich instability in planar reactive shocks, Journal of Fluid Mechanics 879 (2019) 54–84. doi:10.1017/jfm.2019.689. 63, 180

[208] F. A. Williams, Structure of detonations in dilute sprays, The Physics of Fluids 4 (11) (1961) 1434–1443. doi:10.1063/1.1706236. 63, 189

[209] B. Veyssiere, B. Khasainov, Structure and multiplicity of detonation regimes in heterogeneous hybrid mixtures, Shock Waves 4 (4) (1995) 171–186. doi:10.1007/BF01414983. 63

[210] D. Kessler, V. Gamezo, E. Oran, Gas-phase detonation propagation in mixture composition gradients, Philosophical Transactions of the Royal Society A: Mathematical, Physical and Engineering Sciences 370 (1960) (2012) 567–596. doi:10.1098/rsta.2011.0342. 63

[211] F. Ettner, K. G. Vollmer, T. Sattelmayer, Mach reflection in detonations propagating through a gas with a concentration gradient, Shock Waves 23 (3) (2013) 201–206. doi:10.1007/s00193-012-0385-8. 63

[212] S. Prakash, R. Fiévet, V. Raman, J. Burr, K. H. Yu, Analysis of the detonation wave structure in a linearized rotating detonation engine, AIAA Journal (2019) 1–15doi:10.2514/1.j058156. 63

[213] S. Prakash, R. Fiévet, V. Raman, The effect of fuel stratification on the detonation wave structure, in: AIAA Scitech 2019 Forum, 2019, p. 1511. doi:10.2514/6.2019-1511. 63

[214] S. Prakash, S. Raman, Detonation propagation through inhomogeneous fuel-air mixtures, in: International Colloquium on the Dynamics of Explosions and Reactive Systems, 2019, p. 81. 63, 64, 85, 96, 164

[215] X. Mi, A. J. Higgins, H. D. Ng, C. B. Kiyanda, N. Nikiforakis, Propagation of gaseous detonation waves in a spatially inhomogeneous reactive medium, Physical Review Fluids 2 (5) (2017) 053201. doi:10.1103/PhysRevFluids.2.053201. 63, 64, 94, 96, 164

[216] X. Mi, E. V. Timofeev, A. J. Higgins, Effect of spatial discretization of energy on detonation wave propagation, Journal of Fluid Mechanics 817 (2017) 306–338. doi:10.1017/jfm.2017.81. 63, 64, 94, 96, 164

[217] J. W. Meadows, S. Subramanian, Novel approach for modeling non-premixed rotating detonation engine using a 2-D CFD analysis, in: AIAA Propulsion and Energy 2019 Forum, 2019, p. 4130. doi:10.2514/6.2019-4130. 63

[218] K. Kailasanath, Liquid-fueled detonations in tubes, Journal of Propulsion and Power 22 (6) (2006) 1261–1268. doi:10.2514/1.19624. 63

[219] H. Watanabe, A. Matsuo, K. Matsuoka, A. Kawasaki, J. Kasahara, Numerical investigation on propagation behavior of gaseous detonation in water spray, Proceedings of the Combustion Institute 37 (3) (2019) 3617–3626. doi:10.1016/j.proci.2018.07.092. 63, 85, 189

[220] H. Watanabe, A. Matsuo, A. Chinnayya, K. Matsuoka, A. Kawasaki, J. Kasahara, Numerical analysis of the mean structure of gaseous detonation with dilute water spray, Journal of Fluid Mechanics 887. doi:10.1017/jfm.2019.1018. 63, 85, 189

[221] Y. Xu, M. Zhao, H. Zhang, Extinction of incident hydrogen/air detonation in fine water sprays, Physics of Fluids 33 (11) (2021) 116109. doi:10.1063/5.0071405. 63

[222] M. Zhao, H. Zhang, Rotating detonative combustion in partially pre-vaporized dilute n-heptane sprays: Droplet size and equivalence ratio effects, Fuel 304 (2021) 121481. doi:10.1016/j.fuel.2021.121481. 63

[223] L. Massa, M. Chauhan, F. Lu, Detonation–turbulence interaction, Combustion and Flame 158 (9) (2011) 1788–1806. doi:10.1016/j.combustflame.2011.01.014. 63, 80, 84

[224] L. Massa, F. K. Lu, The role of the induction zone on the detonation–turbulence linear interaction, Combustion Theory and Modelling 15 (3) (2011) 347–371. doi:10.1080/13647830.2010.540353. 63, 80, 81, 84

[225] T. Jin, K. Luo, Q. Dai, J. Fan, Simulations of cellular detonation interaction with turbulent flows, AIAA Journal 54 (2) (2016) 419–433. doi:10.2514/1.J054538. 63

[226] S. M. Hussein, Direct numerical simulation of homogeneous isotropic turbulence-a methodology and applications, Ph.D. thesis, The University of Texas at Arlington (2018). 63

[227] T. L. Jackson, A. K. Kapila, M. Y. Hussaini, Convection of a pattern of vorticity through a reacting shock wave, Physics of Fluids A: Fluid Dynamics 2 (7) (1990) 1260–1268. doi:10.1063/1.857626. 63, 64

[228] T. Jackson, M. Hussaini, H. Ribner, Interaction of turbulence with a detonation wave, Physics of Fluids A: Fluid Dynamics 5 (3) (1993) 745–749. 63, 64, 81, 83

[229] C. Huete, A. L. Sánchez, F. A. Williams, Theory of interactions of thin strong detonations with turbulent gases, Physics of Fluids 25 (7) (2013) 076105. doi:10.1063/1.4816353. 63, 64, 75, 79, 179

[230] C. Huete, A. L. Sánchez, F. A. Williams, Linear theory for the interaction of small-scale turbulence with overdriven detonations, Physics of Fluids 26 (11) (2014) 116101. doi:10.1063/1.4901190. 63

[231] J. Griffond, Linear interaction analysis applied to a mixture of two perfect gases, Physics of Fluids 17 (8) (2005) 086101. doi:10.1063/1.1997982. 63, 64

[232] C. Huete, T. Jin, D. Martínez-Ruiz, K. Luo, Interaction of a planar reacting shock wave with an isotropic turbulent vorticity field, Physical Review E 96 (5) (2017) 053104. doi:10.1103/physreve.96.053104. 63, 81, 113, 179

[233] G. Farag, P. Boivin, P. Sagaut, Interaction of two-dimensional spots with a heat releasing/absorbing shock wave: linear interaction approximation results, Journal of Fluid Mechanics 871 (2019) 865–895. doi:10.1017/jfm.2019.324. 64

[234] S. K. Lele, Shock-jump relations in a turbulent flow, Physics of Fluids A: Fluid Dynamics 4 (12) (1992) 2900–2905. doi:10.1063/1.858343. 64, 85

[235] G. Hazak, A. L. Velikovich, J. H. Gardner, J. P. Dahlburg, Shock propagation in a low-density foam filled with fluid, Physics of Plasmas 5 (12) (1998) 4357–4365. doi:10.1063/1.873172. 64, 85

[236] A. Velikovich, C. Huete, J. Wouchuk, Effect of shock-generated turbulence on the hugoniot jump conditions, Physical Review E 85 (1) (2012) 016301. doi:10.1103/physreve.85.016301. 64, 85, 87

[237] Y. Tian, F. A. Jaberi, D. Livescu, Modeling of shock propagation in non-uniform density media, in: AIAA Scitech 2020 Forum, 2020, p. 0101. doi:10.2514/6.2020-0101. 64, 85

[238] J. Li, X. Mi, A. J. Higgins, Effect of spatial heterogeneity on near-limit propagation of a pressure-dependent detonation, Proceedings of the Combustion Institute 35 (2) (2015) 2025–2032. doi:10.1016/j.proci.2014.06.039. 64, 96, 164

[239] B. Zhang, J. Chen, M. Shahsavari, H. Wen, B. Wang, X. Tian, Effects of inert dispersed particles on the propagation characteristics of a H2/CO/air detonation wave, Aerospace Science and Technology 126 (2022) 107660. doi:10.1016/j.ast.2022.107660. 64

[240] D. Brouzet, G. Vignat, M. Ihme, Dynamics and structure of detonations in stratified product-gas diluted mixtures, Proceedings of the Combustion Institutedoi:10.1016/j.proci.2022.07.173. 64

[241] X. Zhao, J. Wang, L. Gao, X. Wang, Y. Zhu, Flame acceleration and onset of detonation in inhomogeneous mixture of hydrogen-air in an obstructed channel, Aerospace Science and Technology 130 (2022) 107944. doi:10.1016/j.ast.2022.107944. 64

[242] Y. Zhou, X. Zhang, L. Zhong, R. Deiterding, L. Zhou, H. Wei, Effects of fluctuations in concentration on detonation propagation, Physics of Fluids 34 (7) (2022) 076101. doi:10.1063/5.0096965. 64

[243] Y. Wang, C. Huang, R. Deiterding, H. Chen, Z. Chen, Numerical studies on detonation propagation in inhomogeneous mixtures with periodic reactant concentration gradient, Journal of Fluid Mechanics 955 (2023) A23. doi:10.1017/jfm.2022.1074. 64

[244] M. Holzer, E. D. Siggia, Turbulent mixing of a passive scalar, Physics of Fluids 6 (5) (1994) 1820–1837. doi:10.1063/1.868243. 65, 67

[245] R. S. Miller, Long time mass fraction statistics in stationary compressible isotropic turbulence at supercritical pressure, Physics of Fluids 12 (8) (2000) 2020–2032. doi:10.1063/1.870448. 65, 67

[246] G. K. Batchelor, The Theory of Homogeneous Turbulence, Cambridge university press, Cambridge, 1953. 67

[247] P. Sagaut, C. Cambon, Homogeneous Turbulence Dynamics, Vol. 10, Springer, Cham, Switzerland, 2008. 67

[248] D. Livescu, Turbulence with large thermal and compositional density variations, Annual Review of Fluid Mechanics 52. doi:10.1146/annurev-fluid-010719-060114. 67, 85

[249] B.-T. Chu, L. S. Kovásznay, Non-linear interactions in a viscous heat-conducting compressible gas, Journal of Fluid Mechanics 3 (5) (1958) 494–514. doi:10.1017/s0022112058000148. 73, 112, 184

[250] Y. Andreopoulos, J. H. Agui, G. Briassulis, Shock wave—turbulence interactions, Annual Review of Fluid Mechanics 32 (1) (2000) 309–345. 83

[251] P. J. Westervelt, The mean pressure and velocity in a plane acoustic wave in a gas, The Journal of the Acoustical Society of America 22 (3) (1950) 319–327. doi:10.1121/1.1906606. 87

[252] D. T. Blackstock, Propagation of plane sound waves of finite amplitude in nondissipative fluids, The Journal of the Acoustical Society of America 34 (1) (1962) 9–30. doi:10.1121/1.1909033. 87

[253] L. Ostrovskii, Second-order terms in a traveling sound wave (traveling sound wave in compressible medium, deriving expressions for time and coordinate averages of perturbations in second order), Soviet Physics-Acoustics 14 (1968) 61–66. 87

[254] C. Park, Nonequilibrium Hypersonic Aerothermodynamics, Wiley, New York, 1990. 99, 100, 139, 154, 167

[255] W. H. Stillwell, X-15 Research Results, Vol. 60, Scientific and Technical Information Division, National Aeronautics and Space Administration, Washington, D.C., 1965. 99

[256] J. Urzay, M. Di Renzo, Engineering aspects of hypersonic turbulent flows at suborbital enthalpies, Annual Research Briefs, Center for Turbulence Research, Stanford University (2020) 7–32. 99

[257] S. P. Schneider, Effects of high-speed tunnel noise on laminar-turbulent transition, Journal of Spacecraft and Rockets 38 (3) (2001) 323–333. doi:10.2514/6.2000-2205. 99

[258] D. Dolling, C. Or, Unsteadiness of the shock wave structure in attached and separated compression ramp flows, Experiments in Fluids 3 (1) (1985) 24–32. doi:10.1007/bf00285267. 99, 142

[259] A. J. Smits, K.-C. Muck, Experimental study of three shock wave/turbulent boundary layer interactions, Journal of Fluid Mechanics 182 (1987) 291–314. doi:10.1017/S0022112087002349. 99, 142

[260] J. Andreopoulos, K. Muck, Some new aspects of the shock-wave/boundary-layer interaction in compression-ramp flows, Journal of Fluid Mechanics 180 (1987) 405–428. doi:10.1017/s0022112087001873. 99, 142

[261] Y. Zhao, S. Yi, L. He, Z. Cheng, L. Tian, The experimental study of interaction between shock wave and turbulence, Chinese Science Bulletin 52 (10) (2007) 1297–1301. doi:10.1007/s11434-007-0177-1. 99, 142

[262] X. I. Yang, J. Urzay, S. T. Bose, P. Moin, Aerodynamic heating in wall-modeled large-eddy simulation of high-speed turbulent flows, AIAA Journal 56 (2018) 731–742. doi:10.2514/1.J056240. 99

[263] P. S. Volpiani, M. Bernardini, J. Larsson, Effects of a nonadiabatic wall on supersonic shock/boundary-layer interactions, Physical Review Fluids 3 (8) (2018) 083401. doi:10.1103/PhysRevFluids.3.083401. 99

[264] P. S. Volpiani, M. Bernardini, J. Larsson, Effects of a nonadiabatic wall on hypersonic shock/boundary-layer interactions, Physical Review Fluids 5 (1) (2020) 014602. doi:10.1103/PhysRevFluids.5.014602. 99

[265] D. Sun, Q. Guo, C. Li, P. Liu, Direct numerical simulation of effects of a micro-ramp on a hypersonic shock wave/boundary layer interaction, Physics of Fluids 31 (12) (2019) 126101. doi:10.1063/1.5123453. 99

[266] W.-Z. Xie, S.-Z. Yang, C. Zeng, K. Liao, R.-H. Ding, L. Zhang, S. Guo, Improvement of the free-interaction theory for shock wave/turbulent boundary layer interactions, Physics of Fluids 33 (7) (2021) 075104. doi:10.1063/5.0050113. 99

[267] L. Fu, M. Karp, S. T. Bose, P. Moin, J. Urzay, Shock-induced heating and transition to turbulence in a hypersonic boundary layer, Journal of Fluid Mechanics 909. doi:10.1017/jfm.2020.935. 99

[268] L. Hesselink, B. Sturtevant, Propagation of weak shocks through a random medium, Journal of Fluid Mechanics 196 (1988) 513–553. doi:10.1017/S0022112088002800. 99, 143

[269] J. Keller, W. Merzkirch, Interaction of a normal shock wave with a compressible turbulent flow, Mineralium Deposita 29 (1) (1994) 241–248. doi:10.1007/bf00187225. 99, 143

[270] S. Barre, D. Alem, J. Bonnet, Experimental study of a normal shock/homogeneous turbulence interaction, AIAA journal 34 (5) (1996) 968–974. doi:10.2514/6.1995-579. 99, 139, 143

[271] K. Inokuma, T. Watanabe, K. Nagata, A. Sasoh, Y. Sakai, Finite response time of shock wave modulation by turbulence, Physics of Fluids 29 (5) (2017) 051701. doi:10.1063/1.4982932. 99

[272] K. Inokuma, T. Watanabe, K. Nagata, Y. Sakai, Statistics of overpressure fluctuations behind a weak shock wave interacting with turbulence, Physics of Fluids 31 (8) (2019) 085119. doi:10.1063/1.5110185. 99

[273] K. Sinha, K. Mahesh, G. V. Candler, Modeling shock unsteadiness in shock/turbulence interaction, Physics of fluids 15 (8) (2003) 2290–2297. doi:10.1063/1.1588306. 99, 143

[274] B. Morgan, K. Duraisamy, N. Nguyen, S. Kawai, S. Lele, Flow physics and RANS modelling of oblique shock/turbulent boundary layer interaction, Journal of Fluid Mechanics 729 (2013) 231. doi:10.1017/jfm.2013.301. 99

[275] J. Wouchuk, C. H. R. de Lira, A. Velikovich, Analytical linear theory for the interaction of a planar shock wave with an isotropic turbulent vorticity field, Physical Review E 79 (6) (2009) 066315. doi:10.1103/physreve.79.066315. 100, 113, 125, 130, 143

[276] Y. B. Zel'dovich, Y. P. Raizer, Physics of Shock Waves and High-Temperature Hydrodynamic Phenomena, Dover Publications, Mineola, New York, 2002. 100

[277] M. Di Renzo, L. Fu, J. Urzay, HTR solver: An open-source exascale-oriented task-based multi-GPU high-order code for hypersonic aerothermodynamics, Computer Physics Communications 255 (2020) 107262. doi:10.1016/j.cpc.2020.107262. 100, 154, 155, 157, 158, 167

[278] M. Di Renzo, S. Pirozzoli, HTR-1.2 solver: Hypersonic Task-based Research solver version 1.2, Computer Physics Communications 261 (2021) 107733. doi:10.1016/j.cpc.2020.107733. 100, 154, 155, 157, 158, 167

[279] M. Di Renzo, HTR-1.3 solver: Predicting electrified combustion using the hypersonic task-based research solver, Computer Physics Communications 272 (2022) 108247. doi:10.1016/j.cpc.2021.108247. 100, 154, 155, 157, 158, 167

[280] C. E. Treanor, P. V. Marrone, Effect of dissociation on the rate of vibrational relaxation, The Physics of Fluids 5 (9) (1962) 1022–1026. doi:10.1063/1.1724467. 100

[281] W. Vincenti, C. H. Kruger, Introduction to physical gas dynamics, John Wlley & Sons, 1965. 103, 136, 142

[282] N. M. Kuznetsov, Stability of shock waves, Soviet Physics Uspekhi 32 (1989) 993–1012. doi:10.1070/PU1989v032n11ABEH002777. 109

[283] R. Menikoff, B. J. Plohr, The Riemann problem for fluid flow of real materials, Reviews of modern physics 61 (1) (1989) 75. doi:10.1103/revmodphys.61.75. 109

[284] J. J. Erpenbeck, Stability of step shocks, Physics of Fluids 5 (10) (1962) 1181–1187. doi:10.1063/1.1706917. 109

[285] N. M. Kuznetsov, Criterion for instability of a shock wave maintained by a piston, Doklady Akademii Nauk SSSR 227 (1) (1984) 65–68. 109

[286] L. D. Landau, E. M. Lifshitz, Fluid mechanics pergamon, New York 61. 109

[287] M. Mond, I. Rutkevich, Spontaneous acoustic emission from strong ionizing shocks, Journal of Fluid Mechanics 275 (1994) 121–146. doi:10.1017/S0022112094002302. 109, 194

[288] M. Mond, I. Rutkevich, E. Toffin, Stability of ionizing shock waves in monatomic gases, Physical Review E 56 (5, B) (1997) 5968–5978. doi:10.1103/PhysRevE.56.5968. 109, 194

[289] M. Mond, I. Rutkevich, Spontaneous acoustic emission from strong shocks in diatomic gases, Physics of Fluids 14 (4) (2002) 1468–1475. doi:10.1063/1.1458005. 109

[290] D. Davies, Shock waves in air at very high pressures, Proceedings of the Physical Society 61 (2) (1948) 105–118. doi:10.1088/0959-5309/61/2/301. 109

[291] M. Kamel, A. Ghoniem, M. Rashed, A. Oppenheim, Blast waves in real gases, Acta Astronautica 4 (3-4) (1977) 439–458. doi:10.1016/0094-5765(77)90061-3. 109

[292] S. Zhang, K. P. Driver, F. Soubiran, B. Militzer, Equation of state and shock compression of warm dense sodium—A first-principles study, The Journal of Chemical Physics 146 (7) (2017) 074505. doi:10.1063/1.4976559. 109

[293] N. Wetta, J.-C. Pain, O. Heuzé, D'yakov-Kontorovitch instability of shock waves in hot plasmas, Physical Review E 98 (3) (2018) 033205. doi:10.1103/physreve.98.033205. 109

[294] B. J. McBride, Computer program for calculating and fitting thermodynamic functions, Vol. 1271, NASA, 1992. 134, 136

[295] B. Bottin, Thermodynamic properties of arbitrary perfect gas mixtures at low pressures and high temperatures, Progress in Aerospace Sciences 36 (7) (2000) 547–579. doi:10.1016/s0376-0421(00)00009-9. 136, 152, 199

[296] A. D'angola, G. Colonna, C. Gorse, M. Capitelli, Thermodynamic and transport properties in equilibrium air plasmas in a wide pressure and temperature range, The European Physical Journal D 46 (1) (2008) 129–150. doi:10.1140/epjd/e2007-00305-4. 136, 166, 199

[297] M. Capitelli, D. Bruno, G. Colonna, C. Catalfamo, A. Laricchiuta, Thermodynamics and transport properties of thermal plasmas: the role of electronic excitation, Journal of Physics D: Applied Physics 42 (19) (2009) 194005. doi:10.1088/0022-3727/42/19/194005. 136

[298] G. Colonna, A. D'Angola, M. Capitelli, Electronic excitation and isentropic coefficients of high temperature planetary atmosphere plasmas, Physics of Plasmas 19 (7) (2012) 072115. doi:10.1063/1.4737190. 136

[299] J. E. Mayer, M. G. Mayer, Statistical mechanics, Vol. 28, John Wiley & Sons New York, 1940. 136

[300] L. D. Landau, E. M. Lifshitz, Statistical Physics: Volume 5, Vol. 5, Elsevier, 1958. 136

[301] L. Quartapelle, A. Muzzio, A simple thermodynamic model of diluted hydrogen gas/plasma for CFD applications, The European Physical Journal D 69 (2015) 1–17. doi:10.1140/epjd/e2015-60124-6. 136

[302] O. Askari, Thermodynamic properties of pure and mixed thermal plasmas over a wide range of temperature and pressure, Journal of Energy Resources Technology 140 (3). doi:10.1115/1.4037688. 136, 152, 166, 170, 199

[303] J. Urzay, N. Kseib, D. F. Davidson, G. Iaccarino, R. K. Hanson, Uncertainty-quantification analysis of the effects of residual impurities on hydrogen–oxygen ignition in shock tubes, Combustion and Flame 161 (1) (2014) 1–15. doi:10.1016/j.combustflame.2013.08.012. 138

[304] J. W. Streicher, A. Krish, R. K. Hanson, K. M. Hanquist, R. S. Chaudhry, I. D. Boyd, Shock-tube measurements of coupled vibration–dissociation time-histories and rate parameters in oxygen and argon mixtures from 5000 K to 10 000 K, Physics of Fluids 32 (7) (2020) 076103. doi:10.1063/5.0012426. 139, 167

[305] P. M. Finch, J. Girard, C. Strand, W. Yu, J. Austin, H. Hornung, R. K. Hanson, Measurements of time-resolved air freestream nitric oxide rotational, vibrational temperature and concentration in the T5 reflected shock tunnel, in: AIAA Paper 2020-3714, 2020. doi:10.2514/6.2020-3714. 139, 167

[306] J. W. Streicher, A. Krish, R. K. Hanson, Coupled vibration-dissociation time-histories and rate measurements in shock-heated, nondilute O2 and O2–Ar mixtures from 6000 to 14000K, Physics of Fluids 33 (5) (2021) 056107. doi:10.1063/5.0048059. 139, 167

[307] J. Mattis, Department of Defense, Washington, United States., Summary of the 2018 National Defense Strategy of the United States of America. 142

[308] V. Theofilis, S. Pirozzoli, P. Martin, Special issue on the fluid mechanics of hypersonic flight (2022). doi:10.1007/s00162-022-00605-2. 142

[309] J. F. Clarke, Chemical reactions in high-speed flows, Philosophical Transactions of the Royal Society of London. Series A: Physical and Engineering Sciences 335 (1637) (1991) 161–199. doi:10.1098/rsta.1991.0042. 142

[310] J. F. Clarke, M. McChesney, The dynamics of real gases, Butterworth, London. doi:10.1063/1.3051243. 142

[311] I. B. Zeldovich, Y. P. Raizer, Physics of Shock Waves and High-temperature Hydrodynamic Phenomena. Volume i, Academic Press New York and London, 1966. 142

[312] J. Urzay, M. Di Renzo, Engineering aspects of hypersonic turbulent flows at suborbital enthalpies, Annual Research Briefs, Center for Turbulence Research (2021) 7–32. 142

[313] R. Hannappel, R. Friedrich, Direct numerical simulation of a Mach 2 shock interacting with isotropic turbulence, Applied scientific research 54 (1995) 205–221. doi:10.1007/bf00849117. 143

[314] K. Mahesh, S. Lee, S. K. Lele, P. Moin, The interaction of an isotropic field of acoustic waves with a shock wave, Journal of Fluid Mechanics 300 (1995) 383–407. doi:10.1017/s0022112095003739. 143

[315] S. Jamme, J.-B. Cazalbou, F. Torres, P. Chassaing, Direct numerical simulation of the interaction between a shock wave and various types of isotropic turbulence, Flow, Turbulence and Combustion 68 (2002) 227–268. doi:10.1023/A:1021197225166. 143

[316] D. A. Donzis, Amplification factors in shock-turbulence interactions: effect of shock thickness, Physics of Fluids 24 (1) (2012) 011705. doi:10.1063/1.3676449. 143, 161

[317] D. A. Donzis, Shock structure in shock-turbulence interactions, Physics of Fluids 24 (12) (2012) 126101. doi:10.1063/1.4772064. 143

[318] X. Gao, I. Bermejo-Moreno, J. Larsson, Parametric numerical study of passive scalar mixing in shock turbulence interaction, Journal of Fluid Mechanics 895 (2020) A21. doi:10.1017/jfm.2020.292. 143

[319] S. Ghosh, P. P. Kerkar, Non-equilibrium effects on DNS of hypersonic shock/-turbulence interaction, in: AIAA SCITECH 2022 Forum, 2022, p. 2015. doi:10.2514/6.2022-2015. 143, 156

[320] P. Thakare, V. Nair, K. Sinha, A weakly nonlinear framework to study shock–vorticity interaction, Journal of Fluid Mechanics 933 (2022) A48. doi:10.1017/jfm.2021.1076. 143, 156

[321] C. H. Chen, Linear analysis on pressure-dilatation behind shock waves, Physics of Fluids 35 (2) (2023) 021701. doi:10.1063/5.0138476. 143

[322] N. E. Grube, M. P. Martín, Compressibility effects on Reynolds stress amplification and shock structure in shock–isotropic turbulence interactions, Journal of Fluid Mechanics 958 (2023) A1. doi:10.1017/jfm.2022.984. 143

[323] M. Smart, Scramjets, The Aeronautical Journal 111 (1124) (2007) 605–619. doi:10.1017/S0001924000004796. 153

[324] C. Williams, M. Di Renzo, J. Urzay, Two-temperature extension of the HTR solver for hypersonic turbulent flows in thermochemical nonequilibrium, Annual Research Briefs, Center for Turbulence Research (2021) 95–107. 154

[325] T. J. Poinsot, S. K. Lele, Boundary conditions for direct simulations of compressible viscous flows, Journal of Computational Physics 101 (1992) 104–129. doi:10.1016/0021-9991(92)90046-2. 154

[326] P. Thakare, K. Sinha, V. Nair, Nonlinear generation of sound and mean pressure drop in shock–shear interaction, Physics of Fluids 35 (1) (2023) 016123. doi:10.1063/5.0133193. 156

[327] B. McManamen, D. Donzis, S. North, R. Bowersox, Velocity and temperature fluctuations in a high-speed shock–turbulence interaction, Journal of Fluid Mechanics 913. doi:10.1017/jfm.2020.1161. 159

[328] O. Askari, G. P. Beretta, K. Eisazadeh-Far, H. Metghalchi, On the thermodynamic properties of thermal plasma in the flame kernel of hydrocarbon/air premixed gases, The European Physical Journal D 70 (8) (2016) 1–22. doi:10.1140/epjd/e2016-70195-4. 166, 170

[329] C. H. Kruger, W. Vincenti, Introduction to physical gas dynamics, John Wiley & Sons. 198

[330] H. R. Griem, High-density corrections in plasma spectroscopy, Physical Review 128 (3) (1962) 997. doi:10.1103/physrev.128.997. 199

[331] K. Drellishak, D. Aeschliman, A. B. Cambel, Partition functions and thermodynamic properties of nitrogen and oxygen plasmas, The Physics of Fluids 8 (9) (1965) 1590–1600. doi:10.1063/1.1761469. 199

[332] C. F. Hansen, Approximations for the thermodynamic and transport properties of high-temperature air, NASA TR R-50 (4150). 199

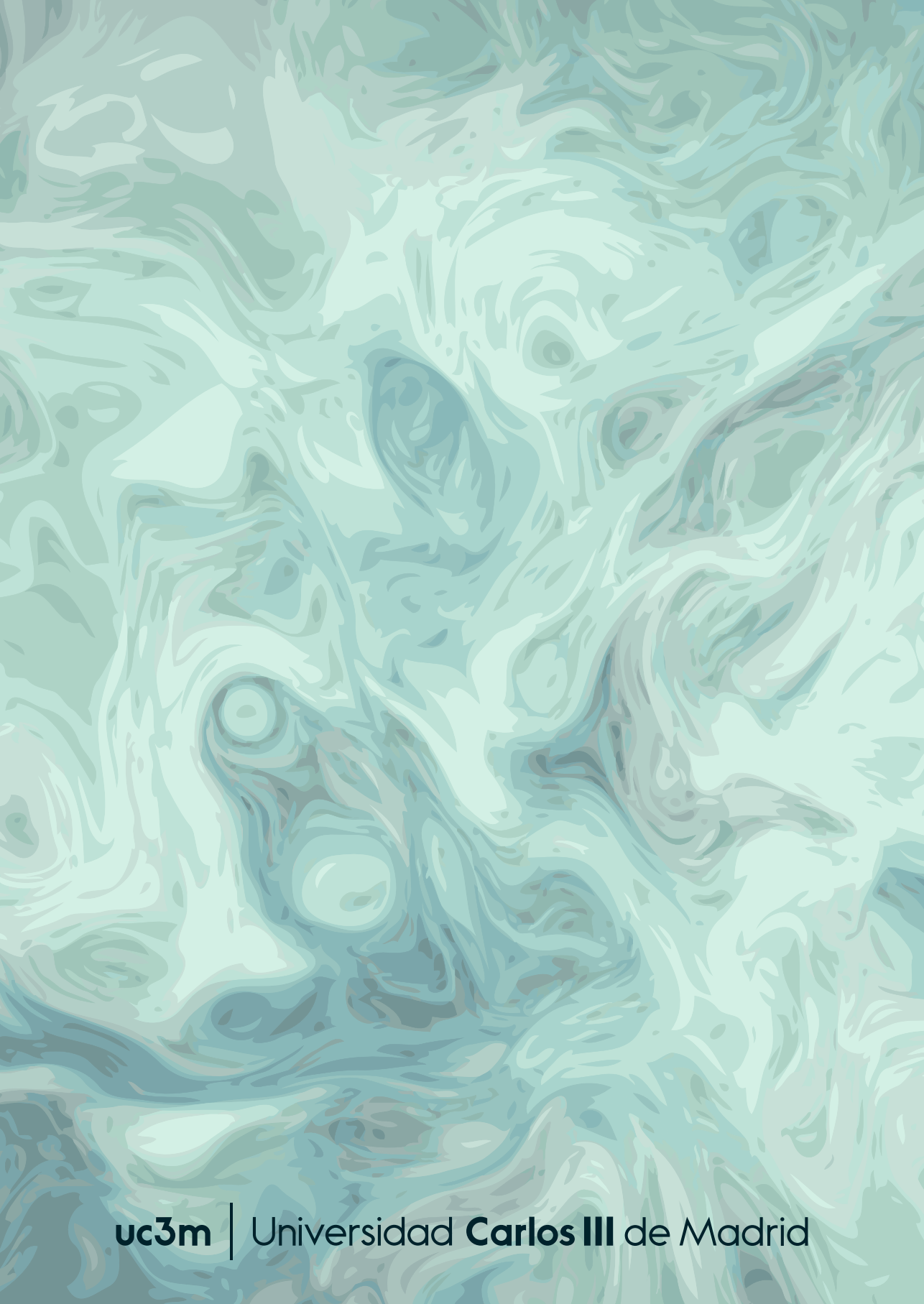

uc3m | Universidad Carlos III de Madrid